Development of novel nanostructured electrodes for biological applications

A thesis submitted for the partial fulfilment of the requirements for the degree of

Doctor of Philosophy in Chemistry

By

David Garrett

The University of Canterbury

2010

Acknowledgements

Without a shadow of a doubt the completion of this PhD will bring to a close one of the most rewarding and challenging times of my life. Along the way I have had many memorable and life changing moments. During the seven plus years I've spent at the University of Canterbury, Cara and I have been blessed with two beautiful energetic sons, Harry and Harvey, a little house in the country, a thriving native garden that we dug into a stony North Canterbury sheep paddock and numerous joyful moments coincident with good exam results and the winning of scholarships including the incredible MacDiarmid, University of Canterbury, IBM visiting scholars program. I have little doubt that winning this scholarship was responsible in no small way for the fantastic position I have now at the University of Melbourne and I thank all those involved in organizing it. All of the academic experiences and successes referred to here were made possible by the academics and staff in the Chemistry Department, and the MacDiarmid Institute, all of whom were open and available and truly appear to have the best interests of the students at heart. Special thanks to Nick, Danny, Wayne, Roger and Steven who make wonderful things and keep everything working in the chemistry building. Thanks to Rob who masterfully made all the special glassware described in this thesis. Thanks to Gary and Helen who taught me microfabrication and endlessly repair the myriad of machines that constantly need help.

Thanks to the Downard group who have all been great company over the last five years and have become good friends. Particular thanks to Xianming Liu who mentored me at the beginning of my PhD and to Frankie Rawson who has taken some elements of my work and got them to sing. Thanks also to Dónal Leech who gave me some great ideas and lab space in Galway and to Ben Flavel and Joe Shapter with whom I shared a very fruitful collaboration. Above all thank you to Prof. Alison Downard who must have wondered what she had gotten into when an over enthusiastic mature student handed in five unreferenced power point slides sporting less than 200 words of text as a fourth year research proposal. It returned to me very rapidly with a note saying "this is not what is

expected of a research proposal". Thankfully I have heard this phrase less frequently lately which is a testament to Alison's patience and fortitude. Thanks for all the advice and for making us aware of all the great travel opportunities and for working so hard for us all, particularly over the last year while being HOD.

Thanks to my parents, Peter and Diane who managed to raise a son with a never ending supply of optimism. I almost always assume that things are going to turn out fine and inevitably they always do. I hope we can give our boys the same sense of self belief. It makes life so much more fun.

Lastly, my eternal gratitude goes to me best friend, my soul mate and my wife, Cara who supported me throughout this long time. It is such a joy to live with you and to have the freedom to finish a thing like a PhD. I can't wait till you start yours. This Thesis is dedicated to you, Harry and Harvey and to the rest of our lives together. I can't imagine the next ten years are going to be any less fun than the last. Where ever we go we always end up having a great time. All my love…..

Dave

Table of contents

Abstract

This thesis describes the development and testing of a range of electrodes designed to be able to measure electrical current produced by the respiration of bacteria in direct contact with the electrode surface. The electrodes are designed to directly wire into redox processes in the cytoskeleton of the bacteria so that electron transfer can be measured in real time without the need for solution based mediator molecules. The rate of electron transfer from the bacteria is enhanced by nanostructuring the surface of graphite electrodes with vertically aligned single and multiwalled carbon nanotubes (CNTs) and covalently coupling mediator molecules to the CNT tips. A selection of the prepared electrodes are tested with the non-electrogenic bacteria *Proteus vulgaris and Bacillus subtilis* to demonstrate the potential of the electrode designs to be used with a wide range of microbial species.

Abbreviations

Commonly used abbreviations

ACN	Acetonitrile
AFM	Atomic force microscopy
AP	4-aminophenyl
Bipy	Bipyridine
CNT	Carbon nanotube
CP	4-carboxyphenyl
CVD	Chemical vapor deposition
DCC	Dicyclohexyl carbodiimide
DCM	Dichloromethane
DMF	Dimethylformamide
DMSO	Dimethylsulfoxide
EDCI	N-(3-dimethylaminopropyl)-N-ethylcarbodiimide hydrochloride
EIS	Electronic impedance spectroscopy
en	Ethylenediamine
EtOH	Ethanol
FcMeOH	Hydroxymethyl ferrocene
GC	Glassy carbon
HOPG	Highly ordered pyrolytic graphite
IPA	Isopropyl alcohol
MeOH	Methanol
MFC	Microbial fuel cell
MWCNT	Multi-walled carbon nanotube
NADH	Nicotine adenine dinucleotide
NHS	N-hydroxy succinimide
NMR	Nuclear magnetic resonance spectroscopy
NP	4-nitrophenyl
PB	Phosphate buffer

PBS	Phosphate buffered saline
PDMS	Polydimethylsiloxane
PVP40	Polyvinylpyrrolidone (Mr = 40,000 g mol^{-1})
PPF	Pyrolysed photoresist film
py	Pyridine
SAM	Self assembled monolayer
SCE	Saturated calomel electrode
SEM	Scanning electron microscope
SWCNT	Single walled carbon nanotube
$TBABF_4$	Tetrabutylammonium tetrafluoroborate
TBAOH	Tetrabutylammonium hydroxide
TEM	Transmission electron microscope
XPS	X-ray photoelectron spectroscopy

Electrochemical abbreviations

AUX	Auxiliary (counter) electrode
CA	Chronoamperometry, chronoamperogram
CV	Cyclic voltammogram, cyclic voltammogram
ΔE_p	CV oxidation and reduction peak potential separation
$E_{1/2}$	Half wave potential
E_{pa}	CV anodic peak potential
E_{pc}	CV cathodic peak potential
LSV	Linear sweep voltammogram
REF	Reference electrode
WE	Working electrode

Published papers

Selective Simultaneous Determination of Paracetamol and Uric Acid Using a Glassy Carbon Electrode Modified with Multiwalled Carbon Nanotube/Chitosan Composite, A Babaei, D.J. Garrett, A J. Downard, Electroanalysis, Accepted Nov 2010 DOI: 10.1002/elan.20100040

Diazonium Salt Derivatives of Osmium Bipyridine Complexes: Electrochemical Grafting and Characterisation of Modified Surfaces, D.J. Garrett, P. Jenkins, M.I.J. Polson, D. Leech, K.H.R. Baronian, A.J. Downard, Electrochimica Acta, Accepted Nov 2010, DOI: 10.10.16/j.electacta 2010.11.070

Electron Transfer from Proteus vulgaris to a Covalently Assembled, Single Walled Carbon Nanotube Electrode Functionalised with Osmium Bipyridine Complex: Application to a Whole Cell Biosensor, F.J Rawson, D.J.Garrett, D. Leech, A.J. Downard, K.H.R. Baronian, Biosensors and Bioelectronics, 26, (2011), 2283

A Simple Approach to Patterned Protein Immobilization on Silicon via Electrografting from Diazonium Salt Solutions, B.S. Flavel, A.J. Gross, D.J. Garrett, V Nock, A.J. Downard, ACS Applied Materials and Interfaces, 2(4), (2010), 1184

Chemically Immobilised Carbon Nanotubes on Silicon: Stable Surfaces for Aqueous Electrochemistry, B.S. Flavel, D. Garrett, J Lehr, J.G. Shapter, A.J. Downard, Electrochimica Acta, 55, (2010), 3995

Patterning of Metal, Carbon, and Semiconductor Substrates with Thin Organic Films by Microcontact Printing with Aryldiazonium Salt Inks, J. Lehr, D.J. Garrett, M.G. Paulik, B.S. Flavel, P.A. Brooksby, B.E. Williamson, A.J. Downard, Analytical Chemistry, 82, (2010), 7027

Robust Forests of Vertically Aligned Carbon Nanotubes Chemically Assembled on Carbon Substrates, D.J. Garrett, B.S. Flavel, J.G. Shapter, K.H.R. Baronian, A.J. Downard, Langmuir, 26(3), (2010), 1848

Chapter 1. Introduction

1.1 Whole cell electrochemistry

1.1.1 Microbial fuel cells (MFC)

Over the last 100 years electrochemical research involving microbes has been dominated by microbial fuel cell research. The first observation that microbial processes generate electricity occurred almost 100 years ago.[1] In that work M.C. Potter inoculated a glucose solution with *Saccharomyces cerevisiae* (baker's yeast) and allowed it to ferment. A porous tube made from dialyzing parchment was filled with the same glucose solution and inserted into the jar to make an inner and outer cylinder (Figure 1.1). Platinum electrodes were inserted into the outer and inner cylinder and the electrical potential (*E)* between them measured. The porous membrane allowed diffusion of ions between the cylinders thus completing the circuit. Under their best conditions a potential of 0.32 V was reached after 10 min of fermentation. The design of Potter's fuel cell is essentially the same as the designs commonly used today. Improvements in the basic design have

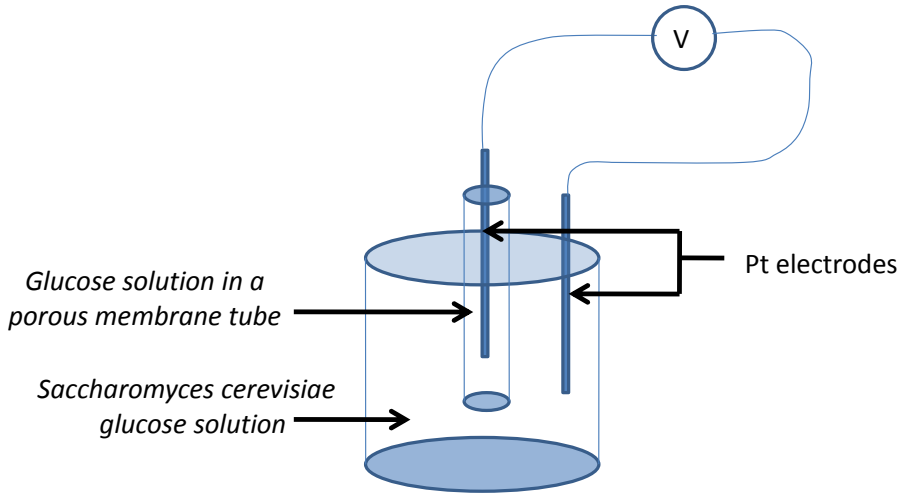

Figure 1.1. Microbial fuel cell design used by M.C. Potter 1911.

included optimization of the membrane material, the electrode composition, the addition of exogenous mediator molecules and the discovery of new strains of bacteria.

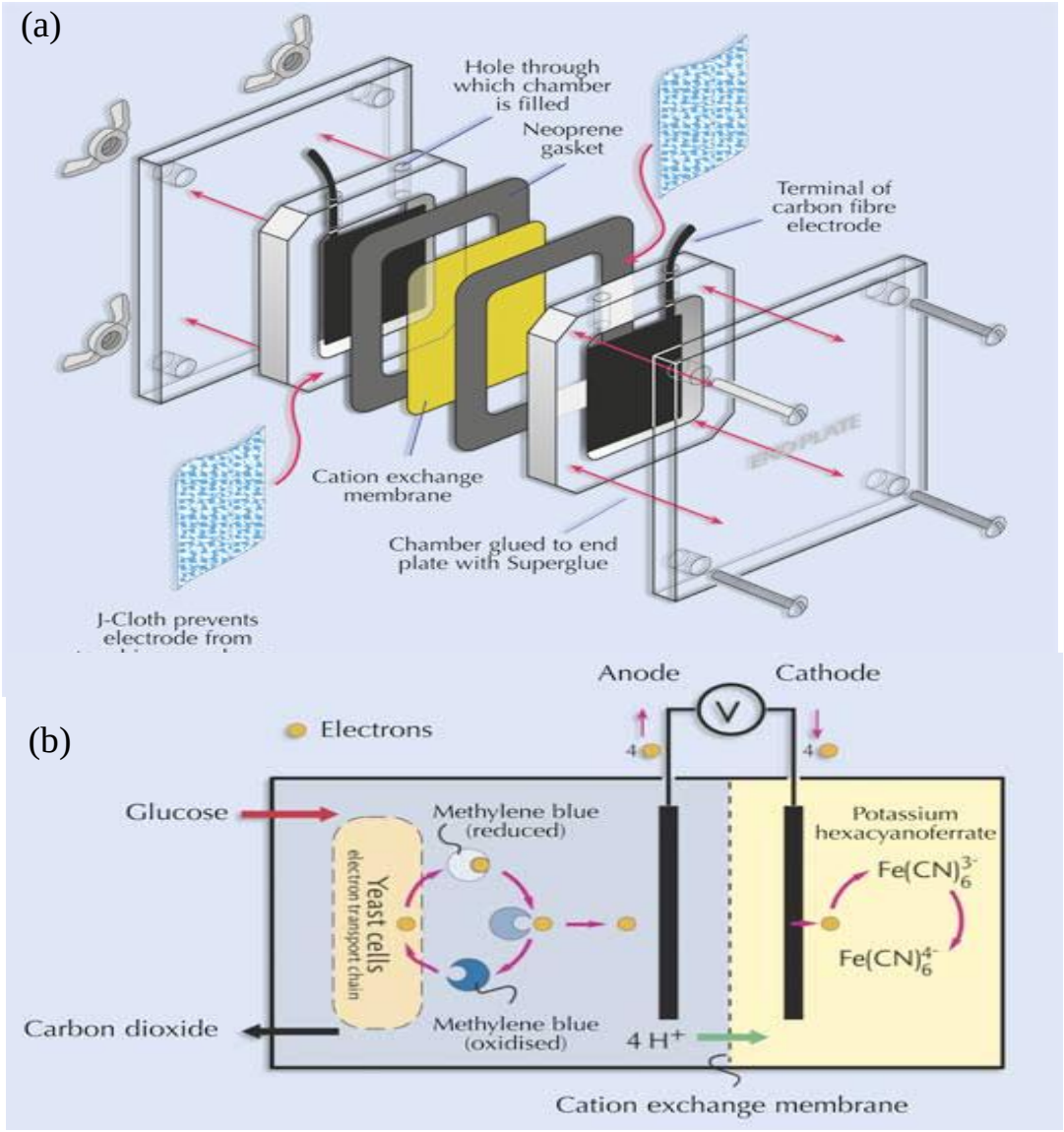

Figure 1. 2. Structure of a modern yeast-based microbial fuel cell (a) and the mediated electrochemical processes occurring in the cell compartments (b). Images courtesy of Dean R. Madden, Dept. Biochemistry, Vail Dartmouth Medical School, Hanover. http://www.scienceinschool.org/2010/issue14/fuelcell

Figure 1. 2 shows the structure of a modern yeast-based microbial fuel cell (a) and the mediated electron transfer chemistry occurring at the anode and cathode of this cell (b). As in Potter's cell, glucose is oxidized by yeast through the normal fermentation

process. The Pt electrodes of Potter have been replaced by high surface area carbon cloth to maximize the electrode contact area with the mediator molecules methylene blue and $Fe(CN)_6^{3-/4-}$. The mediator methylene blue is able to penetrate into the yeast cells and interact with the respiration process inside the cell and become reduced (see section 1.1.2 and 5.1). This means that all of the yeast in the fuel cell can contribute to the power output not just those yeast cells in contact with the electrode. The reduced methylene blue then diffuses to the carbon cloth where it is oxidized transferring electrons to the anode. The driving force for the electron transfer is the presence of $Fe(CN)_6^{3-}$ at the cathode which is more easily reduced than methylene blue (E^o ($Fe(CN)_6^{3-}$) = 0.36 V *vs.* NHE, E^o (methylene blue) = 0.01 V *vs.* NHE [2]). The circuit is completed by proton transport across an efficient proton exchange membrane that permits ionic conduction without mixing of the different chemistries in the compartments. Despite these advances the outlook for MFCs is still poor due to their low power output. The best reported power densities for MFCs are 6 W m^{-2} compared to 800 W m^{-2} for direct methanol fuel cells under optimal conditions.[3]

In recent years MFC research has been dominated by bacterial fuel cells. This rise in research interest can be linked to the discovery of "electrogenic" bacteria. Electrogenic bacteria are a subset of anaerobic bacteria that are capable of electron transfer to solid electrodes. The first of these isolated were a family of Geobacteraceae, found in marine sediment. These were observed to be capable of directly reducing ferric oxides in marine sediments to ferrous compounds.[3-5] The discovery of electrogenic bacteria enabled the production of mediatorless fuel cells such as the one shown in Figure 1.3. The anode of the mediatorless bacterial fuel cell is coated with a living film (bio-film) of electrogenic bacteria. The bio-film consumes (oxidizes) an organic fuel, such as acetate, and passes electrons directly to the anode. The electrons pass around the circuit to reduce an acceptor molecule (O_2 in the presence of H^+ to form water in this instance). The first practical example of a fuel cell of this type was published in 2002 describing a *Geobacteraceae* bio-film on a graphite electrode buried in marine sediment successfully oxidizing organic molecules in the sediment and passing the electrons directly to the electrode resulting in measurable current.[5] This discovery greatly decreased the

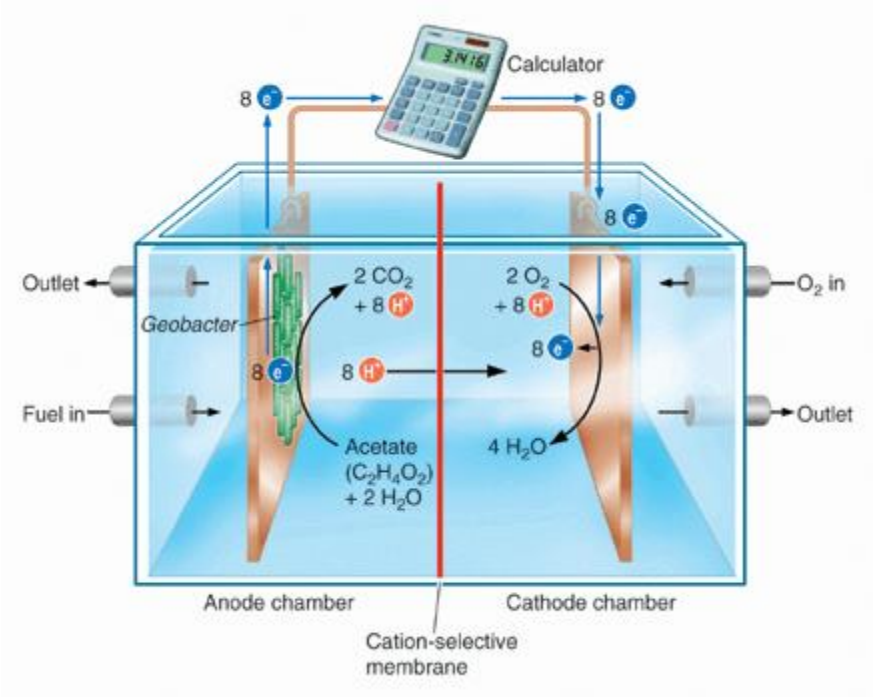

Figure 1.3. Mediatorless *Geobacter* (electrogenic bacteria) fuel cell design. http://www.soultek.com/blog/archives/2008_11_01_archive.html

complexity of microbial fuel cell designs but did not significantly improve their power output. The discovery did, however, lead to an explosion in interest in the mechanisms by which bacteria transfer electrons and the internal cellular redox processes that contribute to charge transfer. The discovery also ignited interest in electrochemical methods as a means of studying redox processes in cells and heralded the utilization of direct microbe / electrode interactions for purposes other than electricity generation.

1.1.2 Electron transport from bacteria to solid electrodes

Direct electron transfer from electrogenic bacteria to solid electrodes is thought to occur via either contact with membrane bound cytochromes,[6-9] contact with conducting pili produced by the bacteria [10-12] or by soluble mediator molecules produced by the bacteria (endogenous mediators).[13-15] Figure 1.4 shows the structure of two such membrane cytochrome proteins showing the redox active heme structures of the proteins in red. These proteins are native to the non-electrogenic Gram-positive bacterium *B. subtilis* but cytochromes of this type are ubiquitous in all bacteria. The key differentiator

between electrogenic and non-electrogenic bacteria is the availability of cytochromes of this type at the periphery of the cell for direct contact reactions with external surfaces. All of the known electrogenic bacteria are Gram-negative which means that they have an inner (cytoplasmic) and outer lipid bilayer membrane with a thin peptidoglycan cell wall between them (refer to the Introduction of Chapter 7 for cell structure information). The natural abundance of electron transfer cytochromes and their orientation and position relative to the bacterial outer membrane dictates the ability of electrogenic bacteria to perform direct electron transfer reactions. Kim *et al.* have shown that the bacterium *Shewanella putrefaciens* develops an increased ability to perform direct electron transfer under anaerobic conditions.[16] It has been previously reported that a high proportion of the membrane

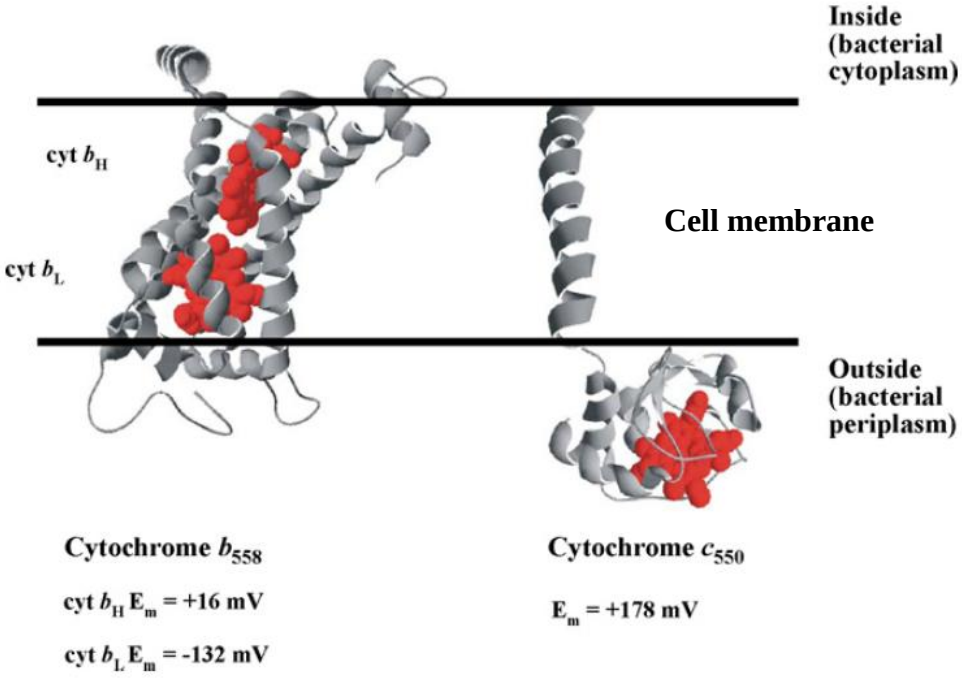

Figure 1.4. Structure of two trans membrane cytochrome proteins native to the bacteria *Bacillus subtilis*. Figure reproduced from reference 8. The cell membrane lies inside a fibrous cell wall.

bound cytochromes in *S. putrefaciens* are located in the outer membrane [17] and that the proportion in the outer membrane is increased under anaerobic conditions.[18] The same authors (Myers and Myers) identified four outer membrane cytochromes and showed that

the UV-Vis absorption of the reduced heme forms of the proteins, rapidly decreased in the presence of iron citrate but not sodium citrate indicating oxidation of the protein by Fe(III).[17]

Non-electrogenic bacteria such as *B. Subtilis* and *P. Vulgaris* (used in this thesis work) are aerobic bacteria and were traditionally thought to be not capable of effectively transfering electrons derived from central metabolism to the outside of the cell [19] because their respiratory proteins are distant from the cell surface. Typical experiments investigating electron transfer from bacteria of this type involve an introduced (exogenous) mediator molecule that can diffuse into the membrane and access redox proteins that are not available at the cell periphery. Many organic and inorganic molecules have been used as soluble mediators [20] including $Fe(CN)_6^{3-/4-}$, [21, 22] neutral red, [21] thionine,[22] napthoquinones,[22] and methylene blue [23] among others. A suspension of *P. vulgaris* has been shown to quantitatively oxidize sucrose and pass the resulting electrons to a solid electrode via the soluble mediator thionine.[24]

Figure 1.5 shows the electron transfer processes that occur during normal aerobic bacterial respiration. Similar to the electron transport chain in the mitochondria of eukaryotic cells, NADH is reduced by NADH reductase and electrons and protons are transferred to the lipid soluble redox molecule ubiquinone (UQ) to produce ubiquinol (UQH_2). UQH_2 is reoxidised by cytochrome bc_1 complex releasing both protons and electrons. The protons contribute to the proton gradient that drives ATP synthase and the electrons are passed via a soluble c type cytochrome to cytochrome c oxidase and ultimately to O_2 producing water. The UQ pool is pivotal in mediating this process and also mediates a number of other parallel pathways including reduction of succinate, formate, glycerol-phoshate and electron-transfering flavoproteins among others. Soluble exogenous mediators can, depending on their redox potential and ability to access the inner cell, potentially interact with any or all of the proteins or redox molecules in the respiratory process.[25] Attempts to isolate the specific proteins that exogenous mediators interact with can involve a process of elimination whereby known proteins are selectively inhibited and the effect on the rate of electron transfer to exogenous mediators measured.

Some experiments of this type conducted by Murphy *et al.* [26-29] are described in the introduction to Chapter 5.

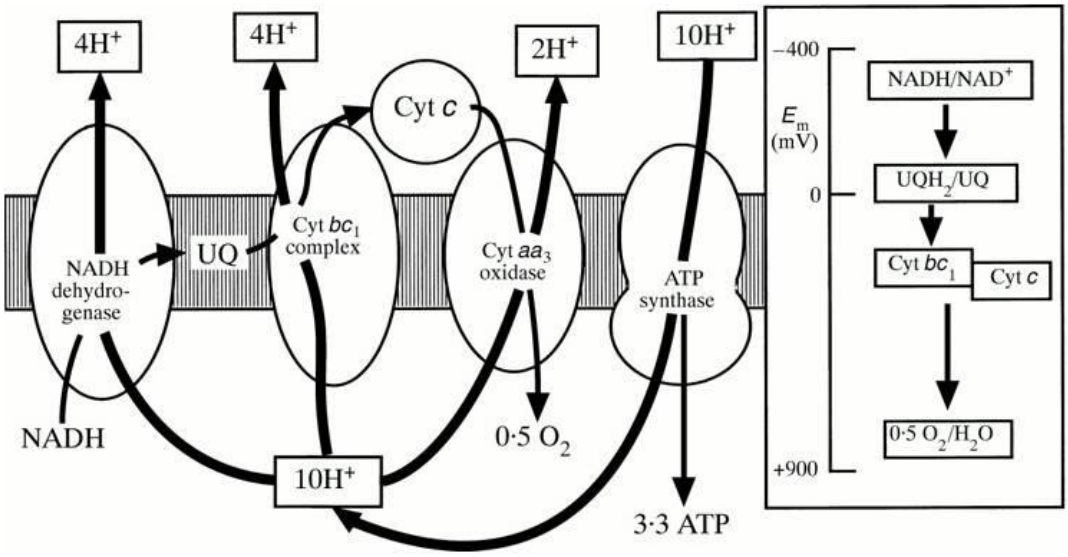

Figure 1.5. A depiction of the electron transfer processes occurring during normal bacterial respiration through the NADH pathway. Also shown are the relative reduction potentials of the molecules in the process which have increasingly positive reduction potentials. Figure reproduced from the lecture material of David J. Richardson, University of East Anglia, Norwich.

In addition to electron transfer mediated by soluble exogenous mediators a third strategy for achieving electron transfer from microbes to solid electrodes is the use of surface confined redox mediator molecules. Clearly surface bound mediator molecules have a significant mobility disadvantage compared to solution-phase mediators and consequently are less able to access redox proteins or molecules that are buried in the internal membranes of microbes. Confinement of all of the mediation chemistry to the electrode however enables less complex, single compartment electrochemical cell designs as there is no opportunity for mixing of mediation chemistries between the anode and the cathode. Firmly attached stable mediator molecules can also be stored dry and hence are an attractive alternative for incorporation into devices. Conceptually, the design of a successful surface confined mediation strategy is the inverse of the approach evolution

has taken to solve the terminal electron transfer problem for anaerobic bacteria. It appears that under evolutionary pressure charge transfer proteins in electrogenic bacteria have migrated to the outer membranes of the bacteria. Analogously surface confined mediators are likely to be most effective when they in close proximity to suitable redox proteins or molecules in the bacteria. In the work of Gorton *et al.* it was found that by tethering mediator molecules to electrodes by long flexible tethers, higher rates of electron transfer from the non-electrogenic bacteria *Glucanobacter oxydans* and *Escherichia coli* were achieved than with short tethers.[8,30] Clearly a more mobile mediator molecule at the end of a flexible tether has a higher chance of gaining access to difficult to reach redox proteins within the bacterial cell. The same authors also reported a factor of 2.5 increase in measured current from the bacterium *Pseudomonas putida* upon the inclusion of 8% multiwalled carbon nanotubes (MWCNT) into a carbon paste electrode mixed with an osmium-based redox polymer.[31] The authors do not attempt to explain the observation but considering the magnitude of the current increase on an already very rough electrode it is unlikely to arise from an increase in surface area alone. Therefore nanostructuring of the electrode surface (in particular with long, thin, conducting structures such as MWCNTs) may help to position redox molecules close to redox active sites in the cell. Other examples of 'wiring' of bacteria to surface confined mediators have been demonstrated with the bacteria *B. subtilis* [32] and *Pseudomonas fluorescen.*[33]

1.1.3 Whole cells in electrochemical sensors

One of the areas where the study of microbes is finding potential device applications is the use of microbes as the recognition element in biosensors. Whole cell biosensors require that the recognition microbe reacts with an analyte in a detectable manner. Typically this is by producing a compound that is optically [34,35] or electrochemically detectable.[35-37] An example of the latter is the work of Tatsuma *et al.* [37] who utilize the known reaction of algae to waterborne toxins. Algae on an electrode surface were exposed to light and the O_2 produced by algal photosynthesis was electrochemically detected. Exposure of the algae to waterborne toxins results in a rapid slowing in the rate of photosynthesis and a corresponding drop in O_2 production. An

example of a mediated microbial ethanol (EtOH) sensor is that of Tkac *et al.* [38] who employ *Gluconobacter oxydans* as a recognition element and $Fe(CN)_6^{3-}$ as a mediator molecule. *Gluconobacter oxydans* has an inner membrane EtOH deydrogenase enzyme that passes electrons and protons to the membrane-soluble coenzyme pyrroloquinoline quinone (PQQ) upon oxidation of EtOH. $Fe(CN)_6^{3-}$ diffusing through the cell wall is reduced by $PQQH_2$ (reduced PQQ) and then diffuses to an electrode poised at a potential sufficient to re-oxidse the $Fe(CN)_6^{4-}$. This results in an increase in the measured electrical current at the electrode.

In the examples described in the previous paragraph, development of a practical biosensor could be advanced by wiring of a microbial recognition element to surface-confined mediators. In order to achieve this, the substrate and attachment strategies must be optimized to give surface confined mediators maximum access to redox active elements inside the target microbe. The majority of this thesis work is dedicated to investigating the fabrication of electrodes and mediator attachment strategies that have the potential to achieve this aim.

1.2 Fabrication of electrodes

1.2.1 Carbon electrochemistry

Although there is a developing field of electrochemical research using doped diamond electrodes by far the majority of carbon electrodes are fabricated from forms of graphite.[39] Since the discovery of carbon paste electrodes by Ralph Adams [40] over 50 years ago [41] graphite has been at the forefront of electrochemistry as an electrode material. Carbon paste electrodes are simply graphite powder mixed with a binding agent. The simplicity and malleability of this system led to the development of graphite inks which are the industry choice for one use analytical electrodes such as those found in blood glucose test kits.[42] In research, graphite powder has the disadvantage that its surface area is difficult to calculate accurately. This, in turn, makes quantification of a range of

experimental variables difficult. Hence where comparative studies are undertaken using graphite electrodes, solid (non powder) forms are generally preferred.

The essential structure of all graphite polymorphs is the same (Figure 1.6) consisting of layers of parallel carbon sheets with the carbon atoms arranged in a flat hexagonal pattern. It is immediately obvious that a single crystal of graphite presents two distinctly different faces. The aromatic face is called the basal plane and is the least electrochemically active surface. Most of the electrochemical activity of graphite arises from the crystal face where the edges of the carbon sheets are exposed, the edge plane.[43, 44] All of the commercially available graphite materials useful for electrochemistry are polycrystalline. The relative electrochemical activities of the various materials are governed by the size and orientation of the graphite crystals from which they are comprised. Materials that present a high proportion of graphite edge planes to the electrolyte solution have the highest electrochemical activities.

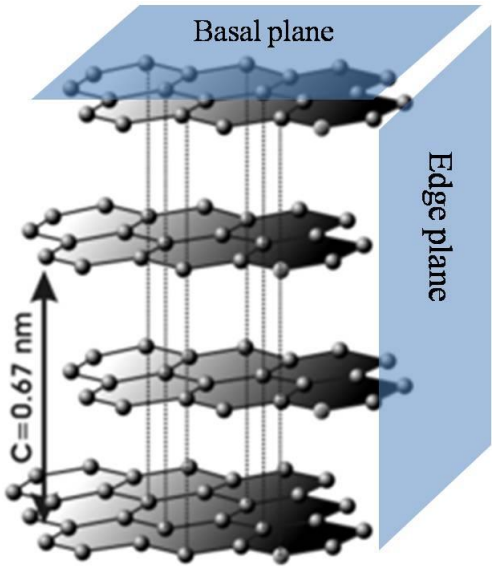

Figure 1.6. Structure of graphite. Figure reproduced from www.karakal.cz

1.2.2 Glassy carbon(GC) and highly oriented pyrolytic graphite (HOPG)

Graphite (like diamond) occurs naturally but it is too rare and impure to be useful for electrochemistry. The commercial variants of carbon are all produced from precursor organic resins or carbon gases by various methods. For electrochemistry the most commonly used form of graphite is GC. GC is generally considered to have been discovered by Bernard Redfern, a diamond scientist, who noticed that the Sellotape used to secure samples took on a unique structure when heated in inert atmospheres (pyrolysis). In fact, Redfern recognized the commercial significance of a material that had been known for some time under the general term non-graphitizing carbon. The term "non-graphitizing" was revealed to be misleading, in part by Rosalind E. Franklin [45] who showed by X-ray crystallography that pyrolysis of polyvinylchloride produced a material with 65 % graphitic character and 35 % amorphous character. The precise structure of modern GC is still under debate but is variously described as interconnected randomly oriented graphitic crystallites or ribbons.[46,47] Figure 1.7 shows transmission electron microscope (TEM) images of samples of commercial GC and illustrates how the degree of graphitization can be controlled by the pyrolysis conditions. Figure 1.7 B shows GC produced at 3000 ^{o}C, clearly exhibiting larger graphitic domains than the more disordered sample formed at 1000 ^{o}C (Figure 1.7 A). GC is often classified by three values which are the average in-plane crystallite size (La), the average graphite stack height (Lc), and the average graphite intersheet spacing (d_{002}). Typically, commercial GC has La and Lc values of 2–7 nm and (d_{002}) values around 0.36 nm.[39] The (d_{002}) value for fully graphitized carbon is 0.335 nm, hence GC is now commonly considered to be a partially graphitized form of carbon.

The fact that GC is "glassy" is perhaps the primary reasons why it enjoys so much use in research electrochemistry. It has exceedingly low chemical reactivity, very high thermal stability and it is impermeable to gases or liquids. It can easily be produced in a variety of shapes and can be quickly polished to sub micron roughness with little effort. Because the crystallites in GC are randomly oriented and very small there is always a high proportion of graphite edge plane sites presented at any surface which results in a

high electrochemical activity. For all of these reasons GC is a natural choice of substrate for many of the experiments conducted in this thesis work.

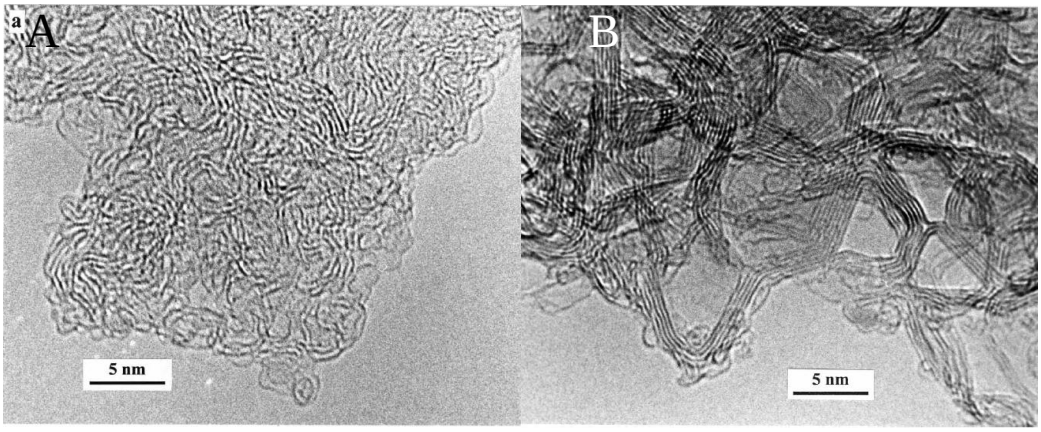

Figure 1.7. TEM images of GC produced by pyrolysis at A) 1000 ^{o}C and B) 3000 ^{o}C. Figure reproduced from reference 46.

HOPG is produced by deposition of gaseous hydrocarbons and compression at high temperature. The crystallites in this form of graphite are much larger than those in GC, often exhibiting *L*a and *L*c values as high as 10 μm.[39] The key difference between GC and HOPG is that the crystallites in HOPG, though rotationally disordered, are highly aligned in the basal plane (*L*a) dimension. This results in a large difference between the electrochemical activity of the basal plane face and edge plane face of HOPG.[43] For most applications HOPG is prohibitively expensive and similar electrochemical performance to HOPG edge planes can be achieved using GC. Hence it is chiefly used in experiments where the fundamental properties of graphite crystal faces are being explored.[44]

1.2.3 Pyrolysed photoresist films (PPF)

For some of the experiments in this thesis work a planar graphitic electrode with sub nanometer roughness is required. The final preparation step of a GC electrode is usually polishing with alumina or diamond paste which gives a surface roughness (average deviation of any point on a surface from a least squares fitted plane) at best, of tens of nanometers. In order to visualize surface features with heights less than 10 nm, roughness values less than 1 nm are required. The roughness values of *ca.* 0.5 nm for

PPF allow for sub 10 nm high features to be visualized by techniques such as depth profiling by atomic force microscopy (AFM) and greatly increase the amount of information that can be drawn from scanning electron microscope (SEM) images.[48-51]

PPF was first introduced by Kinoshita and coworkers in 1998.[52] They spin coated a Novolak style phenol formaldehyde photoresist resin onto a silicon wafer and pyrolysed it at temperatures ranging from 600 to 1000 ^{o}C under nitrogen. The films prepared in this way reduced in thickness from 6 μm to ≈ 2 μm [53] and become glassy. As with GC preparation, the pyrolysis temperature had a marked effect on the properties of the PPF. In the work of Kinoshita *et al.* samples pyrolysed at 600 ^{o}C had sheet resistivities of 100000 Ω □$^{-1}$ and sample pyrolysed at 1000 ^{o}C had sheet resistivities of 10 Ω □$^{-1}$. Raman and X-ray photoelectron spectroscopy (XPS) studies by the same authors show that, like GC, the films display some graphitic character but are highly disordered. The Raman spectra suggest that high pyrolysis temperatures result in a high proportion of edge plane graphite and a disordered structure. The same phenomenon was observed by Sun *et al.* [54] who state that this is consistent with PPF taking on GC-like character at high pyrolysis temperatures. McCreery *et al.* prepared PPF samples in a very similar way to that used in this thesis work [55] and analyzed the samples by Raman spectroscopy, XPS and TEM. They compare the results with their similar study conducted on GC and HOPG three years earlier.[56] They also conclude that the structure of PPF is partially graphitisized with decreasing crystallite size and increasing disorder at high pyrolysis temperatures. The samples prepared at 1100 ^{o}C (similar to the temperature used in this work) were directly compared with that of commercial GC. Graphitic structures have two commonly recognized Raman bands at 1380 cm^{-1} (D band) and 1600 cm^{-1} (E_{2g} band). The ratio of these two bands is an indicator of the ratio of edge plane (E_{2g} band) to basal plane (D band) sites and hence the degree of disorder in the structure.[56] The Raman spectra for the samples pyrolysed at 1100 and 600 ^{o}C by McCreery *et al.* compared with GC are shown in Figure 1.8. The authors do not calculate the relative peak areas but visually it appears that the D:E_{2g} area ratio for GC is similar but slightly higher than that of AZ1100 (PPF). This suggests that PPF may possess slightly higher basal plane to edge

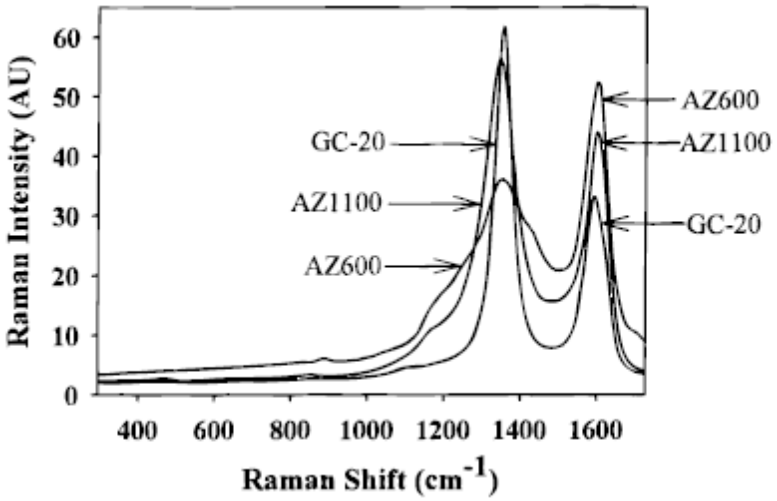

Figure 1.8. Raman spectra of GC and PPF prepared at 600 ^{o}C (AZ600) and 1100 ^{o}C (AZ1100). Figure reproduced from reference 55.

plane ratio and is likely therefore to exhibit slightly lower electrochemical activity. Cyclic voltammetric (CV) studies from the same paper show that this was indeed the case for the common redox probe $Fe(CN)_6^{3-/4-}$ which gave CV oxidation and reduction peak separation (ΔE_p) of 88 mV at PPF pyrolysed at 1100 ^{o}C and 65 mV at GC (a small ΔE_p indicates high electrochemical activity) . Although there are small differences between PPF and GC it is certain that PPF is very GC-like and hence a good substitute for GC when an ultra-flat graphitic surface is required.

1.2.4 Carbon nanotubes

Reports of fibrous carbon materials date back as far as 1889 [57] but the first TEM micrographs revealing the hollow core of multi walled carbon nanotubes (MWCNTs) (Figure 1.9) was published by Radushkevich and Lukyanovich in 1952 in The Journal of Physical Chemistry of Russia.[58] In the early 1990s three papers appeared that formally heralded the beginning of the carbon nanotube era. The first of these was the 1991 paper by Iijima *et .al.* [59] which unequivocally determined the helical nature of MWCNTs formed by an arc discharge process similar to that used in the earlier serendipitous discovery of MWCNTs by John Abrahamson.[60,61] In 1993 two papers appeared that independently verified the synthesis of single walled carbon nanotubes (SWCNT). The

first submitted was from the Iijima group at NEC, Japan [62] and the second, two months later, from Bethune *et al.* from IBM, California.[63]

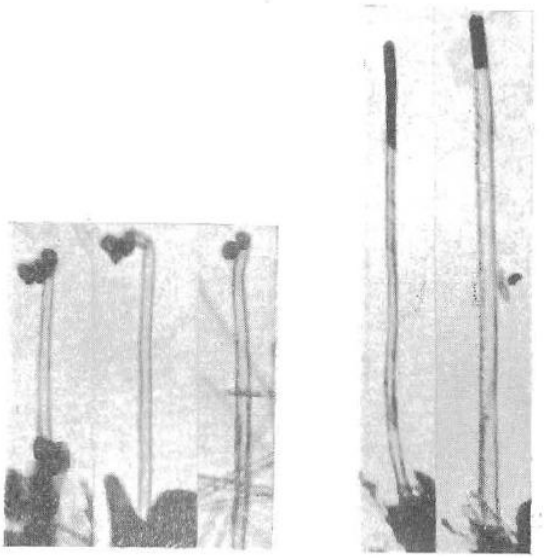

Figure 1.9. TEM images reproduced from reference 58 showing the hollow structure of carbon tubules formed by the thermal decomposition of carbon monoxide on iron.

Perhaps adding to the surge in interest in CNTs was the 1992 paper by Saito and Fujita [64] in which the density of states of various possible chiralities of SWCNTs were calculated predicting metallic and semi-conducting nanotube variants. The paper of Saito *et al.* is also a good example of the chiral indexing system now used world wide to differentiate SWCNTs. The indexing system is a two vector coordinate system that designates the carbon atom on a graphene sheet that coincides with the vector origin when the sheet is rolled into a tube (Figure 1.10). This model dictates that if all wrapping vectors are equally likely then SWCNT should exists in a 3:2 ratio of to semi-conducting to metallic tubes. This prediction and later confirmation [65] coincided with rapidly increasing world wide semiconductor manufacture and the drive to miniaturize electronics. SWCNT nanotubes have now successfully been employed in a number of molecular scale field effect transistors.[66-68] More relevant to the work described in this thesis is the predicted [69] and experimentally determined [70, 71] exceedingly low resistivity of both metallic SWCNTs and MWCNTs.

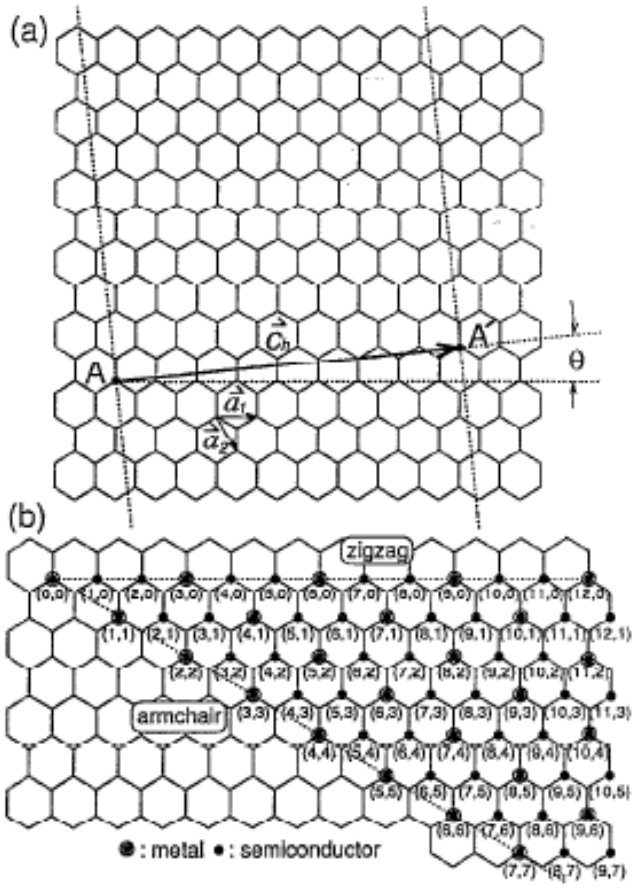

Figure 1.10. The chiral indexing system used by Saito *et al.* to define the various wrapping possibilities of SWCNTs. Reproduced from reference 64

Once it was established that CNTs were efficient nanowires, their inclusion into electrodes for electrochemical experiments was inevitable. Several papers in the late 1990s claimed near perfect electrochemical performance for CNT electrodes and helped build their "electrocatalytic" reputation. In 1996 Britto *et al.* [72] fabricated electrodes made with MWCNTs from an arc discharge process that were mixed with bromoform and packed into a glass tube. A copper wire was inserted into one end of the MWCNT slurry and the other side used as a working electrode. The CV response of dopamine in pH 7.4 phosphate buffered saline (PBS) was recorded and the ΔE_p measured exhibiting ΔE_p = 30 mV at a scan rate of 20 mV s^{-1}. A ΔE_p of 29.5 mV is the theoretical minimum for a 2 electron redox process and is only possible when the rate of electron transfer is significantly faster than the flux of analyte to the electrode (diffusion controlled).[2] In

2001 the same authors published near ideal CVs for the common redox probe $Fe(CN)_6^{3-/4-}$, this time with a bundle of aligned MWCNTs glued to the end of a copper wire with conducting epoxy.[73] In that paper the authors take the view that there must be a fundamental difference in the electrochemical properties of CNTs over other graphite polymorphs. This view arises from the authors' suggestion that "*The surface structure of nanotubes consists entirely of near-perfect atomically smooth graphite basal planes with no dangling bonds or traces of the edge planes*". It is now known that MWCNTs formed under most conditions (in particular arc discharge [74, 75]) are far from ideal and have many defects and imperfections. That fact that the electrodes in question were snapped from the inside of an arc discharge carbon agglomerate also means that they bore freshly cleaved graphitic surfaces. The authors express puzzlement at the observed fast electron transfer rates for $Fe(CN)_6^{3-/4-}$ and state: *"Considering that nanotube surfaces are entirely made of the basal planes (which show very slow ET* [electron transfer] *kinetics), it is puzzling that nanotube electrodes provide the highest possible ET rates for the reactions mentioned above. Surprisingly, in their electrochemical, electrodic behavior, nanotubes respond even faster than the graphite edge planes".* In the light of more recent evidence it is likely that the authors were in fact observing electron transfer kinetics from graphitic edge planes at the tips of the broken MWCNTs and from the large numbers of defect sites on the walls.

One of the questions this thesis work seeks to answer is whether the inclusion of carbon nanotubes on electrode surfaces enhances the rate of electron transfer from living cells. The idea that carbon nanotubes are "electrocatalytic" is one that has been the subject of many publications.[76] More recently several papers have been published which refute this idea and argue that carbon nanotubes are simply a polymorph of graphite and not fundamentally "electrocatalytic" at all.[77-79] The proposition that CNTs are simply another form of graphite was examined by Moore *et al.* who show that the electrochemical responses of NADH, dopamine and epinephrine are not significantly different on graphite powder and MWCNTs immobilized on basal plane HOPG.[77] The same authors carried out a follow-up study the following year that showed the electrochemical activity of CNTs is strongly correlated with defect sites.[79] In further

work the same group showed that catalysis by carbon nanotubes can, in some cases, be attributed to residual metal catalyst remaining from the CNT synthesis.[80]

The reports of Moore, Banks and Compton *et al.* did little to quell the growing enthusiasm for carbon nanotubes but did change the direction of electrochemical CNT research somewhat. As the view that CNT electrochemical activity being located primarily at open tube ends became embraced, alignment of the tubes to maximize the density of tube ends was a logical step. Two methods for achieving this vertical alignment have been developed over the last decade; both of these were employed in this thesis work. The first of these is attachment of SWCNTs from solution to a surface bound tether layer and is introduced and discussed in Chapter 3. The second is growth of vertically aligned CNTs by chemical vapor deposition which is reviewed in the Introduction to Chapter 4.

As well as the electrochemical advantage that vertical alignment brings there are also significant chemical advantages. In this thesis work, some of the CNT constructs are simply conducting supports for electrochemical mediator molecules. Defect free CNTs have low chemical reactivity but many modification strategies have been reported.[75, 81, 82] It is generally acknowledged that the region of most reactivity in perfect closed CNTs is at the ends where strain due to curvature raises the energy of the structure.[75, 81] When the ends of CNTs are open they commonly bear a high number of carboxylic acid functionalities [81, 83] and reactions with nucleophiles (in particular with amines to form amides) is relatively facile. The existing literature presents a vast number of examples of vertically aligned and modified CNT constructs enhancing electrochemical performance. Some of these are reviewed in the Introduction to Chapter 5 where modification strategies are discussed.

1.3 Surface modification using aryl diazonium salts

1.3.1 Introduction

The addition of desirable chemical functionality to an electrode surface naturally requires an attachment strategy. In the simplest case a modifier molecule can simply be adsorbed to an electrode. The blood glucose test kits used by diabetics world wide are a case in point. In that instance the glucose selectivity is introduced by addition of the enzyme glucose oxidase which is simply mixed with graphite powder inks and screen printed onto plastic substrates. These electrodes also require a mediator molecule (often a ferrocene derivative) which is introduced in the same way. The fact that these electrodes are cheaply produced and are single use and that the enzyme glucose oxidase is very stable, permit this. Many other mediators and recognition elements are not so forgiving. In the case of an amperometric immunosensor the strategy for attaching an antibody must permit complexation of the antigen while restricting non specific adsorption of non-target proteins.[84, 85] Clearly, the choice of attachment strategy must be carefully considered

For the work described here the attachment strategy must firstly be non cytotoxic and secondly, because AFM and SEM are to be extensively employed, the substrate and attachment strategy should be as flat as possible. Thirdly, the aim is to make electrodes that are very stable to storage and in a range of solvents to enable a broad range of chemistries to be used in subsequent modification steps. Polymer films [86-88] and sol-gels [89-91] are commonly employed to bind recognition or mediator chemistries, However neither of these behave well under AFM or SEM investigation due to their soft and often porous structure. Furthermore many are incompatible with organic solvents. Molecular monolayer or near monolayer tether layers on flat surfaces are excellent candidates for analysis by AFM and are increasingly of interest in electrochemical systems. Two methods of producing such films that are compatible with electrochemistry are adsorption of thiols onto noble metal electrodes and electrochemical modification with aryl diazonium salts.

Thiol or disulphide molecules are well known to form closely packed, well ordered and aligned monolayers on flat noble metal surfaces, in particular gold.[92, 93] Alkanethiol self assembled monolayers (SAMs) on Au are simple to prepare and form homogeneous mono-layer films but have some disadvantages. They have been shown to be stable over a relatively narrow potential which typically lies between -0.4 and 0.6 V *vs.* Ag/AgCl.[94] The Au-S bond can be unstable with storage in ambient conditions [95] and in biological media.[96] Stability of alkanethiol SAM films has recently been improved by nanostructuring of the Au substrate [97] but still remains an inherently unstable system. In the work described here, carbon nanotubes are to be chemically attached to the electrodes requiring the use of aggressive solvents and long time frame experiments in phosphate buffered saline (PBS) hence alkanethiols SAMs are unsuitable.

The electrochemical reduction of aryl diazonium salts to form covalently grafted tether layers is a well researched field.[49, 98-101] Though spontaneous reduction of aryl diazonium salts occurs at many surfaces,[102] electrochemical assistance (in which the working electrode is the surface to be modified) is more common and provides a greater degree of control. When CV is employed for grafting, the CV is initiated at a potential more positive than the diazonium cation reduction potential and swept in the negative direction. At sufficiently negative potentials diazonium cations are reduced resulting in a cathodic current peak on the CV. Figure 1.11 scan (a) shows a typical grafting peak for the 4-nitrobenzene diazonium cation. If a second CV is recorded immediately following the first there is typically a dramatic decrease in recorded current (Figure 1.11 scan (b)). This is attributed to formation of a blocking film on the electrode surface which inhibits further reaction. Films derived from aryl diazonium salts on graphite can be stable over a potential window as wide as -2 to 1.8 V *vs.* Ag/AgCl.[103]

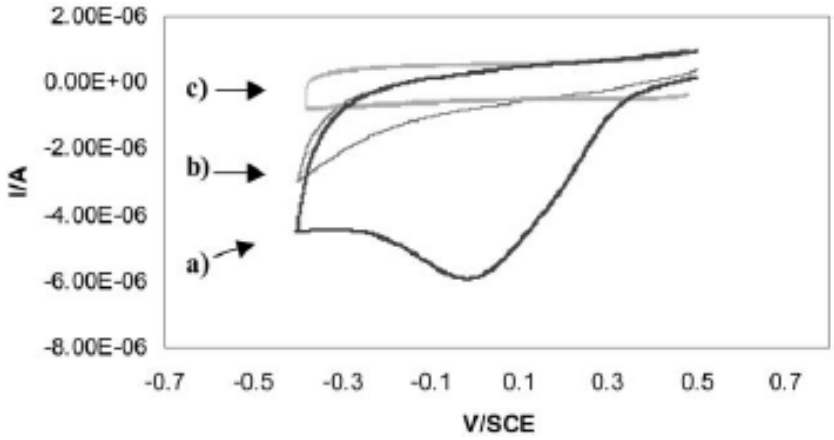

Figure 1.11. CV obtained at a glassy carbon disc electrode in a 2 mM solution of 4-nitrobenzene diazonium salt in 0.1 M $TBABF_4$ / ACN. a) first scan b) second scan and c) a CV of the same electrode in the absence of diazonium salt. Figure reproduced from reference 102.

Scheme 1.1 depicts the generally accepted mechanism for build up of a film formed by electrochemical reduction of a diazonium cation solution. When reduction of the diazonium functionality occurs (Scheme 1.1 A) a single electron is injected into the diazonium cation inducing homolytic cleavage of the C-N bond, liberating $N_{2(g)}$ and producing an aryl radical. (Scheme 1.1 B) The aryl radical attacks the surface forming a covalent bond, [101, 104, 105] either to the substrate electrode (Scheme 1.1 C) or to molecules already attached to the substrate electrode (Scheme 1.1 D). It is now well established that reduction of aryl diazonium salts usually forms loosely packed multilayer films.[48, 49,100, 106, 107]

The disorganization of diazonium salt derived films is perhaps their most significant drawback compared to alkanethiol SAMs. The thickness of diazonium salt derived multilayers depends primarily on the applied potential and time the potential is applied for.[100] The fact that aryl diazonium derived films act as an insulating or passivating layer means that films rapidly approach a limiting thickness dependent on the potential applied.[100] This phenomenon allows for a measure of control over the properties of films derived from aryl diazonium salt methods but not to the degree that alkanethiol

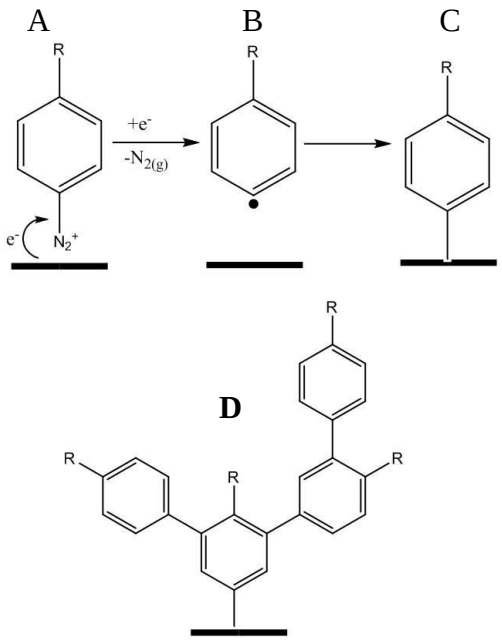

Scheme 1.1. Grafting of multilayer films from diazonium cation reduction

SAMs can be controlled. Where alkanethiol SAMs can be close packed and well organized, diazonium salt derived films are jumbled with some of the desirable functionality buried in the film. Unlike alkanethiol SAMs where individual modifier molecules exist in homogeneous environments, functional groups in aryl diazonium derived films may inhabit vastly different environments depending on their position in the film. This limits the value of techniques such as electrochemical impedance spectroscopy (EIS) due to its dependence on "ideal" models against which experimental data is compared (this is discussed in section 3.3.5). However, electrodes formed by reduction of aryl diazonium salts are inexpensive, rapidly prepared and show little or no degradation on storage over a period of months. For biological sensing (the target of this work) the largely graphitic and covalently coupled systems offers a lower risk of cytotoxic effects from leaching of component molecules due to being graphitic [39] and robust.[99]

1.3.2 Amine terminating tether layers

The majority of the tether layers formed in this thesis are amine terminated to enable coupling of carboxylic acid or aldehyde bearing molecules, by formation of an amide or imine bond respectively. Two methods of preparing thin aminophenyl (AP) films are employed. In the first method a nitrophenyl (NP) film is formed and is subsequently reduced to an AP film. In the second method, AP films are directly electrografted from the corresponding diazonium salt.

The method of formation of AP films by reduction of NP films is best described in the work of Ortiz *et al.*[108] In that work 4-nitrobenzene diazonium tetrafluoroborate salt was synthesized and electrografted to GC electrodes from an ACN electrolyte solution. The resulting NP film was electrochemically reduced in aqueous mineral acid to an AP film. A CV of the nitro reduction process is shown in Figure 1.12. The first reduction scan (Figure 1.12 solid line) shows a large reduction wave at E_{pc} = -0.34 V *vs.*

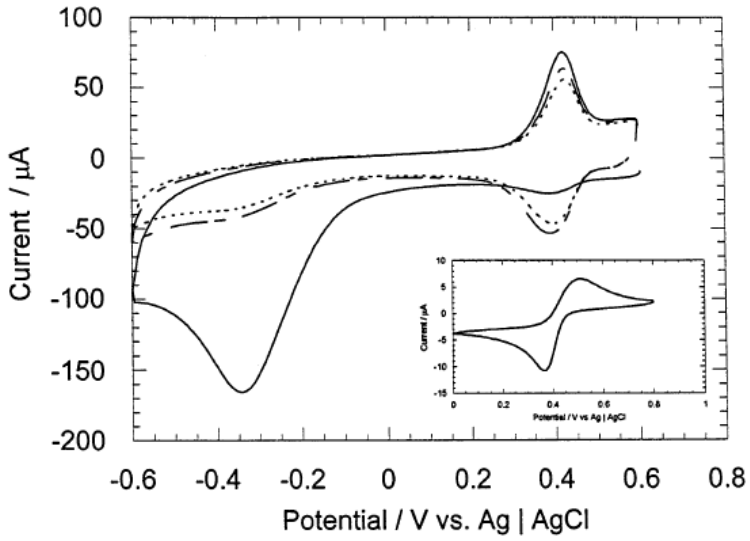

Figure 1.12. CVs of a NP film on GC in 1 M H_2SO_4. First scan (solid line) second scan dashed line and third scan dotted line. The insert is a CV of 5 mM nitrosobenzene in 1 M HCl at a scan rate of 50 mV s^{-1}. Figure reproduced from reference 108.

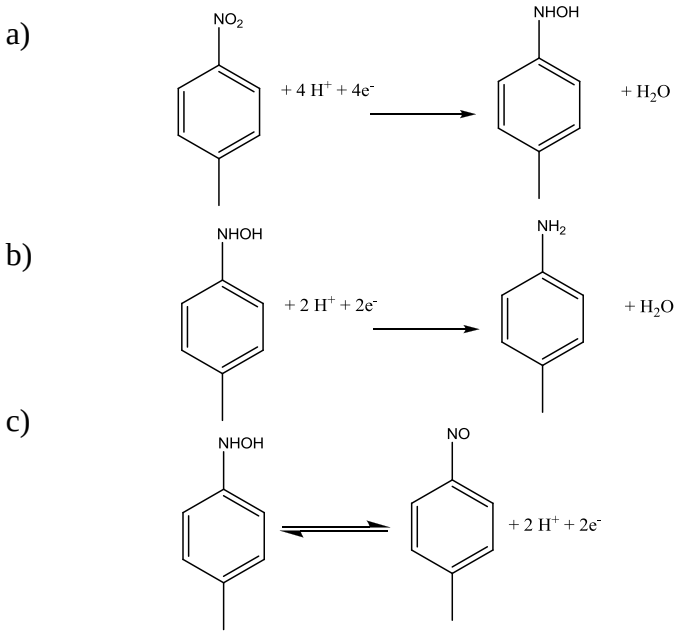

Scheme 1.2 Possible reactions during the electrochemical reduction of NP films in aqueous acid.

Ag/AgCl. On the return scan an oxidation wave appears at E_{pa} = 0.4 V *vs.* Ag/AgCl. On subsequent scans (Figure 1.12 dashed and dotted lines) the reduction wave disappears and the oxidation peak persists as half of an electrochemically quasireversible redox couple. To account for the observed CV behavior Ortiz *et al.* propose the reaction mechanism depicted in Scheme 1.2 which is derived from the earlier work of Rubinstein.[109] The large irreversible peak at -0.34 V is attributed to reduction of the NP film to AP via a 4-hydroxylaminophenyl intermediate (Scheme 1.2 a) and b)) requiring a total of 6 electrons and six protons per molecule. The quasireversible system at 0.4 V is attributed to a portion of the 4-hydroxylaminophenyl intermediate which is not reduced to AP and is reversibly oxidized on the return scan to nitrosophenyl (Scheme 1.2 c)).

The second method of producing AP films employed in this thesis work was derived from the methods of Lyskawa *et al.*[110] In that work 1,4-diaminobenzene was diazotized in solution and grafted directly to gold electrodes. The authors show that reaction of 1,4-diaminobenzene with 1 equivalent of $NaNO_2$ in HCl leads primarily to the

monodiazonium cation which can be electrografted to an electrode forming an AP film (Figure 1.13). The predominance of monodiazotization was proven by reacting the diazotized diamine with potassium iodide in 6 M HCl and analyzing the reaction mixture by GC-MS. In that experiment a 90% yield of monodiazotization products (4-iodoaniline and 4-chloroanaline) were detected and a 10% yield for bisdiazonium cation products. Electrochemical grafting by cyclic voltammetry yielded classic reduction peaks (Figure 1.13 a)) and passivation of the electrode (Figure 1.13. b)) on subsequent scans consistent with film formation. XPS analysis led the authors to propose the film structure depicted in Figure 1.14. The mechanism by which the azo-bonds are incorporated is not well understood but may be via electrophilic aromatic substitution [111] or a radical mechanism.[112]

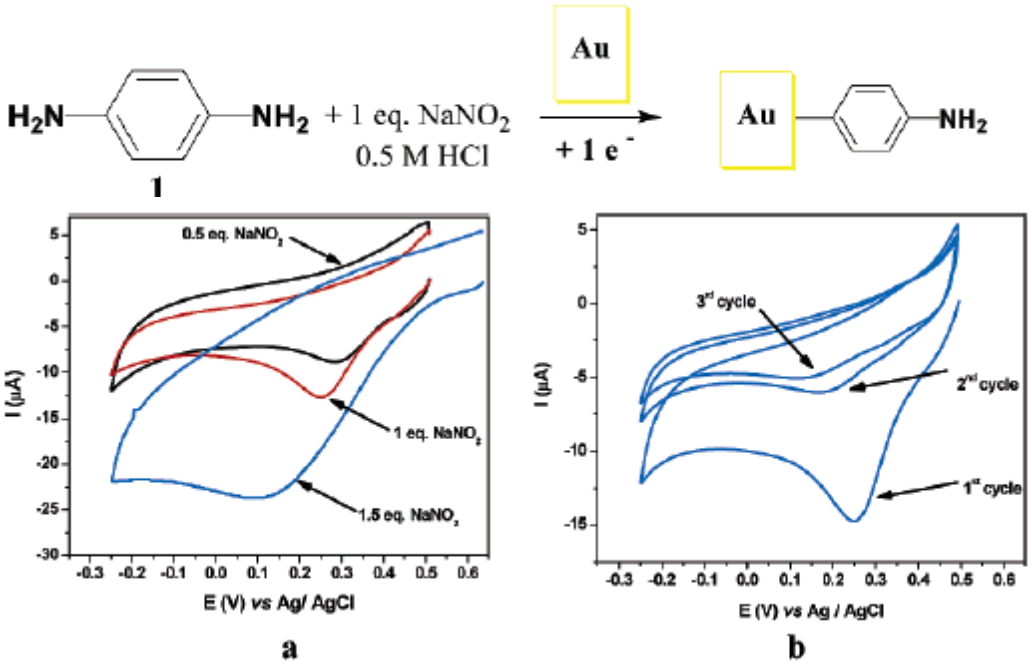

Figure 1.13. Reaction scheme for the monodiazotisation of 1,4-diaminobenzene and grafting CVs for a) a 5 mM solutions of 1,4-diaminobenzene with 0.5, 1 and 1.5 equivalents of $NaNO_2$ in 0.5 M HCl and b) the first three CVs of the solution containing one equivalent of $NaNO_2$. Figure reproduced from reference 112.

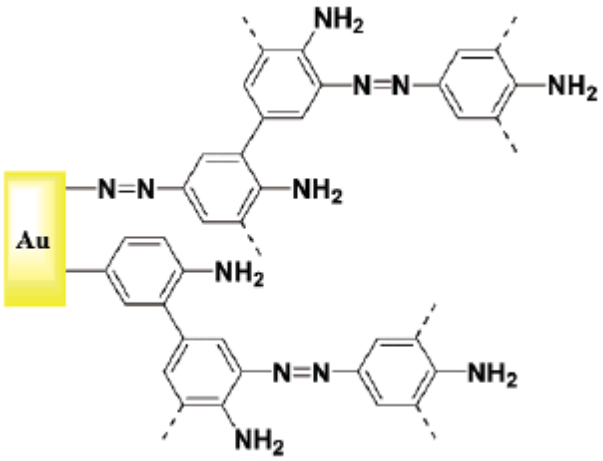

Figure 1.14. Structure of the film electrografted from 4-diazo-1-aminobenzene proposed by Lyskawa *et al.*

Importantly, for the work described in this thesis, Lyskawa *et.al.* confirmed by IRRAS and XPS that their AP films were capable coupling trifluoro acetic anhydride by amide bond formation. Yu *et al.* showed by electrochemical detection of the coupled nitro group and XPS that their reduced NP films were capable of coupling 4-nitrobenzoyl chloride, 4-fluorobenzoyl chloride and 4-nitrobenzoic acid.[113] These results show the utility of AP films as tether layers for further modification.

1.4 Thesis aims and organization

The aim of this thesis work is to develop electrodes and mediator attachment strategies that have the potential to enhance the rate of electron transfer from surface confined non-electrogenic bacteria. A selection of the electrodes were trialed with the bacteria *P. vulgaris* and *B. subtilis* to determine their ability to act as terminal electron acceptors for normal microbial respiration. The thesis is organized as follows.

Chapter 2; General experimental: describes experimental procedures and equipment that are relevant to two or more chapters of this thesis.

Chapter 3; Chemical assembly of single walled carbon nanotubes: describes the use of diazonium salt derived AP tether layers and oxidatively coupled ethylene diamine (en) films on PPF to enable coupling of vertically aligned SWCNTs from solution. The resulting assemblies are electrochemically characterized and patterning strategies for the coupled SWCNTs are explored.

Chapter 4; Synthesis and fabrication of vertically aligned multi walled carbon nanotube electrodes: describes the synthesis of dense vertically aligned forests of MWCNTs on PPF by chemical vapor deposition (CVD). Both conventional evaporated metal and unconventional metal salt catalyst films are used. Patterning strategies for both of the catalyst types are explored. Finally a method is described for encapsulation of the MWCNT forests in epoxy resin to make highly robust, reproducibly fabricated and reusable MWCNT electrodes.

Chapter 5; Modification of electrodes with mediator molecules: explores the coupling of metal centered amine terminated mediator molecules by conventional amide bond formation methods and the coupling of a new UQ mimic to surfaces via reductive amination.

Chapter 6; Electro-grafting of osmium diazonium cation complexes: describes the synthesis and electrochemical grafting of a new class of osmium centered diazonium salt complexes. The ultra thick, redox active films resulting from grafting of these complexes are examined by electrochemical methods, SEM and AFM.

Chapter 7; Measuring electrical current from non-electrogenic bacteria: describes preliminary experiments showing measurable electrical current produced by direct electron transfer from the bacteria *B. subtilis* and *P. vulgaris* to a selection of the electrodes described in Chapters 3-6.

1.5 References

1. Potter, M. C., Electrical effects accompanying the decomposition of organic compounds. *Proc. R. Soc. London, B* **1911,** 84, (571), 260-276.
2. Bard, A. J.; Faulkner, L. R., *Electrochemical Methods Fundamentals and Applications 2nd Ed.* . John Wiley & Sons, Inc.: 2001.
3. Debabov, V. G., Electricity from microorganisms. *Microbiology* **2008,** 77, (2), 123-131.
4. Reimers, C. E.; Tender, L. M.; Fertig, S.; Wang, W., Harvesting energy from the marine sediment-water interface. *Environ. Sci. Technol.* **2001,** 35, (1), 192-195.
5. Bond, D. R.; Holmes, D. E.; Tender, L. M.; Lovley, D. R., Electrode-reducing microorganisms that harvest energy from marine sediments. *Science* **2002,** 295, (5554), 483-485.
6. Logan, B. E., Exoelectrogenic bacteria that power microbial fuel cells. *Nat. Rev. Microbiol.* **2009,** 7, (5), 375-381.
7. Zhao, F.; Slade, R. C. T.; Varcoe, J. R., Techniques for the study and development of microbial fuel cells: an electrochemical perspective. *Chem. Soc. Rev.* **2009,** 38, (7), 1926-1939.
8. Alferov, S.; Coman, V.; Gustavsson, T.; Reshetilov, A.; von Wachenfeldt, C.; Hagerhall, C.; Gorton, L., Electrical communication of cytochrome enriched Escherichia coli JM109 cells with graphite electrodes. *Electrochim. Acta* **2009,** 54, (22), 4979-4984.
9. Shi, L. A.; Richardson, D. J.; Wang, Z. M.; Kerisit, S. N.; Rosso, K. M.; Zachara, J. M.; Fredrickson, J. K., The roles of outer membrane cytochromes of Shewanella and Geobacter in extracellular electron transfer. *Environ. Microbiol. Rep.* **2009,** 1, (4), 220-227.
10. Reguera, G.; McCarthy, K. D.; Mehta, T.; Nicoll, J. S.; Tuominen, M. T.; Lovley, D. R., Extracellular electron transfer via microbial nanowires. *Nature* **2005,** 435, (7045), 1098-1101.
11. Gorby, Y. A.; Yanina, S.; McLean, J. S.; Rosso, K. M.; Moyles, D.; Dohnalkova, A.; Beveridge, T. J.; Chang, I. S.; Kim, B. H.; Kim, K. S.; Culley, D. E.; Reed, S. B.; Romine, M. F.; Saffarini, D. A.; Hill, E. A.; Shi, L.; Elias, D. A.; Kennedy, D. W.; Pinchuk, G.; Watanabe, K.; Ishii, S.; Logan, B.; Nealson, K. H.; Fredrickson, J. K., Electrically conductive bacterial nanowires produced by Shewanella oneidensis strain MR-1 and other microorganisms. *Proc. Natl. Acad. Sci. U. S. A.* **2006,** 103, (30), 11358-11363.
12. Reguera, G.; Nevin, K. P.; Nicoll, J. S.; Covalla, S. F.; Woodard, T. L.; Lovley, D. R., Biofilm and nanowire production leads to increased current in Geobacter sulfurreducens fuel cells. *Appl. Environ. Microbiol.* **2006,** 72, (11), 7345-7348.
13. Wang, Y. F.; Tsujimura, S.; Cheng, S. S.; Kano, K., Self-excreted mediator from Escherichia coli K-12 for electron transfer to carbon electrodes. *Appl. Microbiol. Biotechnol.* **2007,** 76, (6), 1439-1446.
14. Hernandez, M. E.; Newman, D. K., Extracellular electron transfer. *Cell. Mol. Life Sci.* **2001,** 58, (11), 1562-1571.
15. Rabaey, K.; Boon, N.; Siciliano, S. D.; Verhaege, M.; Verstraete, W., Biofuel cells select for microbial consortia that self-mediate electron transfer. *Appl. Environ. Microbiol.* **2004,** 70, (9), 5373-5382.

16. Kim, H. J.; Park, H. S.; Hyun, M. S.; Chang, I. S.; Kim, M.; Kim, B. H., A mediator-less microbial fuel cell using a metal reducing bacterium, Shewanella putrefaciense. *Enzyme Microb. Technol.* **2002,** 30, (2), 145-152.
17. Myers, C. R.; Myers, J. M., Outer membrane cytochromes of Shewanella putrefaciens MR-1: Spectral analysis, and purification of the 83-kDa c-type cytochrome. *Biochim. Biophys. Acta* **1997,** 1326, (2), 307-318.
18. Myers, C. R.; Myers, J. M., Localization of Cytochromes to the Outer-Membrane of Anaerobically Grown Shewanella-Putrefaciens Mr-1. *J. Bacteriol.* **1992,** 174, (11), 3429-3438.
19. Lovley, D. R., Bug juice: harvesting electricity with microorganisms. *Nat. Rev. Microbiol.* **2006,** 4, (7), 497-508.
20. Du, Z. W.; Li, H. R.; Gu, T. Y., A state of the art review on microbial fuel cells: A promising technology for wastewater treatment and bioenergy. *Biotechnol. Adv.* **2007,** 25, (5), 464-482.
21. Park, D. H.; Zeikus, J. G., Electricity generation in microbial fuel cells using neutral red as an electronophore. *Appl. Environ. Microbiol.* **2000,** 66, (4), 1292-1297.
22. Allen, R. M.; Bennetto, H. P., Microbial Fuel-Cells - Electricity Production from Carbohydrates. *Appl. Biochem. Biotechnol.* **1993,** 39, 27-40.
23. Vega, C. A.; Fernandez, I., Mediating Effect of Ferric Chelate Compounds in Microbial Fuel-Cells with Lactobacillus-Plantarum, Streptococcus-Lactis, and Erwinia Dissolvens. *Bioelectroch. Bioener.* **1987,** 17, (2), 217-222.
24. Bennetto, H. P.; Delaney, G. M.; Mason, J. R.; Roller, S. D.; Stirling, J. L.; Thurston, C. F., The Sucrose Fuel-Cell - Efficient Biomass Conversion Using a Microbial Catalyst. *Biotechnol. Lett.* **1985,** 7, (10), 699-704.
25. Schaetzle, O.; Barriere, F.; Baronian, K., Bacteria and yeasts as catalysts in microbial fuel cells: electron transfer from micro-organisms to electrodes for green electricity. *Energ. Environ. Sci.* **2008,** 1, (6), 607-620.
26. Asin-Cayuela, J.; Manas, A. R. B.; James, A. M.; Smith, R. A. J.; Murphy, M. P., Fine-tuning the hydrophobicity of a mitochondria-targeted antioxidant. *FEBS Lett.* **2004,** 571, (1-3), 9-16.
27. Kelso, G. F.; Porteous, C. M.; Coulter, C. V.; Hughes, G.; Porteous, W. K.; Ledgerwood, E. C.; Smith, R. A. J.; Murphy, M. P., Selective targeting of a redox-active ubiquinone to mitochondria within cells - Antioxidant and antiapoptotic properties. *J. Biol. Chem.* **2001,** 276, (7), 4588-4596.
28. Murphy, M. P.; Smith, R. A. J., Targeting antioxidants to mitochondria by conjugation to lipophilic cations. *Annu. Rev. Pharmacol. Toxicol.* **2007,** 47, 629-656.
29. James, A. M.; Sharpley, M. S.; Manas, A. R. B.; Frerman, F. E.; Hirst, J.; Smith, R. A. J.; Murphy, M. P., Interaction of the mitochondria-targeted antioxidant MitoQ with phospholipid bilayers and ubiquinone oxidoreductases. *J. Biol. Chem.* **2007,** 282, (20), 14708-14718.
30. Vostiar, I.; Ferapontova, E. E.; Gorton, L., Electrical "wiring" of viable Gluconobacter oxydans cells with a flexible osmium-redox polyelectrolyte. *Electrochem. Commun.* **2004,** 6, (7), 621-626.
31. Timur, S.; Anik, U.; Odaci, D.; Lo Gorton, L., Development of a microbial biosensor based on carbon nanotube (CNT) modified electrodes. *Electrochem. Commun.* **2007,** 9, (7), 1810-1815.

32. Coman, V.; Gustavsson, T.; Finkelsteinas, A.; von Wachenfeldt, C.; Hagerhall, C.; Gorton, L., Electrical Wiring of Live, Metabolically Enhanced Bacillus subtilis Cells with Flexible Osmium-Redox Polymers. *J. Am. Chem. Soc.* **2009,** 131, (44), 16171-16176.
33. Timur, S.; Haghighi, B.; Tkac, J.; Pazarhoglu, N.; Telefoncu, A.; Gorton, L., Electrical wiring of Pseudomonas putida and Pseudomonas fluorescens with osmium redox polymers. *Bioelectrochem.* **2007,** 71, (1), 38-45.
34. Close, D. M.; Ripp, S.; Sayler, G. S., Reporter Proteins in Whole-Cell Optical Bioreporter Detection Systems, Biosensor Integrations, and Biosensing Applications. *Sensors* **2009,** 9, (11), 9147-9174.
35. D'Souza, S. F., Microbial biosensors. *Biosens. Bioelectron.* **2001,** 16, (6), 337-353.
36. Ding, L.; Du, D.; Zhang, X. J.; Ju, H. X., Trends in Cell-Based Electrochemical Biosensors. *Curr. Med. Chem.* **2008,** 15, (30), 3160-3170.
37. Tatsuma, T.; Yoshida, Y.; Shitanda, I.; Notsu, H., Algal biosensor array on a single electrode. *Analyst* **2009,** 134, (2), 223-225.
38. Tkac, J.; Vostiar, I.; Gorton, L.; Gemeiner, P.; Sturdik, E., Improved selectivity of microbial biosensor using membrane coating. Application to the analysis of ethanol during fermentation. *Biosens. Bioelectron.* **2003,** 18, (9), 1125-1134.
39. McCreery, R. L., Advanced carbon electrode materials for molecular electrochemistry. *Chem. Rev.* **2008,** 108, (7), 2646-2687.
40. Adams, R. N., Carbon Paste Electrodes. *Anal. Chem.* **1958,** 30, (9), 1576-1576.
41. Svancara, I.; Vytras, K.; Kalcher, K.; Walcarius, A.; Wang, J., Carbon Paste Electrodes in Facts, Numbers, and Notes: A Review on the Occasion of the 50-Years Jubilee of Carbon Paste in Electrochemistry and Electroanalysis. *Electroanalysis* **2009,** 21, (1), 7-28.
42. D'Orazio, P., Biosensors in clinical chemistry. *Clin. Chim. Acta* **2003,** 334, (1-2), 41-69.
43. Bowling, R. J.; Packard, R. T.; McCreery, R. L., Activation of Highly Ordered Pyrolytic-Graphite for Heterogeneous Electron-Transfer - Relationship between Electrochemical Performance and Carbon Microstructure. *J. Am. Chem. Soc.* **1989,** 111, (4), 1217-1223.
44. Kneten, K. R.; McCreery, R. L., Effects of Redox System Structure on Electron-Transfer Kinetics at Ordered Graphite and Glassy-Carbon Electrodes. *Anal. Chem.* **1992,** 64, (21), 2518-2524.
45. Franklin, R. E., Crystallite Growth in Graphitizing and Non-Graphitizing Carbons. *Proc. R. Soc. London, A* **1951,** 209, (1097), 196-&.
46. Harris, P. J. F., Fullerene-related structure of commercial glassy carbons. *Philos. Mag. A* **2004,** 84, (29), 3159-3167.
47. Jenkins, G. M.; Kawamura, K., Structure of Glassy Carbon. *Nature* **1971,** 231, (5299), 175-&.
48. Garrett, D. J.; Lehr, J.; Miskelly, G. M.; Downard, A. J., Microcontact printing using the spontaneous reduction of aryldiazonium salts. *J. Am. Chem. Soc.* **2007,** 129, (50), 15456-+.
49. Brooksby, P. A.; Downard, A. J., Electrochemical and atomic force microscopy study of carbon surface modification via diazonium reduction in aqueous and acetonitrile solutions. *Langmuir* **2004,** 20, (12), 5038-5045.

50. Brooksby, P. A.; Downard, A. J., Nanoscale patterning of flat carbon surfaces by scanning probe lithography and electrochemistry. *Langmuir* **2005,** 21, (5), 1672-1675.
51. Yu, S. S. C.; Downard, A. J., Photochemical grafting and activation of organic layers on glassy carbon and pyrolyzed photoresist films. *Langmuir* **2007,** 23, (8), 4662-4668.
52. Kim, J.; Song, X.; Kinoshita, K.; Madou, M.; White, B., Electrochemical studies of carbon films from pyrolyzed photoresist. *J. Electrochem. Soc.* **1998,** 145, (7), 2314-2319.
53. Kostecki, R.; Schnyder, B.; Alliata, D.; Song, X.; Kinoshita, K.; Kotz, R., Surface studies of carbon films from pyrolyzed photoresist. *Thin Solid Films* **2001,** 396, (1-2), 36-43.
54. Sun, Z.; Shi, X.; Wang, X.; Sun, Y., Structure and properties of hard carbon films depending on heat treatment temperatures via polymer precursor. *Diamond Relat. Mater.* **1999,** 8, (6), 1107-1113.
55. Ranganathan, S.; McCreery, R.; Majji, S. M.; Madou, M., Photoresist-derived carbon for microelectromechanical systems and electrochemical applications. *J. Electrochem. Soc.* **2000,** 147, (1), 277-282.
56. Ray, K.; McCreery, R. L., Spatially resolved Raman spectroscopy of carbon electrode surfaces: Observations of structural and chemical heterogeneity. *Anal. Chem.* **1997,** 69, (22), 4680-4687.
57. Monthioux, M.; Kuznetsov, V. L., Who should be given the credit for the discovery of carbon nanotubes? *Carbon* **2006,** 44, (9), 1621-1623.
58. Radushkevich, L. V.; Lukyanovich, V. M., O strukture ugleroda, obrazujucegosja pri termiceskom razlozenii okisi ugleroda na zeleznom kontakte. *Zurn. Fisic. Chim* **1952,** 26, 88-95.
59. Iijima, S., Helical Microtubules of Graphitic Carbon. *Nature* **1991,** 354, (6348), 56-58.
60. Wiles, P. G.; Abrahamson, J., Carbon-Fiber Layers on Arc Electrodes .1. Their Properties and Cool-Down Behavior. *Carbon* **1978,** 16, (5), 341-349.
61. Abrahamson, J.; Rhoades, B. L.; Wiles, P. G., Structure of Carbon-Fibers Found on Carbon-Arc Anodes. *Carbon* **1980,** 18, (1), 63-63.
62. Iijima, S.; Ichihashi, T., Single-Shell Carbon Nanotubes of 1-Nm Diameter. *Nature* **1993,** 363, (6430), 603-605.
63. Bethune, D. S.; Kiang, C. H.; Devries, M. S.; Gorman, G.; Savoy, R.; Vazquez, J.; Beyers, R., Cobalt-Catalyzed Growth of Carbon Nanotubes with Single-Atomic-Layerwalls. *Nature* **1993,** 363, (6430), 605-607.
64. Saito, R.; Fujita, M.; Dresselhaus, G.; Dresselhaus, M. S., Electronic-Structure of Chiral Graphene Tubules. *Appl. Phys. Lett.* **1992,** 60, (18), 2204-2206.
65. Kane, C. L.; Mele, E. J.; Lee, R. S.; Fischer, J. E.; Petit, P.; Dai, H.; Thess, A.; Smalley, R. E.; Verschueren, A. R. M.; Tans, S. J.; Dekker, C., Temperature-dependent resistivity of single-wall carbon nanotubes. *Europhys. Lett.* **1998,** 41, (6), 683-688.
66. Avouris, P., Molecular electronics with carbon nanotubes. *Acc. Chem. Res.* **2002,** 35, (12), 1026-1034.
67. Tans, S. J.; Verschueren, A. R. M.; Dekker, C., Room-temperature transistor based on a single carbon nanotube. *Nature* **1998,** 393, (6680), 49-52.

68. Liu, S.; Shen, Q.; Cao, Y.; Gan, L.; Wang, Z. X.; Steigerwald, M. L.; Guo, X. F., Chemical functionalization of single-walled carbon nanotube field-effect transistors as switches and sensors. *Coord. Chem. Rev.* **2010,** 254, (9-10), 1101-1116.
69. Hamada, N.; Sawada, S.; Oshiyama, A., New One-Dimensional Conductors - Graphitic Microtubules. *Phys. Rev. Lett.* **1992,** 68, (10), 1579-1581.
70. Frank, S.; Poncharal, P.; Wang, Z. L.; de Heer, W. A., Carbon nanotube quantum resistors. *Science* **1998,** 280, (5370), 1744-1746.
71. Anantram, M. P., Current-carrying capacity of carbon nanotubes. *Phys. Rev. B* **2000,** 62, (8), R4837-R4840.
72. Britto, P. J.; Santhanam, K. S. V.; Ajayan, P. M., Carbon nanotube electrode for oxidation of dopamine. *Bioelectroch. Bioener.* **1996,** 41, (1), 121-125.
73. Nugent, J. M.; Santhanam, K. S. V.; Rubio, A.; Ajayan, P. M., Fast electron transfer kinetics on multiwalled carbon nanotube microbundle electrodes. *Nano Lett.* **2001,** 1, (2), 87-91.
74. Kuzmany, H.; Kukovecz, A.; Simon, F.; Holzweber, A.; Kramberger, C.; Pichler, T., Functionalization of carbon nanotubes. *Synth. Met.* **2004,** 141, (1-2), 113-122.
75. Niyogi, S.; Hamon, M. A.; Hu, H.; Zhao, B.; Bhowmik, P.; Sen, R.; Itkis, M. E.; Haddon, R. C., Chemistry of single-walled carbon nanotubes. *Acc. Chem. Res.* **2002,** 35, (12), 1105-1113.
76. Vairavapandian, D.; Vichchulada, P.; Lay, M. D., Preparation and modification of carbon nanotubes: Review of recent advances and applications in catalysis and sensing. *Anal. Chim. Acta* **2008,** 626, (2), 119-129.
77. Moore, R. R.; Banks, C. E.; Compton, R. G., Basal plane pyrolytic graphite modified electrodes: Comparison of carbon nanotubes and graphite powder as electrocatalysts. *Anal. Chem.* **2004,** 76, (10), 2677-2682.
78. Yang, W. R.; Ratinac, K. R.; Ringer, S. P.; Thordarson, P.; Gooding, J. J.; Braet, F., Carbon Nanomaterials in Biosensors: Should You Use Nanotubes or Graphene? *Angew. Chem. Int. Ed.* **2010,** 49, (12), 2114-2138.
79. Banks, C. E.; Davies, T. J.; Wildgoose, G. G.; Compton, R. G., Electrocatalysis at graphite and carbon nanotube modified electrodes: edge-plane sites and tube ends are the reactive sites. *Chem. Commun.* **2005**, (7), 829-841.
80. Banks, C. E.; Crossley, A.; Salter, C.; Wilkins, S. J.; Compton, R. G., Carbon nanotubes contain metal impurities which are responsible for the "electrocatalysis" seen at some nanotube-modified electrodes. *Angew. Chem. Int. Ed.* **2006,** 45, (16), 2533-2537.
81. Tasis, D.; Tagmatarchis, N.; Bianco, A.; Prato, M., Chemistry of carbon nanotubes. *Chem. Rev.* **2006,** 106, (3), 1105-1136.
82. Wildgoose, G. G.; Banks, C. E.; Leventis, H. C.; Compton, R. G., Chemically modified carbon nanotubes for use in electroanalysis. *Microchim. Acta* **2006,** 152, (3-4), 187-214.
83. Liu, J.; Rinzler, A. G.; Dai, H. J.; Hafner, J. H.; Bradley, R. K.; Boul, P. J.; Lu, A.; Iverson, T.; Shelimov, K.; Huffman, C. B.; Rodriguez-Macias, F.; Shon, Y. S.; Lee, T. R.; Colbert, D. T.; Smalley, R. E., Fullerene pipes. *Science* **1998,** 280, (5367), 1253-1256.
84. Gooding, J. J., Advances in interfacial design sensors: Aryl diazonium salts for electrochemical biosensors and for modifying carbon and metal electrodes. *Electroanalysis* **2008,** 20, (6), 573-582.

85. Skladal, P., Advances in electrochemical immunosensors. *Electroanalysis* **1997,** 9, (10), 737-745.
86. Guschin, D. A.; Shkil, H.; Schuhmann, W., Electrodeposition polymers as immobilization matrices in amperometric biosensors: improved polymer synthesis and biosensor fabrication. *Anal. Bioanal. Chem.* **2009,** 395, (6), 1693-1706.
87. Cosnier, S., Biomolecule immobilization on electrode surfaces by entrapment or attachment to electrochemically polymerized films. A review. *Biosens. Bioelectron.* **1999,** 14, (5), 443-456.
88. Teles, F. R. R.; Fonseca, L. R., Applications of polymers for biomolecule immobilization in electrochemical biosensors. *Mat. Sci. Eng. C-Biomim.* **2008,** 28, (8), 1530-1543.
89. Wang, B. Q.; Li, B.; Deng, Q.; Dong, S. J., Amperometric glucose biosensor based on sol-gel organic-inorganic hybrid material. *Anal. Chem.* **1998,** 70, (15), 3170-3174.
90. Lukowiak, A.; Strek, W., Sensing abilities of materials prepared by sol-gel technology. *J. Sol-Gel Sci. Technol.* **2009,** 50, (2), 201-215.
91. Gupta, R.; Chaudhury, N. K., Entrapment of biomolecules in sol-gel matrix for applications in biosensors: Problems and future prospects. *Biosens. Bioelectron.* **2007,** 22, (11), 2387-2399.
92. Love, J. C.; Estroff, L. A.; Kriebel, J. K.; Nuzzo, R. G.; Whitesides, G. M., Self-assembled monolayers of thiolates on metals as a form of nanotechnology. *Chem. Rev.* **2005,** 105, (4), 1103-1169.
93. Nuzzo, R. G.; Allara, D. L., Adsorption of Bifunctional Organic Disulfides on Gold Surfaces. *J. Am. Chem. Soc.* **1983,** 105, (13), 4481-4483.
94. Chow, E.; Hibbert, D. B.; Gooding, J. J., Electrochemical detection of lead ions via the covalent attachment of human angiotensin I to mercaptopropionic acid and thioctic acid self-assembled monolayers. *Anal. Chim. Acta* **2005,** 543, (1-2), 167-176.
95. Willey, T. M.; Vance, A. L.; van Buuren, T.; Bostedt, C.; Terminello, L. J.; Fadley, C. S., Rapid degradation of alkanethiol-based self-assembled monolayers on gold in ambient laboratory conditions. *Surf. Sci.* **2005,** 576, (1-3), 188-196.
96. Flynn, N. T.; Tran, T. N. T.; Cima, M. J.; Langer, R., Long-term stability of self-assembled monolayers in biological media. *Langmuir* **2003,** 19, (26), 10909-10915.
97. Cortes, E.; Rubert, A. A.; Benitez, G.; Carro, P.; Vela, M. E.; Salvarezza, R. C., Enhanced Stability of Thiolate Self-Assembled Monolayers (SAMs) on Nanostructured Gold Substrates. *Langmuir* **2009,** 25, (10), 5661-5666.
98. Delamar, M.; Hitmi, R.; Pinson, J.; Saveant, J. M., Covalent Modification of Carbon Surfaces by Grafting of Functionalized Aryl Radicals Produced from Electrochemical Reduction of Diazonium Salts. *J. Am. Chem. Soc.* **1992,** 114, (14), 5883-5884.
99. Allongue, P.; Delamar, M.; Desbat, B.; Fagebaume, O.; Hitmi, R.; Pinson, J.; Saveant, J. M., Covalent modification of carbon surfaces by aryl radicals generated from the electrochemical reduction of diazonium salts. *J. Am. Chem. Soc.* **1997,** 119, (1), 201-207.
100. Downard, A. J., Electrochemically assisted covalent modification of carbon electrodes. *Electroanalysis* **2000,** 12, (14), 1085-1096.

101. Pinson, J.; Podvorica, F., Attachment of organic layers to conductive or semiconductive surfaces by reduction of diazonium salts. *Chem. Soc. Rev.* **2005,** 34, (5), 429-439.
102. Barriere, F.; Downard, A. J., Covalent modification of graphitic carbon substrates by non-electrochemical methods. *J. Solid State Electrochem.* **2008,** 12, (10), 1231-1244.
103. D'Amours, M.; Belanger, D., Stability of substituted phenyl groups electrochemically grafted at carbon electrode surface. *J. Phys. Chem. B* **2003,** 107, (20), 4811-4817.
104. deVilleneuve, C. H.; Pinson, J.; Bernard, M. C.; Allongue, P., Electrochemical formation of close-packed phenyl layers on Si(111). *J. Phys. Chem. B* **1997,** 101, (14), 2415-2420.
105. Solak, A. O.; Ranganathan, S.; Itoh, T.; McCreery, R. L., A mechanism for conductance switching in carbon-based molecular electronic junctions. *Electrochem. Solid. St.* **2002,** 5, (8), E43-E46.
106. Kariuki, J. K.; McDermott, M. T., Nucleation and growth of functionalized aryl films on graphite electrodes. *Langmuir* **1999,** 15, (19), 6534-6540.
107. Kariuki, J. K.; McDermott, M. T., Formation of multilayers on glassy carbon electrodes via the reduction of diazonium salts. *Langmuir* **2001,** 17, (19), 5947-5951.
108. Ortiz, B.; Saby, C.; Champagne, G. Y.; Belanger, D., Electrochemical modification of a carbon electrode using aromatic diazonium salts. 2. Electrochemistry of 4-nitrophenyl modified glassy carbon electrodes in aqueous media. *J. Electroanal. Chem.* **1998,** 455, (1-2), 75-81.
109. Rubinstein, I., Voltammetric Study of Nitrobenzene and Related-Compounds on Solid Electrodes in Aqueous-Solution. *J. Electroanal. Chem.* **1985,** 183, (1-2), 379-386.
110. Lyskawa, J.; Belanger, D., Direct modification of a gold electrode with aminophenyl groups by electrochemical reduction of in situ generated aminophenyl monodiazonium cations. *Chem. Mater.* **2006,** 18, (20), 4755-4763.
111. Hurley, B. L.; McCreery, R. L., Covalent bonding of organic molecules to Cu and Al alloy 2024 T3 surfaces via diazonium ion reduction. *J. Electrochem. Soc.* **2004,** 151, (5), B252-B259.
112. Doppelt, P.; Hallais, G.; Pinson, J.; Podvorica, F.; Verneyre, S., Surface modification of conducting substrates. Existence of azo bonds in the structure of organic layers obtained from diazonium salts. *Chem. Mater.* **2007,** 19, (18), 4570-4575.
113. Yu, S. S. C.; Tan, E. S. Q.; Jane, R. T.; Downard, A. J., An electrochemical and XPS study of reduction of nitrophenyl films covalently grafted to planar carbon surfaces. *Langmuir* **2007,** 23, (22), 11074-11082.

Chapter 2. General Experimental

2.1 General synthesis and reagents

2.1.1 Reagents

The reagents used in this thesis work and not described elsewhere are listed here in alphabetical order. The abbreviation, purity (if known) and manufacturer are included in the brackets for each compound

1,4-diaminobenzene (phenylenediamine, 98 %, Sigma), 2,2'-bipyridine (bpy, Acros Organics), Acetonitrile (ACN, 99.9 %, ROMIL), aluminium nitrate hydrate ($Al(NO_3)_3$, 55-68 %, $Al(NO_3)_3$, BDH), ammonium acetate (NH_4OAc, 97 %, BDH), ammonium hexafluorophosphate (NH_4PF_6, Alfa Aesar), aniline (BDH), cyano sodiumborohydride ($NaBH_3CN$, 95 %, Aldrich), dichloromethane (DCM, 99.80%, Merck), dicyclohexyl carbodiimide (DCC, 99%, Alfa Aesar), dimethylformamide (DMF, 99.5 %, ROMIL), dimethylsulphoxide (DMSO, 99.5 %, Lab Scan), ethylenediamine (en, 99 %, Merck), ferrocene carboxaldehyde (97 %, Alfa Aesar), iodine (pellets) (I_2, Unilab), iron(III)nitrate ($Fe(NO_3)_3$, 95 %, Riedel-de Haën), N-(3-dimethylaminopropyl)-N-ethylcarbodiimide hydrochloride (EDCI, Alfa Aesar), N-hydroxy succinimide (NHS, 97 %, Aldrich), nicotine adenine dinucleotide (reduced disodium salt) (NADH, Sigma), nitrobenzaldehyde (98 %, Aldrich), osmium tetroxide (0.5 g vials) (OsO_4, JMC), polydimethylsiloxane (PDMS, Sylgard 184, Dow corning), Polyvinylpyrrolidone (PVP40, average weight 40,000 g mol^{-1}, Sigma-Aldrich), potassium chloride (KCl, 99.9 %, J.T. Baker), potassium ferricycanide ($K_3Fe(CN)_6$, 99 %, Aldrich), potassium ferrocycanide ($K_4Fe(CN)_6$, 99 %, Hopkin & Williams Ltd), pyridine (py, BDH), ruthenium hexaammine chloride ($Ru(NH_3)_6Cl_2$, 98 %, Aldrich), sodium borohydride ($NaBH_4$, Fischer Scientific), sodium dithionite ($Na_2S_2O_3$, 85 %, M&B), sodium nitrite ($NaNO_2$, 99 %, Aldrich).

2.1.2 Tetrabutylammonium tetraflouroborate

Tetrabutylammonium tetrafluoroborate ($TBABF_4$) salt was prepared by mixing tetrabutylammonium hydroxide (TBAOH, 40 %, Acros Organics) and fluoroboric acid (50 %, BDH). 5 mL of 50 % HBF_4 was diluted to 25 mL with water and added, with stirring, to 20 mL of 40 % TBAOH that was diluted to 100 mL with water. The white precipitate was washed with water and filtered under vacuum. The electrolyte was dried over night at 60 ^oC and then for 5 days under vacuum at 80 ^oC. $TBABF_4$ was stored under vacuum in a desiccator.

2.1.3 Dry acetonitrile

ACN was dried by refluxing over CaH_2 under nitrogen for at least 1 h before use. Milli-Q water was prepared using a Millipore system and only collected when the measured resistivity was at least 18 MΩ cm.

2.1.4 4-nitrobenzenediazonium tetrafluoroborate

4-nitrobenzenediazonium tetrafluoroborate was synthesized using literature methods.[1] 5 mmol of 4-nitroaniline was dissolved in 2 mL of 50% fluoroboric acid, pre-diluted with 2 mL of Milli-Q water. The mixture was cooled in an ice bath and 5 mmol of sodium nitrite dissolved in 1 mL of Milli-Q water was added slowly to the mixture with stirring. The solution was further cooled in a salted acetone-ice bath for 10 min while the product formed as white crystals. The crude product was obtained by filtration and washed with ice cold Milli-Q water and diethylether. The product was dissolved in the minimum amount of room temperature acetonitrile and reprecipitated by cooling the solution on ice and gradual addition of diethylether. The purified product was dried in a fume cupboard overnight and then stored in the dark under vacuum. ***Caution: diazonium salts are potentially explosive and synthesis should be limited to small amounts.***

2.1.5 Ammonium osmium(II) hexachloride

Two frozen glass vials, each containing 0.5 g of OsO_4, were cracked with a pair of pliers in a fume cupboard over a round bottom flask containing 20 mL of conc. HCl. A second worker was required to hold an upturned beaker over the mouth of the round bottom flask to ensure that all of the glass from the broken vials was directed into the HCl. ***Caution: OsO_4 has toxic vapor which causes damage to eyes, skin and the respiratory system. Synthesis must be conducted under a fume hood with protection of exposed skin.*** The flask was fitted with a water jacket condenser and heated to reflux with stirring overnight. The glass was removed from the solution by filtration and approximately 0.5 g of NH_4Cl was added forming a brick red precipitate. The product was obtained by filtration, resuspended in 50 mL of H_2O, filtered, washed with 5 mL of H_2O and dried at 60 ^oC for 1 h yielding 1.2 g of product.

2.1.6 Phosphate buffered saline (PBS)

For non bacterial work PBS was made using H_3PO_4 (BDH, 99.9 %) and $NaH_2PO_4.2H_2O$ (MERCK) for buffers between pH 2 and pH 5, NaH_2PO_4 and Na_2HPO_4 (BDH, 99 %) for buffers between pH 5 and pH 8 and Na_2HPO_4 and $Na_3PO_4.12H_2O$ (M&B, 98 %)(for buffers between pH 8 and pH 13. The amount of the reagents in each buffer was estimated using the Henderson-Hasselbach equation (equation 2.1.1) where the pK_a corresponds to the acidic proton of the acid base pair in use, $[A^-]$ is the concentration of the base component and [HA] is the concentration of the acidic component.. All buffers were prepared to make a phosphate concentration of 50 mM and the pH adjusted using 0.1 M HCl or 0.1 M NaOH. Finally KCl was added to a

$$pH = pK_a + \log([A^-]/[HA]) \qquad 2.1.1$$

concentration of 0.1 mol L^{-1}. PBS for work with bacteria work was prepared by the standard recipe: 4.036 g Na_2HPO_4, 2.935 g KH_2PO_4, 7.455 g KCl in 1 L of deionised water. The buffers were sterilized in an autoclave at 121 ^oC for 15 min at 15 PSI.

2.2 Electrochemistry

2.2.1 Electrochemical cell designs

Electrochemistry using GC rods was undertaken using a glass pear-shaped cell depicted in Figure 2.1. Inlets at the top of the cell were used to introduce the GC rod working electrode, Pt counter electrode and reference electrode. A fourth inlet (gas line port) was available for nitrogen purging of electrolyte solutions. Modification of PPF plate electrodes or MWCNT / epoxy electrodes (see section 2.5.3) was done using either a modified pear shaped cell or a simple beaker cell. An example of the modified pear shaped cell is shown in Figure 2.2. The base of the cell is flattened and a hole drilled through to allow the electrolyte solution to access the working electrode. The cell is held down to a metal base using hooks and springs and a water tight seal is made to the plate electrode sandwiched between the cell and the base using a rubber o-ring. The area of the

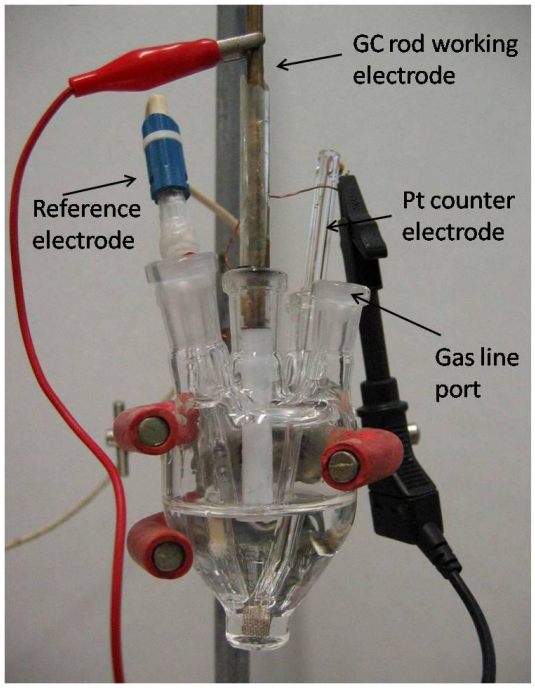

Figure 2.1. Photograph of the electrochemical cell used for experiments involving GC rod working electrodes.

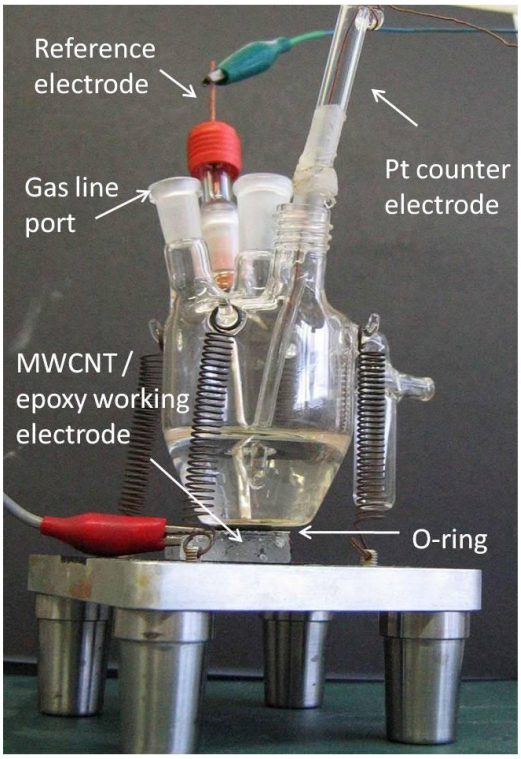

Figure 2.2. Photograph of the electrochemical cell used in experiments involving plate electrodes such as PPF and MWCNT / epoxy electrodes.

working electrode exposed to solution is dictated by the size of o-ring used. The Pt counter electrode, reference and gas lines are introduced from the top of the cell in a similar fashion to the pear shaped cell used for experiments involving GC rods.

Long term chronoamperometric studies of cell suspensions were performed using a purpose built Teflon cell block containing three separate identical cells. An exploded view of the cell components is shown in **Figure 2.3**. The cell is designed so that oxygen can be excluded from the experiment by virtue of the o-rings in contact with the working electrode and cell cap. Three electrochemical cells are included so that bacterial cells prepared on the same day can be compared in parallel varying the working electrode surface. Each of the three cells in the block was attached to a dedicated potentiostat.

Where mentioned PPF electrodes were modified by simply suspending the electrode into a solution in an open beaker. Contact was made with the PPF using an alligator clip with a small copper strip clamped to the PPF surface.

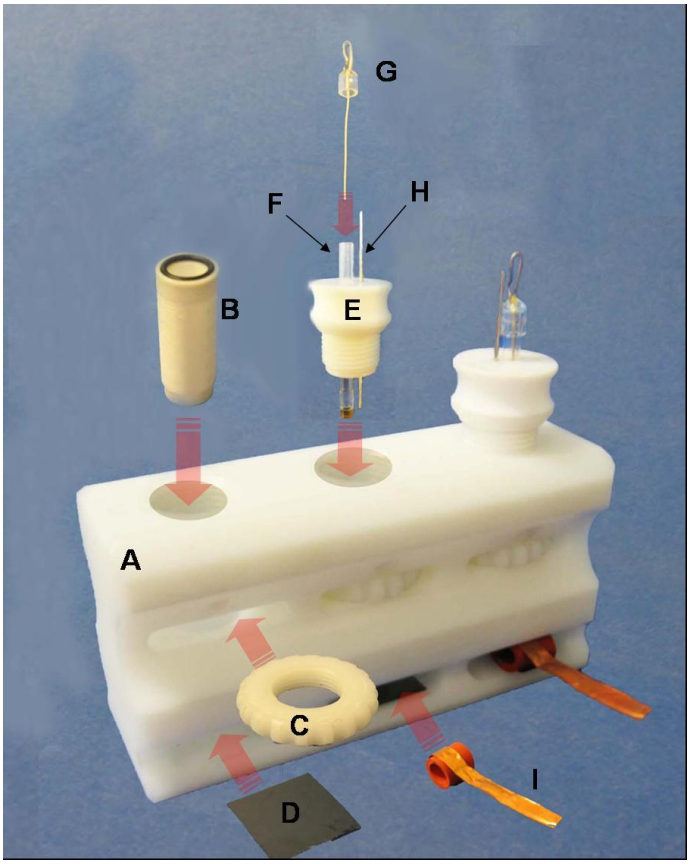

Figure 2.3. Exploded view of the Teflon cell block (3-cells) used for chronoamperometric bacterial cell suspension studies**.** A) Teflon cell body, B) Teflon threaded hollow tube to contain the electrolyte solution and live bacterial culture. O-rings at both tube ends form an airtight seal against the lower plate electrode and the cell cap. The working electrode o-ring defines an area of 0.5 cm^2. (C) Teflon threaded wheel for raising and lowering the cell tube (B). (D) PPF plate working electrode, (E) Teflon threaded cell cap, (F) Reference electrode sleeve is a glass tube fitted with a porous glass frit and contains saturated KCl in Milli-Q H_2O, (G) An Ag wire coated with AgCl formed by anodizing at 1.6 V *vs.* Ag/AgCl for 60 s in a saturated KCl solution. A glass cap is attached to the wire which fits over the reference electrode sleeve (F) forming an airtight seal, (H) Pt counter electrode, (I) Copper foil and rubber spring for making electrical contact with the working electrode.

2.2.2 Reference electrodes

Saturated calomel electrodes (SCE) were purchased from Radiometer Copenhagen. Ag/AgCl reference electrodes were made using a thin glass tube with a Vycor glass frit attached to one end with heat shrunk Teflon tube. A section of 2 mm diameter silver wire was anodized in a KCl solution at 1.6 V *vs.* $Ag_{(wire)}$ for 1 min forming an off white AgCl coating. The glass tube was filled with saturated KCl and the anodized silver wire secured in the KCl solution with Parafilm. Ag/Ag^+ reference electrodes for use in ACN electrolyte solutions were prepared by securing Vycor glass frits to the ends of two glass tubes chosen so that one fitted inside the other. The outer sleeve was filled with an aliquot of the solution being used in the electrochemical cell and the inner sleeve filled with 0.01 M $AgNO_3$ and 0.1 M $TBABF_4$ in ACN. A clean Ag wire was inserted into the inner sleeve to complete the Ag/Ag^+ couple and to act as an electrical contact.

2.2.3 Acquisition and analysis of electrochemical data

The majority of electrochemical experiments described in this thesis were conducted using either an Eco Chemie Autolab, PGSTAT302 or PGSTAT302N potentiostat. All electrochemical experiments, recorded using these potentiostats employed GPES V 4.9.006 (Eco Chemie B.V) software for CV and FRA 4.9.006 (Eco Chemie B.V) software for impedance spectroscopy. Other potentiostats used in this thesis work were: a EG & G PAR173 potentiostat controlled by an ADI Instruments Powerlab 4SP analogue to digital converter which was controlled by a PC running either Echem v. 1.5.2 (ADI Instruments) or Chart v. 4.2.2 (ADI instruments) software. Post processing of electrochemical data was performed using Excel 2007 (Microsoft). All curve fitting and peak area measurements employed LinkFit 4.1 (John S. Loring Copyright 1996-2000) software. Peaks to be integrated were extracted from the CV data set and base lines were calculated only for the data immediately adjacent to the peaks using 3rd order polynomial fits with y-axis intercepts. The peaks were fitted using a mixed Lorentzian / Gaussian algorithm. From the area of the CV peak for a surface confined redox species the surface concentration was calculated using equation 2.2.1 where Γ is the surface concentration (mol cm^{-2}), Q is the total charge (coulombs) corresponding to the CV peak obtained by

dividing the peak area (in V. A) by the scan rate (V s^{-1}) used, *n* is the number of electrons in the redox process, *F* is the Faraday constant (C mol^{-1}) and A (cm^2) is the geometric area of the working electrode.

$$\Gamma = Q/nFA \qquad 2.2.1$$

2.3 Substrate electrode types

2.3.1 Pyrolysed photoresist films (PPF)

Square 13 × 13 mm sections were cut from a phosphorus doped n-type 1,0,0 silicon wafer (Silicon Quest International) using a diamond tipped scribe. Prior to scribing, the silicon was coated with a thin layer of AZ1518 photoresist (Clariant) to protect the surface during cutting and handling. Once cut the protective film was cleaned from the silicon squares by three sequential 30 s washings in HPLC grade acetone in a sonication bath, followed by 30 s of sonication in isopropyl alcohol (IPA) to limit solvent drying marks. The negative photoresist AZ4620 (Clariant) was spun onto the clean silicon wafers at 3000 rpm for 30 s. The resultant photoresist film was soft baked at 60 ^oC for at least 1 h but commonly overnight. The wafers were loaded into a quartz boat and baked under a 3 L min^{-1} stream of 95 % N_2 and 5% H_2 at 550 ^oC for 30 min, 750 ^oC for 30 min and 1060 ^oC for 1 h. The wafers were allowed to cool to less than 80 ^oC under a 0.5 L min^{-1} stream of the same gas mixture before unloading. During baking the dry photoresist films reduced from 6 μm to approximately 1.5 μm in thickness and usually exhibited a surface RMS roughness of approximately 0.5 nm.

Figure 2.4 shows a typical AFM micrograph of a freshly prepared PPF sample. The surface roughness for this sample was 0.522 nm, established by averaging the roughness calculated by the nanoscope AFM software for 10 randomly positioned 250 nm × 250 nm squares (the obvious peaks due to debris on the sample were excluded).

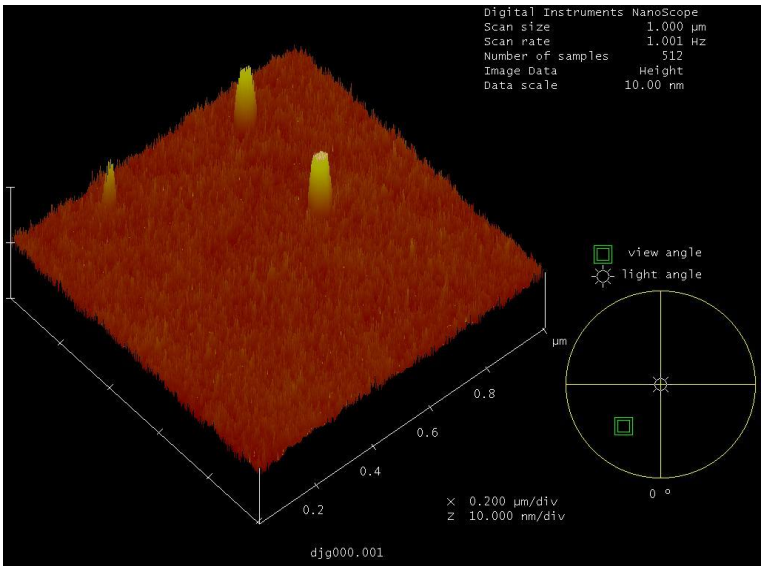

Figure 2.4. AFM micrograph of a freshly prepared PPF sample exhibiting a surface RMS roughness of 0.522 nm.

Before use for electrochemistry PPF electrode resistances were measured using a purpose built probe bearing two parallel 10 mm long flat electrodes 10 mm apart. These were pressed onto the PPF surface with a sprung clamp to ensure that each measurement was recorded under the same compression. The resistance between the probe electrodes was measured using a Digitech QM1320 multimeter. Only samples with a surface resistance between 18 and 25 $\Omega\ \square^{-1}$ were used for electrochemical experiments. Samples with surface resistances as high as 30 $\Omega\ \square^{-1}$ were used as the base of MWCNT electrodes.

2.3.2 Glassy carbon (GC) rods

Short plugs of glassy carbon were cut from a 3 mm diameter cylindrical GC rod. Each plug was embedded in a tight fitting Teflon tube with one flat end flush with the Teflon sleeve and the other housed in the Teflon and in contact with a copper rod (Figure 2.5). The copper rod extended from the Teflon sleeve and acted as the electrical contact for the electrode The Teflon sleeve ensures that only the flat surface of the GC is in contact with electrolyte solutions.

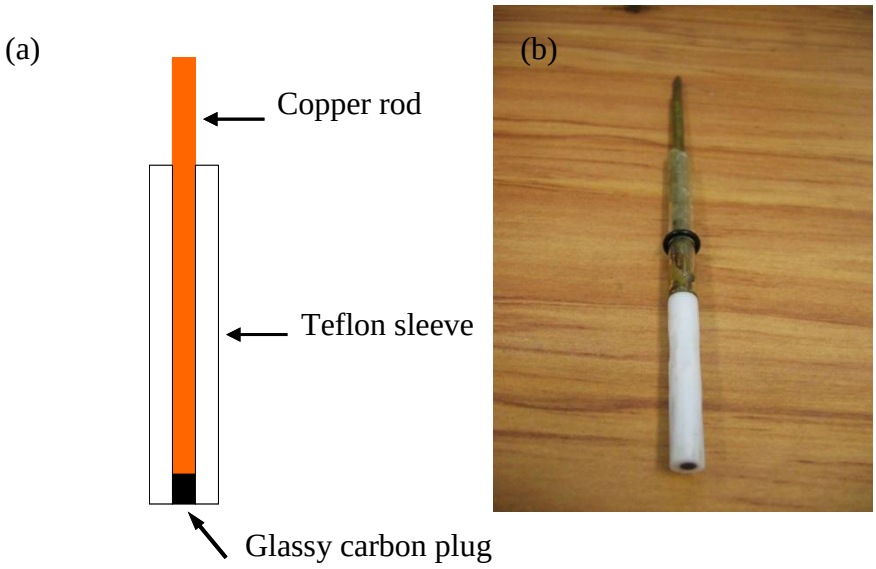

Figure 2.5. (a) Cartoon depiction and (b) photograph of a glassy carbon (GC) rod electrode.

For each new experiment the GC surface was prepared by manual mechanical polishing with wet 1 μm diameter Al_2O_3 powder (Leco Corporation) on an adhesive backed lecloth (Leco Corporation). The GC electrodes were polished until they yielded a Δ*E*p close to 80 mV for a CV recorded in a 1 mM $Fe(CN)_6^{3-}$ solution in 0.1 M KCl at a scan rate of 100 mV s^{-1}. After polishing, the electrodes were cleaned by sonication in Milli-Q water for approximately 1 min.

2.4 Vertically aligned SWCNT electrodes

2.4.1 Grafting of aminophenyl tether layers

Grafting of aminophenyl films formed from in situ produced *p*-aminobenzenediazonium cations was achieved by the method of Lyskawa *et al.*[2] All diazonium salt solutions were prepared by rapidly adding a 10 mM solution of 1,4-diaminobenzene in 0.5 M HCl to solid $NaNO_2$ at a molar ratio of 1:1 1,4-diaminobenzene : $NaNO_2$. The solution was allowed to react for 3 min over which time

the solution colour changed from colorless to yellow. The solution was then added to an electrochemical cell with all electrodes in place so that the CV could be initiated immediately. Electrochemical grafting of the in situ formed 4-aminobenzene diazonium cations was achieved by two sequential CVs from 0.2 V to -0.6 V *vs.* SCE, scan rate = 100 mV s^{-1}, or by two sequential CVs over the same potential range with a 2 min deposition at a fixed potential of -0.6 V *vs.* SCE between the CVs.

Grafting of aminophenyl films by reduction of nitrophenyl films was based on the earlier work of Yu et al.[3] 4-nitrobenzenediazonium tetrafluoroborate was synthesized as described in section 2.1.4. The diazonium cation was grafted from an ACN solution containing 1 mM 4-nitrobenzenediazonium tetrafluoroborate and 0.1 M $TBABF_4$ by one CV scan from 0.2 to -0.6 V *vs.* Ag/Ag^+, scan rate = 100 mV s^{-1}, followed by a 2 min fixed potential deposition at -0.6 V and finally a repeat CV using the same conditions as the first. The electrode (now modified with a nitrophenyl (NP) film) was cleaned by sonication for 10 s in acetone followed by 10 s in water. The NP film was electrochemically reduced to an aminophenyl (AP) film by conducting four CV cycles in 0.1 M H_2SO_4 from 0.5 to -1.0 V *vs.* SCE.

2.4.2 Cutting and coupling of SWCNTS

SWCNTs prepared by the HIPCO process were purchased from Carbon Nanotechnologies Incorporated (CNI). Functionalization with carboxylic acid groups and shortening of the SWCNTs was achieved by the method of Shapter *et al.* [4] which was derived from the earlier work of Smalley and coworkers.[5] Concentrated H_2SO_4 and HNO_3 were mixed in a 3:1 ratio and uncut SWCNTs were added to make a suspension of 25 mg of CNTs in 27 mL of acid. ***Caution: the toxicity of CNTs is not currently known. Some evidence suggests that inhalation of CNTs may damage lung tissue hence all loose CNTs and CNT suspensions were handled under a fume hood and stored in sealed containers.*** The resulting suspension was agitated in a sonication bath for between 4 and 10 h. Ice was added to the bath every 30 min to maintain a temperature close to 20 ^oC. Periodically the reaction vial was shaken vigorously to aid suspension of the CNTs and the cap removed to vent evolved CO_2. Following the sonication period the vial

contents were poured into 500 mL of distilled water and left to settle overnight. The settled nanotubes were filtered through 0.22 μm hydrophilic polytetrafluoroethylene **(**PTFE) filters (Millipore) under suction with washing until the rinse water reached pH 5-7. Once the filtered CNTs cakes were dried they were easily peeled of the filters. Reaction solutions of cut nanotubes were prepared by sonication of the dried CNT mats in DMSO or DMF.

Coupling reactions between amine terminating films and cut SWCNTs were carried out in capped reaction vials containing the AP modified electrodes submerged in a DMSO suspension containing 0.2 mg mL^{-1} of cut SWCNTs. The reactions were heated by placing the vials in an oven at 65 ^{o}C for the allotted period of time. Where specified the reactions were assisted by the coupling agent DCC at a concentration of 0.5 mg mL^{-1}. The DCC was added to the reaction solution immediately prior to introduction of the AP modified electrode.

2.5 MWCNT synthesis by CVD and fabrication of MWCNT epoxy composite electrodes

2.5.1 Electron beam evaporation of metal catalysts

The catalyst layers were deposited by evaporation using an Edwards 3000 electron beam deposition system. Aluminium wires were cleaned by sonication in acetone and IPA, before being loaded into a graphite crucible (Kurt J. Lesker Vacuum Technology). High purity Fe and Al_2O_3 pellets (Kurt J. Lesker Vacuum Technology) were loaded into tungsten crucibles (Kurt J. Lesker Vacuum Technology). Between experiments all metallic targets were stored under high vacuum in a desiccator. Before deposition the e-beam chamber was pumped down to at least 6 x 10^{-6} mbar to avoid oxidation, particularly of the iron layer. The deposition of the metals and Al_2O_3 was monitored with an in situ quartz crystal monitor. After deposition, samples were stored under vacuum in a

desiccator until they were required for CVD. Patterned catalyst films were deposited as above but with a patterned photoresist film pre-prepared on the sample (see section 2.7)

2.5.2 MWCNT preparation by CVD

The furnace employed for all CVD was a Radatherm adjustable power microwave tube furnace (Model 2216e) containing a 35 mm inner diameter quartz tube as the reaction chamber. The gas inlet and outlet were sealed to the quartz tube by purpose-built ground quartz joints sealed with the assistance of a small amount of silicon grease. The gas inlet line to the reaction tube was divided into four independently controllable feed lines. The gases used for the four lines were H_2 (BOC gases), ethylene (C_2H_2, Southern Gas), Ar (Southern Gas) which passed through a water bubbler, and a high flow Ar (Southern Gas) carrier gas line which was also used for the furnace cool-down after reaction. Each line passed through a ball gauge for control of gas mixtures and flow rates.

In a typical preparation of MWCNTs a number of samples with pre-deposited catalyst layers were loaded into a quartz boat which was placed in the reaction tube. At room temperature all gas lines were allowed to flow for at least 5 min to void any collected air in the lines. Following this step a forming gas mixture of 1.2 L min^{-1} Ar and 0.8 L min^{-1} H_2 was flowed through the reaction tube for at least 5 min at room temperature. The furnace was then heated to 750 ^oC under the gas flow for 15-30 min. The CVD reaction was initiated by reducing the H_2 flow rate to near zero and the Ar carrier gas flow rate to 1 L min^{-1} and introducing a flow of 0.4 L min^{-1} of C_2H_2 and 0.05 L min^{-1} of Ar passed through a water bubbler. MWCNT growth was typically allowed to continue for 5 – 10 min. At the end of the growth time the C_2H_2, H_2 and water vapor flow rates were reduced to zero and the furnace was allowed to cool under a flow of Ar. Samples were removed once the furnace had cooled to 180 ^oC unless on PPF where they were cooled to less than 80 ^oC to avoid oxidation of the PPF surface.

2.5.3 MWCNT / epoxy composite electrode assembly

An electrode template was fashioned from two slabs of laboratory rubber sheet and a 20 × 15 mm section of silicon wafer (Figure 2.6 (a)). Two electrode templates were simultaneously cast into a negative mold using a room temperature vulcanizing silicone (M4670A , Barnes). The mold frame was made from plastic strips and electrical tape set onto a glass plate using plasticine (Figure 2.6 (b)). The silicone was mixed as per the manufacturers specifications and degassed under vacuum for 30 min before pouring into the mold frame. Once poured the entire mold was degassed for a further hour under vacuum to ensure that all air bubbles were removed. The mold assembly was removed from vacuum and set aside to cure for 24 h. After 24 h the silicone was sufficiently firm to remove the plasticine after which the mold was cured at 60 ^{o}C for a further 24 h. Once cured the mold frame was removed and slits were cut into the side and top of the silicone mold with a razor blade to aid release of the template. A cartoon view and further explanation of the mold assembly and its use is included in section 4.3.1.2.

MWCNTs forests were grown on half of a PPF modified 13 × 15 mm silicon wafer by CVD as described in sections 2.5.1 and 2.5.2 (Figure 2.6 (c)). A piece of electrical tape was adhered to the exposed PPF to protect the contact area (Figure 2.6 (d)). The mold was greased with a small amount of silicone grease to aid release of the substrate and then the protected PPF contact area was inserted into the mold slot (Figure 2.6. (e)). A two part low viscosity thermal curing epoxy resin (EPO-TEK 301) was thoroughly mixed and pipetted carefully into the mold so that it flooded the MWCNT forest (Figure 2.6 (f)). The mold assembly was placed in a desiccator and the pressure decreased to 60 mbar over 30 min to remove trapped air bubbles from within the CNT mat. Usually during this process the desiccator needed to be repressurized several times to prevent the epoxy foaming and spilling out of the mold and to prevent large air bubbles forming and floating the MWCNT mat off the PPF surface.

Once thoroughly degassed the mold was placed in a 60 ^{o}C oven for 3 – 4 h until the epoxy was hard. The electrode was then removed from the mold as shown in

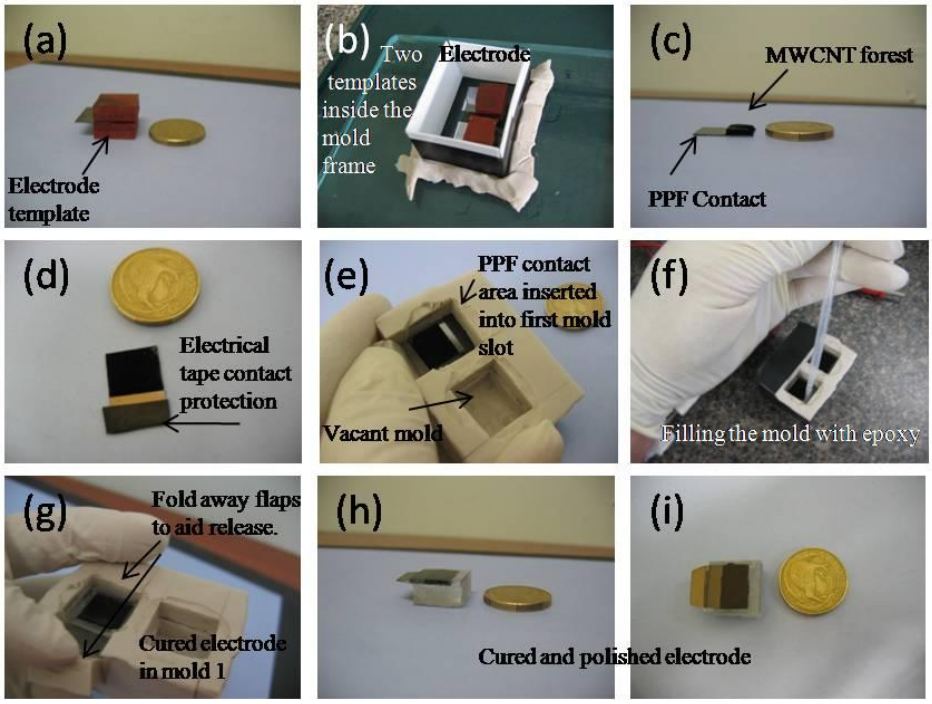

Figure 2.6. Fabrication steps in the making of MWCNT epoxy composite electrodes.

Figure 2.6 (g) and in Figure 4.4(g). The electrodes were left to cure for a further 12 h at room temp to reach full hardness before polishing. A 400 grit wet emery paper on a flat glass plate was used to remove excess epoxy and expose the MWCNT tips. Exposure of the tips was indicated by a change in the colour of the polishing dust in the slurry from white to black. Electrical contact of the MWCNTs to the PPF was confirmed using a multimeter with one lead attached to the PPF contact area with an alligator clip, and the other lead to a copper strip which was pressed onto the MWCNT surface. If an immeasurably high resistance was indicated it was assumed that the MWCNTs had lost contact with the PPF and therefore the electrode was discarded (< 5% of electrodes). The electrodes were polished to a mirror finish using 600 grit wet emery paper followed by 1200 grit wet emery paper and finally 1 µm diamond paste on a silk lecloth (Leco International) lubricated with ethylene glycol. Finished MWCNT electrodes are shown in Figure 2.6 (h) and (i). To regenerate the surfaces between experiments the electrodes were polished with diamond paste or with 1200 grit wet emery paper followed by diamond paste. Regeneration in all cases also included an activation step (usually O_2 plasma, see Chapter 4).

2.6 Imaging

2.6.1 Atomic force microscopy (AFM) imaging

Atomic Force Microscope (AFM) images were attained in air with a Dimension 3100 AFM and Nanoscope IIIa controller (Digital Instruments, Veeco). The AFM was used exclusively in tapping mode using silicon cantilevers (TAP300Al-G series, Innovative Solutions Ltd) which have resonant frequencies close to 300 kHz. The 5 × 5 μm scans recorded for section 2.3.5 were recorded at a resolution of 512 × 512 pixels at a scan rate of 2.5 μm s^{-1}. The amplitude set point and gains were optimized for each sample.

2.6.2 AFM film depth profiling

This film scratching and depth profiling technique has been previously described.[6, 7] The AFM laser was focused on the shortest of the three cantilevers of a CSC12 (Ultrasharp) cantilever. When this cantilever tip is engaged with a surface the tilt of the AFM head causes the longest, central cantilever to dig into the surface film. When the AFM is repeatedly scanned over a 10 × 1.25 μm area, the longest cantilever scratches the surface film away. It has been previously established that an approximately 0.3 nm deep scratch is formed in PPF by this method [7] which is accounted for in all reported measurements. After removal of the film section the AFM cantilever is disengaged and the shortest tip repositioned over the scratch. The scratch is imaged by scanning orthogonally to the scratch direction in tapping mode (typical frequency 350 kHz). The depth of the trench was calculated from the resulting image using the Nanoscope IV step height calculation tool. This enables the user to select and position two boxes, one at the bottom of the trench and one on the film surface. The heights of all of the pixels in each box are averaged and the step height measured is the difference between the two averages.

2.6.3 Scanning and transmission electron microscopy (SEM and TEM)

SEM images were taken using either a JEOL 7000 HRSEM or a Leica S440 SEM each with a typical accelerating voltage of 15 kV. TEM images were obtained using a Phillips CM200.

2.6.4 Image processing

Post processing and digital flattening of AFM images was performed using a combination of Nanoscope IV (Digital Instruments, Veeco) image handling and WSxM 4.0 development 7.5 software (Nanotec Eletronica S.L). Adobe Photoshop elements 6.0 (Copyright 1990-2007 Adobe Systems Incorporated) was used for all other editing of AFM and SEM images. All measurements of features on SEM images were performed using Image J V 1.37. The scale of the images was calibrated by using the scale bar generated by the SEM.

2.7 Photolithography

Photomask computer design files were prepared using L-Edit V 13 (Tanner EDA). The designs were written onto an AZ1518 photoresist (Clariant) coating on a chrome-coated glass plate with a Heidelburg μPG101 mask writer. The mask writer is a printer that uses a λ = 365 nm laser and can resolve a minimum feature size of approximately 1 μm. The photoresist was developed using 2 % tetramethyl ammonium hydroxide (TMAOH, AZ300 MIF developer, AZ Electronic Materials USA Corp) in water to dissolve the exposed resist. The exposed chrome was removed using a 50 mL solution containing ceric ammonium sulphate and perchloric acid.

AZ1518 photoresist was used to pattern all of the surfaces discussed in this thesis. The standard conditions were: spin coat the resist onto the sample at 3000 rpm for 30 s, bake the sample on a hotplate at 95 ^{o}C for 1 min, cool, expose to pattern UV for 20 s using a photomask and a Suss MA6 mask aligner and finally developed in 2 % TMAOH. Samples patterned with photoresist were coated with metal catalyst (as described in

section 2.5.1) and the unwanted catalyst removed by dissolving the remaining photoresist in acetone with sonication. Before application of resist, samples were cleaned by sonication for 30 s in acetone followed by 30 s of sonication in IPA and then dried with a nitrogen gun.

2.8 References

1. Downard, A. J.; Prince, M. J., Barrier properties of organic monolayers on glassy carbon electrodes. *Langmuir* **2001,** 17, (18), 5581-5586.
2. Lyskawa, J.; Belanger, D., Direct modification of a gold electrode with aminophenyl groups by electrochemical reduction of in situ generated aminophenyl monodiazonium cations. *Chem. Mater.* **2006,** 18, (20), 4755-4763.
3. Yu, S. S. C.; Tan, E. S. Q.; Jane, R. T.; Downard, A. J., An electrochemical and XPS study of reduction of nitrophenyl films covalently grafted to planar carbon surfaces. *Langmuir* **2007,** 23, (22), 11074-11082.
4. Yu, J. X.; Shapter, J. G.; Quinton, J. S.; Johnston, M. R.; Beattie, D. A., Direct attachment of well-aligned single-walled carbon nanotube architectures to silicon (100) surfaces: a simple approach for device assembly. *Phys. Chem. Chem. Phys.* **2007,** 9, (4), 510-520.
5. Liu, J.; Rinzler, A. G.; Dai, H. J.; Hafner, J. H.; Bradley, R. K.; Boul, P. J.; Lu, A.; Iverson, T.; Shelimov, K.; Huffman, C. B.; Rodriguez-Macias, F.; Shon, Y. S.; Lee, T. R.; Colbert, D. T.; Smalley, R. E., Fullerene pipes. *Science* **1998,** 280, (5367), 1253-1256.
6. Lehr, J.; Williamson, B. E.; Flavel, B. S.; Downard, A. J., Reaction of Gold Substrates with Diazonium Salts in Acidic Solution at Open-Circuit Potential. *Langmuir* **2009,** 25, (23), 13503-13509.
7. Brooksby, P. A.; Downard, A. J., Electrochemical and atomic force microscopy study of carbon surface modification via diazonium reduction in aqueous and acetonitrile solutions. *Langmuir* **2004,** 20, (12), 5038-5045.

Chapter 3. Chemical assembly of single walled carbon nanotubes

3.1 Introduction

The vertical alignment of SWCNTs by self assembly on planar surfaces has been previously described many times on gold,[1-6] via thiol terminating self assembled monolayer (SAM) tether layers, on silicon via chemical oxidation and ester bond formation [7] and self assembly of SAMs of amine terminating silanes,[8, 9] and on glass and silicon via an electrostatic assembly method using a film of Nafion impregnated with Fe^{3+}.[10] All of these methods follow essentially the same strategy.[11] A planar substrate is functionalized with a tether layer which can interact with the carboxylic acid functionalities primarily at the ends of oxidized SWCNTs.

On gold, SAMs of thiols are formed by a well understood self assembly process.[12] The SAMs form through the reversible formation of Au-S bonds. The reversibility of the Au-S bond enables the SAMs to self heal and become highly organized but limits their thermal and chemical stability (see chapter 1.3.1). When thiol SAMs are amine terminated they can be used to covalently tether SWCNTs by formation of amide bonds between the surface bound amines and carboxylic acid functionalities on the SWCNTs. Liu *et.al.* confirmed that amide bonds were formed when the thiol-amine NH_2-$(CH_2)_2$-SH was coupled to shortened SWCNTs (by DCC assisted coupling) from the appearance of the amide I band at 1600 cm^{-1} in the FT-IR spectrum. Flavel *et al.* showed that chemically oxidized silicon can be coupled to SWCNTs by ester bond formation between hydroxyl functionalities on the substrate and carboxylic acid functionalities on the tubes.[7] The same authors have also demonstrated that SWCNTs can be chemically assembled on silicon via amine terminating silanes which form well ordered SAMs on this substrate.[8, 9] Using SAMs of thiols on gold or silanes on silicon as tether layers relies on a chemical reaction which is specific to the substrate and therefore limits the method to only that substrate. The use of hydroxyl termini to form ester bonds to SWCNTs may well be

viable on other substrates but has not yet been explored. Rusling and Papadimitrakopoulos *et al.* have coated various substrates with $Fe(OH)_3$ crystallites by dipping the substrate into acidic aqueous $FeCl_3$ and transferring the substrate (in some cases modified with a Nafion film) to a basic solution to transform the iron chloride to the iron hydroxide.[5, 10, 13] When oxidatively shortened SWCNTs are present in the basic solution the SWCNTs are coupled to the surface by acid-base interactions between the carboxylic acids functionalities on the SWCNTs and deprotonated $Fe(OH)_3$ on the substrate. Favourable iron / carboxylic acid chelation interactions may also help to immobilize the SWCNTs. This method does not rely on a specific surface / tether layer interaction and therefore is applicable to a wider range of substrates.

Carboxylic acid functionalized SWCNTs assembled on tether films are thought to vertically align because the carboxylic acid functionalization occurs primarily at open tube ends and there are multiple carboxylic acid functionalities at each tube end giving multiple anchor points. Shapter *et al.* observed during assembly of SWCNTs on hydroxyl modified silicon that vertically aligned bundles of SWCNTs increase in diameter with reaction time. This suggests that aggregation of SWCNTs by van der Vaals forces and $\pi - \pi$ interactions between the aromatic tube sidewalls may also assist in vertically aligning the tubes. In 2000 Hwang *et al.* showed [14] and in 2003 Liu *et.al.* proposed [15] that the intensity of the SWCNT Raman signal from a polarized light source is strongly correlated with the alignment direction of the SWCNTs. Diao *et al.* exploited this phenomenon using SWCNTs coupled to a SAM of 11-amino-n-undecylmercaptan on gold. They showed that a polarized Raman signal could only be detected when the beam polarization direction was orthogonal to the gold surface, consistent with vertical alignment. In the same paper they show TEM images of SWCNTs coupled to an ultrathin gold wire (using the same thiol-amine linker) adopting an orthogonal orientation to the gold substrate.

It has been previously shown that vertically aligned SWCNTs are able to interface with biological molecules and act as molecular wires. One of the best examples of this was published in 2005 by Liu and Gooding *et al.*[2] In that work the authors assembled vertically aligned SWCNTs on a cystamine SAM on gold and then coupled glucose

oxidase (GOx) to the SWCNT tips. The GOx was either directly attached to the SWCNTs or reconstituted around flavin adenine dinucleotide (FAD, the active site of GOx) which was attached to the SWCNTs (Figure 3.1). The authors show that in both methods the SWCNTs act as molecular wires enabling direct electron transfer to and from the redox center of the enzyme. This ability is most reasonably attributed to the small size and needle like morphology of the nanotubes enabling them to penetrate into the enzyme protein shell and into close proximity with the FAD. In another example Rusling *et al.* demonstrated a high sensitivity electrochemical detector of cancer biomarkers using SWCNTs assembled on a $Fe(OH)_3$ / Nafion film on basal plane HOPG.[13] The same authors showed that direct electrical connection between SWCNTs and the enzymes horse radish peroxidase and myoglobin is possible.[16] Based on the findings of Gooding's and Rusling's groups, vertically aligned SWCNTs should be capable of direct electronic interaction with charge transfer proteins in the outer membranes of living cells.

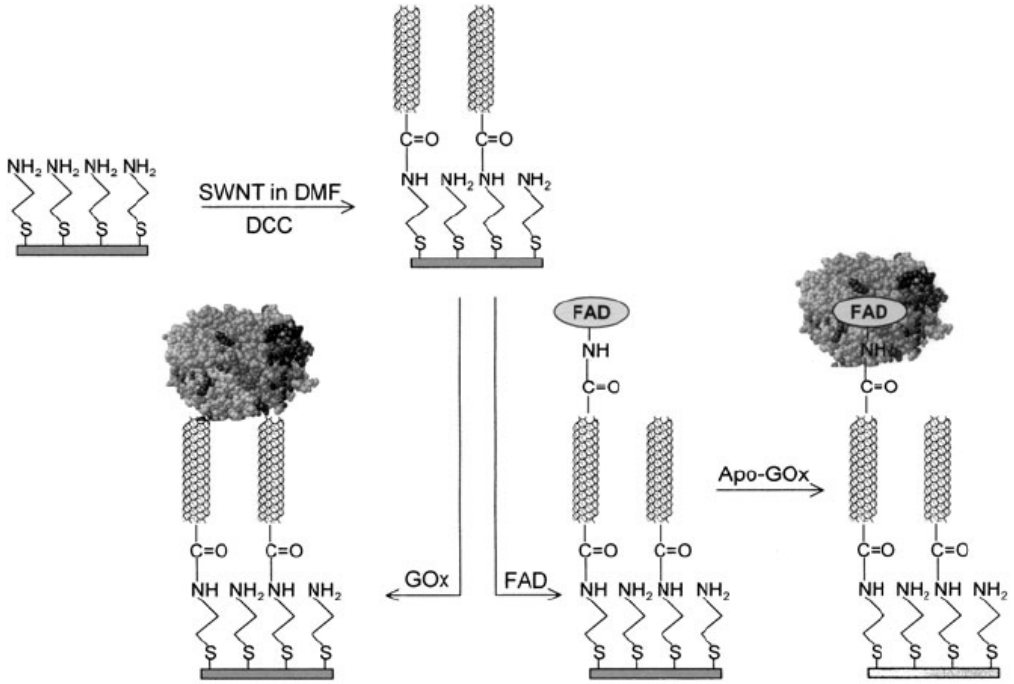

Figure 3.1 Schematic of the procedure used by Liu and Gooding *et al.* to electronically interface with GOx using SWCNTs as molecular wires. Figure reproduced from reference 2.

Chapter 3. Chemical assembly of single walled carbon nanotubes

This chapter describes the preparation of vertically aligned SWCNT electrodes by chemical assembly on covalently grafted tether layers on carbon substrates. As the nanotubes in this work are being incorporated into an electrode, the substrate used must be conducting. This permits the formation of electro-grafted tether layers from diazonium salts (see section 1.3.1, 1.3.2) and aliphatic amines. At the time that this research was being conducted these were both new tether layers for self assembling vertically aligned SWCNTs and the first example of covalent assembly of vertically aligned SWCNTs on graphite.[17] Since then Liu and co-workers have independently reported an almost identical strategy on commercial glassy carbon disc electrodes which they developed into a prototype label-free amperometric immunosensor.[18] Due to the stability of covalently bound tether layers, assemblies of SWCNTs on diazonium salt and electro-grafted amine derived films should have a significant stability advantage over other attachment strategies.

To increase the potential utility of SWCNTs coupled to aryl diazonium salt tether layers, two new patterning techniques were demonstrated. In both cases SWCNT patterning is achieved by patterning of the tether layer. Only a small number of publications describe patterning methods that have been developed specifically to immobilize vertically aligned SWCNTs. Flavel *et al.* used anodic stripping lithography in which a conducting AFM tip is used to selectively oxidize areas of silane coated silicon wafer.[8, 9] Carboxylic acid functionalized SWCNTs assemble on the oxidized areas by forming ester bonds to hydroxyl termini on the silicon or to amine terminating modifiers in the oxidized areas. The method produces nanoscale features but, like many scanning probe techniques, it is very slow and as such is limited to use as a research tool or high value prototyping method. Wei *et al.* describe a method in which a silane layer on silicon is selectively oxidized by passing an electron beam through a TEM grid with subsequent adsorption of Fe^{3+} and patterned assembly of SWCNTs.[19] Oxidation of the silicon by the electron beam creates preferential sites for $Fe(OH)_3$ crystallites to form upon which SWCNTs are subsequently assembled. The same authors also describe a method for patterning Fe^{3+} on gold by UV lithographic methods.[20] Here FeO(OH) and FeOCl films were formed on a gold surface by oxidation of the gold with $FeCl_3$. Patterned films were

formed by photolithographic masking of areas of the surface. SWCNTs were assembled on the patterned iron films by the same electrostatic and metal assisted chelation methods described above. In the work described here patterning was achieved by two methods. Firstly by microcontact printing of amino phenyl films from the corresponding diazonium salts and secondly by electrochemically grafting an aminophenyl tether layer through a photolithographically patterned polymer mask.

3.2 Experimental section

Electrochemical grafting of aminophenyl (AP) films and cutting and coupling of SWCNTs is described in the general experimental chapter sections 2.4.1 and 2.4.2. All of the electrochemically grafted films in this chapter where formed using the electrochemical cell assembly described for use with PPF (section 2.1.2). A 7 mm O-ring was used to define the modification area.

3.2.1 Grafting of ethylene diamine (en) films to PPF

Surface confined en films were produced by electrochemical oxidation of 1 mM en in ACN / 0.1 M $TBABF_4$ by 6 CVs between 0.3 and 1.3 V *vs.* Ag / 0.01 M $AgNO_3$ at scan rate = 100 mV s^{-1}.

3.2.2 Electrochemical analysis

All electrochemical film grafting and analysis was conducted on an ECO CHIMIE PGStat 300 potentiostat with the electrochemical cell placed in a Faraday cage to reduce noise arising from electromagnetic radiation. For electrochemical analysis of grafted films a 4 mm diameter O-ring was used to define the area of the working electrode. The redox probe solutions were either 1 mM ferrocene methanol (FcMeOH) or 1 mM solutions of both $K_4Fe(CN)_6$ and $K_3Fe(CN)_6$. These were prepared with 1 M KCl in Mill-Q water or 0.1 M $TBABF_4$ in ACN (in the case of en film analysis with FcMeOH)

immediately prior to use. Frequency response data was fitted to model circuits by the ECO CHIMIE frequency response analyzer (FRA) software provided with the potentiostat.

3.2.3 Water contact angles

Static contact angle measurements were made by delivering two 1 μL drops of Milli-Q water from a microsyringe onto the sample mounted on an illuminated horizontal stage. A digital image of the drop was recorded using an microscope camera (Edmond Scientific). The water contact angle was measured from the digital photograph using Image J v 1.37 software with a drop analysis plug-in. The stated contact angles are an average of two drops per sample and there is an uncertainty of ± 3^{o} with all reported angles. The uncertainty indicates the range of values obtained.

3.2.4 Surface pKa of en and en / SWCNT films

CVs were recorded using a 1 mM solution of both $K_3Fe(CN)_6$ and $K_4Fe(CN)_6$ adjusted to various pH values over the range of 3.5 - 12. The pH was adjusted using 10 mL of 20 mM phosphate buffer solution (at the appropriate pH) mixed with 10 mL of 2 mM $Fe(CN)_6^{3-/4-}$ solution and finally adjusted to an ionic strength of 0.1 M with $NaClO_4$.

3.2.5 Film stability determination

AP / SWCNT films prepared by 24 h reaction of SWCNTs with the AP layer were sonicated in 0.1 M H_2SO_4, 0.1 M NaOH and pentane. After each sonication step, CVs were recorded using separate 0.1 M KCl solutions containing 1 mM $Fe(CN)_6^{3-}$ and $Fe(CN)_6^{4-}$, 1 mM FcMeOH or 1 mM $Ru(NH_3)_6^{3+}$. To establish a usable electrochemical potential window the films were exposed to potentials increasing from 0.7 to 1.5 V in increments of 0.2 V or to potentials from -0.3 to -1.5 V in 0.2 V increments for 60 s. After each exposure the same three probe solutions as those employed above were used to record CVs to detect degradation of the films. Finally electrodes were subjected to

extended CV cycling in the three probe solutions to establish their electrochemical stability at moderate potentials.

3.2.6 Microcontact printing of aminophenyl tether layers

Microcontact printing was achieved using polydimethyl siloxane (PDMS) stamps fabricated off master molds generated through a photolithographic process which is described elsewhere.[21] The PDMS stamps were extracted in a sequence of solvents designed to remove unreacted monomer from the stamps and reduce PDMS residue transfer from the stamps to the substrates.[22] The procedure for this was 1 day immersion in pentane, 1 day in toluene, 1 day in ethyl acetate, 2 days in acetone and finally 2 days at 120 ^{o}C to evaporate all residual solvent.[23] As the target inking solution employed water as the solvent the surface of the PDMS stamp was oxidized with 20 s of 500 W O_2 plasma to improve its wettabililty.[22] Printing of AP films was achieved by soaking the stamps in a 0.5 M HCl solution containing 10 mM 1,4-diaminobenzene and 10 mM $NaNO_2$ for 5 min. The stamp was removed from the ink solution and dried with a nitrogen gun till almost dry and then placed in contact with the PPF surface for 30 min. Once the stamp was removed the PPF was cleaned sequentially by sonication in acetone and IPA for 20 s in each solvent. The patterned surface was reacted with carboxylic acid functionalized SWCNTs as described in section 2.4.2

3.2.7 Photolithographic patterning of amine terminating tether layers

A polymer mask of the commercial photoresist AZ1518 (Clariant) was patterned onto a PPF surface by the photolithographic methods discussed in the general experimental chapter (section 2.7). AP films were then grafted onto the exposed PPF spaces (where there were voids in the photoresist masks) by the same methods discussed in section 2.4.1. The photoresist was removed by sonication in acetone and IPA to reveal patterned AP film with exposed PPF in the intervening space. SWCNTs were coupled to the patterned AP films by the methods discussed in section 2.4.2.

3.3 Results and discussion

SWCNTs were assembled on three amine terminating films formed by the three methods depicted in Scheme 3.1. The formation of aminophenyl films by electrochemical reduction of 4-nitrobenzene diazonium cations and subsequent electrochemical reduction

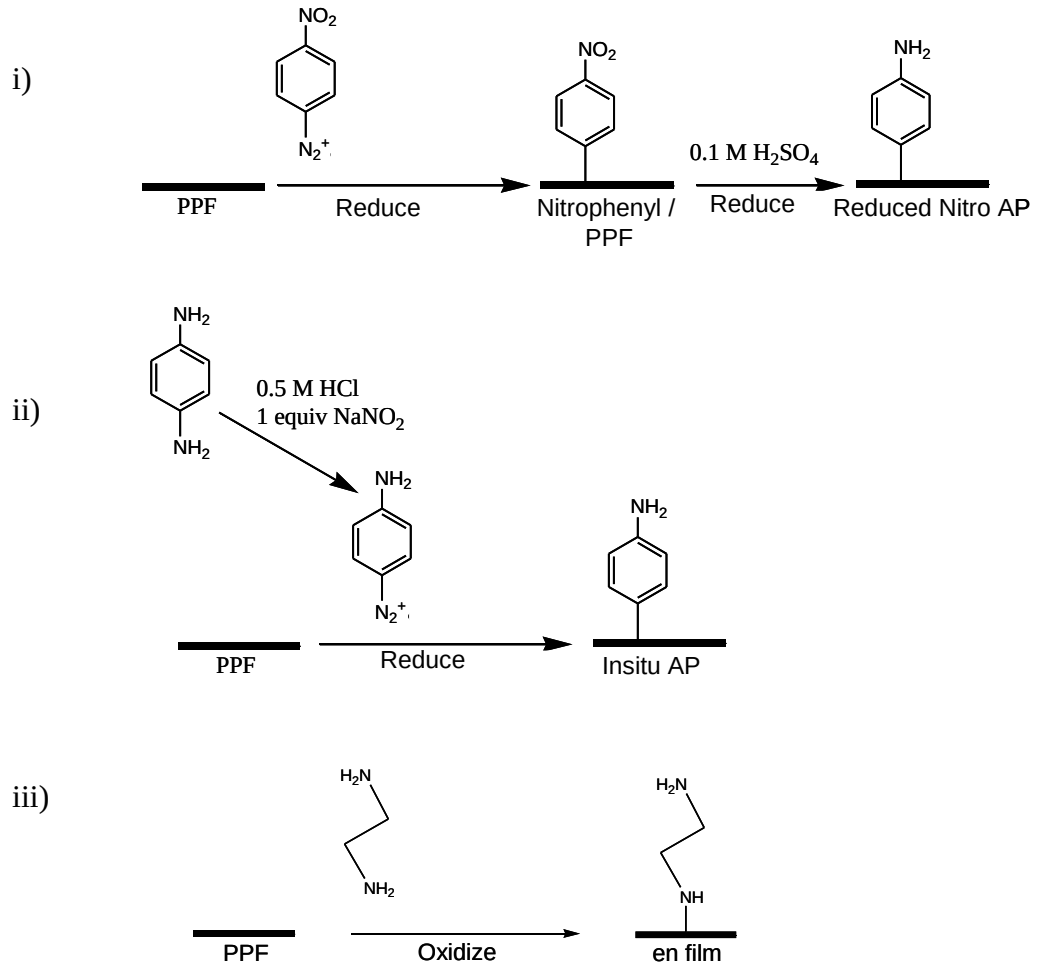

Scheme 3.1. Grafting of amine terminating films by i) electrochemical reductive grafting of 4-nitrobenzene diazonium cations and subsequent electrochemical reduction of the resulting NP film to an AP film, ii) reductive electrochemical grafting of 4-aminobenzene diazonium cations formed in situ to form an AP film, iii) electrochemical oxidative grafting of 1,2-diaminoethane (ethylene diamine (en)) to form en films.

of the resulting NP film ('reduced NP', Scheme 3.1. i)) and by electrochemical reduction of 4-aminobenzene diazonium cations ('in situ AP', Scheme 3.1 ii)) is reviewed in the introduction chapter (sections 1.3.1 and 1.3.2). The formation of films by oxidative electrochemical grafting of primary amines has been previously described.[24-27] Adenier and Pinson *et al.* show that oxidative grafting of ethylene diamine (en) forms a bond through the nitrogen to platinum and gold and, by inference, carbon. They also conclude that a radical mechanism is most likely for the grafting reaction.[27] Coupling of SWCNTs to the amine terminating films was achieved by sonication of commercial SWCNTs in a H_2SO_4 : HNO_3 mixture to shorten the tubes and functionalize the ends with carboxylic acid groups.[28] Functionalization of SWCNTs in this way also aids suspension in solvents and enables the formation of amide bonds between the amine terminating films and carboxylic acid groups at the ends of the tubes. A carbodiimide coupling agent promotes amide bond formation (Scheme 3.2).

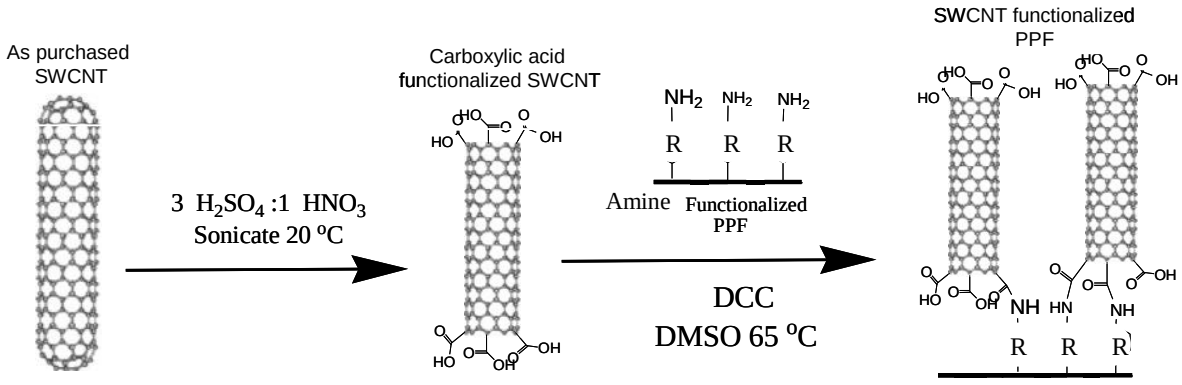

Scheme 3.2. Carboxy **f**unctionalization and coupling of SWCNTs to amine terminating films by dicyclohexyl carbodiimide (DCC) assisted amide bond formation.

3.3.1 Grafting of amine terminating tether layers

Typical CVs for the electrochemical grafting of 4-nitrobenzene diazonium cations to PPF are shown in Figure 3.2 (a). On the first scan, reduction of the diazonium functionality occurs at E_{pc} = - 0.2 V (Figure 3.2 (a) scan i). The featureless CV (scan ii) recorded after a 2 min deposition at -0.6 V shows that electrode has been passivated by the formation of a NP film. The CVs shown in Figure 3.2 (b) were obtained after transfer of the grafted electrode to 0.1 M H_2SO_4, These show the typical nitrophenyl reduction

response in which the NP film is transformed to an AP film (as discussed in the introduction chapter, Section 1.3.2). These films are henceforth referred to as reduced NP films.

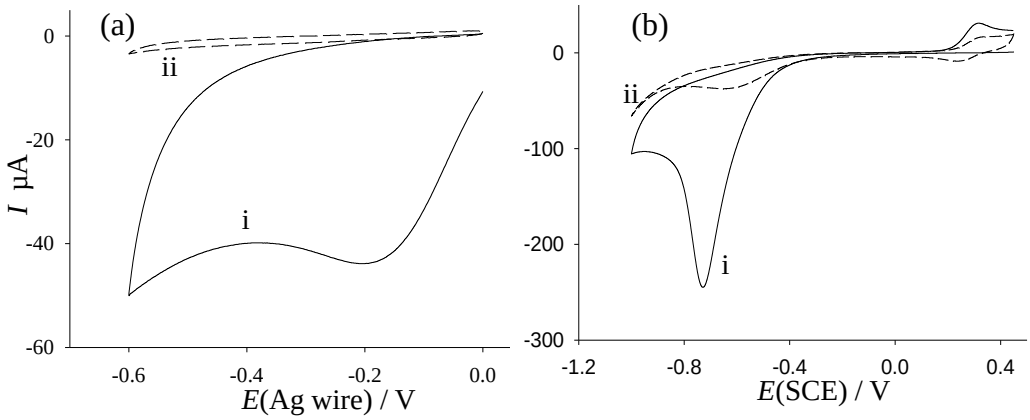

Figure 3.2. Typical CVs for grafting 4-nitrobenzene diazonium cations from ACN / 0.1 M $TBABF_4$ (a) and subsequent reduction of the NP films (b) to AP in 0.1 M H_2SO_4, scan rate = 100 mV s^{-1}. CV (a) i) first scan ii) a repeat scan after a constant potential deposition at -0.6 V for 2 min. (b) i) first reduction scan ii) fourth and final scan in 0.1 M H_2SO_4, scan rate = 100 mVs^{-1}.

CVs of the electrochemical grafting of 4-aminobenzene diazonium are shown in Figure 3.3. The reduction peak potential for the diazonium functionality at $E_{pc} \approx$ -0.2 V (Figure 3.3 i)) is lower than that reported by Lyskawa *at. al.* (0.1 and 0.25 V *vs.* AgCl at a gold electrode) but were reproducibly obtained in this work. The second featureless CV recorded after a 2 min deposition at -0.6 V (Figure 3.3 ii)) is typical of passivation of the electrode by formation of an AP film. This film is henceforth referred to as an in situ AP film. CVs of the oxidative grafting of en are shown in Figure 3.4 and are typical of those observed by others.[26] The decrease in current in repeat scans indicates the formation of a surface film.

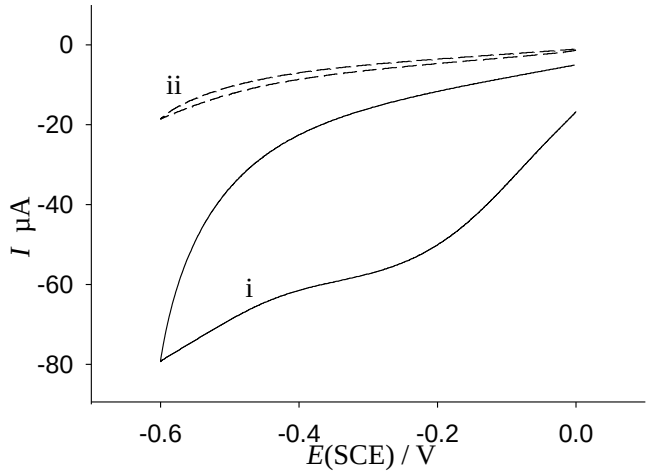

Figure 3.3. Typical CVs for the in situ grafting of 10 mM 4-aminobenzene diazonium cations to PPF. i) first cycle and ii) a second cycle after a fixed potential deposition at -0.6 V *vs.* SCE for 2 min. The grafting solution was 10 mM 1,4-diaminobenzene and 10 mM $NaNO_2$ / 0.5 M HCl , scan rate = 100 mV s^{-1}.

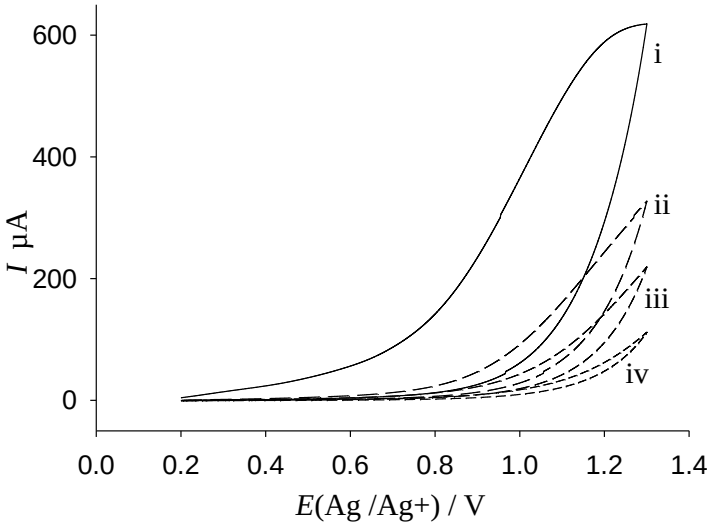

Figure 3.4. Typical CVs for the oxidative grafting of en to PPF. The CVs shown are the first i) second ii) third iii) and sixth iv) in ACN, 0.1 M $TBABF_4$, 1 mM en, scan rate = 100 mV s^{-1}.

3.3.2 Functionalization of SWCNTs

SWNCTs were shortened (cut) and their open ends functionalized by carboxylic acid groups by sonication in H_2SO_4 : HNO_3 as described in section 2.3.2. Samples of cut SWCNTs were dispersed on a silicon square by drop coating a dilute suspension in DMF. The dried samples prepared from SWCNT samples with different sonication times were visualized by high resolution SEM. SEM images of SWCNT sonicated for 8 and 4 h are shown in Figure 3.5 and Figure 3.6 respectively.

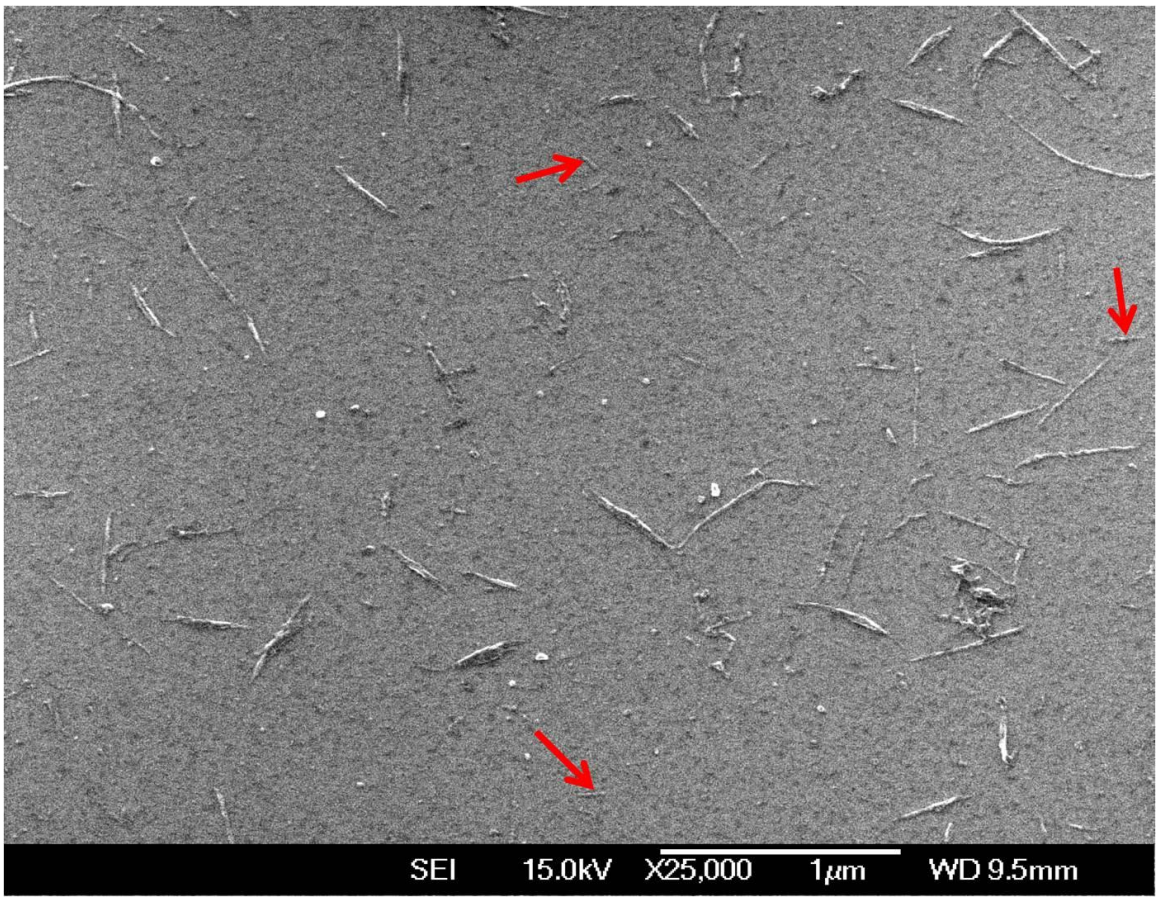

Figure 3.5. SEM image of SWCNTs functionalized by 8 h of sonication in 3:1 conc H_2SO_4 : HNO_3 dispersed on a silicon wafer. The red arrows indicate smaller nanotubes included when measuring tube lengths.

Analysis of the SEM images using a digital measuring tool (Image J) yielded an average tube length of 158 nm after 8 h sonication with a standard deviation of 92 nm attesting to

a broad distribution of tube lengths. A sample of SWCNTs cut for only 4 h is shown in Figure 3.6**.** This sample shows longer tubes and a high degree of bundle formation. The nanotubes were too entangled to allow estimation of the average tube lengths for this sample. The samples cut for 4 h also displayed poor dispersability in DMSO or DMF with flocculation and settling occurring after a few hours. Clearly for the purposes of the work described here longer cutting times are desirable. At the time of writing SWCNTs cut for 8 h had remained dispersed in DMSO for a period of 12 months and were still able to be used in coupling reactions. Other workers have reported that similar cutting times yield SWCNTs with an average length of 73 nm ± 20 nm.[3] The difference between this result and the nanotubes lengths established here could arise for a variety of reasons. The most likely causes are differences in the powers of the ultra-sonicators used, the degree of temperature control used during sonication and the properties of the as-purchased SWCNTs.

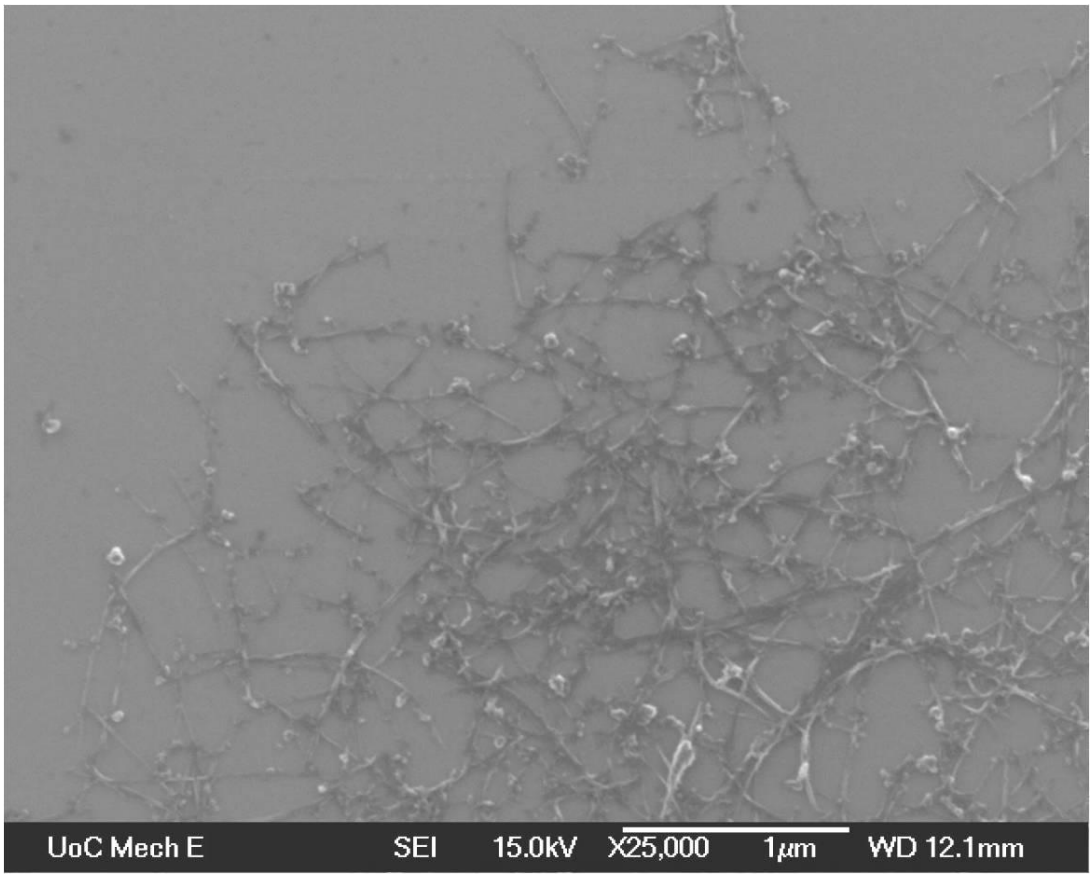

Figure 3.6. SEM image of SWCNTs after 4 h of sonication in 3:1 conc H_2SO_4 : HNO_3

3.3.3 Cyclic voltammetric analysis of AP-SWCNT assemblies

The electrochemical properties of the chemically assembled SWCNT electrodes were examined by CV using redox probe molecules in solution. CVs of the $Fe(CN)_6^{3-/4-}$ couple in 1 M KCl were recorded at AP and en films and AP and en films that had been reacted with SWCNTs for various lengths of time. (Figure 3.7 and Figure 3.8 A**)**. The electrochemical properties of SWCNTs assembled on en films were also analyzed using an ACN and 0.1 M $TBABF_4$ electrolyte solution with FcMeOH as a solution probe (Figure 3.8 B**).** To ensure that changes in electrode response did not result from holes developing in the tether layers or solvent swelling of the films during coupling of SWCNTs, CVs were also recorded at AP films that had been soaked for 24 h in DMSO with the coupling agent DCC present but without SWCNTs.

The CVs recorded at bare in situ AP and reduced NP films (Figure 3.7 A (ii) and B (ii)) are both flat with no discernable oxidation and reduction peaks. As SWCNTs are reacted with the AP films for increasing times, the CVs exhibit increasing cathodic and anodic peak currents and a decrease of the oxidation and reduction peak separation (ΔE_p) (Figure 3.7 scans (iii) and (iv)). It is well known that AP films can act as a barrier layer between an electrode and a redox species in solution.[29] The impact of the film on the rate of electron transfer is described by equation 3.2.3.1 where: k^0 is the standard heterogeneous rate constant for electron transfer at unmodified PPF; k^0_{obs} is the observed rate constant after modification with an AP film; β is a tunneling parameter which is determined by the film and d is the thickness of the film.

$$k^0_{obs} = k^0 \exp(-\beta d) \qquad 3.2.3.1$$

Equation 3.2.3.1 shows that the observed electron transfer rate will decrease with increasing film thickness. Slow electron transfer has the effect of increasing the ΔE_p and decreasing the peak currents of a CV.[30] When electron transfer rates are fast, peak currents approach a theoretical maximum based on the area of the electrode and the rate of diffusion of the probe species in solution. The ΔE_p approaches a theoretical minimum

of 59 mV for a one electron redox molecule diffusing to the electrode. The decrease in the peak separation shown in Figure 3.7 and Figure 3.8 indicates that the overall rate of electron transfer through the SWCNT assembly increases with SWCNT reaction time and that the blocking properties of the AP films are reduced. This implies that the β value and therefore the barrier to electron tunneling through the film is decreasing with increasing reaction time with SWCNTs.

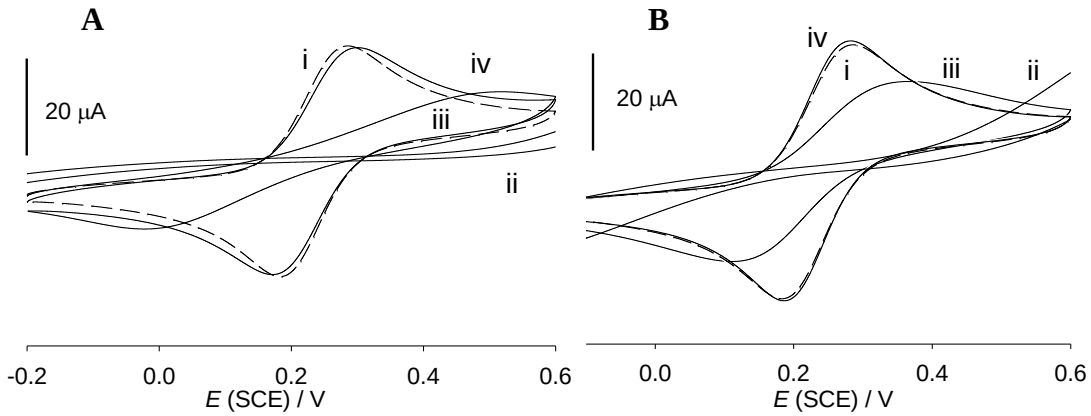

Figure 3.7. Cyclic voltammograms of 1 mM $Fe(CN)_6^{3-/4-}$ / 1 M KCl at (**A**) an in situ AP film and **(B)** a reduced NP film. (i) Bare PPF, (ii) AP film soaked for 24 h in DMSO and DCC, (iii) the film after 4 h of reaction with SWCNTs and (iv) after 24 h of reaction with SWCNTs.

In the case of CVs of $Fe(CN)_6^{3-/4-}$ recorded at an en film the CV exhibits a slightly smaller ΔE_p than that recorded at bare PPF (Figure 3.8 A (i) and (ii)). There is a small but significant increase in ΔE_p with increasing reaction time with SWCNTs (Figure 3.8 A (iv)). The small increase in electron transfer rate at an en film compared with PPF is likely due to a favorable electrostatic interaction between the cationic amine film and the anionic redox probe. In 1 M KCl an aliphatic amine film will be significantly protonated and therefore cationic which lowers the approach distance of anionic $Fe(CN)_6^{3-/4-}$ in solution. The slower electron transfer rate after reaction with SWCNTs is consistent with a build up of anionic carboxylic acid groups at the SWCNT film and hence some repulsion of the anionic redox probe.

The lack of blocking ability of en films in aqueous conditions has been previously reported.[26] It has also been reported that en films do exhibit limited blocking of ferrocene methanol (FcMeOH) in acetonitrile electrolyte solutions.[26] Hence CVs were recorded with FcMeOH at fresh en films and en films after reaction with SWCNTs. Figure 3.8 B ii**)** shows the response of FcMeOH at the en film. The CV shape is somewhat sigmoidal with low oxidation and reduction peak currents but a small ΔE_p. Pinholes in the film can expose bare PPF areas of various size and / or spacing analogous to an electrode array. The shape of a CV for an electrode array is dependent on the size and spacing of the array electrodes. (discussed in full in section 4.2.3.2). The CV in question does not show a perfect sigmoidal shape which suggests that the pinholes are either very close together, such that there is overlap of diffusion zones, or that the pinholes are large enough for some linear diffusion behavior to be observed at scan rate = 100 mV s^{-1}. After reaction with SWCNTs, the FcMeOH response returns to close to that of a bare PPF electrode (Figure 3.8 B iii and iv). As with the result for the AP film this indicates that the β value for the en film, and hence the barrier to electron tunneling through the film, has decreased.

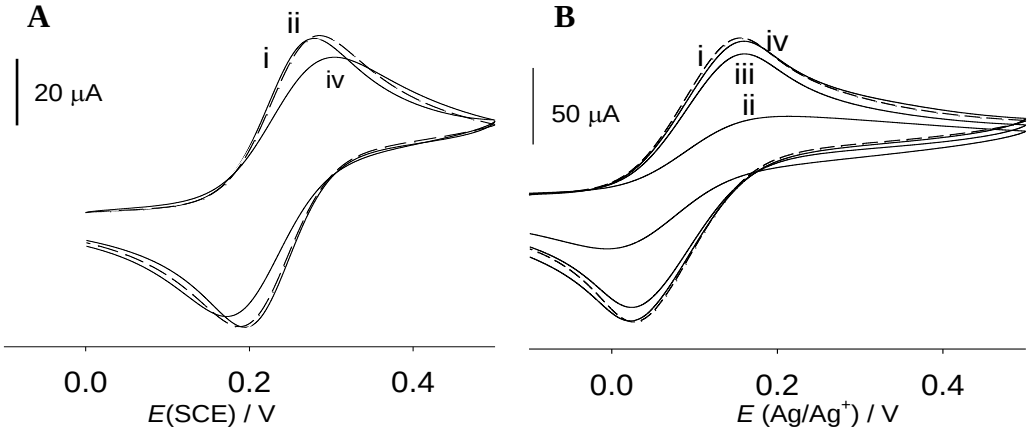

Figure 3.8. CVs of en film electrodes with (**A**) 1 mM $Fe(CN)_6^{3-/4-}$ / 1 M KCl and (**B**) 1 mM FcMeOH in ACN / 0.1 M $TBABF_4$ at (i) bare PPF, (ii) bare en film, (iii) after 4 h reaction with SWCNTs and (iv) 24 h of reaction with SWCNTs.

The observation that the coupling of SWCNTs to a blocking film increases the apparent rate of electron transfer to solution redox probes has been made previously.[7, 11, 31, 32] The reason for the reduction in the blocking property of the tether layer is not fully

understood but Diao *et al* propose that attached SWCNTs act as coulombic islands "funneling" electrons though the films by efficient though bond tunneling.[31] They found that the redox response of $Ru(NH_3)_6^{2+}$ in solution was detectable after coupling SWCNTs to a gold electrode passivated with an 11-amino-n-undecylmercaptan SAM.[32] The same phenomenon was reported by Shapter *et al.* who show that the blocking properties of a silicon dioxide film on silicon was reduced after coupling of SWCNTs.[7] In that work the silicon dioxide film was functionalized with hydroxyl groups by chemical oxidation and the SWCNTs were coupled to the surface via ester bonds. A similar phenomenon has also been observed by Freeman *et al.* [33] when silver and gold nanoparticles were covalently coupled to a thiol SAM on platinum. They observed a very small voltage drop across the SAM when electrochemically interrogating the Raman spectra of the nanoparticles suggesting a low resistivity for the SAM.

It is generally agreed that electron transport to solution mediators through SWCNTs assembled on tether films is best conceptualized as three steps. These are: electron transport through the tether layer; electron transport through the SWCNTs, and transport between the SWCNT tips and the solution redox species.[11] The transport from the SWCNT tips to a solution redox species has been shown to be similar to that of edge plane graphite [34] where barriers to charge transfer depend primarily on the solution redox species. It is been previously shown that charge transport through SWCNTs assembled on substrates is very fast hence resistance from the tubes themselves should be very low.[3] Why the attachment of metallic modifiers to a passivating tether layer lowers the apparent resistance of that layer has not been fully answered but a number of hypotheses exist.[11] The theory of Diao *et al.* that coupling of SWCNTs permits a low energy charge transfer pathway through efficient through bond tunneling predicts a decreasing exponential relationship between charge transfer rates and increasing tether layer length (see equation 3.2.3.1). Gooding and co-workers showed that this is the case by coupling SWCNTs to various thicknesses of SAMs on gold.[35] They conclude that electron transport through the SAM is via electron tunneling but note that the impact on the charge transfer rates per $-CH_2-$ unit in the linker layer does not match precisely with prediction. Gooding *et al.* repeated the experiment using gold nanoparticles assembled on

the same SAMs as those used in their SWCNT experiment.[36] In this case they observe no change in the electron transfer rates between the nanoparticles and $Ru(NH_3)_6^{2+}$ in solution with changing tether layer length. They explain this observation by arguing that the electron transfer rate-determining step is between the nanoparticle and the $Ru(NH_3)_6^{2+}$. As a result of this, electron transport through even very long tether layers is too fast to manifest as changes in the electrochemical response of the $Ru(NH_3)_6^{2+}$. In this case the authors favor the argument of Fermin *et al.* who, using a similar system, conclude that transfer through the SAM via a conventional " hopping mechanism" is unlikely. Fermin *et al.* propose that electron transfer through the film may occur via a resonant electron-transfer mechanism "similar to resonant tunneling transport from a STM tip to a surface modified by redox-active species in the low-bias regime".[37] It is clear that more evidence is required before charge transport processes of this type are fully understood.

3.3.4 Surface pKa determination of en and en / SWCNT films

To determine the effect of chemical assembly of SWCNTs on the deprotonation constant of an en film surface, a series of CVs were conducted at an en film and an en film reacted with SWCNTs for 24 h. The redox probe was 1 mM $Fe(CN)_6^{3-}$ in 10 mM phosphate buffer with pH values between 3.5 and 12.8 made up to an ionic strength of 0.1 with $NaClO_4$.

The ΔEp values for CVs recorded at both surfaces increased with increasing pH and the plots of ΔEp vs pH resembled the classic sigmoidal shape of a titration curve (Figure 3.9**)**. Analysis of curves obtained by least squares fitting to the two data sets indicates an inflection point at approximately pH 9 for the en film and pH 7 for the en / SWCNT assembly. The reasons for the pH dependency of ΔEp are likely to be electrostatic.[30] The anionic probe species is initially attracted by a protonated, cationic amine film at low pH. This electrostatic attraction allows for a reduced approach distance for $Fe(CN)_6^{3-/4-}$ to the film and therefore a lower energy barrier to charge transfer and faster kinetics. Fast kinetics result in a CV with a low oxidation and reduction peak separation (ΔE_p). The electrostatic attraction is lost as the film is deprotonated at higher

pH and becomes neutral. For a SWCNT film primarily terminating with carboxylic acid residues the surface is likely to be neutral at low pH and anionic at high pH.

The deprotonation constant of 9 established for an en film (Figure 3.9 A) is close to the value of 9.8 for the second deprotonation constant of en in solution. The pKa value of carboxylic acid functionalized SWCNTs has been previously measured at 4.5 [38] compared with the value of approximately 7 established here (Figure 3.9 B). The higher pKa is consistent with a contribution from unreacted AP functionalities in the film raising the overall pKa. The broad slope of the plot for the SWCNT modified film indicates a range of proton environments consistent with a complex film structure.

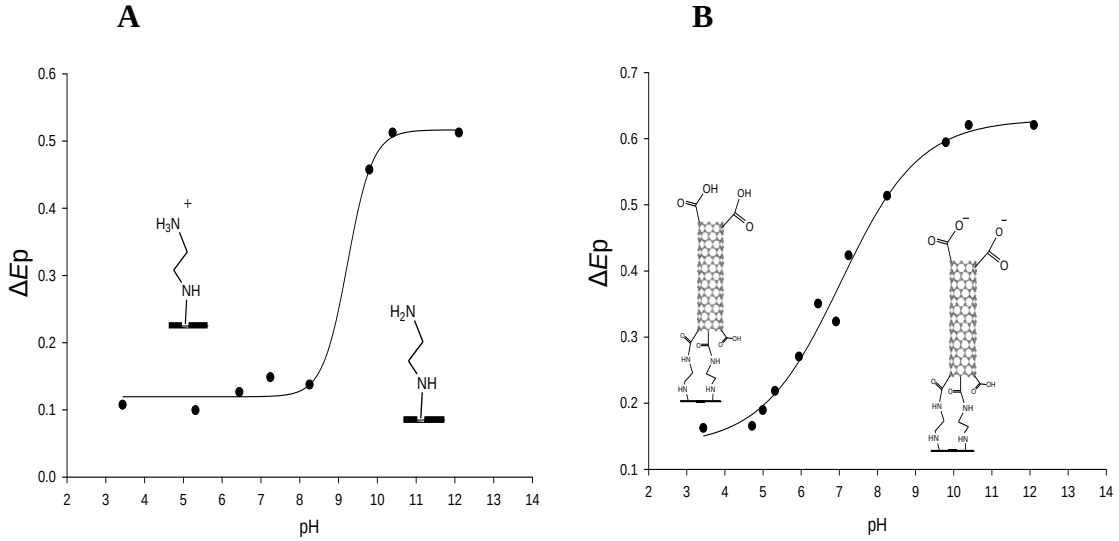

Figure 3.9. Plots of Δ*E*p *vs*. pH for CVs of 1 mM $Fe(CN)_6^{3-/4-}$ / 0.1 M $NaClO_4$ at (**A**) an en film and (**B**) an en film reacted with SWCNTs for 24 h.

3.3.5 Electrochemical impedance spectroscopy (EIS)

EIS was employed to confirm the observation that chemical coupling of SWCNTs reactivates electrodes blocked by AP films. An AC frequency range of 10000 to 0.1 Hz was employed at a potential of 0.23 V which is the measured $E_{1/2}$ of the $Fe(CN)_6^{3-/4-}$ couple *vs.* SCE. The results presented here are for the samples described in section 3.3.3 with the addition of a surface prepared by reacting AP films with SWCNTs in the absence of DCC. The data gathered was fitted to a Randles circuit (**Figure 3.10**) by a

least squares fitting method provided with the impedance analyzer software. The Randles circuit is a generic circuit commonly employed to model the impedance behavior of a diffusing redox active molecule to a planar electrode surface. The electronic components of the model circuit are chosen to model the composition of the electrode..**Figure 3.10** shows the Randles model circuit along side the film composition to illustrate how the imaginary and real systems can be reconciled.

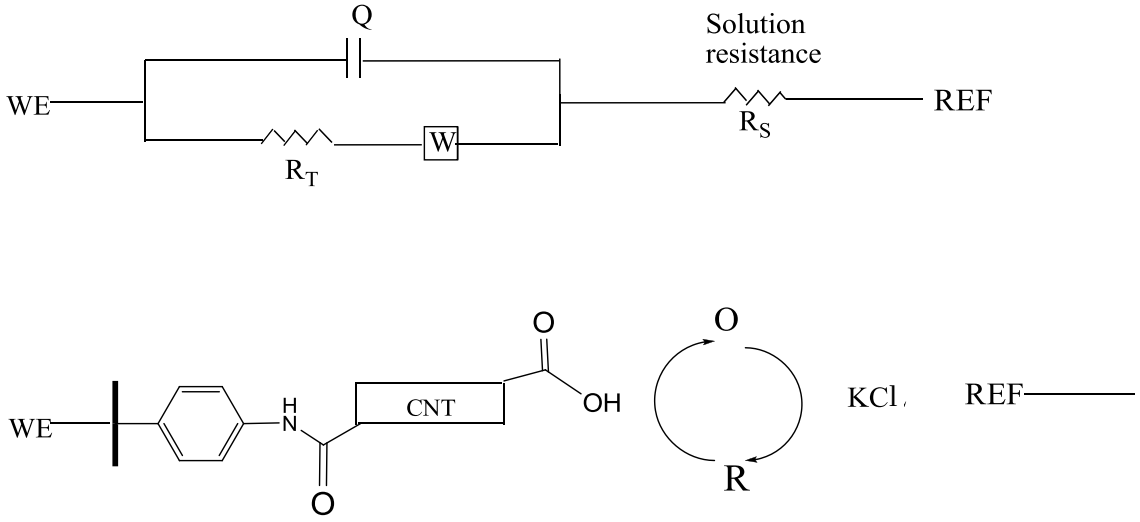

Figure 3.10. The Randles equivalent model circuit used to fit impedance data alongside the AP / SWCNT film composition. WE and REF are the working and reference electrodes respectively; R_T = resistance to charge transfer to the redox probe species; Q = the double layer capacitance of the solution / electrode interface; W = the Warburg resistance caused by the delay in species diffusing to the electrode; R_S = the resistance of the solution between the electrode surface and the reference electrode.

It is immediately apparent that the Randles circuit focuses heavily on the interaction of the redox probe with the electrode interface and bundles all resistance to charge transfer into the single resistor parameter R_T. The R_T value is intended to model the barrier to charge transfer between the surface and the redox molecule but in reality models a number of resistors in the circuit such as electrical contacts between the copper and the PPF and the resistance of the AP tether layer. Potentially the most interesting variable in this case, namely the decreasing resistance of the AP tether layer, is not isolated. Several attempts were made to treat the EIS data with more complex models in

order to obtain a resistance value for the AP film. It became clear however that the complexity and inhomogeneity of these films limits the usefulness of EIS for theoretical deconstruction. The component values of more complex model circuits often converged to a number of local minima which could not be rationally separated. This makes EIS no more illuminating than cyclic voltammetry at a qualitative level for these assemblies. Quantitatively however it does provide a resistance to charge transfer value (R_T) for the whole assembly and redox process. It is important to appreciate that this value could represent a number of potentially competing changes in the electrode such as charge resistance through the film and barrier to charge transfer at the interface.

Since the rate of electron transfer across the SWCNT assembly is of primary importance to this work the overall resistance to charge transfer R_T is the most informative parameter to consider. In agreement with the qualitative observations from the CV experiments, the data (Table 3.1**)** shows that the resistance to charge transfer to $Fe(CN)_6^{3-/4-}$ in solution decreases as SWCNTs are coupled to the films for increasing lengths of time. Interestingly the control electrode fabricated without the coupling agent DCC also shows a substantial decrease in electron transfer resistance. The EIS spectra recorded for both bare AP films showed such high charge transfer resistance that only a fraction of the spectra was visible in the window of frequencies used. As a result a satisfactory fit to the Randles circuit parameters could not be obtained for the AP films. Although the fit to the Randles circuit was very poor it was still apparent that R_T values are many times higher than for the samples reacted with SWCNTs. Estimated R_T values for the AP films are likely to be in excess of 30 kΩ for both films.

The observation that the SWCNT assemblies prepared without the DCC coupling agent show R_T values within the range found for assemblies prepared with DCC raises questions concerning the importance of amide linkages and electrostatic interactions in the assembly reaction. Tour *et al* suggest that electrostatic and covalent interactions probably coexist [39] and other research has demonstrated that electrostatic assembly of SWCNTs can be surprisingly stable.[10] Recently Flavel and co-workers assembled SWCNTs on amine terminating diazonium salt derived tether layers on highly doped

silicon with and without the assistance of DCC.[40] In that work SWCNTs assembled without DCC

Reduced NP	Q^a μF	n^a	R_T Ω	error %	W $s^{1/2}\Omega^{-1}$	R_s Ω
4 h reaction	4.977	0.83	3050	0.418	3.81E-04	37.7
12 h reaction	5.174	0.89	600	0.393	4.99E-04	37
24 h reaction	7.13	0.87	472	0.569	5.02E-04	37.5
24 h No DCC	4.765	0.87	995	0.465	4.67E-04	37.1
In situ AP						
4 h reaction	4.76	0.83	14470	0.756	1.90E-04	37.3
12 h reaction	4.51	0.84	9580	1.048	2.13E-04	35.4
24 h reaction	12.79	0.79	856	1.296	4.90E-04	39.6
24 h No DCC	4.16	0.85	10440	1.331	1.89E-04	35.6
AP films			> 30000			

Table 3.1. Randles circuit parameter best fits for impedance data gathered for AP films produced by the reduced NP and in situ AP methods and reacted with cut SWCNTs for the stated lengths of time.

[a] The circuit element Q is a constant phase element that has the frequency behavior $1/(j\omega Q)^n$. The element behaves as an ideal capacitor when n = 1. Values of less than 1 indicate non-ideal frequency dependant impedance for the capacitor arising from inhomogeneity in the surface solution interface such as surface roughness.

still showed a significant increase in the rate of electron transfer to $Ru(NH_3)_6^{2+/3+}$ compared to the AP film. The authors compared the relative amounts of unreacted amine functionalities between assemblies formed with and without DCC by electrochemical oxidation of the amines in 0.1 M H_2SO_4. They showed that the amine concentration of DCC assisted SWCNT films was significantly lower than those assembled without DCC. This shows that DCC does lead to a reduction in amount of unreacted amines, presumably through the formation of amide bonds with the SWCNTs. However it also supports the proposition of Tour and co-workers that electrostatic adsorption of SWCNTs to amine surfaces could be a factor in self assembled films of the type described here.

3.3.6 Atomic force microscope (AFM) analysis

Identical films to those employed in sections 3.3.5 and 3.3.3 were prepared and analyzed by AFM and SEM microscopy. Since the electrochemical results for reduced NP and in situ AP films were similar, only in situ AP films were examined.

Figure 3.11 shows 5 × 5 μm AFM images of the surface morphology of an AP film before reaction with SWCNTs and after various reaction times with SWCNTs. Also shown in Figure 3.11 are 250 nm^2 AFM and SEM images recorded after each reaction time. As the reaction proceeds the bare AP film (Figure 3.11(a)) changes to a columnar structured film of increasing feature height and roughness after 4 and 8 h of reaction (Figure 3.11(b) and (c)), followed by feature widening and a decrease in variation of feature heights. This is attributed to initial reaction of small bundles of SWCNTs with the surface and some aggregation of SWCNTs from solution forming columnar bundles up to 8 h. After 8 h it appears that the bundles expand by further aggregation of solution SWCNTs and vacancies in the structure become filled resulting in a flatter overall surface and lower RMS roughness. The high magnification AFM images (Figure 3.11 (f-j)) and SEM images (Figure 3.11 (k-o)) clearly illustrate the formation of circular features growing to an average diameter of approximately 14.6 (standard deviation 1.3), 16.4 (2.2), 16.7 (1.9) and 18.1 nm (2.7 nm) after 4, 8, 12 and 24 h of reaction. On Figure 3.11(l) the arrows indicate SWCNT bundles that have attached laterally and are clearly differentiated from vertically aligned features. Increasing feature width for chemically assembled SWCNTs on oxidized silicon dioxide has been previously observed by Shapter *et al.*[7] In that case the bundle diameter after 20 h was 110 nm (average) which is substantially larger than the bundle sizes reported here. A comparison of the images recorded by Shapter *et al.* and those in Figure 3.11 reveal a higher density of small islands at short reaction times in the work described here. The high density of islands is likely to limit the SWCNT bundle diameters by crowding. Figure 3.11 (b-e) shows a maximum feature height of 60 nm which is significantly less than the average cut SWCNT length of 158 nm established in section 3.3.2. This is an expected consequence of the inability of AFM

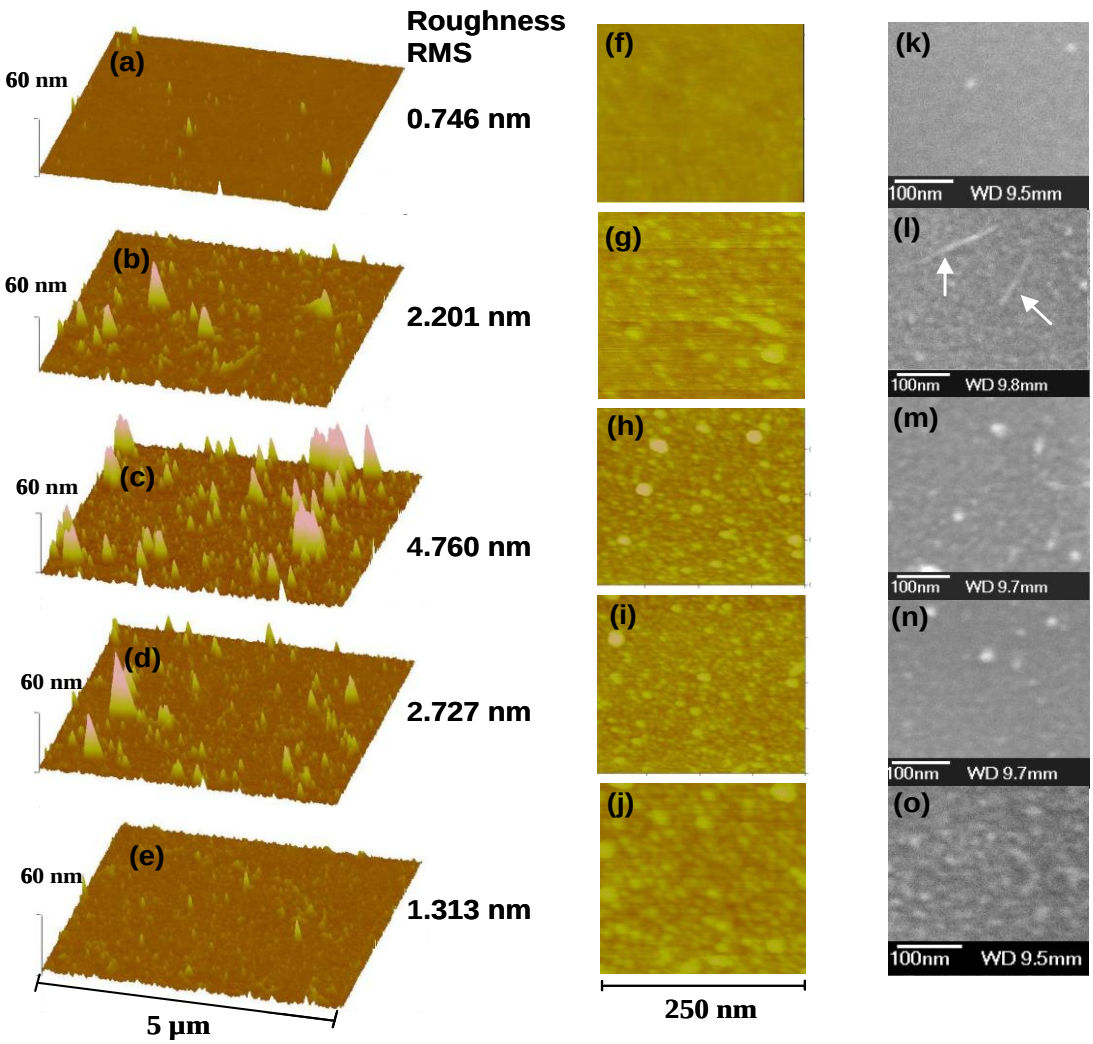

Figure 3.11. AFM and SEM micrographs of SWCNTs reacted with AP films on PPF for (a,f,k) 0 h (b,g,l) 4 h (c,h,m) 8 h (d,i,n) 12 h and (e,j,o) 24 h. The rms surface roughness of each sample was calculated from AFM data over a surface area of 25 μm^2. The arrows in image (l) indicate bundles of SWCNTs lying horizontally on the surface.

to image between high aspect ratio closely spaced features (nominal AFM tip radius 10 nm). Additionally some measured height could be lost due to bending of SWCNTs under the AFM tip. It is also possible that shorter nanotubes preferentially react with the surface

due to increased dispersibility and mobility. It is established that oxidation of SWCNTs causes carboxylic acid functionalization primarily at the ends of the nanotubes where the strain is greatest. Statistically the shortest tubes have the highest ratios of end to side wall functionalities and are more likely to attach in a vertical manner.

3.3.7 Water contact angle measurements

Water contact angle measurements were conducted to compare the relative hydrophobicity of the en and AP films before and after reaction with SWCNTs. Figure 3.12 shows that the surface of both en and AP films becomes more hydrophilic after reaction with SWCNTs, consistent with an increase in carboxylic acid functionalized SWCNTs on the surface. The en film exhibited a water contact angle of 32 ^{o} which decreased to 16 ^{o} after 24 h of reaction with SWCNTs. The corresponding in situ AP film had a water contact angle of 66 ^{o} which decreased to 50 ^{o} with 24 h of reaction with SWCNTs. The relatively high contact angle for SWCNTs assembled on AP suggests that the underlying tether layer contributes to the hydrophobicity of the surface. This is consistent with the pKa value of 7 established in section 3.2.4 which suggests that unreacted amines, on an en film coupled to SWCNTs, raise the pKa above that expected for SWCNTs alone (4.5). Clearly water can penetrate through the SWCNT layer and access the underlying tether film. The surface roughness change in the films reacted with SWCNTs is also likely to effect the wettability of the surfaces

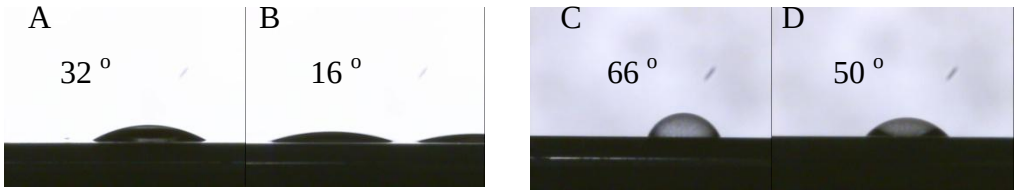

Figure 3.12. Digital images and measured contact angles for 1 μL water drops on (A) an en film, (B) an en film reacted with CNTs for 24 h, (C) an AP film and (D) an AP film reacted with CNTs for 24 h.

3.3.8 Stability of vertically aligned SWCNT assemblies

Films produced by 24 h of reaction of SWCNTs with an in situ produced AP film were subjected to CV with a range of upper and lower potential limits using the redox probe molecules FcMeOH, $Ru(NH_3)_6^{2+}$ and $Fe(CN)_6^{3-}$ in water with 0.1 M KCl as the supporting electrolyte. The aim of the study was to establish the stability of the surfaces by determining the potential range over which there was no change in the redox probe response. A change in response was assumed to indicate a change in the surface film structure or composition.

Potential cycling of the films in FcMeOH (0 to 0.6 V) and $Ru(NH_3)_6^{3+}$ (0.1 to -0.5 V) over 50 cycles caused no changes in the CVs indicating that the films are stable under these conditions. Additionally sonication in 0.1 M H_2SO_4, 0.1 M NaOH and pentane for up to 5 min had no effect on the CVs of either probe. The assemblies were also exposed to incrementally more negative potentials to the lower limit of -1.5 V for 1 min with no observable changes in the CVs of FcMeOH and $Ru(NH_3)_6^{3+}$. One minute exposure to potentials more positive than 1.3 V resulted in distortion of the FcMeOH CV and a slight lowering of the peak currents for the $Ru(NH_3)_6^{3+}$ CV. This is likely caused by some degree of oxidative damage either to the SWCNTs themselves or the underlying PPF substrate and/or loss of some SWCNT material from the film. After 1 min at -1.5 V the CV of $Fe(CN)_6^{3-/4-}$ exhibited an increase in ΔEp from 125 mV to 267 mV and after 1 min at 1.3 V an increase to ΔEp = 289 mV. A CV recorded of $Fe(CN)_6^{3-/4-}$ after pretreatment at 1.5 V was badly distorted indicating again that significant oxidative damage occurs above 1.3 V in aqueous conditions for SWCNT/AP/PPF assemblies. For the sample exposed to a potential of -1.5 V, 30 min of rest and 20 cycles in the $Ru(NH_3)_6^{3+}$ solution returned the $Fe(CN)_6^{3-/4-}$ CV to a ΔEp of 159 mV. Surprisingly the apparently damaged electrode that had been exposed to 1.5 V for 1 min also recovered to a 'normal' CV with a ΔEp of 162 mV and only slightly reduced peak currents after the same rest period and cycling in $Ru(NH_3)_6^{3+}$.

Potential cycling of AP / SWCNT assemblies in the $Fe(CN)_6^{3-/4-}$ solution over the potential range -0.2 to 0.7 V resulted in a gradually increasing ΔEp (from 125 to 172 mV)

over 50 cycles. This increase was found to be at least partially reversible. The Δ*E*p decreased to 154 mV after resting for 30 min and 20 cycles in a non $Fe(CN)_6^{3-/4-}$ probe solution. Sonication in acid and pentane for 5 min resulted in no change to the $Fe(CN)_6^{3-/4-}$ CV but sonication in 0.1 M NaOH resulted in a substantial Δ*E*p increase to 244 mV suggesting some loss of CNT material and exposure of the AP film in this medium.

In summary the AP / SWCNT assemblies reacted for 24 h show good mechanical stability in mild acid and pentane with substantial sonication. Sonication in NaOH results in moderate deterioration of the electrode performance most likely caused by loss of CNT material, perhaps by hydrolysis of the linking amide bonds or disruption of electrostatic interactions between the AP film and carboxyl groups on the SWCNTs. The AP / SWCNT has a usable electrochemical window between 1.3 and at least –1.5 V *vs.* SCE (lower potentials were not tested) and are not damaged by cycling between -0.5 and 0.6 V for at least 50 cycles. The increase in the Δ*E*p of $Fe(CN)_6^{3-/4-}$ in the cycling and potential limits experiments was found to be mostly reversible which suggests that the temporary increase is not due to loss of SWCNT material but to some unexplained interaction or fouling occurring between $Fe(CN)_6^{3-/4-}$ and the films.

3.3.9 Patterning of self assembled SWCNTs

Patterning of SWCNT assemblies was achieved by the two methods depicted in Figure 3.13**.** The first patterning method (Figure 3.13 1A-C) is derived from earlier work [21] and employs microcontact printing of aryl diazonium salts in order to pattern the SWCNT tether layer. It has been shown a number of times that spontaneous reduction of aryl diazonium cations occurs at carbon surfaces [41, 42] and hence the use of microcontact printing is a viable method.[21, 43] Briefly, patterned PDMS stamps were inked with an acidic solution of 4-aminobenzene diazonium cations and placed in contact with the PPF surface. The stamps were removed and the resulting patterned AP films were coupled to SWCNTs as described in section 2.4.2. The success of the patterning method was assessed by SEM (Figure 3.14) and AFM (Figure 3.16). SEM micrographs of the areas with SWCNTs assembled appear bright against a dark background (Figure 3.14 A). High magnification inspection reveals small bundles of vertically aligned SWCNTs

interspersed with longer bundles that have attached horizontally on the printed area (Figure 3.14 B). The vertically aligned bundles on the printed sample are notably less dense than those assembled on electrochemically grafted films. This likely reflects inhomogeneity in the film due to a non-optimized stamping process. The bare graphite shows no evidence of vertically aligned bundles but there is some lateral adsorption of bundles of the order of 100 to 200 nm in length (Figure 3.14 C). An atomic force microscopy (AFM) micrograph recorded from the same sample as that inspected by SEM reveals a SWCNT film with a maximum height of approximately 60 – 70 nm in height at the peaks (Figure 3.16).

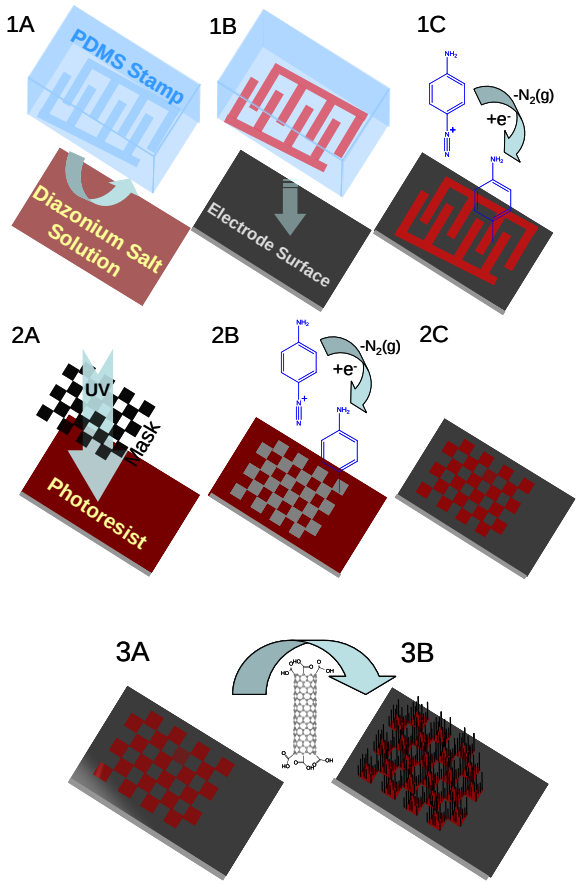

Figure 3.13. Patterning strategies employed for coupling SWCNTs to PPF surfaces. 1A-C depicts patterning by microcontact printing and 2A-C by a sacrificial film of photolithographically patterned photoresist. 3A-B depicts coupling of SWCNTs to the patterned AP film and is common to both methods.

The second patterning method employed a photolithographically patterned photoresist film to mask off areas of the electrode before electrochemical grafting of an AP film (Figure 3.13 2 A–C). Based on the success of the work described here the method was subsequently extended to patterning of highly doped silicon with protein. [44]

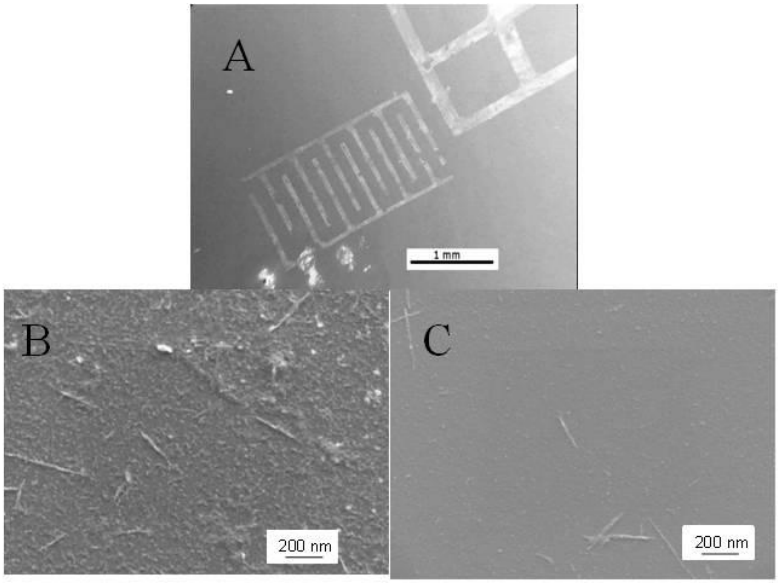

Figure 3.14. SEM images of SWCNTs attached to a patterned microcontact printed AP film (A and B). SEM image of the graphite substrate outside the printed area (C).

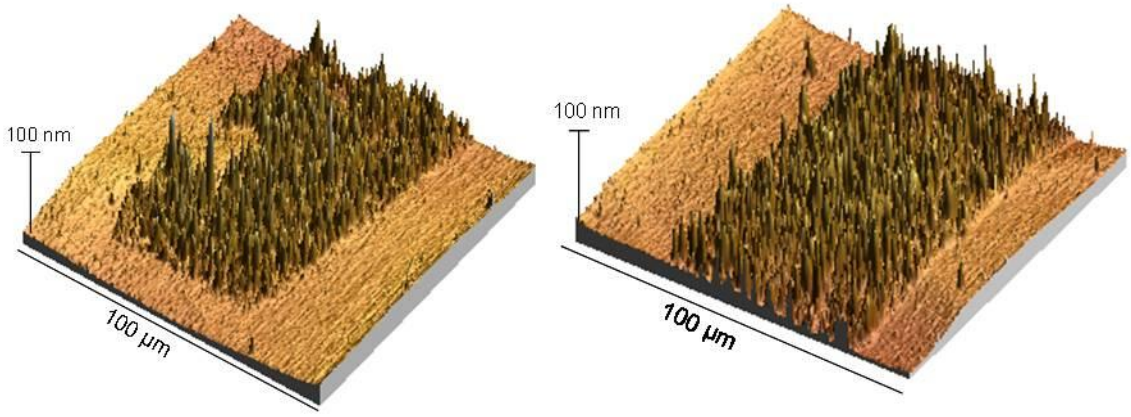

Figure 3.16. AFM micrographs across printed lines of the sample in Figure 3.14 showing SWCNT bundles approximately 60 -70 nm in height.

Figure 3.17 A) shows an AFM image of an AP film patterned in a 15 × 15 µm checkerboard pattern and reveals an AP film height of 4-5 nm which is consistent with previous findings for the grafting conditions used.[45] Figure 3.17 B shows an AFM image of a 45 µm diameter spot of AP after 24 h of reaction with SWCNTs (taken from a different area of the sample). 40 – 50 nm tall needle like structures are observed consistent with those previously described. The difference in the heights of the SWCNT features between the microcontact printed and photolithographically patterned samples is due to use of SWCNTs from different cutting batches.

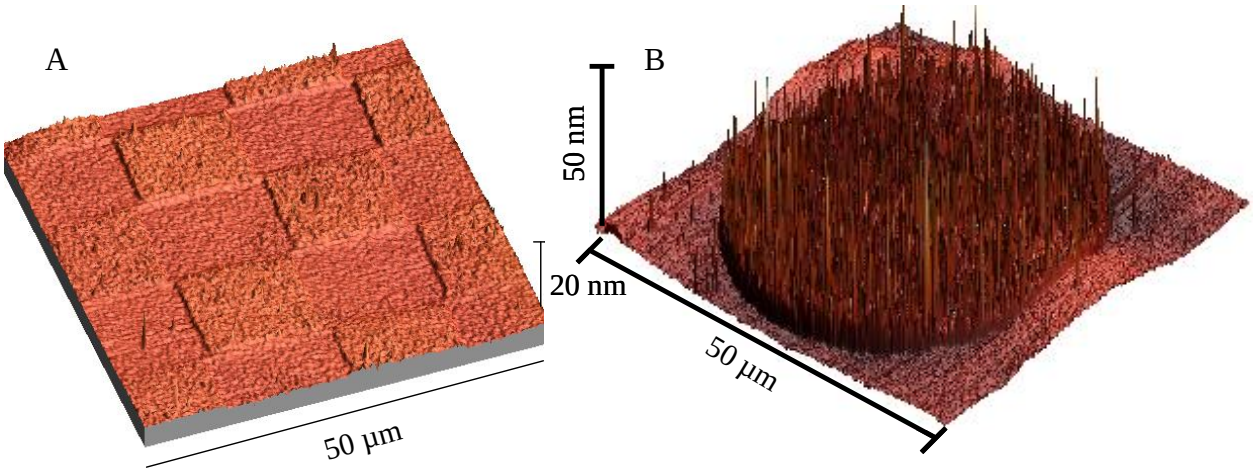

Figure 3.17. AFM images of a photolithographically patterned and electrochemically grafted AP film (A), and (B) a 45 µm diameter circular spot of AP after reaction with SWCNTs for 24 h.

3.4 Conclusion

Single walled carbon nanotubes were oxidized to functionalize them with carboxylic acid groups and successfully attached to preformed amine terminating tether layers. The attachment of the SWCNTs to the tether layers was found by CV and EIS to increase the rate of electron transfer to aqueous solution based redox molecules. This phenomenon enables the assemblies to function as high performing working electrodes for further modification or electrochemical interrogation. This is the first demonstration of covalent vertical alignment of SWCNTs on a graphitic surface and the first use of an

electro-grafted tether layer to assemble vertically aligned SWCNTs. Films derived from diazonium salts have been formed on a wide variety of surfaces by spontaneous grafting from solution and electrochemical induction therefore the method described here should be applicable to a wide range of substrates.

The SWCNTs were observed by SEM and AFM to form predominantly vertically aligned bundles approximately 50 – 70 nm in height on all the tether layers used. A few longer tubes were observed attached horizontally. AFM analysis showed that attachment of the SWCNTs had commenced after 4 h of coupling to form isolated islands and a high roughness film. Progressively, over a further 20 h of reaction, the bundles became closely packed and the SWCNT film became less rough and more homogeneous.

The AP / SWCNT assemblies exhibited high electrochemical and hydrodynamic stability. The assemblies were shown to function over a potential window between -1.5 and 1.3 V *vs*. SCE without significant changes in performance. Sonication of the assemblies in 0.1 M H_2SO_4 and pentane resulted in no change in electrochemical performance but sonication in 0.1 M NaOH did cause some deterioration. The high stability is likely to be a result of the established stability of diazonium salt derived films and the covalent amide bonds between the SWCNTs and the AP films.

Microcontact printing and photolithographic masking were employed to pattern AP tether films which successfully assembled patterned SWCNT films. Both methods produced good replication of the master design and excellent selectivity for attachment of SWCNTs on the desired areas. Facile patterning strategies for these assemblies are highly desirable for integration of the methods into future devices. Further optimization however is needed to improve the reproducibility of the patterns and the electrochemical reproducibility of the SWCNT assemblies. Successful patterning by microcontact printing relies heavily on the degree of drying of the stamp surface before contacting the substrate therefore automation of this step would be likely to improve pattern reproducibility. AP films formed by the in situ method are prone to variation and require further optimization due to their pivotal role in the electrochemical performance of the

final assembly. Finally, a higher degree of process control of the synthesis and cutting of the SWCNTs would lead to better reproducibility of the SWCNT assemblies.

3.5 References

1. Liu, Z. F.; Shen, Z. Y.; Zhu, T.; Hou, S. F.; Ying, L. Z.; Shi, Z. J.; Gu, Z. N., Organizing single-walled carbon nanotubes on gold using a wet chemical self-assembling technique. *Langmuir* **2000,** 16, (8), 3569-3573.
2. Liu, J. Q.; Chou, A.; Rahmat, W.; Paddon-Row, M. N.; Gooding, J. J., Achieving direct electrical connection to glucose oxidase using aligned single walled carbon nanotube arrays. *Electroanalysis.* **2005,** 17, (1), 38-46.
3. Gooding, J. J.; Wibowo, R.; Liu, J. Q.; Yang, W. R.; Losic, D.; Orbons, S.; Mearns, F. J.; Shapter, J. G.; Hibbert, D. B., Protein electrochemistry using aligned carbon nanotube arrays. *J. Am. Chem. Soc.* **2003,** 125, (30), 9006-9007.
4. Gooding, J. J., Nanostructuring electrodes with carbon nanotubes: A review on electrochemistry and applications for sensing. *Electrochim. Acta* **2005,** 50, (15), 3049-3060.
5. Yu, X.; Chattopadhyay, D.; Galeska, I.; Papadimitrakopoulos, F.; Rusling, J. F., Peroxidase activity of enzymes bound to the ends of single-wall carbon nanotube forest electrodes. *Electrochem. Commun.* **2003,** 5, (5), 408-411.
6. Patolsky, F.; Weizmann, Y.; Willner, I., Long-range electrical contacting of redox enzymes by SWCNT connectors. *Angew. Chem. Int. Ed.* **2004,** 43, (16), 2113-2117.
7. Yu, J. X.; Shapter, J. G.; Quinton, J. S.; Johnston, M. R.; Beattie, D. A., Direct attachment of well-aligned single-walled carbon nanotube architectures to silicon (100) surfaces: a simple approach for device assembly. *Phys. Chem. Chem. Phys.* **2007,** 9, (4), 510-520.
8. Flavel, B. S.; Yu, J. X.; Shapter, J. G.; Quinton, J. S., Patterned attachment of carbon nanotubes to silane modified silicon. *Carbon* **2007,** 45, (13), 2551-2558.
9. Flavel, B. S.; Yu, J. X.; Shapter, J. G.; Quinton, J. S., Electrochemical characterisation of patterned carbon nanotube electrodes on silane modified silicon. *Electrochim. Acta* **2008,** 53, (18), 5653-5659.
10. Chattopadhyay, D.; Galeska, I.; Papadimitrakopoulos, F., Metal-assisted organization of shortened carbon nanotubes in monolayer and multilayer forest assemblies. *J. Am. Chem. Soc.* **2001,** 123, (38), 9451-9452.
11. Diao, P.; Liu, Z. F., Vertically Aligned Single-Walled Carbon Nanotubes by Chemical Assembly - Methodology, Properties, and Applications. *Adv. Mater.* **2010,** 22, (13), 1430-1449.
12. Love, J. C.; Estroff, L. A.; Kriebel, J. K.; Nuzzo, R. G.; Whitesides, G. M., Self-assembled monolayers of thiolates on metals as a form of nanotechnology. *Chem. Rev.* **2005,** 105, (4), 1103-1169.
13. Yu, X.; Munge, B.; Patel, V.; Jensen, G.; Bhirde, A.; Gong, J. D.; Kim, S. N.; Gillespie, J.; Gutkind, J. S.; Papadimitrakopoulos, F.; Rusling, J. F., Carbon nanotube amplification strategies for highly sensitive immunodetection of cancer biomarkers. *J. Am. Chem. Soc.* **2006,** 128, (34), 11199-11205.

14. Hwang, J.; Gommans, H. H.; Ugawa, A.; Tashiro, H.; Haggenmueller, R.; Winey, K. I.; Fischer, J. E.; Tanner, D. B.; Rinzler, A. G., Polarized spectroscopy of aligned single-wall carbon nanotubes. *Phys. Rev. B* **2000,** 62, (20), R13310-R13313.
15. Liu, P. J.; Liu, L. Y.; Zhang, Y. F., Alignment characterization of single-wall carbon nanotubes by Raman scattering. *Phys. Lett. A* **2003,** 313, (4), 302-306.
16. Rusling, J. F.; Yu, J. X.; Munge, B.; Kim, H. S.; Papadimitrakopoulos, F., *Engineering the Bioelectronic Interface: Applications to Analyte Biosensing and Protein Detection* Royal Society of Chemistry: 2009.
17. Garrett, D. J.; Flavel, B. S.; Shapter, J. G.; Baronian, K. H. R.; Downard, A. J., Robust Forests of Vertically Aligned Carbon Nanotubes Chemically Assembled on Carbon Substrates. *Langmuir* **2010,** 26, (3), 1848-1854.
18. Liu, G. Z.; Gooding, J. J., Towards the fabrication of label-free amperometric immunosensors using SWNTs. *Electrochem. Commun.* **2009,** 11, (10), 1982-1985.
19. Wei, H.; Kim, S. N.; Kim, S.; Huey, B. D.; Papadimitrakopoulos, F.; Marcus, H. L., Site-specific forest-assembly of single-wall carbon nanotubes on electron-beam patterned SiOx/Si substrates. *Mat. Sci. Eng. C-Biomim.* **2008,** 28, (8), 1366-1371.
20. Wei, H.; Kim, S.; Kim, S. N.; Huey, B. D.; Papadimitrakopoulos, F.; Marcus, H. L., Patterned forest-assembly of single-wall carbon nanotubes on gold using a non-thiol functionalization technique. *J. Mater. Chem.* **2007,** 17, (43), 4577-4585.
21. Garrett, D. J.; Lehr, J.; Miskelly, G. M.; Downard, A. J., Microcontact printing using the spontaneous reduction of aryldiazonium salts. *J. Am. Chem. Soc.* **2007,** 129, (50), 15456-+.
22. Perl, A.; Reinhoudt, D. N.; Huskens, J., Microcontact Printing: Limitations and Achievements. *Adv. Mater.* **2009,** 21, (22), 2257-2268.
23. Lee, J. N.; Park, C.; Whitesides, G. M., Solvent compatibility of poly(dimethylsiloxane)-based microfluidic devices. *Anal. Chem.* **2003,** 75, (23), 6544-6554.
24. Deinhammer, R. S.; Ho, M.; Anderegg, J. W.; Porter, M. D., Electrochemical Oxidation of Amine-Containing Compounds - a Route to the Surface Modification of Glassy-Carbon Electrodes. *Langmuir* **1994,** 10, (4), 1306-1313.
25. Liu, J. Y.; Dong, S. J., Grafting of diaminoalkane on glassy carbon surface and its functionalization. *Electrochem. Commun.* **2000,** 2, (10), 707-712.
26. Cruickshank, A. C.; Tan, E. S. Q.; Brooksby, P. A.; Downard, A. J., Are redox probes a useful indicator of film stability? An electrochemical, AFM and XPS study of electrografted amine films on carbon. *Electrochem. Commun.* **2007,** 9, (7), 1456-1462.
27. Adenier, A.; Chehimi, M. M.; Gallardo, I.; Pinson, J.; Vila, N., Electrochemical oxidation of aliphatic amines and their attachment to carbon and metal surfaces. *Langmuir* **2004,** 20, (19), 8243-8253.
28. Liu, J.; Rinzler, A. G.; Dai, H. J.; Hafner, J. H.; Bradley, R. K.; Boul, P. J.; Lu, A.; Iverson, T.; Shelimov, K.; Huffman, C. B.; Rodriguez-Macias, F.; Shon, Y. S.; Lee, T. R.; Colbert, D. T.; Smalley, R. E., Fullerene pipes. *Science* **1998,** 280, (5367), 1253-1256.
29. Downard, A. J., Electrochemically assisted covalent modification of carbon electrodes. *Electroanalysis* **2000,** 12, (14), 1085-1096.
30. Nicholson, R. S.; Shain, I., Theory of Stationary Electrode Polarography - Single Scan + Cyclic Methods Applied to Reversible Irreversible + Kinetic Systems. *Anal. Chem.* **1964,** 36, (4), 706-&.

31. Diao, P.; Liu, Z. F., Electrochemistry at chemically assembled single-wall carbon nanotube arrays. *J. Phys. Chem. B* **2005,** 109, (44), 20906-20913.
32. Diao, P.; Liu, Z. F.; Wu, B.; Nan, X. L.; Zhang, J.; Wei, Z., Chemically assembled single-wall carbon nanotubes and their electrochemistry. *Chemphyschem* **2002,** 3, (10), 898-901.
33. Freeman, R. G.; Grabar, K. C.; Allison, K. J.; Bright, R. M.; Davis, J. A.; Guthrie, A. P.; Hommer, M. B.; Jackson, M. A.; Smith, P. C.; Walter, D. G.; Natan, M. J., Self-Assembled Metal Colloid Monolayers - an Approach to Sers Substrates. *Science* **1995,** 267, (5204), 1629-1632.
34. Banks, C. E.; Davies, T. J.; Wildgoose, G. G.; Compton, R. G., Electrocatalysis at graphite and carbon nanotube modified electrodes: edge-plane sites and tube ends are the reactive sites. *Chem. Commun.* **2005**, (7), 829-841.
35. Chou, A.; Eggers, P. K.; Paddon-Row, M. N.; Gooding, J. J., Self-Assembled Carbon Nanotube Electrode Arrays: Effect of Length of the Linker between Nanotubes and Electrode. *J. Phys. Chem. C* **2009,** 113, (8), 3203-3211.
36. Shein, J. B.; Lai, L. M. H.; Eggers, P. K.; Paddon-Row, M. N.; Gooding, J. J., Formation of Efficient Electron Transfer Pathways by Adsorbing Gold Nanoparticles to Self-Assembled Monolayer Modified Electrodes. *Langmuir* **2009,** 25, (18), 11121-11128.
37. Bradbury, C. R.; Zhao, J. J.; Fermin, D. J., Distance-independent charge-transfer resistance at gold electrodes modified by thiol monolayers and metal nanoparticles. *J. Phys. Chem. C* **2008,** 112, (27), 10153-10160.
38. Wong, S. S.; Woolley, A. T.; Joselevich, E.; Cheung, C. L.; Lieber, C. M., Covalently-functionalized single-walled carbon nanotube probe tips for chemical force microscopy. *J. Am. Chem. Soc.* **1998,** 120, (33), 8557-8558.
39. Cai, L. T.; Bahr, J. L.; Yao, Y. X.; Tour, J. M., Ozonation of single-walled carbon nanotubes and their assemblies on rigid self-assembled monolayers. *Chem. Mater.* **2002,** 14, (10), 4235-4241.
40. Flavel, B. S.; Garrett, D. J.; Lehr, J.; Shapter, J. G.; Downard, A. J., Chemically immobilised carbon nanotubes on silicon: Stable surfaces for aqueous electrochemistry. *Electrochim. Acta* **2010,** 55, (12), 3995-4001.
41. Adenier, A.; Cabet-Deliry, E.; Chausse, A.; Griveau, S.; Mercier, F.; Pinson, J.; Vautrin-Ul, C., Grafting of nitrophenyl groups on carbon and metallic surfaces without electrochemical induction. *Chem. Mater.* **2005,** 17, (3), 491-501.
42. Barriere, F.; Downard, A. J., Covalent modification of graphitic carbon substrates by non-electrochemical methods. *J. Solid State Electrochem.* **2008,** 12, (10), 1231-1244.
43. Lehr, J.; Garrett, D. J.; Paulik, M. G.; Flavel, B. S.; Brooksby, P. A.; Williamson, B. E.; Downard, A. J., Patterning of Metal, Carbon, and Semiconductor Substrates with Thin Organic Films by Microcontact Printing with Aryldiazonium Salt Inks. *Anal. Chem.* **2010,** 82, (16), 7027-7034.
44. Flavel, B. S.; Gross, A. J.; Garrett, D. J.; Nock, V.; Downard, A. J., A Simple Approach to Patterned Protein Immobilization on Silicon via Electrografting from Diazonium Salt Solutions. *ACS Appl. Mater. Interfaces* **2010,** 2, (4), 1184-1190.
45. Brooksby, P. A.; Downard, A. J., Electrochemical and atomic force microscopy study of carbon surface modification via diazonium reduction in aqueous and acetonitrile solutions. *Langmuir* **2004,** 20, (12), 5038-5045.

Chapter 4. Synthesis and fabrication of vertically aligned multi walled carbon nanotube electrodes

4.1 Introduction

The first report of catalytic growth of MWCNTs by thermal decomposition of carbon gas (chemical vapor deposition, CVD) occurred in 1993 by Jose-Yacaman *et al.* through a collaboration with Mobil Research.[1] The researchers used a graphite substrate impregnated with a water / methanol solution of iron (III) oxalate as the catalytic surface. The substrates were pretreated at 350 ^{o}C with N_2 / H_2 in a tube furnace, to reduce Fe(III) to metallic iron, before flowing an acetylene / N_2 gas mixture over the substrates at 700 ^{o}C. Subsequent TEM analysis of the carbonaceous product revealed a mixture of amorphous carbon nanofibres and crystalline MWCNTs. Rapidly following this report, water soluble iron salts were replaced with evaporated metal films as the catalyst, primarily because of the compatibility of evaporation techniques with photolithographic patterning.[2] Discreet patterns of aligned CNTs were first produced by Sohn and Lee in 2002 [2] by pulsed laser deposition (PLD) of iron onto a photolithographically masked silicon wafer. Following lift off of the photoresist mask and CVD, discreet regions of aligned MWCNTs were produced (Figure 4.1). This general method is widely used by a large number of research groups with a variety of catalyst films and CVD growth conditions.

Vertical alignment of MWCNTs under thermal CVD growth is thought to occur primarily because of crowding of the tubes forcing them to grow away from the surface. This is most predominant in situations where the tubes grow away from catalyst particles that stay attached to the substrate (base growth).[3] The alternative is CNT growth from a catalyst particle that is pushed along at the tip of the growing nanotube (tip growth). This growth mode typically results in mats of curly intertwined CNTs with less propensity to vertically align.[4] Zhu *et al.*(who use the same catalyst system as that employed in the

work described here) used SEM to observe the effect of heating of the catalyst film under nitrogen and hydrogen.[5] They found that the catalyst films separated into small islands with an average diameter of 10 nm and a spacing of 15 nm. SEM observation of MWCNTs grown from these films revealed CNTs with similar diameters and spacing to the catalyst islands leading to the conclusion that the morphology of the catalyst dictates the size and nature of the CNTs that grow by CVD.

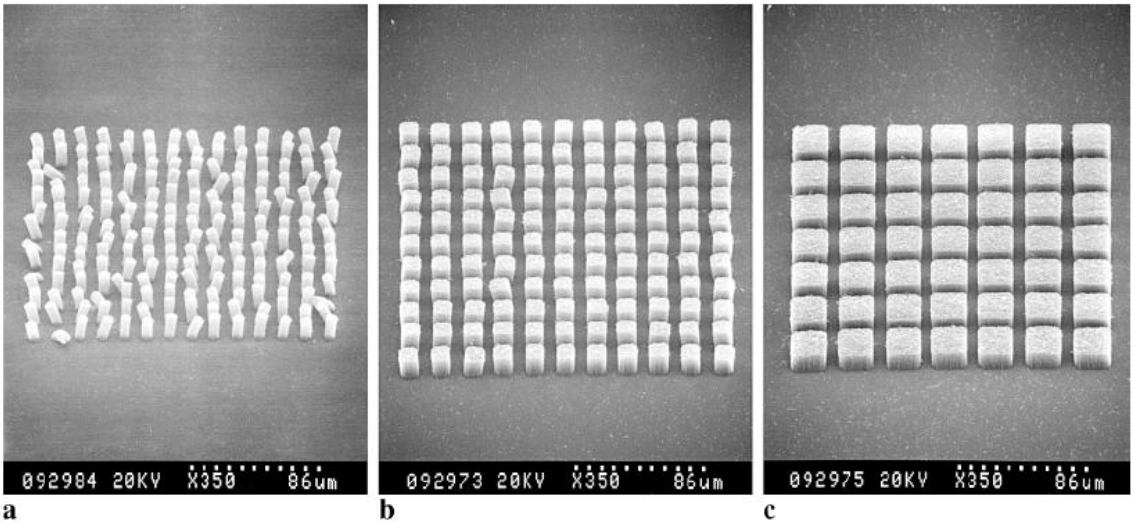

Figure 4.1. Patterned MWCNTs produced by CVD on a PLD deposited Fe catalyst film patterned by photolithography. Figure reproduced from reference 3.

The MWCNT synthesis methods used in this work were inspired by Hata and Iijima *et al.*[3] Hata and Iijima used thin films of evaporated metal catalyst (including Al_2O_3, Al and Fe) and a thermal CVD system to generate highly vertically aligned CNT forests. In an effort to produce high purity CNTs they included a small amount of water vapor with the ethylene / Ar gas flow to act as a weak oxidant and remove amorphous carbon. They discovered that the water vapor not only improved purity but produced much longer CNTs than any previously observed. Based on the observations of Helveg *et al.* [6] the authors attributed this to an increased catalyst lifetime. Helveg *et al.* grew MWCNTs on Ni nanoparticles within a TEM instrument and recorded the growth process. They observed that CNT growth ceased when a graphite shell completely encapsulated the nanoparticle leading them to conclude that at least one metal facet of the

particle must be in contact with the gas phase in order for CNT growth to occur. More recently several groups of researchers have considered the impact of Ostwald ripening of the Fe catalyst particles on the growth rate and morphology of MWCNTs grown by thermal CVD.[7-9] Kim *et al.* [9] showed that termination of growth of MWCNTs by thermal CVD is correlated with an increase in the catalyst cluster size on the surface and diffusion of the catalyst into the barrier layer (Al_2O_3 in this case). They observed the catalyst particles present after a variety of annealing and growth conditions and concluded that Ostwald ripening is responsible for the aggregation of catalyst clusters. Amama *et al.* showed that the morphology of the Al_2O_3 barrier layer [8] and the presence of water vapor in the CVD gas flows [7] inhibit Ostwald ripening of the catalyst particles and produces the highest MWCNT growth rates. This finding correlates with that of Gohier *et al.* who studied the relationship between catalyst particle size and CVD growth rate of CNTs for Co, Ni and Fe catalysts using TEM.[10] They found that for all the metals tested the highest catalytic activity was exhibited by the smallest catalyst particles. Interestingly Gohier *et al.* also observed that a change in the growth mode of the CNTs from base to tip growth occurred with increasing catalyst particle size. For all the metals tested tip growth occurred once the catalyst particles exceeded 15 nm in diameter. Hata and Iijima comment that in their system, when the grown CNTs were physically removed from the substrate, the substrate could be returned to the furnace and new CNTs grown. They conclude that a base growth mechanism must be operating in order for an active catalyst film to remain on the substrate.[3] A recent comprehensive study by Xinwei *et al.* showed that CNTs prepared by water assisted CVD are thicker, longer and cleaner than those grown without water assistance.[11] They also showed that the CNTs initially increase in length with increasing growth time to an upper limit after which the width of the CNTs increases (Figure 4.2). Gohier *et al.* observed large many walled CNTs only with large catalyst particles and a tip growth mechanism.[10] Considering the growth rates achieved by Xinwei *et al.* it is likely that base growth from small active particles was occurring in their work. Importantly they found that the MWCNTs continue to form outer walls after catalytic growth has ceased. For the purposes of the work described here, long vertically aligned MWCNTs with high density are desirable, primarily for ease of handling of the samples in subsequent fabrication steps.

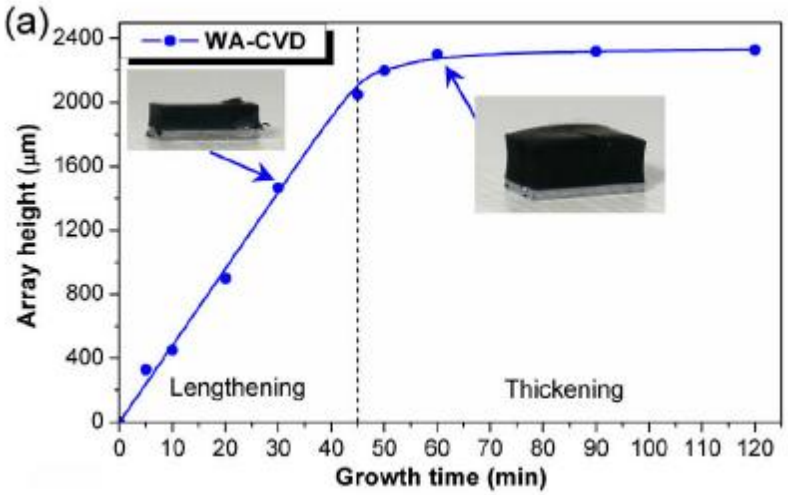

Figure 4.2. Plot of the measured height of an array of MWCNTs with increasing growth time. The array was grown by water assisted CVD from an Al_2O_3 / Fe catalyst film with an ethylene / Ar / H_2 / Ar(H_2O) gas mixture. Figure reproduced from Reference 11.

In order to incorporate CNT forests into electrodes, an electrical contact to the MWCNTs is required. This can be achieved either by growing the MWCNTs on a conducting substrate or lifting the MWCNT forest off the growth substrate and adhering it to a separate conducting substrate. Direct growth on a conducting substrate is the simplest approach to electrode preparation. CNTs have been grown on a number of metals and alloys [12-14] and conducting ceramics.[15] The growth of MWCNTs on alloys and conducting ceramics [15] employed aqueous solutions of iron and aluminium nitrate salts as the catalyst films. Under typical thermal CVD pretreatment conditions (700 – 800 ^oC H_2 / N_2 atmosphere) $Fe(NO_3)_3$ is expected to be reduced to metallic iron and $Al(NO_3)_3$ to Al_2O_3 [16, 17] providing a suitable catalyst layer for CNT growth. During the optimization of the CVD equipment used for the research described here, a method was developed for direct growth of MWCNTs on PPF.[18, 19] This remains the only description of thermal CVD growth of MWCNTs on a planar graphitic substrate.

MWCNT forests designed for use as electrodes for electrochemical measurements are frequently encapsulated in a non conducting matrix. Encapsulation of MWCNT electrodes in a non conducting matrix not only improves the electrochemical performance of the electrode but stabilizes the assembly. As-grown MWCNT forests are very fragile and can be easily dislodged, sometimes with air movement during normal handling. Furthermore, if the forests are wetted they commonly densify upon evaporation of the solvent [20] (due to capillary action) and often delaminate from the substrate. This may prevent wet chemical modification of MWCNT forests and also their repeated use as electrodes. Liu *et al.* [18] and Talapatra *et.al.* [14] both examined the solution based electrochemical properties of the as grown MWCNT forests on conducting substrates. In both cases the results show very high double layer capacitances for the electrodes due to the very high surface area of the as grown MWCNT forests. Talapatra *et al.* promote this as a highly desirable feature for the development of super capacitors or field emission devices. In the work of Liu *et al.* the authors point out that high capacitance adversely effects the sensitivity of electrodes in amperometric analytical devices due to raising the background current and therefore lowering signal to noise ratio, in particular when linear sweep voltammetry is used. Encapsulation of CVD grown CNT assemblies has been described a number of times. Liu *et al.*[19] encapsulated the sides of the MWCNTs in epoxy resin exposing only the CNT tips. The resulting encapsulated microelectrode arrays yielded low capacitance, sigmoidal CVs with solution redox probes. The sigmoidal shape shows that the diffusion of the redox probes to the electrodes was via radial diffusion and the low capacitance shows that solution access to the MWCNT sidewalls was blocked. Yun *et al.* describe 1 mm diameter towers of MWCNTs that were peeled off the growth substrate, cast into epoxy, glued to a wire with conducting epoxy and finally polished with diamond paste to reveal the CNT tips.[21] A 2003 paper by Li *et al.* describes nanotubes grown on 200 nm diameter Ni spots formed by electrochemical deposition.[22] The nanotube arrays were encapsulated in a film of SiO_2 deposited by CVD and mechanically polished to reveal the CNT tips. Esplandiu *et al.* mixed commercial MWCNTs with epoxy and cured the slurry in a plastic tube to make electrodes that successfully enhanced the electrochemical response of horse heart myoglobin.[23] A similar method was used by Chen *et al.* who set an epoxy MWCNT slurry in a capillary for use

as a microelectrode for detection of thiols.[24] Many of the methods described are technically difficult to achieve and in at least one case the authors admit problems with reproducibility.[21]

This chapter describes the development and characterization of highly robust, reusable and reproducibly fabricated MWCNT epoxy composite electrodes. CVD-grown MWCNT forests are time consuming to prepare, hence reusability and reproducibility along with consistent electrochemical performance of the assemblies are the key factors for optimization. Optimization of the CVD process and the method of encapsulation of the electrodes are discussed in detail. As an alternative to evaporated metal catalysts an aqueous $Al(NO_3)_3$ / $Fe(NO_3)_3$ catalyst system is explored. This is shown to successfully produce MWCNT / epoxy composite electrodes without the need for metal evaporation equipment. Patterning methods for both evaporated and aqueous salt catalyst systems are also developed to facilitate the development of electrode arrays. For MWCNT forests grown from both catalyst systems, O_2 plasma and H_2O_2 / H_2SO_4 (piranha) solution treatments of the MWCNT / epoxy composite surfaces are investigated as a means of activation of the surfaces prior to use as electrodes.

4.2 Experimental section

The process of evaporating metal catalyst films and growth of carbon nanotubes is described in the general experimental chapter (section 2.5.1 and 2.5.2). Photolithographic patterning of the catalyst films is described in the general experimental (section 2.6). Fabrication of vertically aligned MWCNT / epoxy composite electrodes is described in the general experimental chapter (section 2.5.3). The standard CVD conditions referred to below were 750 ^oC, 1.2 L min^{-1} Ar and 0.8 L min^{-1} H_2 for 30 min then 750 ^oC, 0.4 L min^{-1} ethylene, <0.01 L min^{-1} H_2, 1 L min^{-1} Ar and 0.05 L min^{-1} Ar(H_2O) for 5 – 10 min.

4.2.1 Electrochemical analysis

All electrochemical analysis was undertaken on an ECO CHEMIE potentiostat using the solutions and redox probes described in the Results and Discussion section. Electrochemical analysis of the MWCNT / epoxy composite electrodes employed a 3 mm diameter O-ring to define the working electrode area and the electrochemical cell designed for work on PPF described in section 2.2.1.

4.2.2 Activation and regeneration of the MWCNT / epoxy composite electrodes

O_2 plasma activation of the MWCNT / epoxy composited electrodes employed an Emitech K1050X plasma asher operating at 100 W. Unless otherwise stated an ashing time of 5 min was used. Alternatively a solution of 3:1 H_2SO_4 : H_2O_2 (piranha) was prepared by careful addition of H_2SO_4 to a small volume (<10 mL) of H_2O_2 avoiding excessive boiling. This solution was dropped onto the surface for a short time (5-10 s) before washing off with Milli-Q water. The electrodes in all cases were polished before activation steps. Where the term 'regeneration' is used the procedure is polishing to a mirror finish with 1 μm diamond paste followed by an activation step (usually O_2 plasma).

4.2.3 Growing MWCNTs from aqueous metal salt solutions

Catalyst films for CVD growth of MWCNTs were prepared from $Fe(NO_3)_3$ and $Al(NO_3)_3$ at a variety of concentrations in water. These were applied to PPF substrates by spin coating at either 3000 or 4000 rpm for 30 s as specified. In most cases an amount of polyvinylpyrrolidone (PVP40, average molecular weight 40,000 g mol^{-1}) was added to improve the spin properties of the solution. The spin speeds and drying procedures used in each experiment are described in the Results and Discussion section. The CVD conditions used were identical to those used for catalyst films formed by e-beam evaporation and are described in section 2.5.2.

4.2.4 Patterning of MWCNTs grown from aqueous salt solutions.

Photoresist masks were fabricated on PPF samples by the photolithographic methods described in section 2.7. $Fe(NO_3)_3$ / $Al(NO_3)_3$ / PVP40 solutions of various concentrations in H_2O were spin or drop coated onto the masked PPF samples and dried either on a hot plate set to 100 ^oC for 1 min or using a nitrogen gun. The unwanted catalyst and photoresist were removed by flushing the sample with a high flow of acetone from a squirt bottle while the sample was spinning at 4000 rpm.

4.2.5 Imaging of MWCNTs and epoxy composite electrodes

Low resolution SEM images were obtained using a Leica S440 SEM. High magnification images were obtained using a JEOL 7000 FESEM. To prevent charging of the MWNCT / epoxy electrodes during SEM imaging a copper strip was attached to the PPF contact area and the metal sample holder to allow accumulated electrons to transfer to the holder. TEM images were obtained using a Phillips CM200 TEM. The samples for TEM analysis were prepared using a small amount of CNT material in MeOH containing approximately 0.5 % PVP40 w/w and sonicating for at least 2 h. Immediately following sonication 2-3 drops of the resulting suspension were dropped onto a holey carbon / copper TEM grid. The TEM grids were dried under vacuum for 24 h before use. AFM images were recorded using the equipment described in section 2.6.1. High gains were required to image the O_2 plasma activated samples due to the deep pores in the surface.

4.3 Results and discussion

4.3.1 MWCNT / epoxy composite electrodes derived from evaporated metal catalyst films

4.3.1.1 Characterization of MWCNT forests derived from evaporated metal catalysts

MWCNT forests grown for 10 min on PPF using the standard conditions described in the experimental section (4.2) were investigated by SEM. The samples examined were grown from a catalyst film of 10 nm Al_2O_3 / 2 nm Fe (Al_2O_3 / Fe) or 10 nm Al / 2 nm Fe (Al / Fe). High and low magnification images of the resulting MWCNT forests are shown in Figure 4.3. The film grown from the Al_2O_3 / Fe catalyst film was 2 mm in height after 10 min of growth (typical heights were 1-2 mm). At high magnification (Figure 4.3 top right) it can be seen that the vertical alignment is not perfect and that a proportion of the tubes are 'braided'. Clearly however there is a degree of alignment occurring hence base growth of the CNTs is likely. The high growth rate for these films is consistent with the presence of small catalyst particles and also indicates a base growth mechanism.[10] The sample grown from the Al / Fe catalyst film was 1 mm in height (typically < 1 mm), shorter than the Al_2O_3 / Fe sample grown under the same conditions. This was a phenomenon that was repeatedly observed. The high magnification image of the MWCNT forest grown from Al / Fe (Figure 4.3 bottom right) shows more nanotube braiding than that grown from Al_2O_3 / Fe with no apparent vertical alignment by gross observation of the SEM images. The origins of the differences in degree of alignment for MWCNT grown from the two catalyst systems are not clear. A study by Patole *et al.* on Fe catalyzed CVD growth of CNTs using Al as a barrier layer points out several complicating factors for this metal including high sensitivity to changes in the pretreatment conditions and the ability of Al to diffuse into the substrate.[25] Some bright spots are evident in the high magnification SEM image of the Al / Fe sample which may be catalyst particles indicating that tip growth may be present to a degree in this sample probably due to Ostwald ripening forming large catalyst particles.[7-10]

The densities of the MWCNTs grown using the two catalyst films were calculated from the high magnification SEM images using a digital image measuring tool (Image J) and counting the number of nanotubes in the field of focus along ten 1 μm lines (assuming a depth of focus of 1 μm, magnification × 50000 and aperture = 30 μm). Both catalyst films produced high density CNT forests of $2.7 \pm 0.5 \times 10^9$ CNT cm^{-2} for Al_2O_3 / Fe (error = 2 standard deviations of the mean) and $2.9 \pm 0.4 \times 10^9$ CNT cm^{-2} for Al / Fe. Other workers using the same equipment as was employed for this work but using 5 nm Al : 5 nm Fe catalyst films have reported MWCNT densities higher than 10^8 CNTs cm^{-2}.[18] and densities of 3×10^9 CNT cm^{-2} have been reported for MWCNTs grown on Ni.[22]

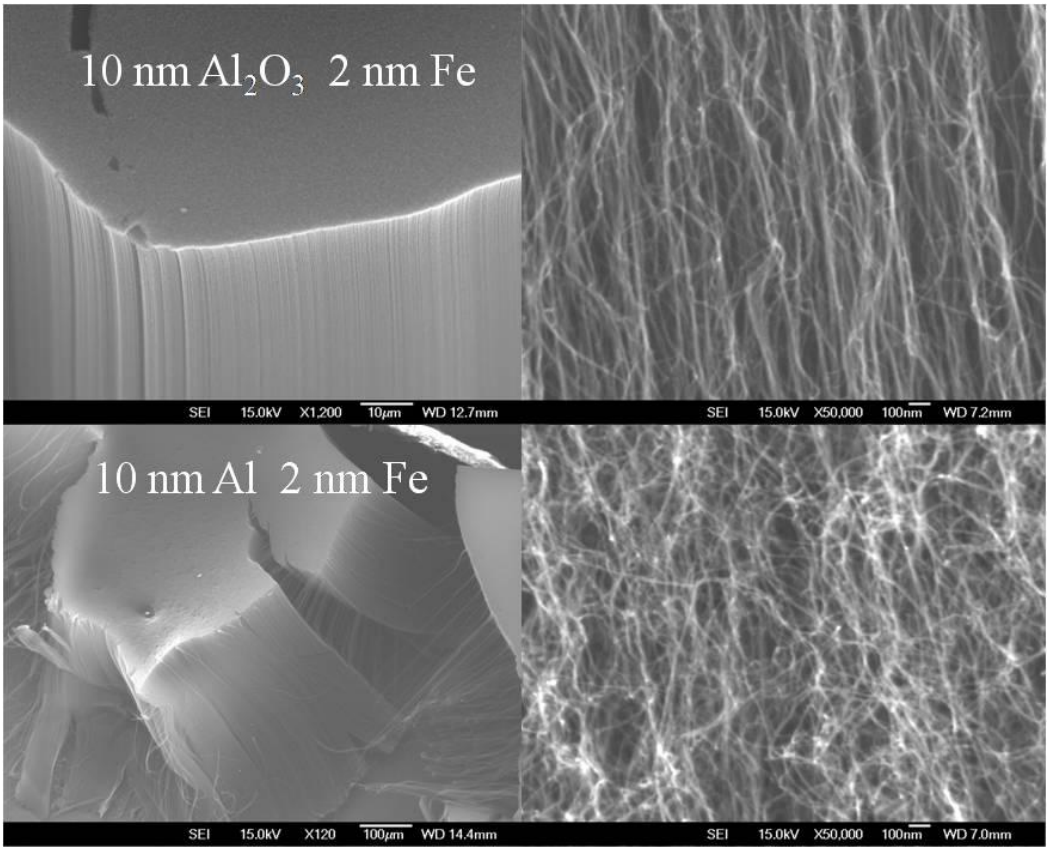

Figure 4.3. SEM images of MWCNT forests grown by CVD from e-beam evaporated metal films, the composition of which is indicated on the figures. The right hand images are magnified views of those on the left.

4.3.1.2 Fabrication of MWCNT / epoxy electrodes

The fabrication process for MWCNT / epoxy composite electrodes described in the general experimental chapter (section 2.5.3) is the result of an extensive optimization process, developed over the three year period of the research described here. In order to achieve the aims of reusability and reproducibility several technical issues needed to be addressed. The first of these was a mold design that enabled facile release of the epoxy encapsulated electrode while leaving an area of PPF exposed to act as an electrical contact. Two mold materials were trialed for the final design, these were PDMS (polydimethylsiloxane, Sylgard 184, Dow Corning) mixed in a 10:1 ratio and a polysiloxane modeling silicone (M4670A, Barnes). The PDMS proved to be too brittle to function as a mold material for this application and frequently split when releasing the MWCNT / epoxy electrodes. The polysiloxane used was a firm curing variety and required two flaps to be cut into the mold to facilitate release of the electrodes without breakage (Figure 4.4). The PPF contact area was generated by a tight fitting slot in the mold which was intended to exclude epoxy from an area of the electrode (Figure 4.4 **A**). In practice, epoxy did penetrate into the slot and a piece of electrical tape was required to protect the contact area before each casting. Before each casting, a mold release agent was required to stop the epoxy sticking to the polysiloxane. During the course of this research silicone grease, silicone cooking spray and aerosol Teflon spray were used and all worked equally well as release agents. Silicone grease was the most readily available and became the method of choice.

Considering the encapsulation of MWCNTs, it was clear from existing literature [21] that a low viscosity epoxy was required in order to penetrate into the forest and conformally wet the CNTs. EPO-TEK 301 is a hard curing low viscosity epoxy with excellent biocompatibility and high resistivity ($> 3.5 \times 10^{14}\ \Omega$ cm) and was used for encapsulation of all electrodes. The earliest MWCNT / epoxy composite designs in this work were fabricated simply by pouring an amount of epoxy directly onto the MWCNT forest and allowing the epoxy to cure. The resulting forests were then polished as described in section 2.5.3. This strategy produced electrodes that were prone to delamination of the epoxy from the surface during polishing and when exposed to

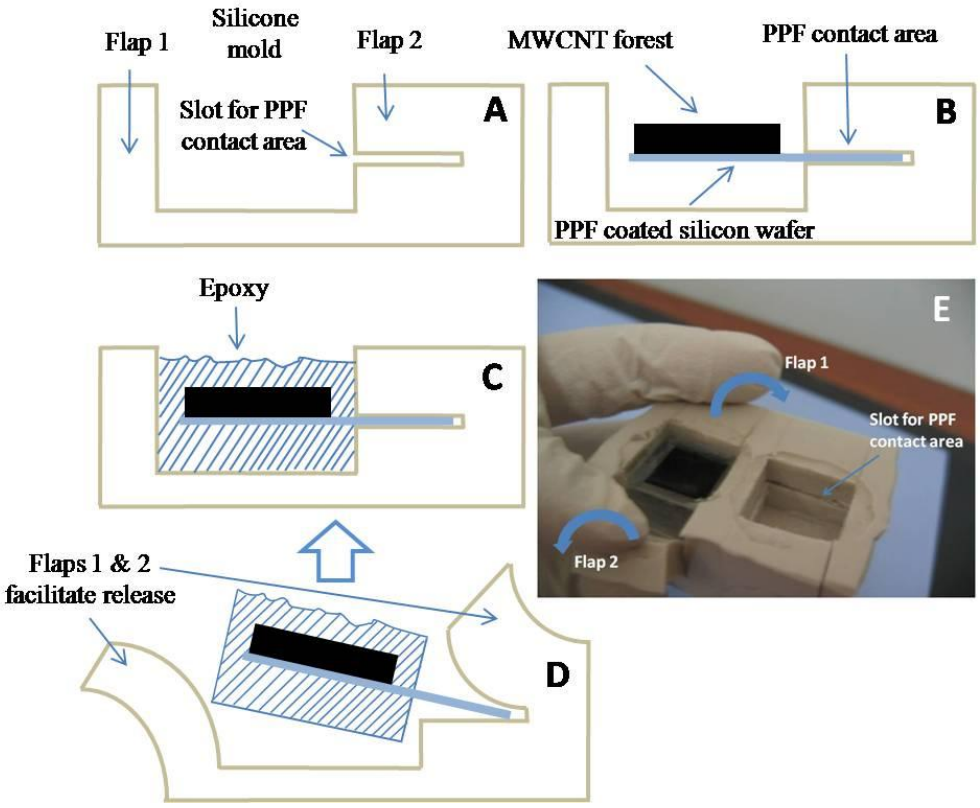

Figure 4.4. Process of fabricating MWCNT / epoxy electrodes**. A** Cross section elevation of the silicone mold, **B** MWCNT forest on a PPF wafer inserted into the silicone mold, **C** MWCNT modified PPF flooded with epoxy, **D** the cured assembly is removed, facilitated by flexible flaps 1 & 2, **E** photograph of two side by side molds. Flaps 1 & 2 are shown on the mold to left with an electrode in situ and the slot that forms the PPF contact area is shown on the mold to the right.

solvents during subsequent chemical modification steps. Furthermore, despite the low viscosity, the uncured epoxy resin did not fully penetrate the MWCNT forests at atmospheric pressure. This resulted in trapped air bubbles at the MWCNT bases that were exposed during polishing. In the optimized fabrication strategy, vacuum was applied to the uncured epoxy in the mold, to draw out air bubbles in the MWCNT forest. The vacuum was applied gradually to avoid large air bubbles forming and lifting the MWCNT forest off the substrate. Three cycles over 10 min of gradual application of vacuum from atmospheric pressure to 60 mTorr was sufficient to remove all air bubbles

from the forest such that none were evident under SEM investigation after polishing of the cured assemblies. Vacuum could be applied more rapidly to MWCNT forests produced from Al / Fe catalyst films because they were shorter and therefore contained less trapped air and they had better adhesion to the substrate than those grown from Al_2O_3 / Fe.

The polishing method for the assemblies is discussed in section 2.5.3. SEM images of the polished surface are shown in Figure 4.5. The surface of the electrodes show regions where the MWCNTs have separated forming seams of epoxy resin. This is most likely due to a small amount of densification by capillary forces that commonly occur with aligned CNT assemblies are exposed to liquids.[26]

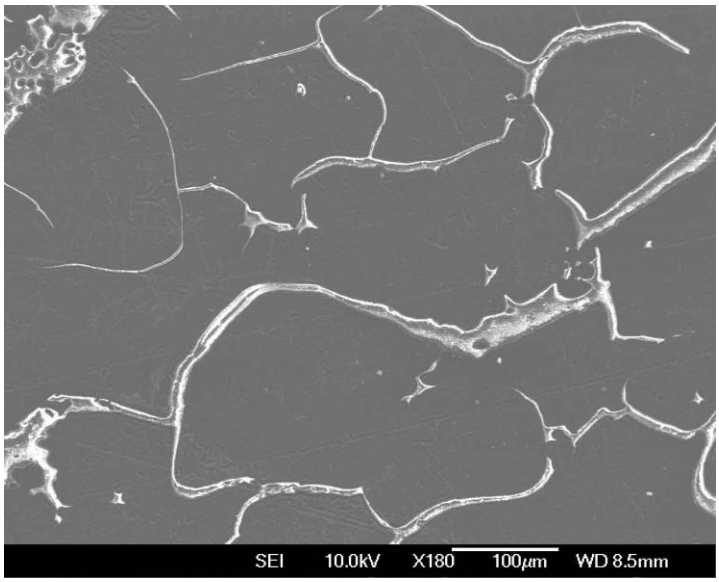

Figure 4.5. Low magnification SEM image of a MWCNT / epoxy electrode surface showing seams of epoxy resin where cracking in the MWCNT field has occurred.

4.3.1.3 Electrochemical performance and activation

Figure 4.6 shows CVs of 1 mM $Fe(CN)_6^{3-}$ and $Ru(NH_3)_6^{2+}$ (in pH 7 PBS) obtained using three MWCNT / epoxy electrodes. CVs recorded in pH 7 PBS with no redox probe molecule present are also shown. Two of the three electrodes used were prepared from Al_2O_3 / Fe catalyst films and one from an Al / Fe catalyst film. A first set of CVs was recorded using freshly polished electrodes and a second set was recorded after O_2 plasma activation. The second cycle of the CVs recorded using polished electrodes in pH 7, PBS (Figure 4.6 a (i)) are featureless with a low background current of approximately 5 µA for the MWCNT / epoxy electrodes derived from Al_2O_3 / Fe catalyst films (black and red solid line) and 3 µA for the electrode derived from a Al / Fe catalyst film (green solid line). The first cycle of the CV for one of the electrodes is shown (black dashed trace) which almost overlaps the trace for the second cycle showing that there is no break-in process with the assembly. The low background current shows that the double layer capacitance for the electrode is small, consistent with conformal encapsulation of the MWCNTs with epoxy resin lowering the electrode area in contact with the electrolyte. The CVs recorded after O_2 plasma (Figure 4.6 a (ii)) exhibit similar background currents to the polished electrodes indicating that the active electrode area in contact with the electrolyte has not increased significantly. There is a single cycle break-in process indicated by a broad oxidation peak ($E_{pa} \approx 0.8$ V) on the first cycle (black dashed trace) which is typical of graphitic electrodes. Two of the three electrodes tested show a small reversible redox system with $E_{1/2} \approx 0.25$ V (black and green trace). This redox system is likely to arise from quinonoid functionalities formed during plasma activation. Such functionalities have pH-dependent $E_{1/2}$ redox values and hence CVs of the plasma activated electrodes were recorded in a range of buffers with differing pH. Unfortunately the peaks were only sporadically observed and usually reduced in size with repeat scanning hence the redox system could not be assigned.

CVs recorded in 1 mM $Ru(NH_3)_6^{2+}$, pH 7 PBS using the same three electrodes as above are shown in Figure 4.6 (b) after regeneration by polishing (i) and after O_2 plasma treatment (ii). The CVs of the three polished electrodes are very different in appearance

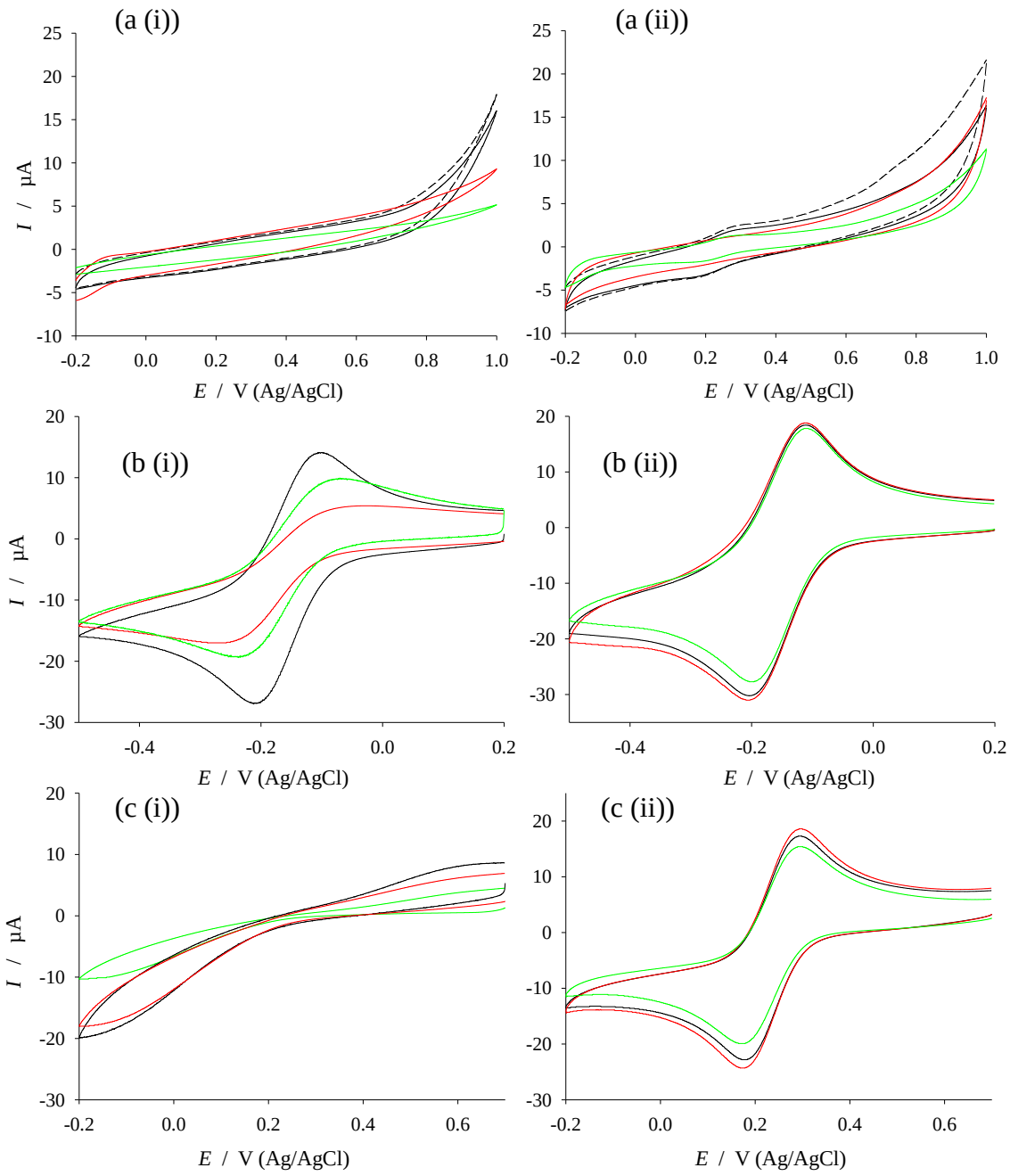

Figure 4.6. CVs recorded using MWCNT / epoxy electrodes derived from Al_2O_3 / Fe (black and red) and Al / Fe (green) catalyst films. The CVs were recorded in (a) pH 7 PBS, (b) 1 mM $Ru(NH_3)_6^{2+}$ in pH 7 PBS and (c) 1 mM $Fe(CN)_6^{3-}$ in pH 7 PBS when freshly polished (i) and after 5 min of 100 W O_2 plasma (ii), scan rate = 100 mV s^{-1}. In (a (i)) and (a (ii), the solid lines show the second cycle for each electrode and the dashed black line is the first cycle using the electrode corresponding to the solid black trace.

despite the same polishing procedure being used for each electrode. One of the electrodes exhibits a well behaved macro electrode CV (black) and two exhibit CVs that are more sigmoidal in shape (red and green). This is most reasonably explained by considering the diffusion behavior of micro and nano electrode arrays. The example most pertinent to this case is that of Banks and Compton *et al.* in which the authors explain the electrochemical behavior of graphite and carbon nanotube modified electrodes.[27] Figure 4.7 shows the effect of decreasing electrode spacing on the diffusion of redox molecules to a micro-disc electrode array.

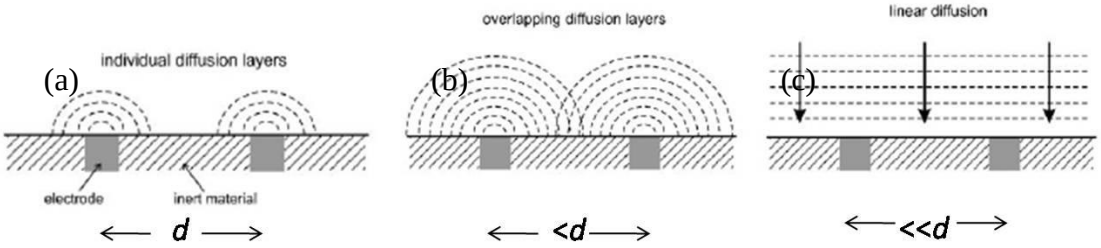

Figure 4.7. The diffusion zone behavior of micro / nano electrode arrays with decreasing electrode separation (*d*). Figure reproduced from reference 27.

Figure 4.7 (a) shows that when the micro-disc electrodes are well separated hemispherical concentration gradients develop in solution and the molecules diffuse radially to the electrodes. Radial diffusion results in a sigmoidal CV shape. When the spacing between the electrodes is reduced (Figure 4.7 (b)) the diffusion zones partially overlap generating high depletion zones between the electrodes leading to mixed linear and radial diffusion and CVs that are somewhat sigmoidal in shape. When the spacing between the electrodes is small and the diffusion zones sufficiently overlap, the heavily depleted regions between the electrodes generate a linear diffusion field in the bulk solution (Figure 4.7 (c)). In a CV, linear diffusion manifests as a peaked CV such as those that result from macro-disc electrodes. The black trace in Figure 4.6 b (i) is thus consistent with linear diffusion resulting either from a macro-sized electrode or from closely spaced micro or nano electrodes. It is assumed that either the top surface of the CNT forest is exposed or that there are numerous closely-spaced islands of exposed CNT bundles with epoxy in between. The green and red traces are consistent with some

overlap of the diffusion zones causing mixed linear and radial diffusion behavior. The three CVs recorded after O_2 plasma activation (Figure 4.6 b (ii)) all exhibit linear diffusion behavior and therefore have CNT electrodes that are closely spaced. Importantly the traces shown for the three electrodes are very similar. This was repeatedly observed for all of the plasma activated MWCNT / epoxy electrodes fabricated in a large number of CVs that are not shown here. The results shown here indicate that polishing can produce electrodes that give well behaved electrochemistry but O_2 plasma activation is much more reliable.

CVs recorded in 1 mM $Fe(CN)_6^{3+}$, pH 7 PBS, using the same three electrodes as those above, are shown in Figure 4.6 (c) after polishing (i) and after O_2 plasma treatment (ii). The CVs recorded at the polished electrodes feature a large ΔE_p (> 800 mV) which indicates slow kinetics for the $Fe(CN)_6^{3-/4-}$ couple at these electrodes. The same CVs recorded at the O_2 plasma treated electrodes have defined peaks and $\Delta E_p \approx 100$ mV indicating fast kinetics for the $Fe(CN)_6^{3-/4-}$ couple. This differs from the CVs of $Ru(NH_3)_6^{2+/3+}$ (Figure 4.6 (b)) where the ΔE_p does not change significantly between the polished and plasma treated samples. The kinetics of the $Fe(CN)_6^{3-/4-}$ couple are well known to depend on the chemical functionalities at the electrode surface, in particular on the presence of oxygen functionalities which promote fast kinetics.[28] Conversely, the kinetics of the $Ru(NH_3)_6^{2+/3+}$ couple are known to be insensitive to surface functionalities [28] hence these experiments suggest that O_2 plasma functionalizes the CNT tips with oxygen containing functionalities. A recent detailed XPS and Raman study by Zschoerper *et al.* [29] found that treatment of MWCNTs with 20 W RF generated O_2 plasma for 5 min with a chamber pressure of 970 µbar gave the following ratio of oxygen functionalities per 100 C atoms: 0.23 [OH] : 1.28 [C=O] : 0.84 [COOH]. Interestingly they found that the ratio of oxygen functionalities could be drastically altered by changing the chamber pressure and plasma gas constituents. Using 5 min of 20 W H_2O plasma and a chamber pressure of 120 µbar the ratio of oxygen functionalities was 1.91 [OH] : 2.25 [C=O] : 1.16 [COOH] per 100 atoms of carbon. None of the conditions used in the research of Zschoerper *et al.* were similar to those described here therefore no inference can be made about the ratios of oxygen functionalities formed on the MWCNT / epoxy electrodes in

this work. The results of Zschoerper *et al.* do however show that oxygen functionalities are highly likely to be present at the surface of the plasma treated MWCNT / epoxy electrodes at a greater concentration than before plasma treatment and that tailoring the ratio of functionalities should be possible.

Figure 4.8 shows CVs of 1 mM $Fe(CN)_6^{3-/4-}$ in pH 7 PBS recorded at plasma activated MWCNT / epoxy electrodes (prepared from an Al / Fe catalyst film (pink) and an Al_2O_3 / Fe catalyst film (blue)) and a polished GC plate electrode (black). The same 3 mm O-ring was used to define the working electrode area on all three electrodes. The MWCNT / epoxy electrodes used to record the CVs had undergone numerous regenerations by polishing followed by an activation step. Activation involved either O_2

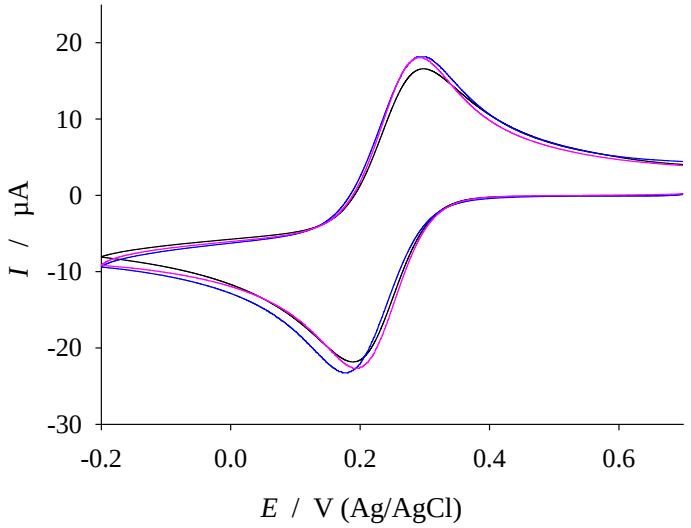

Figure 4.8. CVs of in 1 mM $Fe(CN)_6^{3-}$, pH 7 PBS obtained at MWCNT / epoxy electrodes (pink, Al / Fe and blue, Al_2O_3 / Fe) and GC, polished (black), scan rate = 100 mV s^{-1}. Both MWCNT / epoxy electrodes were activated with 5 min 100 W O_2 plasma.

plasma treatment, piranha treatment, sonication in 0.5 M HNO_3, electrochemical oxidation at 1.6 V in 1 M KOH , boiling in water and chemical coupling of redox mediators (alternative activation strategies are discussed in subsequent sections and coupling of mediator molecules is discussed in chapter 5). The electrode derived from the Al_2O_3 / Fe catalyst film is estimated to have been regenerated 80 – 100 times. The CVs obtained at the two MWCNT / epoxy electrodes are remarkably similar to that obtained at

polished GC (of the same geometric area) showing that there is linear diffusion over the entire area of the MWCNT electrodes. Importantly the consistency with which the plasma treated MWCNT / epoxy electrodes produced well defined, nearly identical CVs even after extended use shows that the goals of reproducibility and reliability have been met and the electrodes are suitable for use in subsequent experiments. Furthermore, there was no difference between electrodes derived from Al_2O_3 / Fe or Al / Fe catalyst films and therefore the two electrode types were henceforth used interchangeably and there will be no further reference to the evaporated catalyst film used to fabricate the electrodes in the remainder of this thesis

4.3.1.4 Further electrode activation strategies

Numerous activation strategies have been reported for graphitic carbon electrodes and several of these were investigated as alternatives to O_2 plasma activation for MWCNT / epoxy electrodes. Boiling the electrodes in water for 10 min,[30] boiling in 0.5 M HNO_3, [30] sonication for 10 min in 0.5 M HNO_3 and electrochemical oxidation by applying 1.6 V *vs*. SCE to the electrode in 1 M KOH [22] all resulted in no activation of the electrode for the $Fe(CN)_6^{3-/4-}$ couple or NADH oxidation. Application of a 3:1 piranha solution to the electrode surface for 5 – 10 s did result in activation of the electrode for the $Fe(CN)_6^{3-/4-}$ couple but not NADH oxidation. Herbert *et al.* have previously reported that activation of PPF electrodes by dipping in a 7:1 piranha solution improved the detection limit for dopamine for that electrode.[31] CVs recorded using MWCNT / epoxy electrodes in pH 7 PBS and 1 mM $Fe(CN)_6^{3-}$ / pH 7 PBS are shown in Figure 4.9. The CV recorded in PBS (Figure 4.9(a)) have an increased background current compared to the equivalent CV recorded using a plasma activated electrode (Figure 4.9 (a) grey dashed). The CVs recorded in $Fe(CN)_6^{3--}$ (Figure 4.9 (b)) have well defined peaks with ΔE_p = 130 mV and ΔE_p = 170 mV for the $Fe(CN)_6^{3-/4-}$ couple indicating moderately fast kinetics. Interestingly the $E_{1/2}$ for the $Fe(CN)_6^{3-/4-}$ couple with the piranha etched electrodes decreases to 168 mV from the value of 230 mV established at plasma etched MWCNT / epoxy electrodes (Figure 4.9 (b) grey dashed). This could be due to a specific interaction between the piranha and the MWCNTs generating functionalities on the MWCNT tips. Datsyuk *et al.* confirm that piranha treatment of MWCNTs increases the

oxygen functionalities and the acidity of MWCNTs but they do not determine the ratios of different oxygen functionalities.[32]

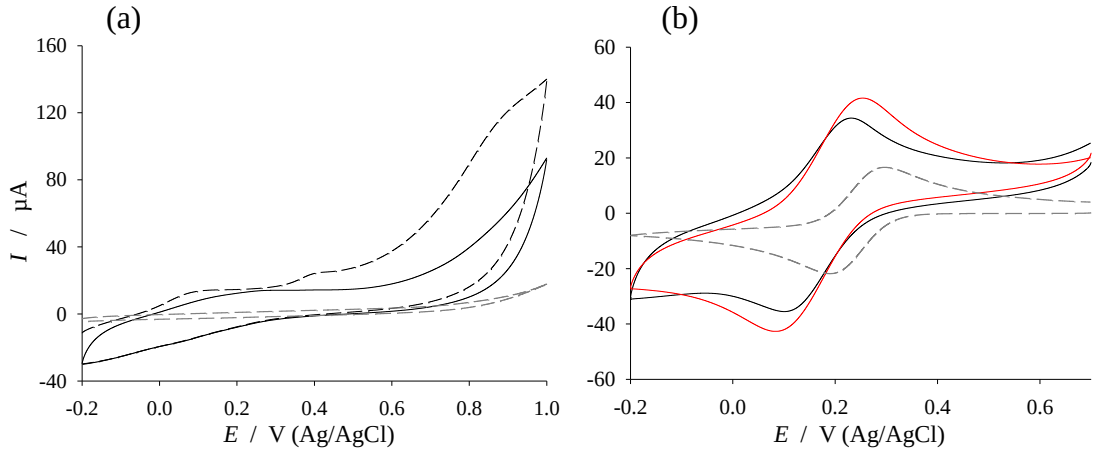

Figure 4.9 CVs recorded using MWCNT / epoxy electrodes activated for 5 s in 3:1 piranha solution in (a) pH 7 PBS, 1st scan (black dash), 2nd scan (black) and (b) two different electrodes (red and black) in 1 mM $Fe(CN)_6^{3-}$, pH 7 PBS at scan rate = 100 mV s^{-1}. In both figures the grey dashed CVs were recorded at a plasma activated MWCNT / epoxy electrode of the same geometric area.

4.3.1.5 SEM and AFM investigation

The surfaces of polished, plasma treated and piranha activated MWCNT / epoxy electrodes were examined by SEM and AFM. SEM images could not be obtained of the polished surfaces because the non conducting epoxy resin became charged under the electron beam affecting the focus of the instrument. The O_2 plasma and piranha treated samples could be imaged by SEM with the aid of a copper strip, taped between the PPF contact area and the metal sample holder to act as an electron conductor. SEM images of a MWCNT / epoxy electrode treated with O_2 plasma are shown in Figure 4.10. The low magnification image (Figure 4.10 (a)) shows a pitted surface which is typical of plasma etching. The higher magnification images (Figure 4.10 (b) and (c)) show CNT tips extending out of the polymer matrix. This is most likely caused by a faster etch rate for the epoxy polymer than MWCNTs.

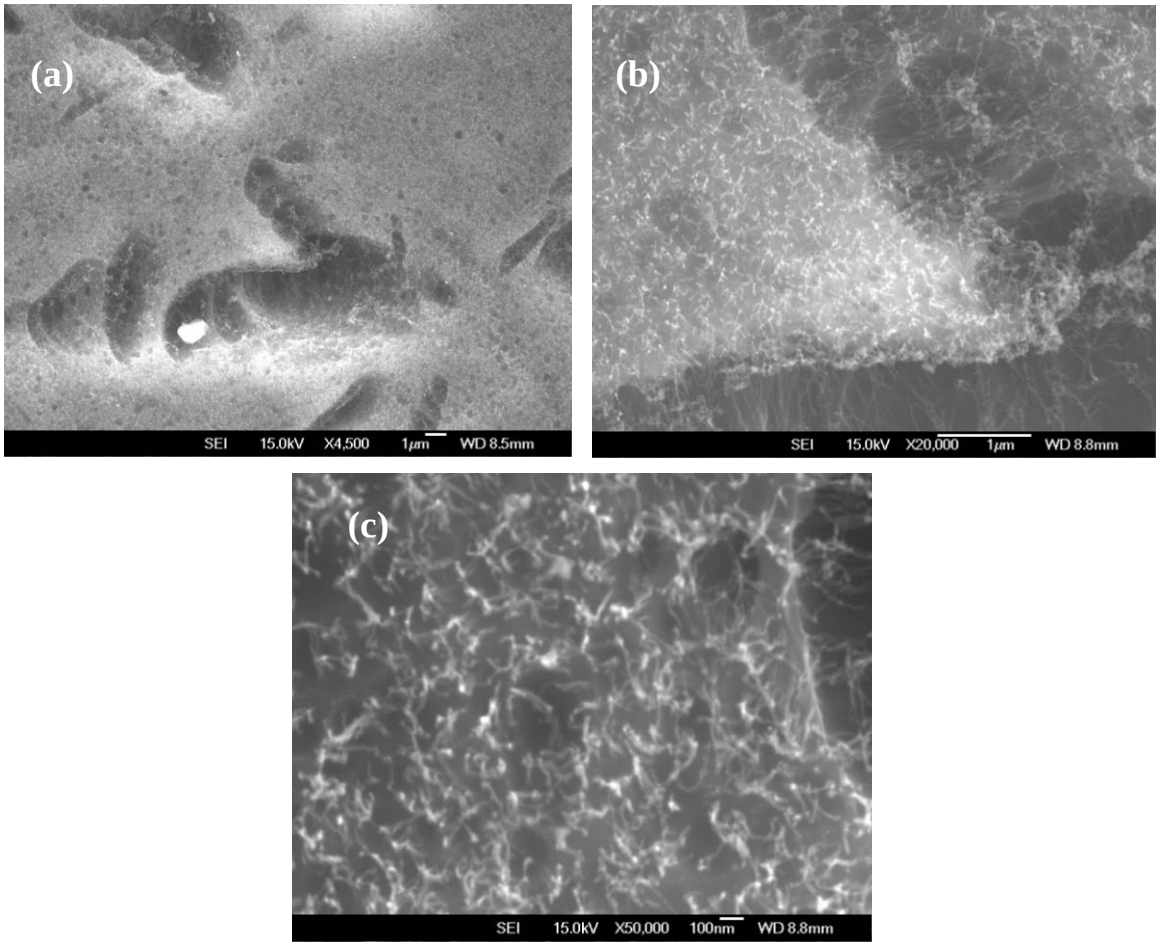

Figure 4.10. SEM images of a MWCNT / epoxy electrode surface after treatment with O_2 plasma, magnified (a) × 4500 (b) × 20000, (c) × 50000.

AFM images of a MWCNT / epoxy surface before and after plasma treatment are shown in Figure 4.11. Also shown is a scan across a solid epoxy seam in the electrode surface before and after O_2 plasma to illustrate the relative etch resistance of the epoxy compared to the MWCNT / epoxy composite. The AFM images of the surface before plasma treatment (Figure 4.11(a) Polished) show that the surface is undulating with

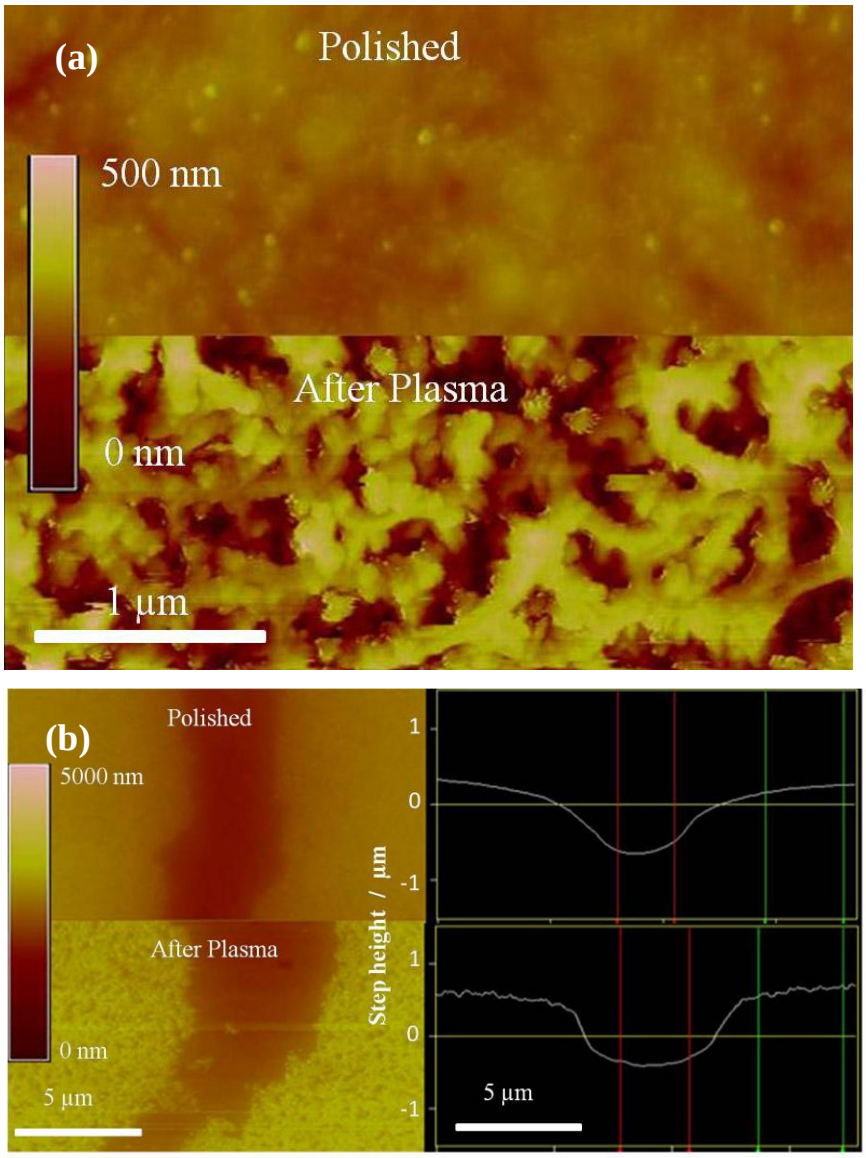

Figure 4.11. (a) AFM images of MWCNT / epoxy electrode surfaces before and after O_2 plasma activation. (b) AFM images (left) and line profiles (right) of solid epoxy seams in the MWCNT / epoxy surface before and after plasma.

occasional MWCNTs protruding from the surface. After plasma treatment (Figure 4.11 (a) After Plasma) the surface becomes very rough as the epoxy resin has been etched away from the MWCNTs. Clearly, considering the CV results from section 4.2.3.2 and the AFM images, plasma treatment increases the number of electrochemically active

MWCNTs available at the electrode surface. The AFM images of the solid epoxy seam (Figure 4.11 (b)) of a polished surface shows that seam is recessed by 0.84 μm indicating that polishing removes epoxy at a faster rate than the surrounding MWCNT / epoxy composite. After plasma treatment the recessed seam is slightly deeper (1.00 μm) and the trench sides are steeper indicating a faster O_2 plasma etch rate for epoxy than the MWCNT / epoxy composite.

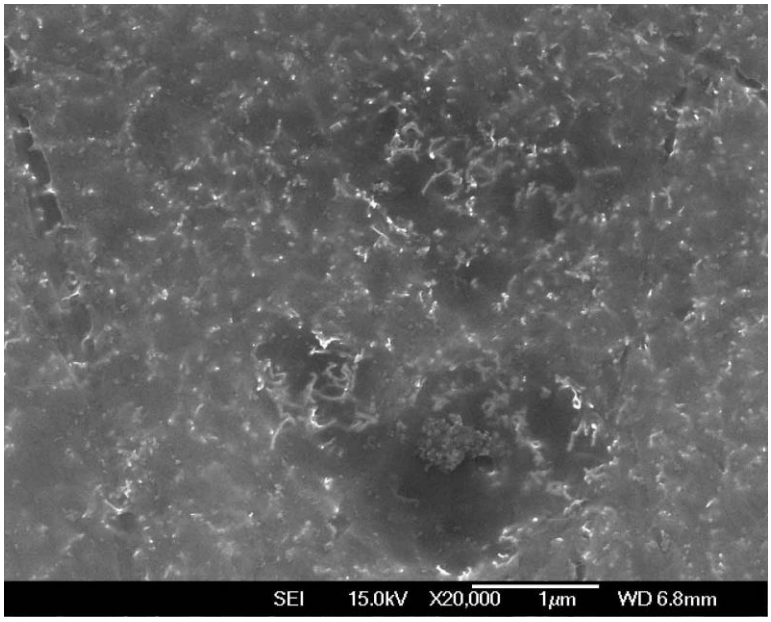

Figure 4.12. SEM image of a MWCNT / epoxy composite electrode derived from an Al / Fe film after 10 s of etching with 3:1 piranha solution.

An SEM image of a MWCNT / epoxy electrode after polishing followed by 5 s of 3:1 piranha activation is shown in Figure 4.12. The image shows that the MWCNTs do not protrude as far from the surface as the corresponding plasma etched sample (Figure 4.10 (b)). This is most likely the result of a difference in the relative etch rates between epoxy and the MWCNT / epoxy composite in piranha compared to O_2 plasma. The CVs recorded using piranha activated electrodes (section 4.3.1.4) exhibited high background currents suggesting that the electrolyte solution is able to penetrate into the surface and contact a much higher surface area of MWCNTs. Surprisingly, the SEM image shown here does not appear to show a more porous structure than that of the O_2 plasma activated

sample (Figure 4.10 (b)) making the source of the high background current uncertain. Clearly however piranha etching of polished MWCNT / epoxy electrodes increases the active surface area of MWCNTs at the surface leading to linear-diffusion of redox probe molecules.

4.3.1.6 Oxidation of NADH

The ability to catalyze oxidation of NADH is an important fabrication aim because of the vast number of dehydrogenase enzymes and therefore potential biosensors that rely on the NADH / NAD^+ couple.[30] Hence the performance of the MWCNT / epoxy electrodes for oxidation of NADH oxidation was assessed by recording CVs of 1 mM NADH in pH 7 PBS. The electrodes were freshly polished (Figure 4.13 (a)) or were treated with O_2 plasma (Figure 4.13 (b)). The CVs recorded at the freshly polished electrodes all show a poorly defined oxidation peak at approximately 0.8 to 1.0 V which is typical of an untreated carbon electrode. After treatment with O_2 plasma the oxidation peaks are clearly defined and the E_{pa} values are reduced to 0.54, 0.54 and 0.59 V. at the three electrodes. Catalytic oxidation of NADH has been previously reported for CNTs activated by a range of methods.[30] Wooten and Gorski report that SWCNTs drop coated onto a GC electrode result in E_{pa} = 0.38 V vs Ag /AgCl at pH 7.[30] Oxidation of the SWCNTs, (before drop coating) by either boiling in water or microwaving in HNO_3,

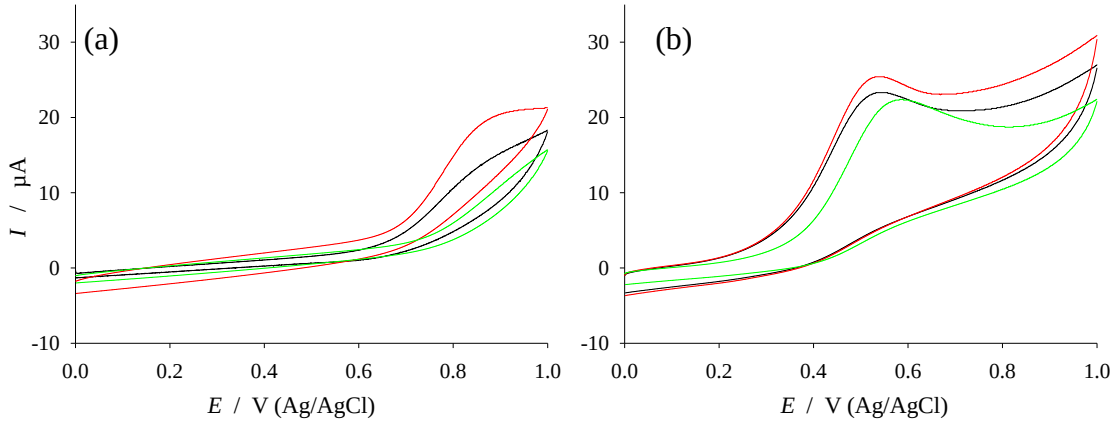

Figure 4.13. CVs obtained using three MWCNT / epoxy electrodes in 1 mM NADH, pH 7 PBS, scan rate = 100 mV s^{-1}, (a) freshly polished and (b) after 5 min 100 W O_2 plasma treatment.

resulted in a further decrease in the oxidation potential of NADH to $E_{pa} \approx 0$ V vs Ag/ AgCl. The authors attribute the catalysis to functionalization of the CNTs with quinone moieties which have previously been shown to be efficient catalysts of NADH oxidation.[33] Although the strategy of Wooten and Gorski resulted in low overpotentials for NADH oxidation, the drop-coated electrodes suffered from high background currents due to the high capacitance of electrodes of this type. The electrodes fabricated in this work gave higher potentials but exhibited a 10 fold increase in current density for oxidation of NADH compare with those of Wooten and Gorski under the same conditions. As the background currents between the two types of electrodes are similar, the electrodes described here have a higher signal to noise ratio than those of Wooten and Gorski.

None of the alternative activation strategies discussed in section 4.3.1.4 resulted in electrodes capable of catalyzing oxidation of NADH. The lack of catalysis of NADH oxidation by the piranha activated sample is interesting and suggests that the catalysis may be due to specific functionalities at the CNT tips that are formed during O_2 plasma etching but are not formed during piranha etching. The difference of 60 mV in the $E_{1/2}$ for the $Fe(CN)_6^{3-/4-}$ couple between piranha and plasma activated MWCNT / epoxy electrodes is further evidence that that the different activation strategies produce different surfaces. Although it is likely that quinones (in particular orthoquinones) [33] are the functionalities responsible for catalytic NADH oxidation, no conclusive evidence for this was obtained. Further investigation into the functionalities at the MWCNT tips and their impact on the oxidation of NADH is required in future work.

4.3.1.7 Patterning of evaporated metal catalysts

Having optimized the fabrication of vertically aligned MWCNTs, patterning of the MWCNT forests was examined. Patterned metal catalyst films were prepared by photolithography as described in the general experimental chapter section 2.7. MWCNTs were grown from the catalyst patterns by CVD using the standard conditions described in section 4.2. SEM images of patterned MWCNTs grown from a 10 nm Al_2O_3 / 2 nm Fe catalyst pattern on silicon are shown in Figure 4.14. The patterned MWCNTs grew to 2

mm in height with excellent retention of the catalyst pattern. The best pattern retention occurred in negative relief where the aspect ratio of the vertically aligned MWCNT bundles was relatively low (Figure 4.14 (a), (b)). Figure 4.14 (b) shows retention of 2-3 µm wide spaces in the small lettering retained through a 2 mm tall MWCNT bundle which equates to an aspect ratio of 670 – 1000. Isolated MWCNT features with high aspect ratios are not self supporting. This is seen on the isolated columns that make the center of the letters R,B and O (Figure 4.14 (b)). Figure 4.15 shows 3 µm line width lettering that has grown to a height of 1.5 mm (aspect ratio 500). At this aspect ratio the towers are not self supporting and have become jumbled. The patterning method, catalyst recipe and growth conditions used here have been explored in depth in existing literature, [3, 5] therefore no further optimization or characterization was undertaken as part of the work described here.

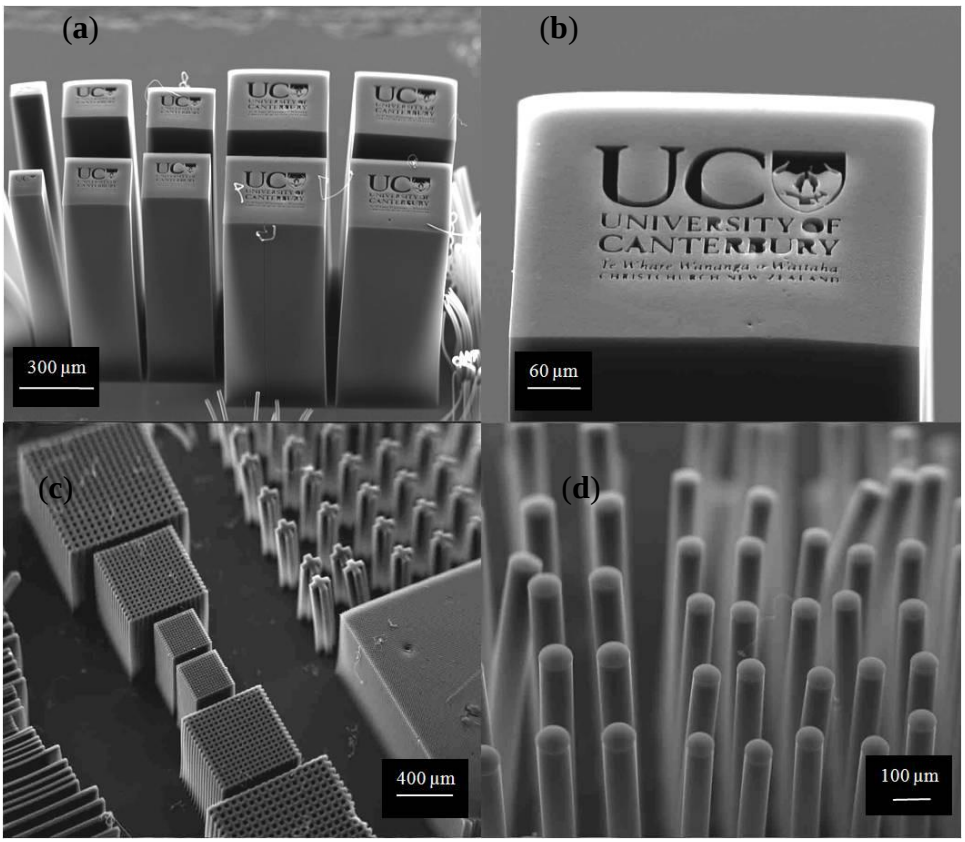

Figure 4.14. SEM images of MWCNTs grown on a patterned catalyst film consisting of 10 nm Al_2O_3 : 2 nm Fe.

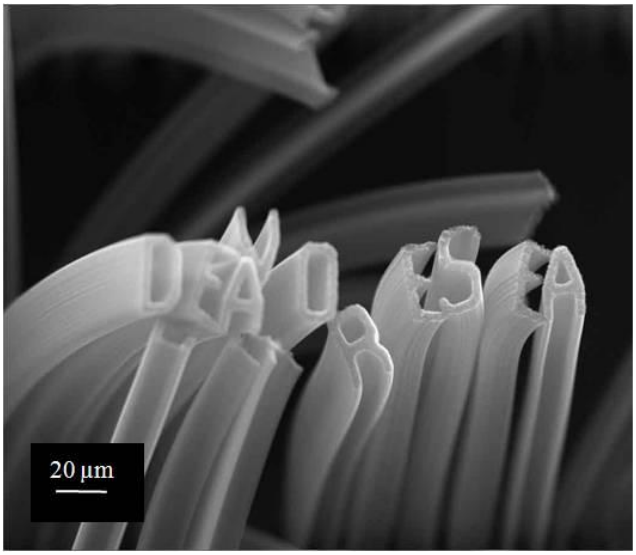

Figure 4.15. SEM images of high aspect ratio, positive MWCNT letter patterns. The pillars are jumbled as the high aspect ratio towers are not self supporting.

4.3.2 MWCNT / Epoxy composited electrodes derived from metal salt catalysts

4.3.2.1 Characterization of MWCNT forests derived from metal salt catalysts

MWCNT forests were grown from catalyst films prepared by spin coating mixtures of $Fe(NO_3)_3$, $Al(NO_3)_3$ and PVP40 dissolved in water onto PPF wafers. The salt combination used in this work is inspired by the earlier work of Parthangal *et al.* [15] who employed the same salts as were used here to grow aligned MWCNT forests on Si, Au, Ag, W and Al. Figure 4.16 shows low (a) and high (b) magnification images of a uniform forest of MWCNTs grown from a catalyst film prepared from a solution of 1 M $Fe(NO_3)_3$ and 1 M $Al(NO_3)_3$ and 1 mg mL^{-1} PVP40 spin coated onto a PPF wafer at 4000 rpm. When more concentrated catalyst solutions were used and / or lower spin speeds, the MWCNTs lifted off the substrate.

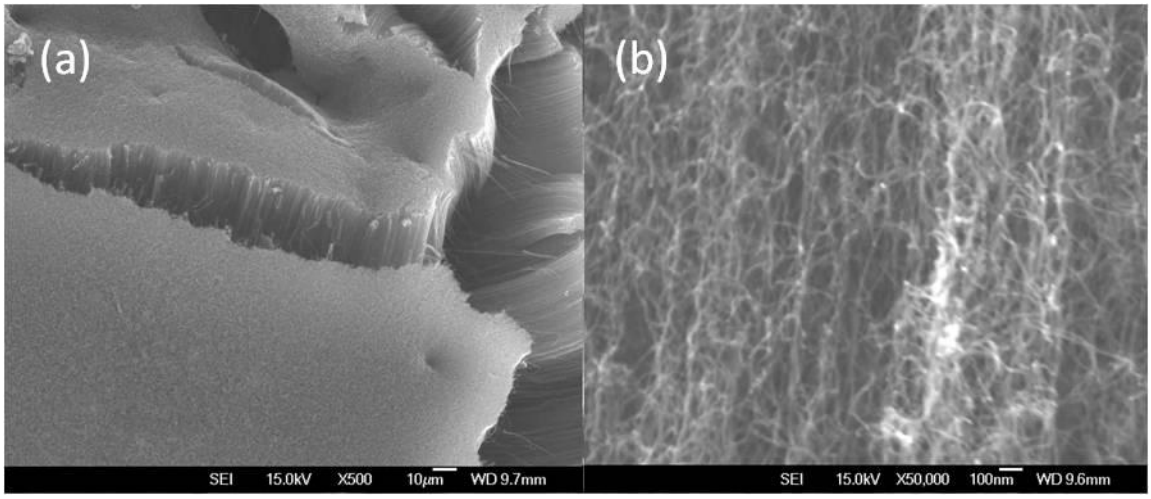

Figure 4.16. SEM images of a forest of a MWCNTs grown from a catalyst film of 1 mM $Fe(NO_3)_3$ and $Al(NO_3)_3$ with 1 mg mL^{-1} PVP40 spin coated onto PPF at 4000 rpm at a magnification of (a) × 500 and (b) × 50,000

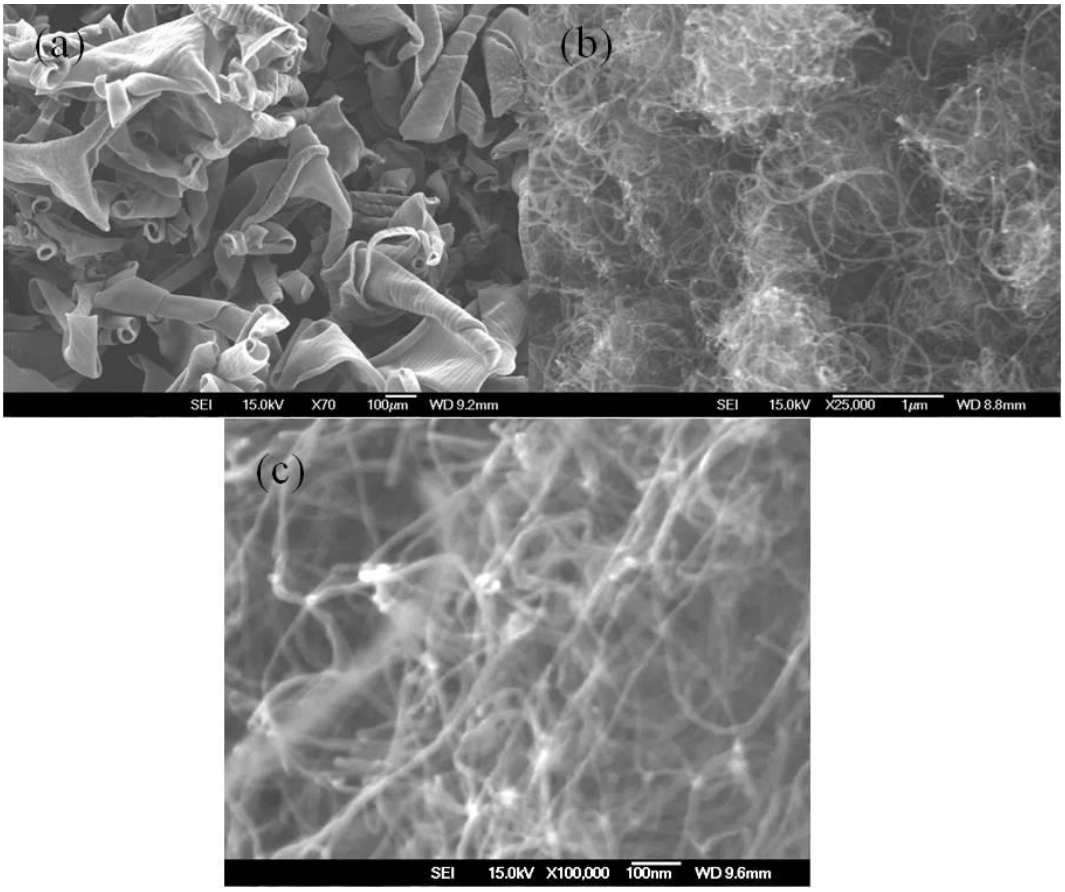

Figure 4.17. SEM images of forests of intertwined MWCNTs grown from a catalyst film of 2 M $Fe(NO_3)_3$ and $Al(NO_3)_3$ with 1 mg mL^{-1} PVP40 spin coated at 3000 rpm at a magnification of (a) × 70, (b) × 25,000 and (c) × 100,000.

Figure 4.17 shows forests of highly intertwined MWCNTs grown using a catalyst solution of 2 M $Fe(NO_3)_3$ and 2 M $Al(NO_3)_3$ and 1 mg mL^{-1} PVP40 spin coated at 3000 rpm. Clearly the catalyst film was too thick for vertical alignment of the tubes and excessive growth has caused the film to lift off the PPF substrate and curl. The higher magnification images (Figure 4.17 (b) and (c)) shows the CNTs in the curls are not aligned. Figure 4.17 (c) shows that the CNTs have diameters of approximately 10 – 30 nm and there are clearly catalyst particles at the tips of some CNTs. However, the distinction between tip and base growth for these MWCNT forests can not be made because the CNTs are no longer in contact with the substrate.

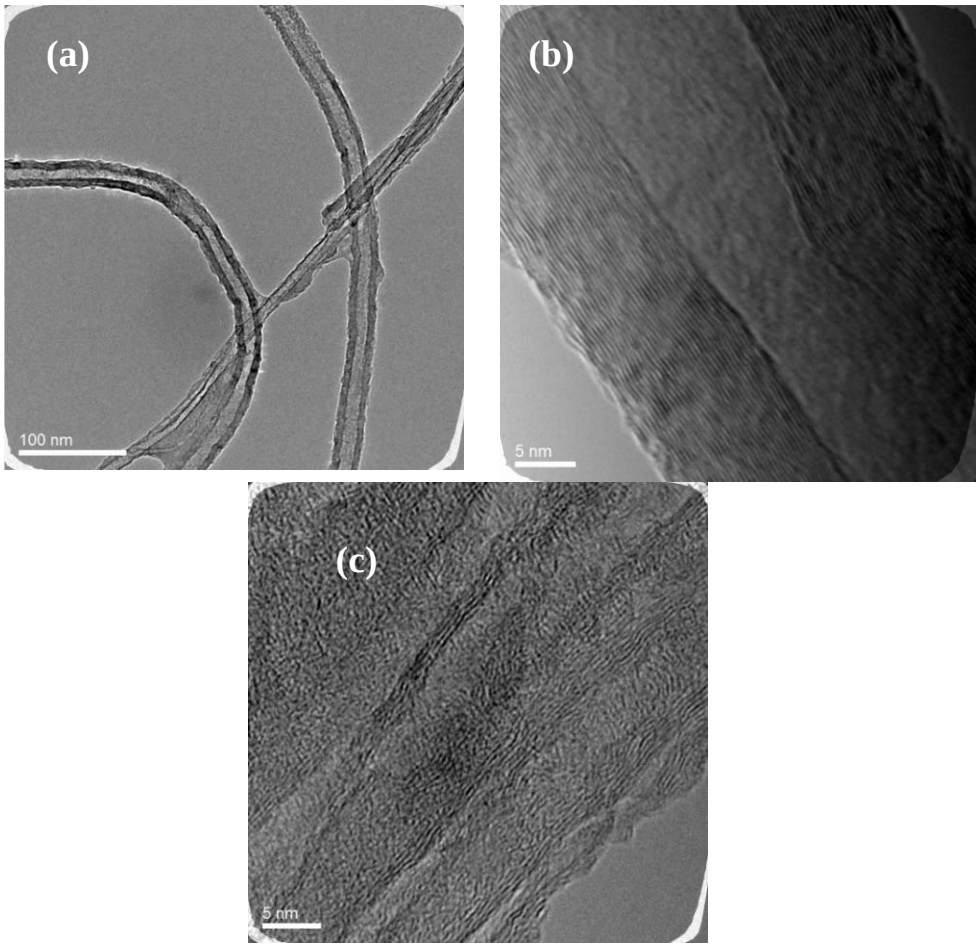

Figure 4.18. TEM images of large (a) and (b) and small (c) MWCNTs grown by CVD from a film of 1 M $Fe(NO_3)_3$ and 1 M $Al(NO_3)_3$ spin coated onto a silicon wafer.

TEM images of a sample of MWCNTs grown from a 1 M $Fe(NO_3)_3$ and 1 M $Al(NO_3)_3$ solution catalyst film are shown in Figure 4.18. Figure 4.18 (a) shows long tubes with a hollow core. Figure 4.18 (b) is a high magnification image of a section of (a) and clearly shows shells with 0.34 nm spacing consistent with the graphene layer spacing of MWCNTs. The MWCNT depicted in (b) is the largest observed in this work. It has 32 walls and is 40 nm in diameter. A number of MWCNTs are shown in Figure 4.18 (c) which are approximately 6 - 8 nm in diameter with between 4 and 5 walls and were the smallest observed in this work. Due to time constraints only a few TEM images were obtained and no statistical analysis of the tube sizes could be undertaken. Clearly however the aqueous salt catalyst produces MWCNTs over a wide range of diameters and wall counts.

4.3.2.2 Electrochemical characterization of MWCNT epoxy composite electrodes derived from metal salt catalysts

Two forests of MWCNTs grown from catalyst films of 1 M $Fe(NO_3)_3$, 1 M $Al(NO_3)_3$ and 1 mg mL^{-1} PVP40 in water were cast into epoxy block electrodes by the same procedure as described for MWCNT forests derived from evaporated metal catalyst films. CVs of the electrodes in 1 mM $Fe(CN)_6^{3-}$, pH 7 PBS after O_2 plasma are shown in

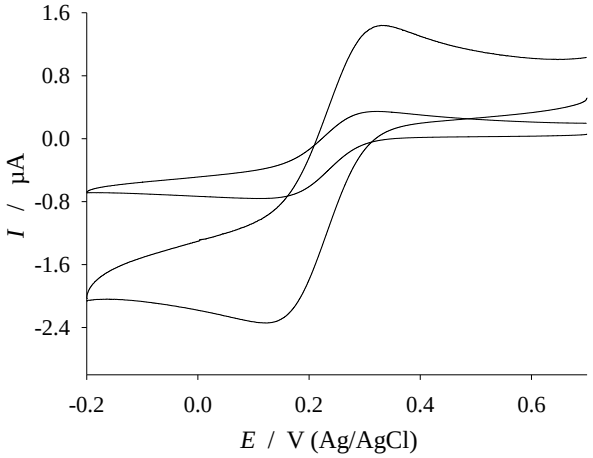

Figure 4.19. CVs recorded using two plasma activated MWCNT / epoxy electrodes derived from a 1 M $Fe(NO_3)_3$, 1 M $Al(NO_3)_3$ and 1 mg mL^{-1} PVP40 catalyst films in 1 mM $Fe(CN)_6^{3-}$, pH 7 PBS, scan rate = 100 mV s^{-1}.

Figure 4.19. Both of the electrodes exhibit a somewhat sigmoidal CV shape and peak currents that are much lower than the CVs obtained using the electrodes fabricated from evaporated metal catalyst films (Figure 4.6 c(ii), all electrodes had the same geometric area). Clearly both the electrodes fabricated from metal salt catalysts show a mixture of linear and radial diffusion of redox molecules to the surface. This is likely to arise from non-uniform activity across the electrode surface. MWCNT forests grown from salt catalyst films are less uniform in height and adhesion to the substrate is poorer than those derived from evaporated metal catalysts. Non-uniform activity across the electrode surface could arise from taller areas of the MWCNTs being exposed by polishing and plasma treatment while shorter areas remain covered, and / or from areas of the MWCNT forest lifting off the substrate and losing electrical contact. The large difference in the peak currents between the two aqueous catalyst derived electrodes indicates that it may be difficult to fabricate reproducible electrodes by this method.

The aqueous salt derived electrodes also exhibited catalytic oxidation of NADH. Figure 4.20 shows a CV of the low peak current electrode from Figure 4.19 after regeneration by polishing (dashed) and plasma activation (solid) in 1 mM NADH, pH 7 PBS. The very low background currents exhibited by these electrodes leads to very high signal to noise ratios for electrochemical detection of NADH and therefore encapsulated microelectrode arrays of this type are promising as sensor substrates.

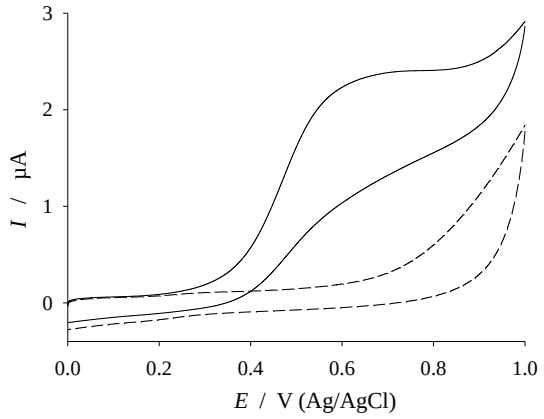

Figure 4.20. CVs recorded using a MWCNT / epoxy electrode derived from a 1 M $Fe(NO_3)_3$, 1 M $Al(NO_3)_3$ and 1 mg mL^{-1} PVP40 catalyst film in 1 mM NADH, pH 7 PBS, scan rate = 100 mV s^{-1} before (dashed) and after (solid) O_2 plasma activation.

4.3.2.3 Patterning of aqueous salt catalysts

To extend the utility of the aqueous salt catalyst system a method of patterning aqueous salt catalyst films was developed. Patterned catalyst films were initially prepared from a 1 mM solution of $Fe(NO_3)_3$ and $Al(NO_3)_3$ (no PVP40), drop coated onto a photo resist-masked silicon wafer and dried with a nitrogen gun. The key step to the patterning method is the subsequent removal of the photoresist without disruption of the catalyst film in contact with the substrate. This was achieved using a high flow of acetone while the sample was spinning at 4000 rpm. Acetone dissolves the photoresist and washes away any catalyst film that is on the photoresist but the insoluble metal salt in gaps in the photoresist film remains attached to the substrate. Figure 4.21 (A) shows 50 µm diameter circles of the dried catalyst which show occasional cracking of the dried films. Larger catalyst features (Figure 4.21 (B)) exhibited extensive cracking and a tendency to lift off the substrate. This is presumed to be caused by shrinkage of the catalyst patterns during drying. MWCNTs were grown on the catalyst patterns using the same CVD conditions as those used for evaporated metal catalyst films. SEM images of some of the resulting MWCNT patterns are shown in Figure 4.22. The features grown from intact catalyst pads are 30 - 50 µm high, much shorter than CNTs grown for the same length of time using Al_2O_3 / Fe catalyst films (1.5 - 2 mm). The patterns are also clearly susceptible to variations, such as cracking or thickness, across the catalyst pads. Figure 4.22 (A) shows MWCNT patterns that have grown at various angles due to variation in the thickness of the catalyst spots.

Patterned CNT arrays were prepared by Ding *et al.* [34] from microcontact printed ethonolic solutions of Fe_2O_3. Golovko *et al.* [35] and Bennett *et al.* [36] both describe patterning of carbon nanofibres or CNTs by microcontact printing of metal containing colloids. In earlier work Kind *et al.* [37] describe patterning of CNTs by CVD growth from microcontact printed aqueous solutions of $Fe(NO_3)_3$, $Ni(NO_3)_2$ and $Co(NO_3)_2$. During the course of the present work a similar method for the patterning and growth of SWCNTs from aqueous salt solutions was developed by Jeong *et al.*[38] In that work aqueous solutions of 0.05 mM $Fe(NO_3)_3$, 0.015 mM $MoO_2(acac)_2$ and 0.1 wt % PVP40 in water with a quantity of alumina nanoparticles were successfully patterned by a similar

photolithographic process to that developed here. CVD of the resulting patterned catalyst resulted in sparse non aligned SWCNTs which were integrated into a prototype SWCNT – field effect transistor.

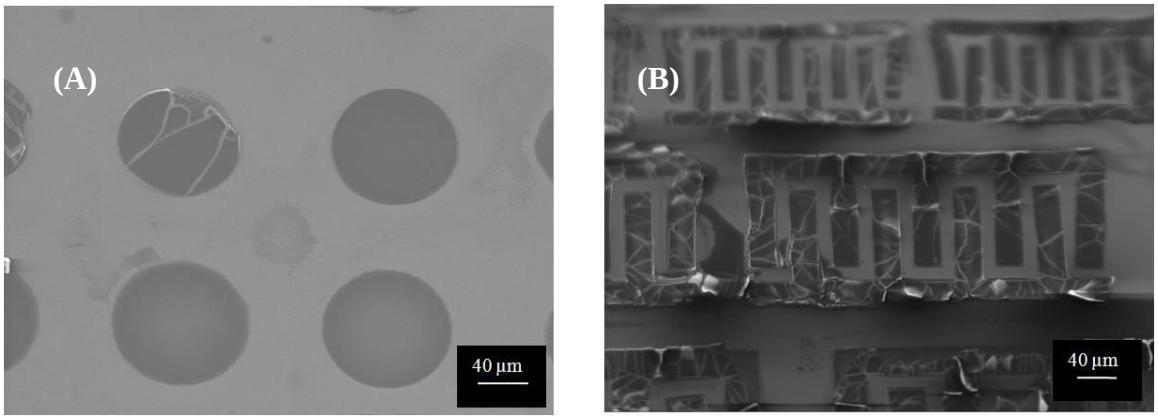

Figure 4.21. SEM images of patterned catalyst pads showing (A) smaller features where catalyst features remained largely intact and (B) patterns with a dimension longer than 50 µm where extensive cracking and peeling of the catalyst films has occurred.

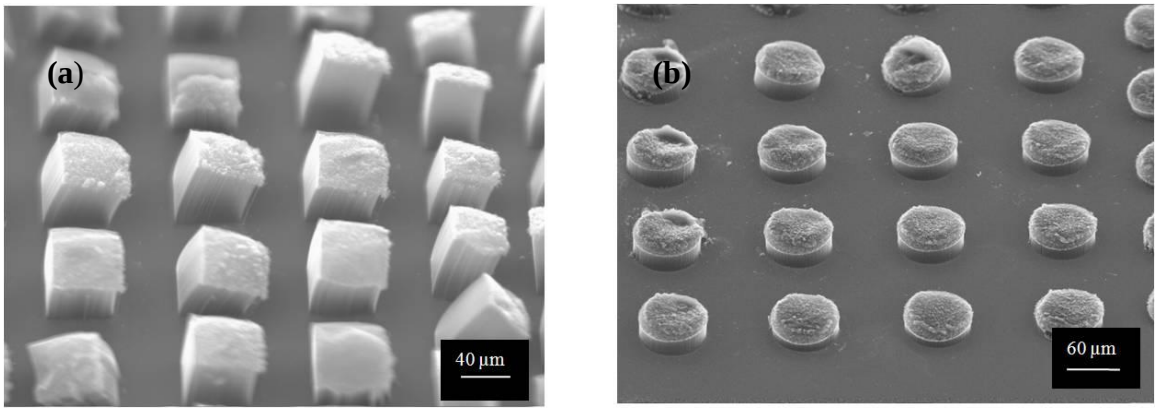

Figure 4.22. SEM images of MWCNT towers grown from well-formed catalyst pads. (a) shows leaning square towers resulting from non-uniform thickness of the catalyst pads and (b) straight round towers grown from a sample where catalyst pads had uniform thickness.

To improve the reliability of the method and increase the feature sizes achievable a small amount of PVP40 was added to the catalyst solution to improve the spin properties and prevent cracking of the catalyst films during drying. Figure 4.23 shows SEM images

of patterned MWCNTs with feature sizes larger than 50 µm grown from a solution of 5 mg mL^{-1} PVP40, 1 M $Fe(NO_3)_3$ and 1 M $Al(NO_3)_3$ spin coated at 3000 rpm for 30 s and dried at 100 ^oC on a hotplate for 1 min. The patterns show no evidence of cracking or delamination but the squares in Figure 4.23 (B) show a catalyst skin that has remained attached to some of the features. The catalyst skin results when the photoresist mask is dissolved in acetone but not all of the catalyst film covering the photoresist is removed. When this high PVP40 concentrations was used catalyst skinning between the features was worst on the smallest features (Figure 4.24).

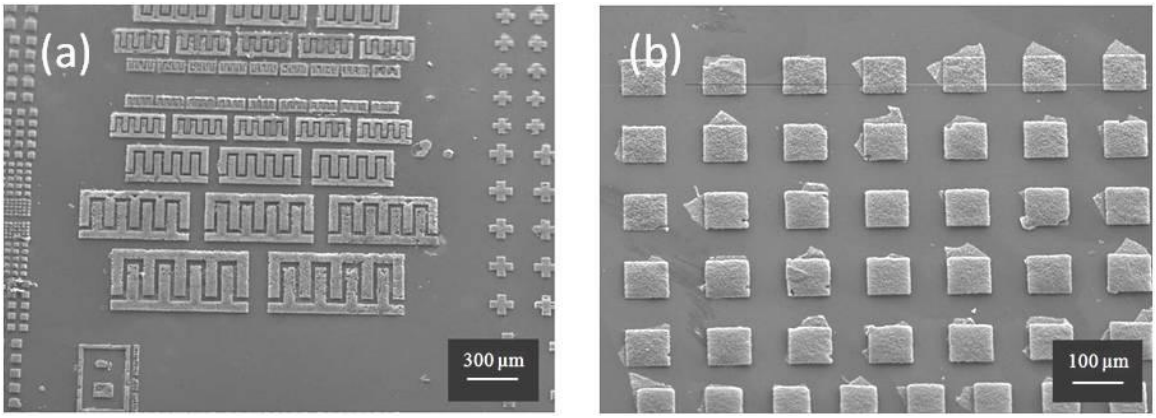

Figure 4.23. SEM images of >50 µm wide MWCNT features patterned with the inclusion of 5 mg mL^{-1} of PVP40 in the 1 M $Fe(NO_3)_3$ and $Al(NO_3)_3$ catalyst solution spin coated at 3000 rpm.

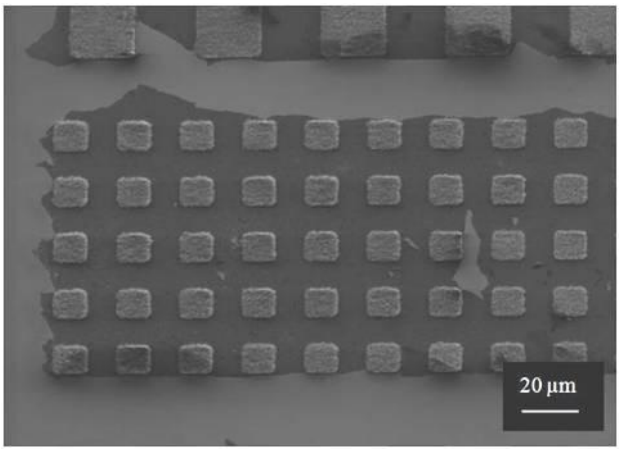

Figure 4.24. SEM images of 10 µm wide MWCNT features showing retained catalyst skin between features using 5 mg mL^{-1} PVP40, 1 M $Fe(NO_3)_3$ and $Al(NO_3)_3$ catalyst solution which was coated at 3000 rpm.

Lower concentrations of PVP40 improved the problem of skin formation on small features but lowered the maximum feature size achievable without cracking of the catalyst film. Figure 4.25 shows clearly resolved sub 10 µm wide MWCNT lettering grown to a height of 10 µm with no evidence of catalyst skin formation between the letters. The catalyst solution contained 1 mg mL^{-1} PVP40, 1 M $Fe(NO_3)_3$ and 1 M $Al(NO_3)_3$ and was spin coated at 3000 rpm.

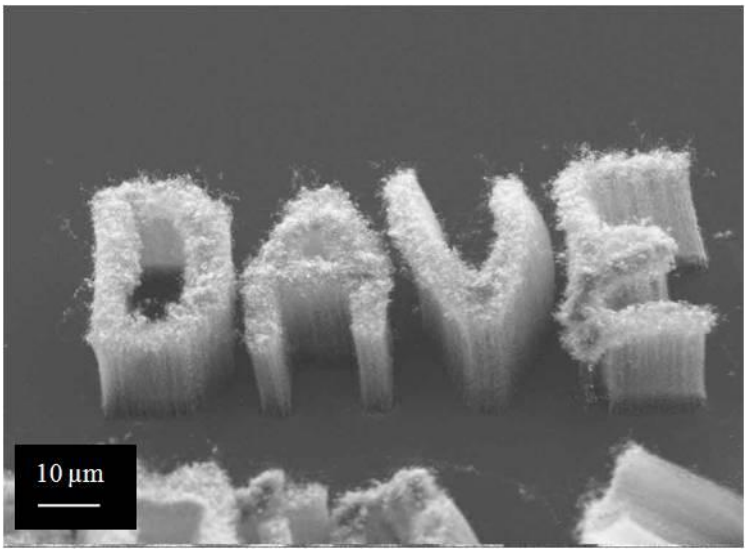

Figure 4.25. SEM images of sub 10 µm wide lettering patterned using a 1 mg mL^{-1} PVP40, 1 M $Fe(NO_3)_3$ and $Al(NO_3)_3$ catalyst solution, spin coated at 3000 rpm.

Overall, the addition of PVP40 to the catalyst solutions improved pattern fidelity and increased the range of feature sizes over which the catalyst system could be used. The problem of skin formation dictates that a specific catalyst composition is only optimal for a limited feature size range. In samples where a limited range of feature sizes are present however, a suitable catalyst composition can be formulated.

4.4 Conclusion

Robust MWCNT / epoxy composite electrodes were fabricated from vertically aligned MWCNT forests derived from either evaporated metal or aqueous salt catalysts. The simple procedure for fabricating the electrode mold using standard laboratory equipment means that the method can be easily replicated in other research facilities. The flexible flaps incorporated into the mold design discussed here were necessary because of the rigidity of the polysiloxane used. Softer, more flexible polysiloxanes are available and may have been a better choice for this application.

Electrodes activated with O_2 plasma and derived from evaporated metal catalysts exhibited highly reproducible electrochemical performance between electrodes. Polished electrodes derived from metal salt catalyst occasionally gave good electrochemical performance indicating that polishing may be a viable activation strategy provided a high degree of process control is used. O_2 plasma activated electrodes derived from aqueous salt catalysts exhibited fast electron transfer for the $Fe(CN)_6^{3-/4-}$ couple but inconsistent peak currents between electrodes. This is assumed to be a result of non-uniform electrochemical activity across the electrode surfaces resulting from different active electrode areas between samples. Importantly, all of the MWCNT / epoxy electrodes tested could be regenerated without any deterioration in their electrochemical performance over at least 80 regeneration cycles. The MWCNT / epoxy electrodes are an effective and efficient tool for the study of electrochemical processes at carbon nanotube electrodes.

Of a range of alternative activation strategies examined, only oxidation with piranha improved the performance of the electrode with respect to $Fe(CN)_6^{3-/4-}$ electrochemistry. O_2 Plasma and piranha are both general etching strategies that remove both epoxy and MWCNT material. This is the likely reason for the success of these activation methods over the others tested. As an illustration of the potential use of the MWCNT / epoxy electrodes a preliminary electrochemical study of NADH oxidation

after activation using O_2 plasma was undertaken. All of the electrodes fabricated exhibited a 300 to 400 mV reduction in the overpotential required to oxidize NADH. Piranha activated electrodes were not catalytically active for oxidation of NADH. It is likely that O_2 plasma generates specific functionalities on the MWCNTs that are able to mediated charge transfer from NADH. In future work it would be interesting to vary the conditions of the O_2 plasma treatment in an attempt to optimize the response for NADH at MWCNT / epoxy composite electrodes.

CV, SEM and AFM investigation revealed that activation of the electrodes by plasma and piranha etching exposed greater numbers of MWCNTs at the electrode surface. A side by side comparison revealed a faster O_2 plasma etch rate of epoxy resin than the MWCNT / epoxy composite explaining the improved electrochemistry of the activated surfaces. For MWCNT / epoxy electrodes derived from evaporated metal catalyst the activated electrodes had exposed areas of MWCNTs sufficiently close together that the assemblies exhibited linear diffusion of redox molecules during CV. CVs recorded using electrodes derived from aqueous salt catalysts showed combined linear and radial diffusion behavior indicating a wider spacing of the electroactive MWCNT regions on the electrode.

Patterning of evaporated metal catalyst films by commonly used methods was demonstrated and a new method for patterning vertically aligned MWCNTs grown from aqueous metal salt catalyst films was developed. The simplicity of the new patterning method and its compatibility with common microfabrication techniques makes it a promising method for producing high throughput cost effective MWCNT arrays.

4.5 References

1. Joseyacaman, M.; Mikiyoshida, M.; Rendon, L.; Santiesteban, J. G., Catalytic Growth of Carbon Microtubules with Fullerene Structure. *Appl. Phys. Lett.* **1993,** 62, (2), 202-204.
2. Sohn, J. I.; Lee, S., Micropatterned vertically aligned carbon-nanotube growth on a Si surface or inside trenches. *App. Phys. A-Mater.* **2002,** 74, (2), 287-290.

3. Hata, K.; Futaba, D. N.; Mizuno, K.; Namai, T.; Yumura, M.; Iijima, S., Water-assisted highly efficient synthesis of impurity-free single-waited carbon nanotubes. *Science* **2004,** 306, (5700), 1362-1364.
4. Wei, Y. Y.; Eres, G.; Merkulov, V. I.; Lowndes, D. H., Effect of catalyst film thickness on carbon nanotube growth by selective area chemical vapor deposition. *Appl. Phys. Lett.* **2001,** 78, (10), 1394-1396.
5. Zhu, L. B.; Xu, J. W.; Xiu, Y. H.; Sun, Y. Y.; Hess, D. W.; Wong, C. P., Growth and electrical characterization of high-aspect-ratio carbon nanotube arrays. *Carbon* **2006,** 44, (2), 253-258.
6. Helveg, S.; Lopez-Cartes, C.; Sehested, J.; Hansen, P. L.; Clausen, B. S.; Rostrup-Nielsen, J. R.; Abild-Pedersen, F.; Norskov, J. K., Atomic-scale imaging of carbon nanofibre growth. *Nature* **2004,** 427, (6973), 426-429.
7. Amama, P. B.; Pint, C. L.; McJilton, L.; Kim, S. M.; Stach, E. A.; Murray, P. T.; Hauge, R. H.; Maruyama, B., Role of Water in Super Growth of Single-Walled Carbon Nanotube Carpets. *Nano Lett.* **2009,** 9, (1), 44-49.
8. Amama, P. B.; Pint, C. L.; Kim, S. M.; McJilton, L.; Eyink, K. G.; Stach, E. A.; Hauge, R. H.; Maruyama, B., Influence of Alumina Type on the Evolution and Activity of Alumina-Supported Fe Catalysts in Single-Walled Carbon Nanotube Carpet Growth. *Acs Nano* **2010,** 4, (2), 895-904.
9. Kim, S. M.; Pint, C. L.; Amama, P. B.; Zakharov, D. N.; Hauge, R. H.; Maruyama, B.; Stach, E. A., Evolution in Catalyst Morphology Leads to Carbon Nanotube Growth Termination. *J. Phys. Chem. Lett.* **2010,** 1, (6), 918-922.
10. Gohier, A.; Ewels, C. P.; Minea, T. M.; Djouadi, M. A., Carbon nanotube growth mechanism switches from tip- to base-growth with decreasing catalyst particle size. *Carbon* **2008,** 46, (10), 1331-1338.
11. Cui, X. W.; Wei, W. F.; Chen, W. X., Lengthening and thickening of multi-walled carbon nanotube arrays grown by chemical vapor deposition in the presence and absence of water. *Carbon* **2010,** 48, (10), 2782-2791.
12. Wang, B. A.; Liu, X. Y.; Liu, H. M.; Wu, D. X.; Wang, H. P.; Jiang, J. M.; Wang, X. B.; Hu, P. A.; Liu, Y. Q.; Zhu, D. B., Controllable preparation of patterns of aligned carbon nanotubes on metals and metal-coated silicon substrates. *J. Mater. Chem.* **2003,** 13, (5), 1124-1126.
13. Hiraoka, T.; Yamada, T.; Hata, K.; Futaba, D. N.; Kurachi, H.; Uemura, S.; Yumura, M.; Iijima, S., Synthesis of single- and double-walled carbon nanotube forests on conducting metal foils. *J. Am. Chem. Soc.* **2006,** 128, (41), 13338-13339.
14. Talapatra, S.; Kar, S.; Pal, S. K.; Vajtai, R.; Ci, L.; Victor, P.; Shaijumon, M. M.; Kaur, S.; Nalamasu, O.; Ajayan, P. M., Direct growth of aligned carbon nanotubes on bulk metals. *Nature Nanotech.* **2006,** 1, (2), 112-116.
15. Parthangal, P. M.; Cavicchi, R. E.; Zachariah, M. R., A generic process of growing aligned carbon nanotube arrays on metals and metal alloys. *Nanotech.* **2007,** 18, (18).
16. Wieczorek-Ciurowa, K.; Kozak, A. J., The thermal decomposition of Fe(NO3)(3)center dot 9H(2)O. *J. Therm. Anal. Calorim.* **1999,** 58, (3), 647-651.
17. Lin, H. Y.; Chen, Y. W.; Li, C. P., The mechanism of reduction of iron oxide by hydrogen. *Thermochim. Acta* **2003,** 400, (1-2), 61-67.

18. Liu, X. M.; Baronian, K. H. R.; Downard, A. J., Direct growth of vertically aligned carbon nanotubes on a planar carbon substrate by thermal chemical vapour deposition. *Carbon* **2009,** 47, (2), 500-506.
19. Liu, X.; Baronian, K. H. R.; Downard, A. J., Patterned Arrays of Vertically Aligned Carbon Nanotube Microelectrodes on Carbon Films Prepared by Thermal Chemical Vapor Deposition. *Anal. Chem.* **2008,** 80, (22), 8835-8839.
20. Wardle, B. L.; Saito, D. S.; Garcia, E. J.; Hart, A. J.; de Villoria, R. G.; Verploegen, E. A., Fabrication and characterization of ultrahigh-volume-fraction aligned carbon nanotube-polymer composites. *Adv. Mater.* **2008,** 20, (14), 2707-+.
21. Yun, Y. H.; Shanov, V.; Schulz, M. J.; Dong, Z. Y.; Jazieh, A.; Heineman, W. R.; Halsall, H. B.; Wong, D. K. Y.; Bange, A.; Tu, Y.; Subramaniam, S., High sensitivity carbon nanotube tower electrodes. *Sensor. Actuat. B-Chem.* **2006,** 120, (1), 298-304.
22. Li, J.; Ng, H. T.; Cassell, A.; Fan, W.; Chen, H.; Ye, Q.; Koehne, J.; Han, J.; Meyyappan, M., Carbon nanotube nanoelectrode array for ultrasensitive DNA detection. *Nano Lett.* **2003,** 3, (5), 597-602.
23. Esplandiu, M. J.; Pacios, M.; Cyganek, L.; Bartroli, J.; del Valle, M., Enhancing the electrochemical response of myoglobin with carbon nanotube electrodes. *Nanotech.* **2009,** 20, (35).
24. Chen, G.; Zhang, L. Y.; Wang, J., Miniaturized capillary electrophoresis system with a carbon nanotube microelectrode for rapid separation and detection of thiols. *Talanta* **2004,** 64, (4), 1018-1023.
25. Patole, S. P.; Yu, S. M.; Shin, D. W.; Kim, H. J.; Han, I. T.; Kwon, K. W.; Yoo, J. B., The effect of barrier layer-mediated catalytic deactivation in vertically aligned carbon nanotube growth. *J. Phys. D: Appl. Phys.* **2010,** 43, (9).
26. Yu, M.; Funke, H. H.; Falconer, J. L.; Noble, R. D., High Density, Vertically-Aligned Carbon Nanotube Membranes. *Nano Lett.* **2009,** 9, (1), 225-229.
27. Banks, C. E.; Davies, T. J.; Wildgoose, G. G.; Compton, R. G., Electrocatalysis at graphite and carbon nanotube modified electrodes: edge-plane sites and tube ends are the reactive sites. *Chem. Commun.* **2005**, (7), 829-841.
28. Chen, P. H.; McCreery, R. L., Control of electron transfer kinetics at glassy carbon electrodes by specific surface modification. *Anal. Chem.* **1996,** 68, (22), 3958-3965.
29. Zschoerper, N. P.; Katzenmaier, V.; Vohrer, U.; Haupt, M.; Oehr, C.; Hirth, T., Analytical investigation of the composition of plasma-induced functional groups on carbon nanotube sheets. *Carbon* **2009,** 47, (9), 2174-2185.
30. Wooten, M.; Gorski, W., Facilitation of NADH Electro-oxidation at Treated Carbon Nanotubes. *Anal. Chem.* **2010,** 82, (4), 1299-1304.
31. Hebert, N. E.; Snyder, B.; McCreery, R. L.; Kuhr, W. G.; Brazill, S. A., Performance of pyrolyzed photoresist carbon films in a microchip capillary electrophoresis device with sinusoidal voltammetric detection. *Anal. Chem.* **2003,** 75, (16), 4265-4271.
32. Datsyuk, V.; Kalyva, M.; Papagelis, K.; Parthenios, J.; Tasis, D.; Siokou, A.; Kallitsis, I.; Galiotis, C., Chemical oxidation of multiwalled carbon nanotubes. *Carbon* **2008,** 46, (6), 833-840.
33. Gorton, L., Chemically Modified Electrodes for the Electrocatalytic Oxidation of Nicotinamide Coenzymes. *J. Chem. Soc., Faraday Trans.* **1986,** 82, 1245-1258.

34. Ding, L.; Zhou, W. W.; Chu, H. B.; Jin, Z.; Zhang, Y.; Li, Y., Direct preparation and patterning of iron oxide nanoparticles via microcontact printing on silicon wafers for the growth of single-walled carbon nanotubes. *Chem. Mater.* **2006,** 18, (17), 4109-4114.
35. Golovko, V. B.; Cantoro, M.; Hofmann, S.; Kleinsorge, B.; Geng, J.; Jefferson, D.; Ferrari, A. C.; Robertson, J.; Johnson, B. F. G., Selective growth of vertically aligned carbon nanofibres in sub-micron patterns and Raman mapping of produced arrays. *Diamond Relat. Mater.* **2006,** 15, (4-8), 1023-1028.
36. Bennett, R. D.; Hart, A. J.; Miller, A. C.; Hammond, P. T.; Irvine, D. J.; Cohen, R. E., Creating patterned carbon nanotube catalysts through the microcontact printing of block copolymer micellar thin films. *Langmuir* **2006,** 22, (20), 8273-8276.
37. Kind, H.; Bonard, J. M.; Emmenegger, C.; Nilsson, L. O.; Hernadi, K.; Maillard-Schaller, E.; Schlapbach, L.; Forro, L.; Kern, K., Patterned films of nanotubes using microcontact printing of catalysts. *Adv. Mater.* **1999,** 11, (15), 1285-+.
38. Jeong, S. Y.; Jeon, S. H.; Han, G. H.; An, K. H.; Bae, D. J.; Lim, S. C.; Hwang, H. R.; Han, C. S.; Yun, M.; Lee, Y. H., Efficient synthesis of individual single-walled carbon nanotube by water-based catalyst with poly(vinylpyrrolidone). *J. Nanosci. Nanotechnol.* **2008,** 8, (1), 329-334.

Chapter 5. Modification of electrodes with mediator molecules

5.1 Introduction

Mediation of charge transport from bio-molecules to solid electrodes has been demonstrated many times either when the mediator molecules are in solution or when they are fixed to the electrode surface. Mediation strategies are reviewed in the Introduction Chapter, Section 1.1.2.

This chapter describes the coupling of a range of mediator molecules to PPF and to the CNT electrodes described in Chapters 3 and 4, using existing and new coupling strategies. The first of the strategies described is the coupling of amine terminating inorganic mediator molecules to carboxylic acid terminating films via the formation of amide bonds. The methods used in the work described here are taken directly from the work of Boland *et al.* [1, 2] who show that carboxylic acid terminating films can be coupled to amine terminating osmium complexes via amide bonds using traditional carbodiimide coupling agents. In that work Boland *et al.* seek to find stable and controllable coupling strategies, building on their work coupling osmium complexes within polyvinylimidazole films to form osmium-based redox polymers.[3, 4] Boland, Kavanagh, Jenkins and Leech have previously shown that osmium-based redox polymers can efficiently mediate charge transfer between a *Melanocarpus albomyces* laccase enzyme and the GC cathode of a glucose / O_2 biofuel cell.[4] The same authors show that subtle manipulation of the reduction potential and structure of the osmium complexes contained in the redox polymers can be used to optimize charge transfer from a range of laccase enzymes with different copper reduction potentials in their active sites.[3] The same osmium-based redox polymers have been previously shown by Vostiar *et al.* to increase direct electron transfer from the bacterium *Gluconobacter oxydans* to a gold electrode. The authors

speculate that the pendant osmium complexes are able to interact with membrane-bound pyrroloquinoline quinone (PQQ) which has been shown to be capable of reducing small inorganic mediator molecules in solution.[5, 6]

A recent review of electron transfer from *Gluconobacter sp,* [6] specifically focusing on the role of dehydrogenase enzymes, cites the work of Babkina *et al.* who successfully employed surface adsorbed ferrocene and 1,4-benzoquinone derivatives to mediate electron transfer from *Gluconobacter oxydans.*[7] In that work the authors show that 1,2-napthoquinone has no ability to mediate charge transfer from *Gluconobacter oxydans* and speculate that the 1,4-dione structure found in ubiquinone (the primary natural electron acceptor from PQQ-glucose dehydrogenase of *Gluconobacter oxydans*) is essential for efficient electron transfer to the mediator. The structures of the quinones used in that work and the structure of ubiquinone are shown in Figure 5.1.

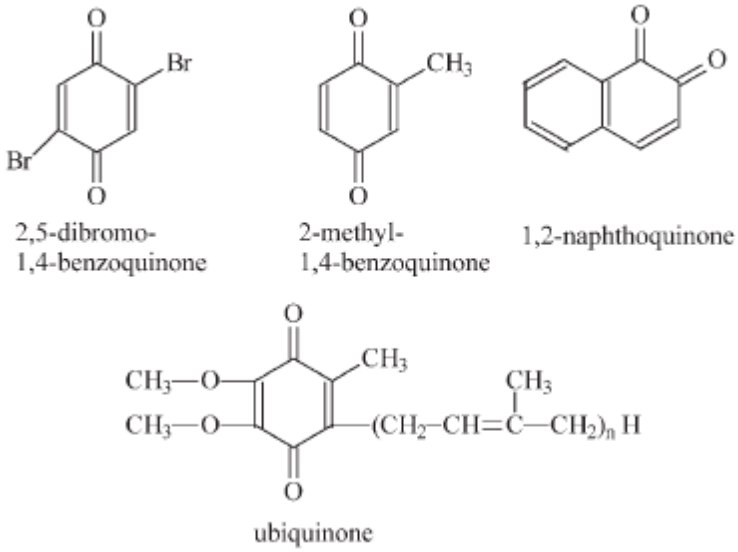

Figure 5.1. Structures of ubiquinone and the quinones employed as surface confined charge transfer mediators from *Gluconobacter oxydans* used in reference 7.

Ubiquinone analogues have also been shown to participate in a variety of redox reactions in the mitochondrial membranes of eukaryotic cells. This is best illustrated by

the body of work of Murphy and co-workers [8-11] who have developed ubiquinone analogues as mitochondrial membrane antioxidant compounds. Ubiqinones are known to be pivotal in the mitochondrial electron transport chain, in particular in transferring charge from NADH and succinate dehydrogenases to cytochrome c. Protons delivered during the redox transformation between ubiquinone and ubiquinol provide the proton gradient required to drive ATP synthase. The electrons liberated during oxidation of ubiquinol by cytochrome c are ultimately passed to O_2 bound in the active site of cytochrome c oxidase forming two molecules of H_2O (Figure 5.2).

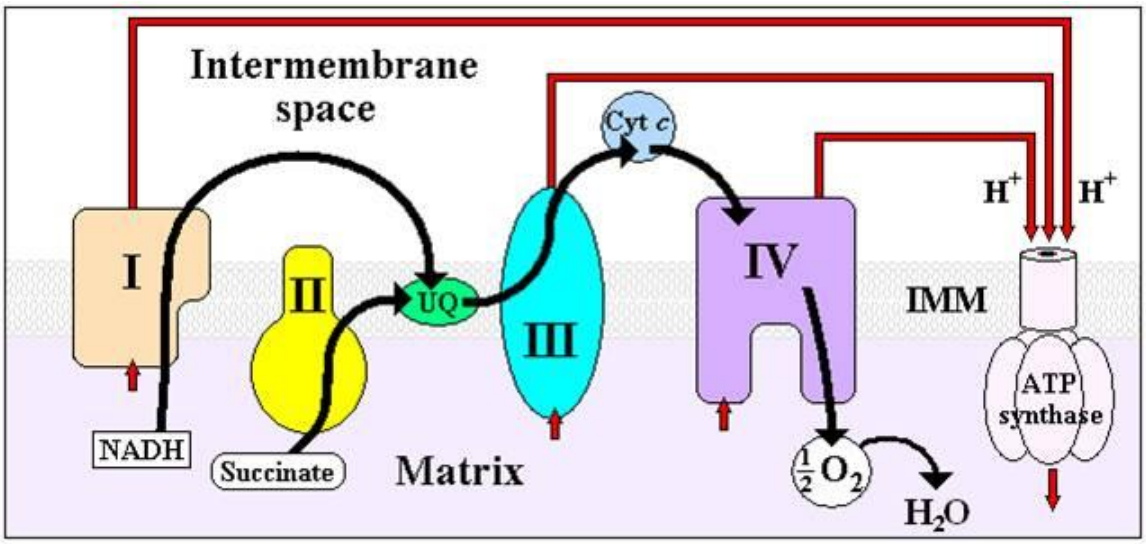

Figure 5.2. Cartoon depiction of the mitochondrial electron transport chain. (I) NADH dehydrogenase, (II) succinate dehydrogenase, (UQ) ubiquinone, (III) cytochrome bc_1 complex, (IV) cytochrome c oxidase. Movement of protons is shown by the red arrows and movement of electrons by the black arrows.

Murphy and co-workers synthesized molecules using the head group of ubiquinone with a simple alkyl chain tail, terminating in a cationic triphenyl phosphonium. They refer to this molecule throughout their work as 'MitoQ' (Figure 5.3). The cationic MitoQ molecule is electrostatically attracted to anionic mitochondria becoming sequestered in the mitochondrial membrane.[9] Murphy and co-workers showed that $MitoQH_2$ (the reduced form of MitoQ) was gradually oxidized to MitoQ when incubated with beef heart mitochondrial membranes presumably through the action of cytochrome bc_1 complex (Figure 5.2, complex III). Addition of the complex III inhibitor myxothiazol halted the

oxidation process. When succinate was added to the MitoQ / beef heart mitochondrial membrane mixture the reverse trend was observed (MitoQ was gradually reduced to $MitoQH_2$) presumably through the action of succinate dehydrogenase (Figure 5.2, complex II). Addition of the complex II inhibitor, malonate, also halted the reduction

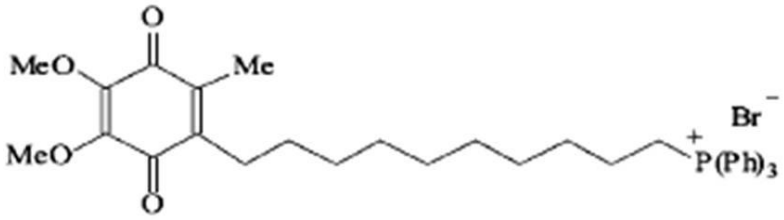

Figure 5.3. Structure of 'MitoQ' developed by Murphy and co-workers as a mitochondrial membrane antioxidant.

process. In more recent work James *et al.* show that MitoQ is a relatively poor substrate for complex I and III but a very good substrate for complex II [11] explaining the overall trend towards reduction of MitoQ in the mitochondrial membrane when succinate is present. MitoQ is now in phase II clinical trials as a treatment for a number of conditions that cause mitochondrial damage through oxidative stress.[12-14]

In the work described here, strategies were developed for the covalent attachment of two osmium bipyridine complexes and a ferrocene derivative to PPF and CNT electrodes. Building on the work of Babkina *et al.* and Murphy *et al.* a strategy was developed for covalent attachment of a MitoQ analogue. Methods were developed to tether this molecule to amine terminating films by reductive amination. The various tether layers discussed throughout this thesis were assessed for their ability to couple high concentrations of aldehyde terminating MitoQ analogues and facilitate fast electron transfer between the mediator and the substrate electrodes.

5.2 Experimental section

5.2.1 Synthesis of osmium complexes, 5.1 and 5.2

Os(4,4'-dichloro-2,2'-bipyridine)$_2$Cl(methylaminopyrazine).PF_6 (Figure 5.4, compound **5.2**) was a gift from Dónal Leech (The National University of Ireland, Galway). Os(2,2'-bipyridine)$_2Cl_2$ was synthesized by the method described in section 6.2.7 with 2,2'-bipyridine in place of 4-aminophenyl-2,2'-bipyridine. Os(2,2'-bipyridine)Cl(4-aminomethylpyridine).PF_6 (Figure 5.4, compound **5.1**) was synthesized by the methods of Zakeeruddin *et al.*[15] A solution of 100 mg of Os(2,2'-bipyridine)Cl_2 was refluxed with a 1.1 molar equivalent of methylaminopyridine in ethylene glycol for 1 h, allowing the solution to cool to room temperature and adding excess NH_4PF_6 with stirring on ice for 1 h. The fine black precipitate product was obtained by vacuum filtration using 0.2 µm PTFE filters. Successful synthesis of the complexes was indicated using CV by matching the $E_{1/2}$ for the $Os^{2+/3+}$ couple with the published values obtained by Boland *et al.* [1] for the same complex. CVs of saturated solutions of **5.1** and **5.2** in PBS were obtained using a 3mm GC disc electrode as described in section 5.3.1.1.

5.2.2 Synthesis of ferrocenemethylamine hydrochloride, 5.3

Synthesis of ferrocenemethylamine (Figure 5.4, Compound **5.3**) was achieved using the reductive amination method described by Kraatz.[16] 7.7 g (0.1 M) of ammonium acetate was added to a solution of 2.14 g (10 mM) of ferrocenecarboxaldehyde in 100 mL of MeOH at 0 ^oC then stirred for 30 min. 0.44 g (7 mM) of $NaBH_3(CN)$ was added to the cold solution. The solution was stirred overnight then the volume was reduced to 20 mL by rotary evaporation before addition of 10 mL of water. 1 M HCl was added until the acidity of the solution reached pH 2 then $KOH_{(s)}$ was added until the solution reached pH 8. The solution was extracted with 4 × 40 mL of CH_2Cl_2. The organic phase was washed with 3 × 50 mL of water, dried using anhydrous $MgSO_4$ and the solvent was removed by rotary evaporation yielding a brown oil. The oil was redissolved in 10 mL of MeOH and 5 mL of 1 M HCl before removal of the solvent by evaporation. The crude product was purified from a small volume of MeOH by elution through a 5 cm alumina plug with

CH_2Cl_2. Evaporation of the CH_2Cl_2 yielded a dull yellow powder of ferrocenemethylamine hydrochloride

5.2.3 Coupling and electrochemical analysis of surface bound inorganic mediator molecules

PPF electrodes modified with carboxyphenyl (CP) films were prepared by a method analogous to that described in section 2.4.1 (Grafting of in situ generated 4-aminobenzene diazonium) with 4-carboxyaniline in place of 1,4-diaminobenzene. For the chemically assembled SWCNT and MWCNT / epoxy electrodes, coupling was achieved using the carboxylic acid functionalities generated during the chemical oxidation step in the case of SWCNTs (section 2.4.2) and during O_2 plasma activation in the case of MWCNT / epoxy electrodes (section 4.2.2). In all cases the carboxylic acid groups on the various electrodes were activated towards amide bond formation by incubation at room temperature in an aqueous solution of 40 mM EDCI and 10 mM NHS for 1 h. The substrates were then transferred to a 1 mM solution of the amine terminating inorganic mediator molecule in 4:1, pH 6 PB: EtOH for 24 h (EtOH was required to enhance the solubility of the complexes). Before electrochemical analysis the samples were cleaned by sequential sonication in EtOH and Milli-Q water.

Electrochemical analysis of the modified electrodes was conducted using the cell designed for use with PPF (section 2.2.1) and a 4 mm diameter O-ring (Viton or Kalrez). In all cases the electrolyte solution was pH 7 PBS and the potentiostat was an Eco Chemie, Autolab, PGSTAT302. All potentials reported in this chapter are referenced to an Ag/AgCl reference electrode.

5.2.4 Synthesis of 4-nitro-N-phenylbenzylamine

A solution of aniline (10 mM) and *p*-nitrobenzaldehyde (10 mM) in MeOH was allowed to react for 1 h at room temperature and then divided into two equal portions. To one portion, 1.5 molar equivalents of $NaBH_4$ was added at room temperature to reduce the imine to a secondary amine. The second portion was left to stand overnight yielding

large yellow crystals of the imine product. The reduced portion was evaporated to dryness over 3 days in a fume cupboard yielding a pale yellow powder. The precipitate was washed with acetone and then analyzed by H^1 NMR in DMSO. Reduction of the compound was confirmed by the appearance of an aliphatic proton peak at 4.41 ppm in an approximately 1 : 1 integral ratio with the aromatic protons appearing at shifts of 6.53 ppm, 7.03 ppm, 7.61 ppm, and 8.81 ppm. The final aromatic proton (C4) appears at 6.43 ppm.

5.2.5 Coupling of 4-nitrobenzaldehyde to amine terminating films on PPF by reductive amination

In situ produced AP films and reduced NP films were grafted to GC rods by the standard methods described in the general experimental chapter (section 2.4.1). Once modified with amine terminating films the GC rods were suspended in a 20 mM 4-nitrobenzaldehyde MeOH solution for 1 h before transferring to a 10 mM $NaBH_4$ solution in MeOH to reduce the imine to a secondary amine. The rods were then washed by 30 s of sonication in clean MeOH to remove unreacted aldehyde before the terminal nitro groups of the coupled species were reduced in 0.1 M H_2SO_4 by 3 sequential CVs from 0.5 to -1 V *vs.* SCE, scan rate = 100 mV s^{-1}.

5.2.6 Electrochemical characterization of 6-decanaldehyde-2,3-dimethoxy-5-methyl-1,4-benzoquinone (DDMB) in solution

DDMB solutions were prepared by injection of 50 µL of 10 mM DDMB in MeOH into 10 mL of degassed 20 mM PBS. CVs were recorded at 100 mV s^{-1} using a 3 mm diameter GC disc electrode. The pH of the PBS ranged from 2 to 13. CVs were recorded approximately 3 s after mixing by N_2 purging.

5.2.7 Coupling of DDMB to amine terminating films

AP films on the GC electrodes were prepared by performing sequential CVs of a 10 mM 1,4-diamonobenzene solution with 1 equivalent of $NaNO_2$ from 0 to -0.6 V *vs.* SCE

as described in the Results and Discussion section and also in section 2.4.1. Coupling of DDMB to the films was achieved by immersion of the films in a 1 mM solution of DDMB in MeOH for 1 hr and then reduction of the resulting imine by transfer of the films to a 10 mM $NaBH_4$ solution in MeOH for 15 min. The films were cleaned by 1 min sonication in MeOH and dried with N_2.

5.3 Results and discussion

5.3.1 Coupling of inorganic mediator molecules to carboxylic acid terminating films by amide bond formation

Three primary amine terminated mediator molecules were attached to CP modified PPF, to SWCNT modified PPF and to MWCNT / epoxy electrodes by the method depicted in Figure 5.4.[1]

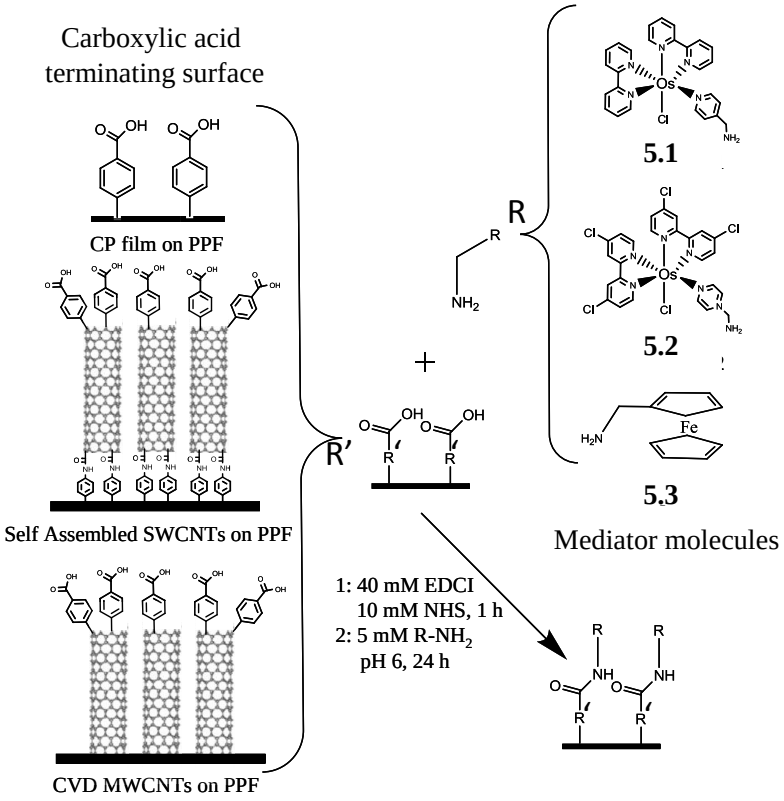

Figure 5.4. The procedure for coupling of carboxylic acid terminating PPF and CNT surfaces with amine terminated mediator molecules. The carboxylic acid groups depicted at the termini of the CNTs are those generated during oxidative shortening of SWCNTs and plasma activation of MWCNTs.

5.3.1.1 Solution characterization of the mediator complexes

CVs were recorded using saturated solutions of the three mediator molecules shown in Figure 5.4 in pH 7 PBS to establish the $E_{1/2}$ values for the complexes. The CVs are shown in Figure 5.5 and yield $E_{1/2}$ = 316 mV for **5.1**, $E_{1/2}$ = 378 mV for **5.2,** $E_{1/2}$ = 347

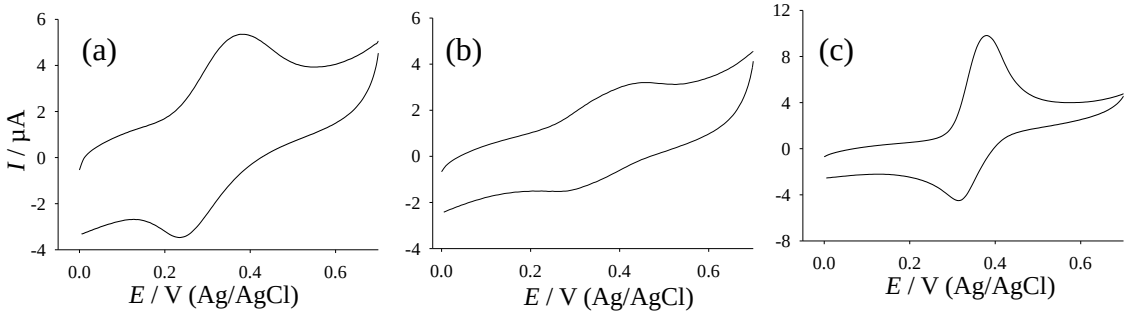

Figure 5.5. CVs recorded at a GC rod electrode of saturated solutions of (a) complex **1**, (b) **2,** (c) **3** in pH 7 PBS, scan rate = 100 mV s^{-1}.

mV for **5.3**. The peak currents in the CVs reflect the relative solubilities of the complexes in PBS. The CVs of the two osmium complexes (Figure 5.5 (a) and (b)) show chemically reversible redox couples consistent with the known stability of osmium bipyridine complexes in both the Os^{2+} and Os^{3+} oxidation states. The small reduction peak on the CV of $FcMeNH_2$ (Figure 5.5 (c)) suggests that the ferrocinium ion oxidation state is unstable in PBS or that adsorbed neutral **5.3** rapidly desorbs upon oxidation to the charged ferrocinium ion.

5.3.1.2 Surface attachment

After coupling of **5.1**, **5.2**, and **5.3** to CP modified PPF, vertically aligned SWCNTs on PPF and MWCNT / epoxy composite electrodes, the electrodes were cleaned by sonication in EtOH and Milli-Q water and CVs were recorded in fresh pH 7 PBS. The surface concentrations of the coupled mediators were calculated from the area under the oxidation peak of each of the CVs obtained at 100 mV s^{-1}. The calculated surface

concentrations for **5.1**, **5.2** and **5.3** coupled to the various electrodes are shown in Table 5.1. The concentration of **5.2** on MWCNT / epoxy electrodes was not obtained due to limited availability of this complex.

		Surface conc. mol cm^{-2} x 10^{-10}
$Os(bpy)_2Cl$ **(1)**	PPF	1.45 (0.64)
	SWCNTs	0.40 (0.14)
	MWCNTs	1.52 (0.15)
$Os(bpyCl_2)_2Cl$ **(2)**	PPF	0.60 (0.25)
	SWCNTs	0.31 (0.2)
	MWCNTs	–
$FcMeNH_2$ **(3)**	PPF	1.3 (*)
	SWCNTs	1 (*)
	MWCNTs	0.72 (0.2)

Table 5.1. Surface concentrations of mediators **5.1**, **5.2** and **5.3** coupled to PPF, PPF/CNT and MWCNT /epoxy electrodes. The reported values are an average of at least 5 samples and the standard deviation of the means are shown in brackets ((*) denotes samples where only 2 repeats were performed therefore no standard deviation is reported).

Table 5.1 shows that for SWCNT modified PPF the surface concentrations of modifiers were lower than for the CP modified PPF. This may be a result of a lower concentration of carboxylic acid termini available for bonding at the SWCNT electrode. The plasma treated MWCNT / epoxy electrodes have significantly higher surface area

than either of the other electrode formats (see section 4.3.1.5) but coupling of the amine modifiers is restricted to carboxylic acid functionalities leading to similar modifier concentrations at these surfaces to those at CP modified PPF. The concentrations of modifiers achieved here were lower than those obtained by Boland *et al.* [1] who reported 2.9×10^{-10} mol cm^{-2} for **5.1** coupled to GC by an identical method. The significantly higher surface roughness of polished GC than PPF is likely to account for the difference.

Figure 5.6. shows typical CVs recorded at PPF (black), SWCNT / PPF (green) and MWCNT / epoxy (red) electrodes modified with **5.1** (a) and **5.3** (b) in pH 7 PBS. The SWCNT / PPF electrodes yielded broad oxidation and reduction peaks with a large background current. By comparison the PPF and MWCNT / epoxy electrodes exhibited more defined oxidation and reduction peaks and had smaller ΔE_p values. The ΔE_p values for the samples shown in Figure 5.6 (a) are 91 mV for PPF and 65 mV for the MWCNT / epoxy electrode. The CVs for **5.2** on PPF and SWCNTs are not shown as the trends were similar to **5.1**. The CVs recorded for the samples modified with **5.3** are shown in

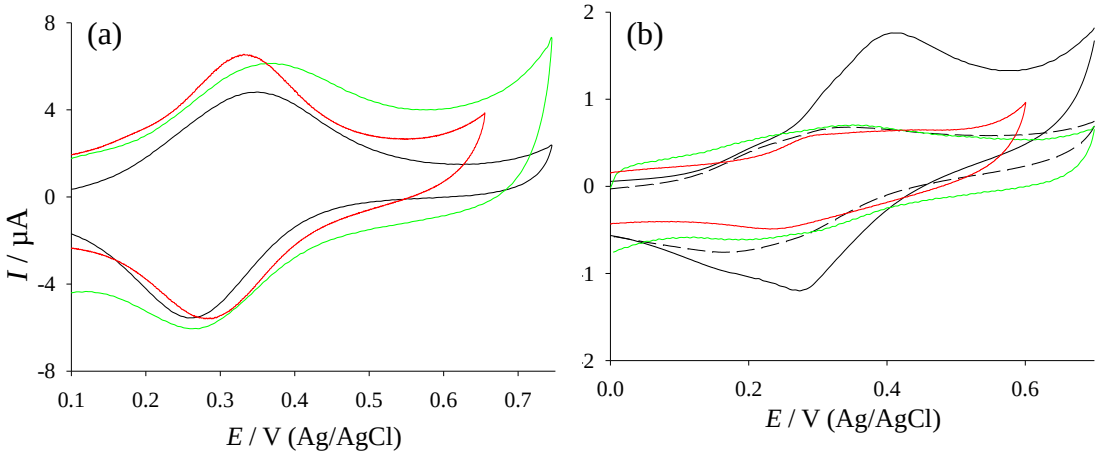

Figure 5.6. CVs of **5.1** (a) and **5.3** (b) attached to PPF (Black, solid line = 1st cycle, dashed line = 10th cycle) SWCNTs (green) and MWCNT / epoxy (red) in pH 7 PBS, scan rate = 500 mV s^{-1} for (a) and 100 mV s^{-1} for (b).

Figure 5.6 (b). Unlike the osmium centered complexes **5.3** is unstable when oxidized. The 1st and 10th cycle for the CVs recorded for the sample with **5.3** attached to PPF are shown in Figure 5.6 (b) (black trace) showing how the concentration of **5.3** at the

surface decreases dramatically between the 1st cycle (solid line) and 10th cycle (dashed line). Because of this instability electrodes modified with **5.3** were not employed in further experiments.

5.3.2 Characterization and coupling of 6-decanaldehyde-2,3-dimethoxy-5-methyl-1,4-benzoquinone (DDMB)

DDMB (Figure 5.7), synthesized by Lesley Larson at the University of Otago, was electrochemically characterized and coupled to electrode surfaces by reductive amination.

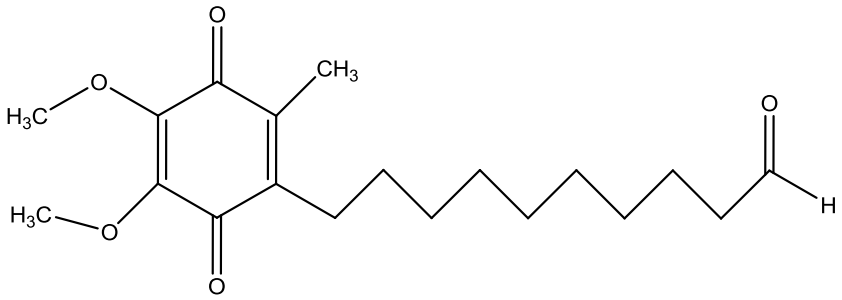

Figure 5.7. 6-decanaldehyde-2,3-dimethoxy-5-methyl-1,4-benzoquinone (DDMB)

Due to the limited quantities of DDMB available, model compounds were used to test standard methods for reductive amination coupling in solution and to ascertain if the reductive amination reaction was effective when confined to a surface.

5.3.2.1 Model experiments for reductive amination coupling

Coupling in solution by reductive amination was undertaken to establish the suitability of methanol as a solvent and $NaBH_4$ as a reducing agent for later experiments using DDMB. The model compounds employed were aniline, to model surface bound AP, and 4-nitrobenzaldehyde to model an aldehyde in solution (Figure 5.8). 4-nitrobenzaldehyde provided electrochemically active NP functionality for analysis of the surface reaction in later experiments (see 1.3.2).

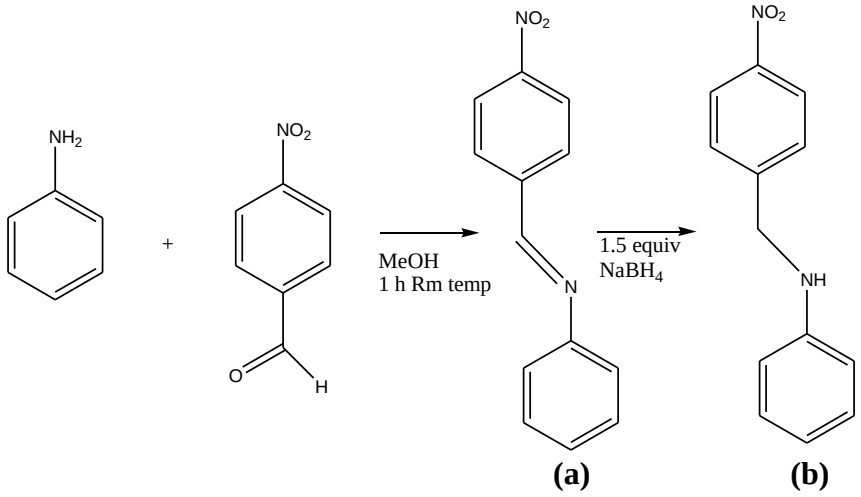

Figure 5.8. Coupling of aniline and 4-nitrobenzaldehyde by reductive amination

The intermediate imine (Figure 5.8 (a)) spontaneously precipitated as large yellow crystals when the reaction solution was allowed to stand overnight without the addition of $NaBH_4$. To identify this product its structure was determined by X-ray crystallography and is shown in Figure 5.9. The crystallographic data pertaining to the structure is shown in Table 5.2.

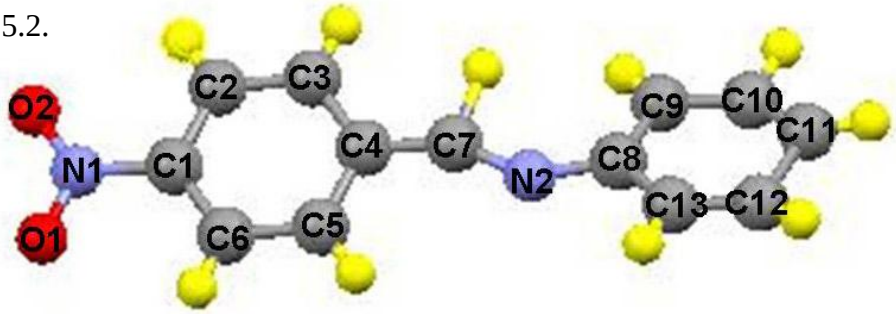

Figure 5.9. X-ray derived structure of the intermediate product shown in Figure 5.8 (a).

Crystallographic Data.

Unit Cell: Monoclinic Space Group: P2(1)/n

a	14.6297(4) Å	alpha	90 ^{o}
b	10.8260(4) Å	beta	101.932(2) ^{o}
c	14.7401(5) Å	gamma	90 ^{o}

Cell volume : 2284.11(13) $Å^3$ Multiplicity: 8

Crystallographic R factor: 0.206

Table 5.2. Crystallographic data for intermediate (a).

The high R factor for this crystallographic structure determination indicates that there is a relatively poor fit between the proposed atomic model and the observed diffractogram. In this case the poor fit arises from each of the two molecules in the asymmetric unit being disordered over two positions, probably because the diffractogram was recorded at room temperature. Furthermore, the carbon atoms in the phenyl rings have been constrained to regular hexagons for the purposes of illustration. The atomic structure of the molecule however is not in question owing to a match of the unit cell dimensions to existing literature structures for this compound.[17] Reaction of the intermediate with $NaBH_4$ yielded a yellow powder which was identified as the desired product (Figure 5.8 (b)) by NMR spectroscopy. These experiments thus established that the conditions used were appropriate for reductive amination coupling in solution.

To investigate coupling by reductive amination to a surface, 4-nitrobenzaldehyde was coupled to three amine terminating surfaces prepared by different methods, namely: an AP film produced by reduction of a NP film (reduced NP), an in situ produced AP film formed by direct reduction of 4-aminobenzenediazonium cations in solution (in situ AP) (see section 2.4.1) and an ethylene diamine film formed by oxidation of ethylenediamine (en) in an ACN solution (see section 3.2.1). The general reaction strategy is depicted in Figure 5.10 for an AP film and the analogous strategy was employed for en films.

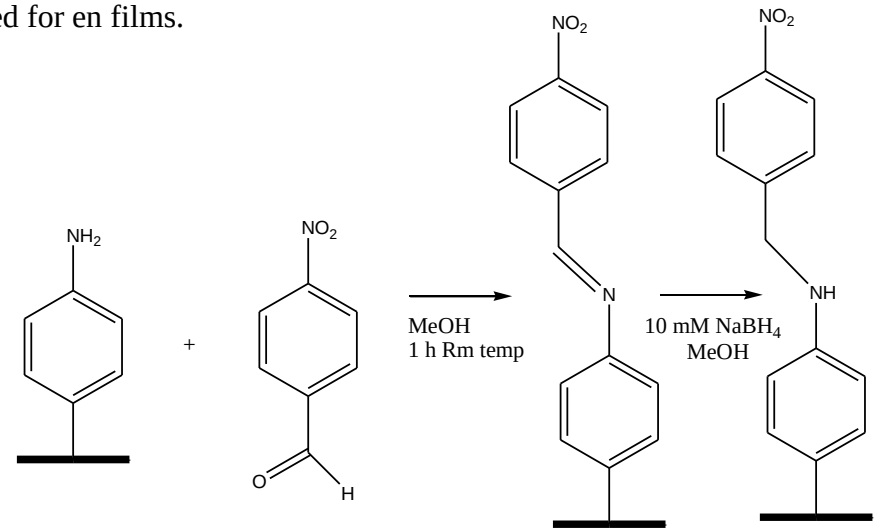

Figure 5.10. Coupling strategy employed for coupling of 4-nitrobenzaldehyde to amine terminating films by reductive amination.

To estimate the surface concentration of the coupled species, the terminal NP functionalities were electrochemically reduced in 0.1 M H_2SO_4 (see section 1.3.2) and the surface concentrations were calculated by the method of Ortiz *et al.*[18] (section 1.3.2).

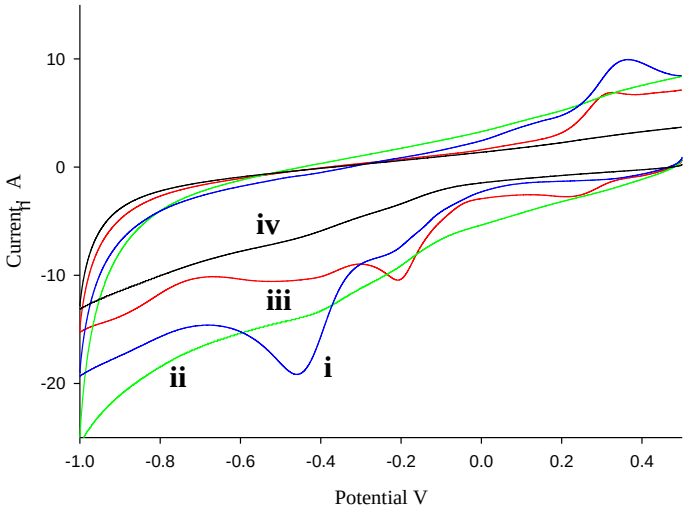

Figure 5.11. NP reduction CVs for 4-nitrobenzaldehyde coupled to (i) an in situ AP film, ii) an en film, iii) a reduced NP film and iv) a bare GC rod. The CVs were recorded in 0.1 M H_2SO_4 at scan rate = 100 mV s^{-1}.

The in situ produced AP film (Figure 5.11 (i)) gave the highest yield of coupled NP with an estimated surface concentration of 5.9 x 10^{-10} mol cm^{-2}. The corresponds to approximately half the concentration of a theoretical close packed monolayer for this molecule.[19] Reduction of 4-nitrobenzaledhyde coupled to an en film (Figure 5.11 (ii)) gave no evidence of a NP reduction peak but showed a large background current. The reduced NP film (Figure 5.11 (iii)) showed two small reduction peaks at –0.2 V and -0.5 V. The broad peak at -0.5 V is assigned to NP reduction but the peak at -0.2 V was not assigned. The in situ produced AP film clearly gave the highest concentration of electroactive NP and best peak definition and was therefore employed in all subsequent reductive amination couplings. It should be noted that the lack of evidence for successful coupling of 4-nitrobenzaldehyde to the en film could be due to poor electron transfer kinetics across the aliphatic en film. Likewise the reduced NP film may have had slower rates of electron transfer than the in situ AP film. As the goal of the coupling strategy is

to facilitate electrochemical detection of the coupled molecule, the in situ AP film clearly is the best choice for this application.

5.3.2.2 Solution characterization of DDMB

In order to establish the $E_{1/2}$ values and pH dependent electrochemical behavior of DDMB a series of CVs were recorded at a GC disc electrode in PBS solutions from pH 2.5 to 12 (Figure 5.13). 1,4-benzoquinones exhibit three distinctive electrochemical pathways depending on the pH of the electrolyte solution and the pKa values for the first and second deprotonation of the diol. At low pH the redox couple proceeds via a two proton two electron mechanism (Figure 5.12 i). At near neutral pH the couple usually proceeds via two electrons and one proton (Figure 5.12 ii) And at pH above the second deprotonation constant for the diol, the couple is independent of protons (Figure 5.12 iii). This redox chemistry results in pH dependent potentials for the quinone / hydroquinone couple. The $E_{1/2}$ values are predicted to become more positive as the pH decreases and the protonated (reduced) form of the molecule is favored. The CVs in Figure 5.13 clearly show this behavior. At pH 12, where there are no protons involved in the redox couple, the CV shows the theoretical peak separation of 29.5 mV for an electrochemically reversible, 2-electron redox couple.

Analysis of the clearly defined, reversible, reduction peak at pH 12 was used to establish a diffusion coefficient for DDMB making use of the Randles-Sevcik equation

$$i_p = 0.4462\ (F^3 / RT)^{1/2} n^{3/2} A D_o^{1/2} C_o v^{1/2} \qquad 5.3.2.1$$

(equation 5.3.2.1). This describes the peak current (i_p) of a fully reversible CV as a function of electrode area A, the diffusion coefficient and concentration of the redox species (D_o and C_o respectively), the number of electrons in the redox couple (n), the scan rate (v) and the conventional constants F, R and T. Solving equation 5.3.2.1 gives D_o = 1.7 x 10^{-6} cm^2 s^{-1} for DDMB in 50 mM phosphate buffer 0.1 M KCl, pH 12 at 25 ^oC. This is a reasonable value considering the size of the molecule.

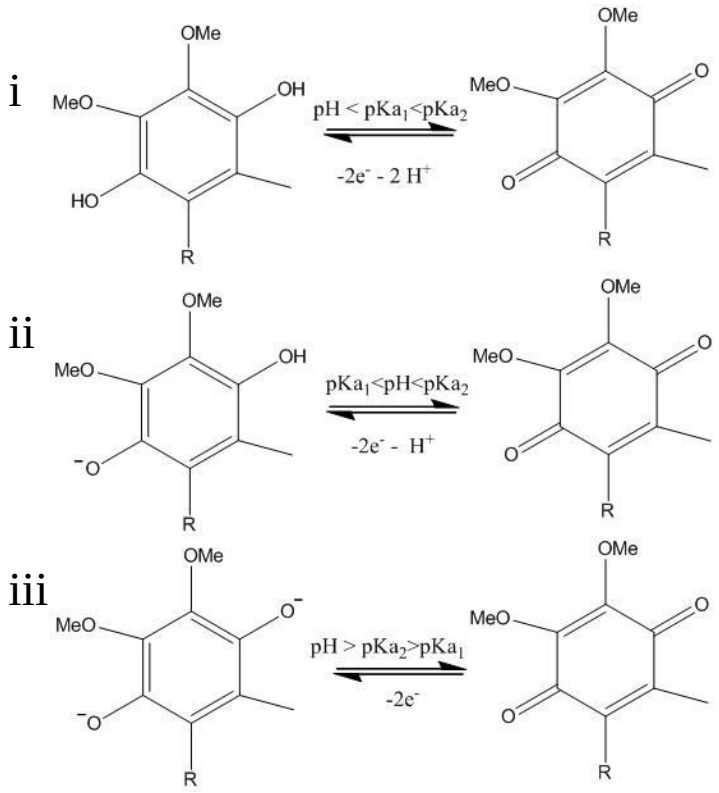

Figure 5.12. Expected redox reactions for DDMB

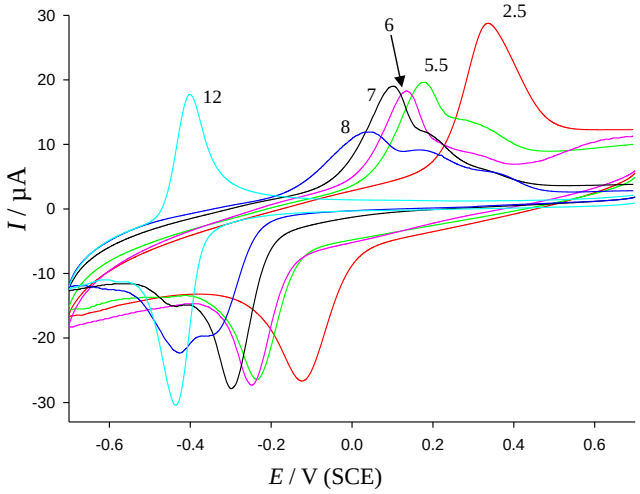

Figure 5.13. CVs of 0.25 mM DDMB in PBS at various pH (pH indicated on the plots), *vs.* Ag/AgCl, scan rate =100 mV s^{-1} .

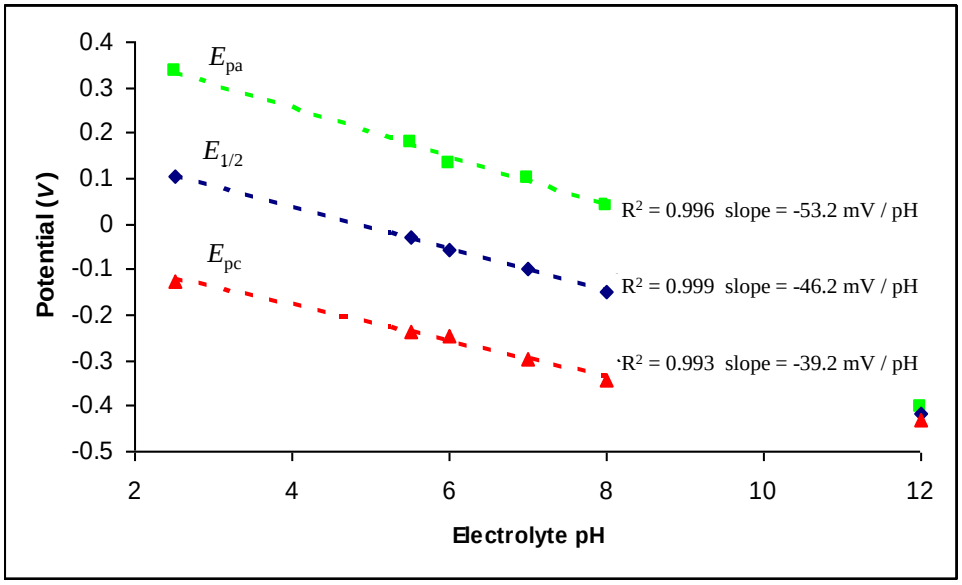

Figure 5.14. Plots of E_{pa}, E_{pc} and $E_{1/2}$ for CVs of DDMB in PBS at various pH. Data obtained at a scan = 100 mV s^{-1}. For pH 5.5, 6, 7 and 8 the major peak was used.

5.3.2.3 Coupling of DDMB to in situ produced AP films

To immobilize DDMB on electrode surfaces AP tether layers were grafted to GC disc electrodes. DDMB was subsequently reacted with the film forming an imine bond which was then reduced to give a secondary amine covalent bond. AP films were grafted using the in situ method described in section 2.3.1. The AP films were prepared by three different methods designed to produce films of varying thickness. A medium thickness film was produced by a two repeat CVs of the 10 mM diazonium salt solution from 0.2 to -0.6 V *vs.* SCE. A thicker film was produced by the same method with the addition of a two min deposition at -0.6 V between the two CVs. A thin film was produced by allowing a film to form on the glassy carbon electrode by spontaneous reaction (without electrochemical assistance) at room temperature for 20 min using the same diazonium salt solution. Coupling of DDMB was achieved by submerging the AP modified GC electrodes in a 1 mM DDMB solution in MeOH for 1 h before transferring to a 10 mM $NaBH_4$ solution in MeOH to reduce the imine to a secondary amine (Figure 5.15). The

DDMB modified surfaces were examined by obtaining CVs in 0.1 M KCl in H_2O, 0.1 M H_2SO_4 and 0.1 M NaOH solutions. Reaction of DDMB with the medium thickness AP

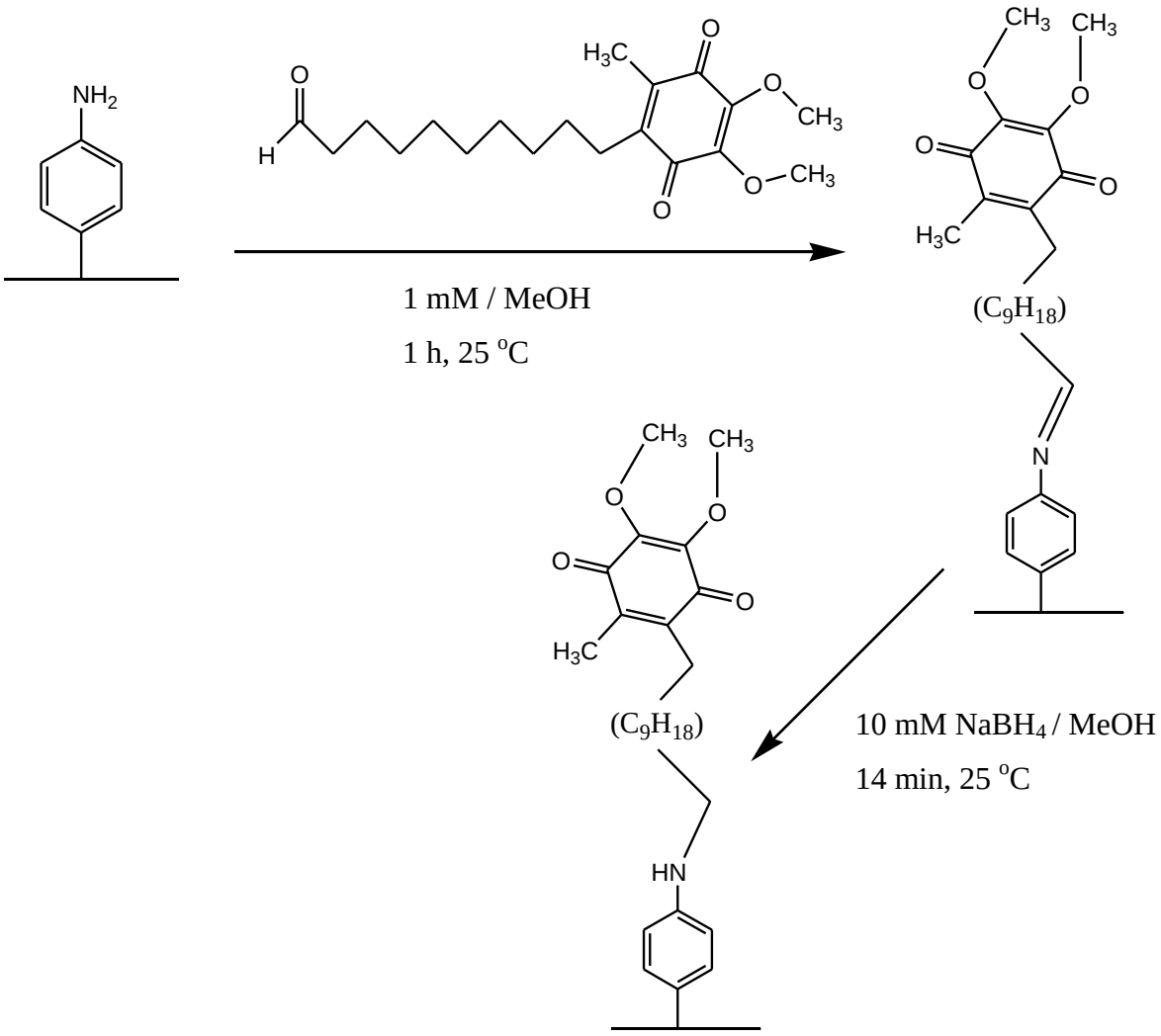

Figure 5.15. Coupling of DDMB to AP films by reductive amination

film yielded a CV with the best defined and largest peaks for the quinone / hydroquinone couple. The CV was poorly defined in 0.1 M KCl but at higher and lower pH the redox couple is clearly discernable. Figure 5.16 shows the CV obtained in 0.1 M H_2SO_4. At pH 1, the CV of surface bound DDMB has ΔE_p = 572 mV and an $E_{1/2}$ = 202 mV *vs.* SCE. Extrapolation of the $E_{1/2}$ values obtained in PBS (Figure 5.14) to pH 1 gives a value of ≈

200 mV. In 0.1 M NaOH the diol of DDMB is expected to be deprotonated. Under these conditions the oxidized form is favored and reaction kinetics are greatly increased due to the redox couple being independent of protons. Figure 5.17 (a) shows CVs of DDMB coupled to a medium thickness AP film and cycled in 0.1 M NaOH at various scan rates. At 100 mV s^{-1} the $E_{1/2}$ = –0.51 V and ΔE_p = 52 mV. A plot of the oxidation peak area for the couple *vs.* CV scan rate was linear indicating that the species is surface bound (Figure 5.17 (b)). Integration of the CV oxidation peaks yielded a surface concentration of (7 ± 2) x 10^{-10} mol cm^{-2}, averaged over 3 samples. This value is close to the predicted value of 10 x 10^{-10} mol cm^{-2} for a close packed monolayer of phenyl groups.

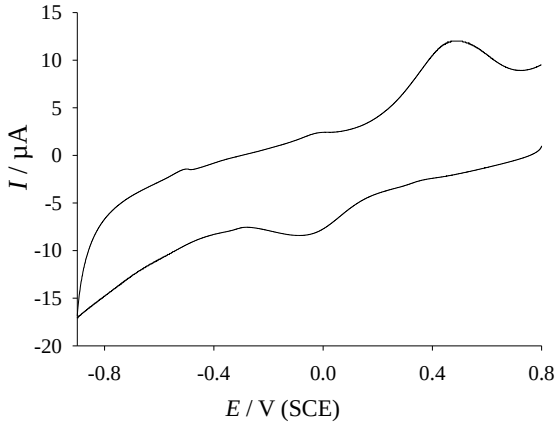

Figure 5.16. CV of DDMB coupled to an AP film on GC in 0.1 M H_2SO_4 at scan rate = 100 mV s^{-1}.

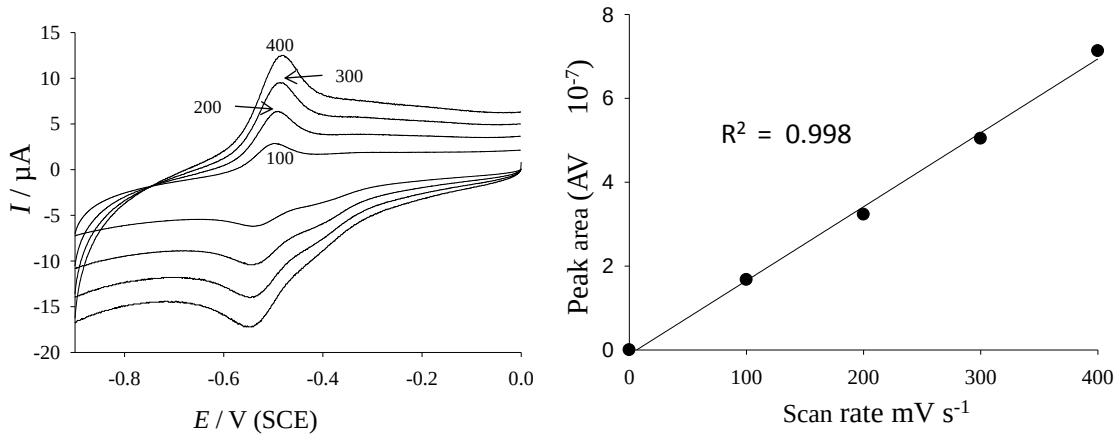

Figure 5.17. (a) CVs of a DDMB modified AP film on GC at the scan rate indicated on the plot in 0.1M NaOH. (b) a plot of cathodic peak area *vs.* scan rate for the CVs depicted in (a)

When very thick or very thin AP films were employed for coupling of DDMB the apparent surface concentrations were lower. It is likely that coupling efficiency increases with increasing thickness, however the resistance to charge transfer of the film also increases with increasing thickness. The decrease in response may be caused by the film becoming too resistive to electron transfer and effectively shielding coupled DDMB molecules from the underlying electrode.

5.4 Conclusion

Two amine terminating osmium complexes and one amine terminating ferrocene derivative were successfully coupled to PPF, chemically assembled SWCNTs on PPF and to MWCNT / epoxy electrodes using established literature methods. PPF and MWCNT / epoxy electrodes exhibited the highest concentrations of attached mediator molecules and also exhibited the lowest background currents and best oxidation and reduction peak definition. All of the electrodes exhibited mediator concentrations between 0.4 and 1.5 × 10^{-10} mol cm^{-2} which is lower than those reported at GC using the same coupling methods. Although the MWCNT / epoxy electrodes and SWCNT electrodes have significantly higher roughness and therefore higher surface area than the PPF samples, it is clear that only a fraction of these surfaces are decorated with the carboxylic acid functionalities that are required to form amide bonds.

A method was developed for the attachment of aldehydes in solution to amine terminating films by reductive amination. This method was employed to covalently tether an analogue (DDMB) of the known biological redox mediator ubiquinone. AP films derived by the in situ method and of moderate thickness, coupled the highest concentrations of DDMB. During solution characterization of DDMB a diffusion coefficient of 1.68 x 10^{-6} cm^2 s^{-1} for DDMB in 50 mM phosphate buffer 0.1 M KCl, pH 12 at 25 ^{o}C was established for the molecule.

5.5 References

1. Boland, S.; Foster, K.; Leech, D., A stability comparison of redox-active layers produced by chemical coupling of an osmium redox complex to pre-functionalized gold and carbon electrodes. *Electrochim. Acta* **2009,** 54, (7), 1986-1991.
2. Boland, S.; Barriere, F.; Leech, D., Designing stable redox-active surfaces: Chemical attachment of an osmium complex to glassy carbon electrodes prefunctionalized by electrochemical reduction of an in situ-generated aryldiazonium cation. *Langmuir* **2008,** 24, (12), 6351-6358.
3. Jenkins, P. A.; Boland, S.; Kavanagh, P.; Leech, D., Evaluation of performance and stability of biocatalytic redox films constructed with different copper oxygenases and osmium-based redox polymers. *Bioelectrochem.* **2009,** 76, (1-2), 162-168.
4. Kavanagh, P.; Boland, S.; Jenkins, P.; Leech, D., Performance of a Glucose/O-2 Enzymatic Biofuel Cell Containing a Mediated Melanocarpus albomyces Laccase Cathode in a Physiological Buffer. *Fuel Cells* **2009,** 9, (1), 79-84.
5. Tkac, J.; Vostiar, I.; Gorton, L.; Gemeiner, P.; Sturdik, E., Improved selectivity of microbial biosensor using membrane coating. Application to the analysis of ethanol during fermentation. *Biosens. Bioelectron.* **2003,** 18, (9), 1125-1134.
6. Tkac, J.; Svitel, J.; Vostiar, I.; Navratil, M.; Gemeiner, P., Membrane-bound dehydrogenases from Gluconobacter sp.: Interfacial electrochemistry and direct bioelectrocatalysis. *Bioelectrochem.* **2009,** 76, (1-2), 53-62.
7. Babkina, E.; Chigrinova, E.; Ponamoreva, O.; Alferov, V.; Reshetilov, A., Bioelectrocatalytic oxidation of glucose by immobilized bacteria Gluconobacter oxydans. Evaluation of water-insoluble mediator efficiency. *Electroanalysis* **2006,** 18, (19-20), 2023-2029.
8. Asin-Cayuela, J.; Manas, A. R. B.; James, A. M.; Smith, R. A. J.; Murphy, M. P., Fine-tuning the hydrophobicity of a mitochondria-targeted antioxidant. *FEBS Lett.* **2004,** 571, (1-3), 9-16.
9. Kelso, G. F.; Porteous, C. M.; Coulter, C. V.; Hughes, G.; Porteous, W. K.; Ledgerwood, E. C.; Smith, R. A. J.; Murphy, M. P., Selective targeting of a redox-active ubiquinone to mitochondria within cells - Antioxidant and antiapoptotic properties. *J. Biol. Chem.* **2001,** 276, (7), 4588-4596.
10. Murphy, M. P.; Smith, R. A. J., Targeting antioxidants to mitochondria by conjugation to lipophilic cations. *Annu. Rev. Pharmacol. Toxicol.* **2007,** 47, 629-656.
11. James, A. M.; Sharpley, M. S.; Manas, A. R. B.; Frerman, F. E.; Hirst, J.; Smith, R. A. J.; Murphy, M. P., Interaction of the mitochondria-targeted antioxidant MitoQ with phospholipid bilayers and ubiquinone oxidoreductases. *J. Biol. Chem.* **2007,** 282, (20), 14708-14718.
12. Gane, E. J.; Weilert, F.; Orr, D. W.; Keogh, G. F.; Gibson, M.; Lockhart, M. M.; Frampton, C. M.; Taylor, K. M.; Smith, R. A. J.; Murphy, M. P., The mitochondria-targeted anti-oxidant mitoquinone decreases liver damage in a phase II study of hepatitis C patients. *Liver Int.* **2010,** 30, (7), 1019-1026.
13. Mackenzie, R. M.; Hamilton, C. A.; Miller, W. H.; Salt, I. P.; Murphy, M. P.; Delles, C.; Dominiczak, A. F., MitoQ(10) Reduces Mitochondrial Reactive Oxygen

Species Production and AMP-Activated Protein Kinase Activity in Vessels from Patients with Type 2 Diabetes and Coronary Artery Disease. *Hypertension* **2009,** 54, (4), E40-E40.
14. Cocheme, H. M.; Kelso, G. F.; James, A. M.; Ross, M. F.; Trnka, J.; Mahendiran, T.; Asin-Cayuela, J.; Blaikie, F. H.; Manas, A. R. B.; Porteous, C. M.; Adlam, V. J.; Smith, R. A. J.; Murphy, M. P., Mitochondrial targeting of quinones: Therapeutic implications. *Mitochondrion* **2007,** 7, S94-S102.
15. Zakeeruddin, S. M.; Fraser, D. M.; Nazeeruddin, M. K.; Gratzel, M., Towards Mediator Design - Characterization of Tris-(4,4'-Substituted-2,2'-Bipyridine) Complexes of Iron(Ii), Ruthenium(II) and Osmium(II) as Mediators for Glucose-Oxidase of Aspergillus-Niger and Other Redox Proteins. *J. Electroanal. Chem.* **1992,** 337, (1-2), 253-283.
16. Kraatz, H. B., Synthesis and electrochemistry of ferrocenemethylamine and its conjugated acid. Crystal structure of ferrocenemethylammonium chloride. *J. Organomet. Chem.* **1999,** 579, (1-2), 222-226.
17. Harada, J.; Harakawa, M.; Ogawa, K., Conformational change of N-benzylideneanilines in crystals. *Acta Crystallogr., Sect. B: Struct. Sci.* **2004,** 60, 589-597.
18. Ortiz, B.; Saby, C.; Champagne, G. Y.; Belanger, D., Electrochemical modification of a carbon electrode using aromatic diazonium salts. 2. Electrochemistry of 4-nitrophenyl modified glassy carbon electrodes in aqueous media. *J. Electroanal. Chem.* **1998,** 455, (1-2), 75-81.
19. Liu, Y. C.; McCreery, R. L., Reactions of Organic Monolayers on Carbon Surfaces Observed with Unenhanced Raman-Spectroscopy. *J. Am. Chem. Soc.* **1995,** 117, (45), 11254-11259.

Chapter 6. Electro-grafting of osmium diazonium cation complexes

6.1 Introduction

Osmium complexes are gaining popularity as redox mediator molecules in a number of biological applications. They exhibit well defined redox chemistry across a wide potential window, [1, 2] which depends on the ligand shell attached, and have proved to be highly stable in both oxidized and reduced forms. [1, 2] There are examples of surface confined osmium complexes successfully mediating electron transfer in both microbial [3, 4] and enzymatic systems [5-8] hence they are a candidate for use as charge transfer mediators from living cells.

In all of the previously published work on surface immobilized osmium complexes the complexes are covalently bound to a pre-formed surface tether layer or covalently linked to a polymer film on the substrate. Jenkins *et. al* [5] and Hudak *et al.* [6] both use osmium complex decorated polyvinylimidazole which is either drop coated or cross linked onto the electrode. Habermuller and Schumman *et al.* use an osmium complex modified polypyrrole which is electrodeposited onto electrodes. [7] Boland and Leech *et al.* have directly attached osmium complexes to SAMs of alkanethiols on gold [9] and electrochemically grafted diazonium salt thin films [9] (as discussed in chapter 5). All of these methods require efficient methods for attaching the tether layer and coupling of the osmium complex. This results in complex, time consuming modification procedures which can be subject to poor reproducibility (see chapter 5). The concentration of the modifier is also limited by the surface area of the substrate.

The reductive grafting of aryl diazonium salts is a route whereby a surface confined film can be formed without the need for an intervening tether layer. Several ruthenium centered diazonium salts have been isolated and electrochemically grafted to GC and carbon nanotube electrodes [10] and later to boron doped diamond [11] by Jousellme *et al.*

The same authors have also patented a range of metal diazonium salt complex structures based around ruthenium, osmium and iridium. [12] During electrografting of $Ru(bpy)_2(bpy\text{-}ph\text{-}N_2^+).3PF_6$ Jousellme *et al.* discovered that the electrodes were not passivated by the growing film resulting in a film that continues to grow with continued application of reducing potentials. One of the diazonium salt complexes used in that paper and CVs of the complex are shown in Figure 6.1. The $Ru^{2+/3+}$ couple appears at 1 V *vs.* Ag/Ag^+ in the CV depicted in Figure 6.1 and shows the surface concentration of surface confined complexes increasing with each CV.

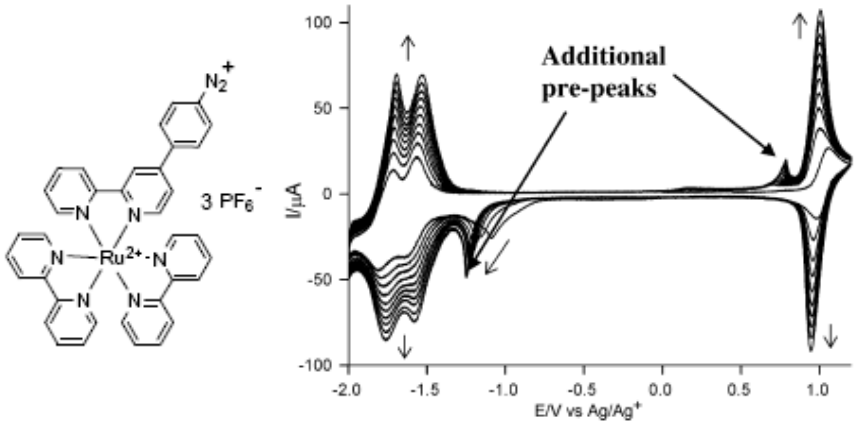

Figure 6.1. Structure of $Ru(bpy)_2(bpy\text{-}ph\text{-}N_2^+).3PF_6$ and CVs of the complex (1 mM in 0.1 M $TBAPF_6$ / ACN). Figure reproduced from reference 10

The lack of passivation exhibited by the growing ruthenium films described by Jousellme *et al.* is only briefly mentioned in their initial publication. [10] The subsequent patent however focuses on this phenomenon as the characteristic of most interest. [12] Typically the growth of diazonium salt derived films self terminates at some limiting thickness dependent on the applied grafting potential and the grafting time. These metal complex films do not self limit but continue to grow with grafting time. This phenomenon is typical of electrografting of conducting polymers and therefore it appears that these metal complex films are able to conduct electrons to the surface and effect further reduction of diazonium cations. Jousellme *et al.* propose that this conductivity is the result of electron hopping through the metal centres in the polymeric matrix. [10] A similar mechanism is proposed by Schuhman *et al.* [7] who co-imobilized osmium

complexes in polypyrrole matrices. In the 2008 patent, Jousellme *et. al* focus on the high, broad spectrum light absorption of the derived films and speculate about their potential use as dye sensitizer films for photovoltaic applications. This is a promising application considering the similarity of the ruthenium complexes to existing dye sensitizer molecules. The applicability to photovoltaics is enhanced by the fact that the films can be made very thick and that they are conducting.

In terms of the utility of immobilized metal films for mediated whole cell electrochemistry (i.e sensors or microbial fuel cells), the potential of the $Ru^{2+/3+}$ couple in bipyridine complexes is likely to be too positive. In water this potential is between 1.2 and 1.3 V *vs.* Ag/AgCl. Osmium complexes typically have potentials for metal-based redox couples approximately 500 mV lower than their ruthenium analogue, which makes them more suitable for use in biological systems. Osmium complexes analogous to the ruthenium complex depicted in Figure 6.1 offer a route to surface confined mediator films without the need for a tether layer. Additionally, the single step process and potentiometric control should facilitate reproducible preparation of films with a range of surface concentrations.

This chapter describes the synthesis and characterization of three new osmium complexes which have aminophenyl functionalities at their extremities. These complexes were diazotized and electrochemically grafted to GC and PPF electrodes. The electrochemical behavior of the complexes and the resulting films along with film topography and thickness are examined. The patent by Bidan *et al.* appeared during the course of this work describing similar or the same complexes as those described here however, no details regarding their electrochemistry or characterization were given.

6.2 Experimental section

The strategy for the synthesis of 4-(4-aminophenyl)-2,2′-bipyridine was that of Johansson *et.al.* [13] and is depicted in Scheme 6.1**.**

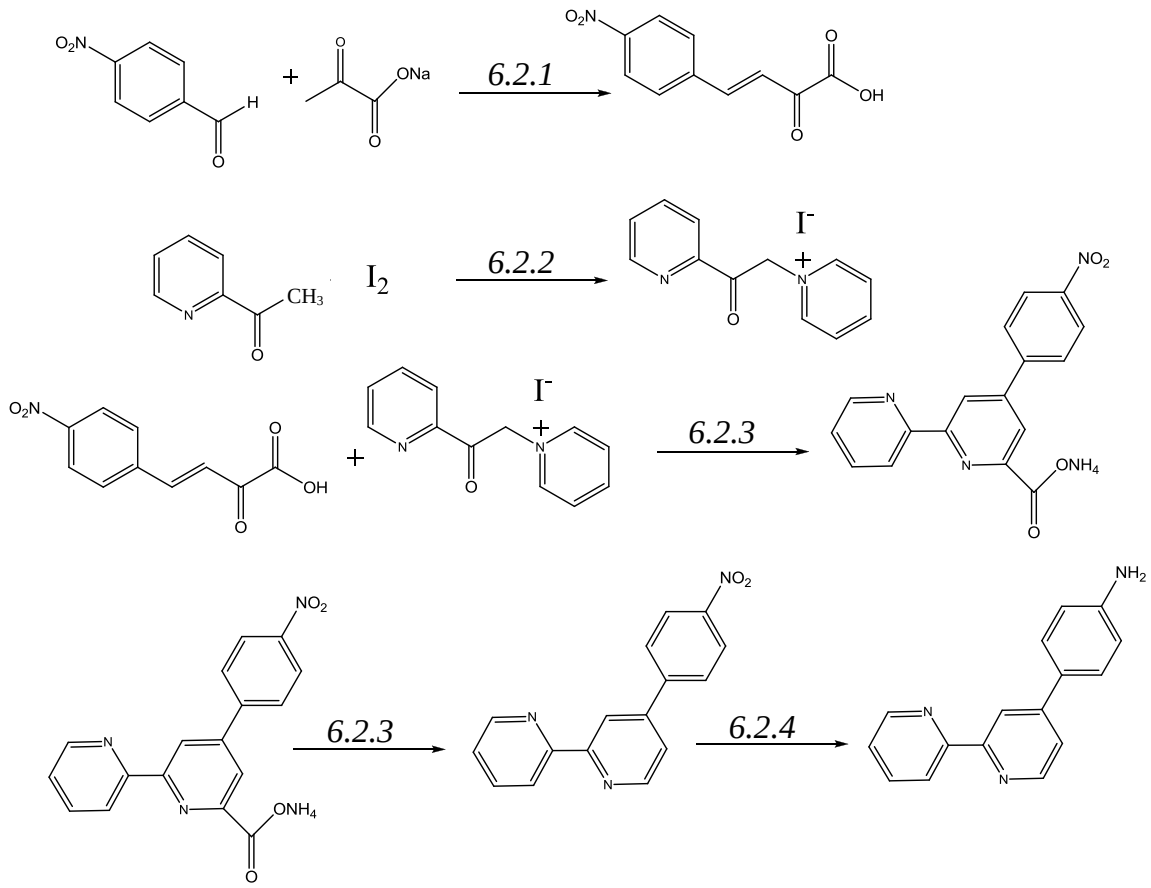

Scheme 6.1. Synthesis of 4-(4-aminophenyl)-2,2′-bipyridine. The numbered reaction arrows indicates the section which describes the indicated step

6.2.1 Synthesis of (E)-4-(4-nitrophenyl)-2-oxo-3-butenoic Acid

4.13 g (27.33 mmol) of *p*-nitrobenzaldehyde (Aldrich) was dissolved in 50 mL of EtOH at 70 ^{o}C. 3.1 g (28.17 mmol) of sodium pyruvate dissolved in 15 mL of H_2O was added with stirring and then the solution was cooled on ice and allowed to stand for 2.5 h. The burnt orange suspension was neutralized with 2 M HCl (approximately 5 mL) giving

a thick yellow suspension. The product was filtered, washed with EtOH and dried in air yielding 3.97 g of product.

6.2.2 Synthesis of pyridacyl pyridinium iodide

Synthesis of the precursor reagent pyridacyl pyridinium iodide was achieved following the method of Priimov *et.al.* [14] 12.7 g (50 mmol) of solid I_2 was dissolved in 60 mL of pyridine. To the stirred I_2 / pyridine solution 6.04 g (50 mmol) of 2-acetylpyridine was added dropwise. The solution was brought to reflux for 1 h then cooled to room temperature giving a thick black precipitate. The precipitate was filtered and washed with 50 mL of 9:1 diethylether : EtOH. The product was redissolved in 100 mL of hot MeOH and approximately 0.5 g of activated charcoal was added. The product solution was filtered through a celite pad heated with hot MeOH and the product washed through with additional hot MeOH. The MeOH cleaning process was repeated two more times yielding a clear yellow solution which formed yellow crystals upon cooling. The crystals were collected by filtration to give 9.82 g of product.

6.2.3 Synthesis of 4-(4-nitrophenyl)-2,2′-bipyridine

2.98 g of (13.5 mmol) of (E)-4-(4-nitrophenyl)-2-oxo-3-butenoic acid and 4.4 g (13.5 mmol) of pyridacyl pyridinium iodide and 8.3 g of NH_4OAc were added to 90 mL of H_2O and brought to reflux for 5 h forming a green solid of 4-(4-nitrophenyl)-6-carboxylate-2,2'-bipyridine. The solid was obtained by filtration and washed with 70 mL of water and 70 mL of acetone and then dried. 1.33 g of 4-(4-nitrophenyl)-6-carboxylate-2,2'-bipyridine was placed in a round bottom flask to which a vacuum was applied for 30 min. The product was heated under vacuum with a heat gun until it blackened and bubbled. Once CO_2 elution had ceased the black residue was redissolved in 100 mL of ethylacetate to which approximately 0.5 g of activated charcoal was added. The product was refluxed for 15 min before filtering through celite and evaporating to dryness yielding 0.87 g of the product as a rusty brown solid.

6.2.4 Synthesis of 4-(4-aminophenyl)-2,2′-bipyridine

0.8 g (2.85 mmol) of 4-(4-nitrophenyl)-2,2′-bipyridine was added to 30 mL of EtOH and 0.3 g of 10% Pd / carbon powder. The suspension was refluxed for 1 h before addition of 1.5 mL of hydrazine mixed with 2 mL of H_2O followed by refluxing for a further hour. The hot suspension was filtered through celite which was rinsed with 30 mL of dichloromethane. The filtrate was transferred to a separating funnel and washed with 30 mL of H_2O and 30 mL of brine. The organic fraction was dried with Na_2SO_4 and evaporated to dryness yielding 0.58 g of a yellow solid.

6.2.5 Synthesis of Os(2,2'-bpy-4(ph-NH_2))$_3$.2PF_6 and Os(bpy)$_3$.2PF_6

Synthesis of osmium complexes followed the general method of Zakeeruddin *et al.* [1] with some modifications. 50 mg (0.114 mmol) of NH_4OsCl_6 was added to 6 mL of ethylene glycol and stirred under nitrogen for 15 min. 3.1 molar equivalents of 2,2-bipyridine-4(4-aminophenyl) (87 mg 0.35 mmol) or 2,2-bypyridine was added and the solution heated to reflux under nitrogen for 4 h. The solution was cooled to room temperature and 2.1 molar equivalents of NH_4PF_6 (39 mg 0.24 mmol) in 6 mL of H_2O was added. The product suspension was stirred in an ice bath for a further 1 h before filtering and washing with 10 mL of H_2O and 30 mL of diethylether. The filtered product was dried at 60 ^oC overnight and purified by silica gel column chromatography. The eluting solution was 40 : 1 ACN : NH_4PF_6 (H_2O saturated). The product was eluted as a single band with some black impurities remaining on top of the column.

6.2.6 Synthesis of Os(2,2'-bpy)$_2$(2,2'-bpy-4(ph-NH_2)).2PF_6

100 mg of Os(bpy)$_2Cl_2$ (0.175 mmol prepared by the method described in 6.2.7) was added to 10 mL of ethylene glycol and stirred for 15 min under nitrogen. 47.4 mg of bpy-ph-NH_2 (1.1 molar equivalents, 0.192 mmol) was added and the solution heated to reflux for 4 h. The solution was cooled to room temperature and 2.1 molar equivalents of NH_4PF_6 in 10 mL of H_2O was added. The suspension was stirred in an ice bath for 1 h and filtered, washed, dried and purified as described for Os(bpy-ph-NH_2)$_3$.2PF_6.

6.2.7 Synthesis of Os(2,2'-bpy-4(ph-NH_2))$_2Cl_2$

100 mg of NH_4OsCl_6 (0.23 mmol) was added to 10 mL of ethylene glycol and stirred for 15 min under nitrogen. 2.1 molar equivalents of bpy-ph-NH_2 (120 mg 0.483 mmol) was added and the solution brought to reflux under nitrogen for 1 h. The solution was cooled to room temperature and 10 mL of saturated $Na_2S_2O_4$ was added to ensure full reduction of the osmium center. The product was filtered and washed by the same methods used in 6.2.5. The neutral complex exhibited low solubility in ACN and hence was unsuitable for column chromatography hence the product was used without purification.

6.2.8 Synthesis of diazonium tetrafluoroborate salts of osmium complexes

10 mg of the osmium complex for diazotization was added to 1.5 mL of 25% HBF_4, briefly sonicated to aid suspension and then stirred on ice for 10 min. A 3 fold excess of $NaNO_2$ to amine substituted ligands of the osmium complex was dissolved in minimum water and added dropwise to the stirred suspension. The suspension was stirred for a further hour before filtering through 0.2 µm PTFE membrane filters and washing with a small amount of ice cold water. The fine dark brown powders were dried in air and used immediately without further purification.

6.2.9 Electrochemistry

All experiments in ACN were conducted using an ECO CHIMIE potentiostat with 0.1 M $TBABF_4$ as the supporting electrolyte. The working electrodes were glassy carbon disc electrodes with a geometrical area of 0.07 cm^2 or PPF plates with an electrode area defined by an O-ring (Viton). A platinum counter electrode was used for all experiments. Aqueous reactions were either referenced to Ag/AgCl (3 M KCl) or SCE and all experiments in ACN were referenced to Ag/Ag+ (0.01 M $AgNO_3$ in 0.1 M $TBABF_4$ / ACN).

6.2.10 Rinsing of grafted surfaces

After all grafting and blank experiments the glassy carbon electrodes were washed with copious amounts of Milli-Q water and sonicated in EtOH for 3 min to remove any physisorbed species.

6.3 Results and discussion

6.3.1 Characterization of osmium amine complexes

6.3.1.1 NMR and mass spectrometry

The aryl amine complexes used in the work are displayed in Figure 6.2**.** The details of the syntheses of the various diazonium salts are discussed in the Experimental section (6.2).

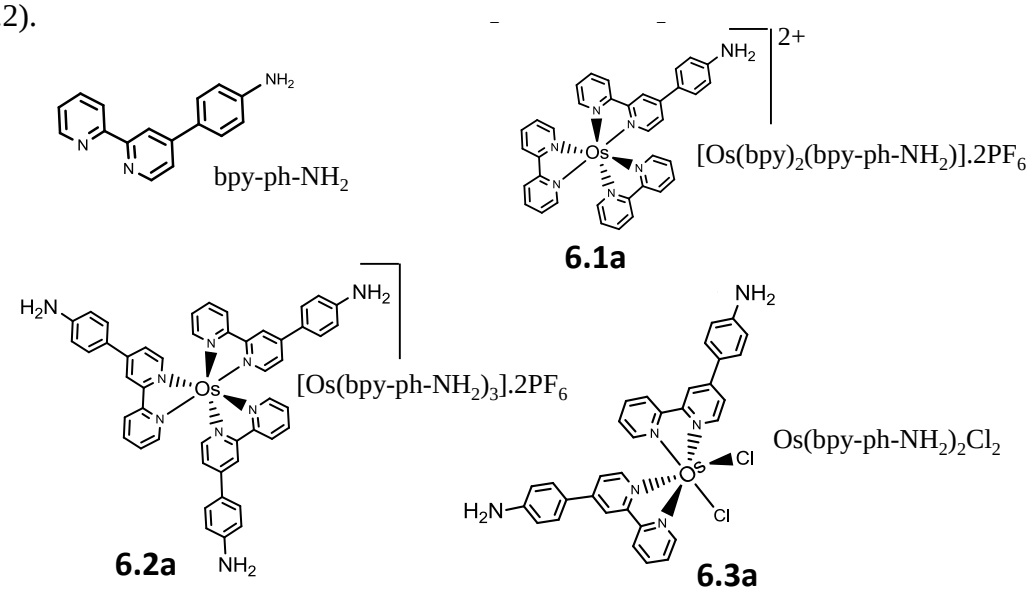

Figure 6.2. Osmium complexes and ligand used for diazonium salt preparation. The letter **(a)** (e.g. **6.1a**) denotes the amine of the complex and **(d)** (e.g. **6.1d**) denotes the corresponding diazonium tetrafluoroborate salt.

^{1}H NMR spectra for the complexes **6.1a**, **6.2a** and **6.3a** were obtained but could not be assigned. The spectrum for **6.1a** had discreet peaks but with a high degree of overlap,

hence no assignments could be made. As this complex exists as two enantiomers but no other isomers it appears that purification was not sufficient for successful NMR. The ^{1}H NMR spectrum for **6.2a** gave only a single broad peak from 7 to 9 ppm. There are several factors which could account for this spectrum. The most obvious is that tri substitution with a bidentate unsymmetric ligand (such as is used here) results in facial and meridional isomers. Several attempts to separate these isomers by altering the concentration of NH_4PF_6 or replacing NH_4PF_6 with KNO_3 in the chromatographic eluting solution were made without success. Additionally the aryl amine groups on the complexes may have been partially protonated which would also distort the ^{1}H NMR spectrum. Compound **6.3a** was not purified for the reasons discussed in the experimental section, hence it did not give an interpretable ^{1}H NMR spectrum. Because of the difficulties encountered with NMR, electrospray ionisation mass spectrometry (ESI-MS) and electrochemistry were used to identify the complexes.

Complexes **6.1a**, **6.2a** and **6.3a** were examined by positive ion ESI-MS, all yielding cationic species consistent with calculated molecular masses for the target molecules. Osmium possesses 7 stable isotopes and hence, considering the possible combinations of these isotopes with those of carbon and chlorine, the experimental results were compared with a theoretical model. The model spectra were generated by an online tool (Sheffield Chemputer Copyright 1993-2001 Mark Winter [University of Sheffield, England]). The experimental data for the largest m/z value species found for each complex and the computer generated spectra are depicted in Figure 6.3. Complexes **6.1a** and **6.2a** both yielded peaks consistent with the loss of one PF_6^- anion (Figure 6.3 a) and b)). Both spectra are in excellent agreement with the theoretical model. The largest peak for **6.3a** occurred in the positive ion spectrum, consistent with a singly protonated complex. Again the experimental data is in excellent agreement with the theoretical model (Figure 6.3 c)).

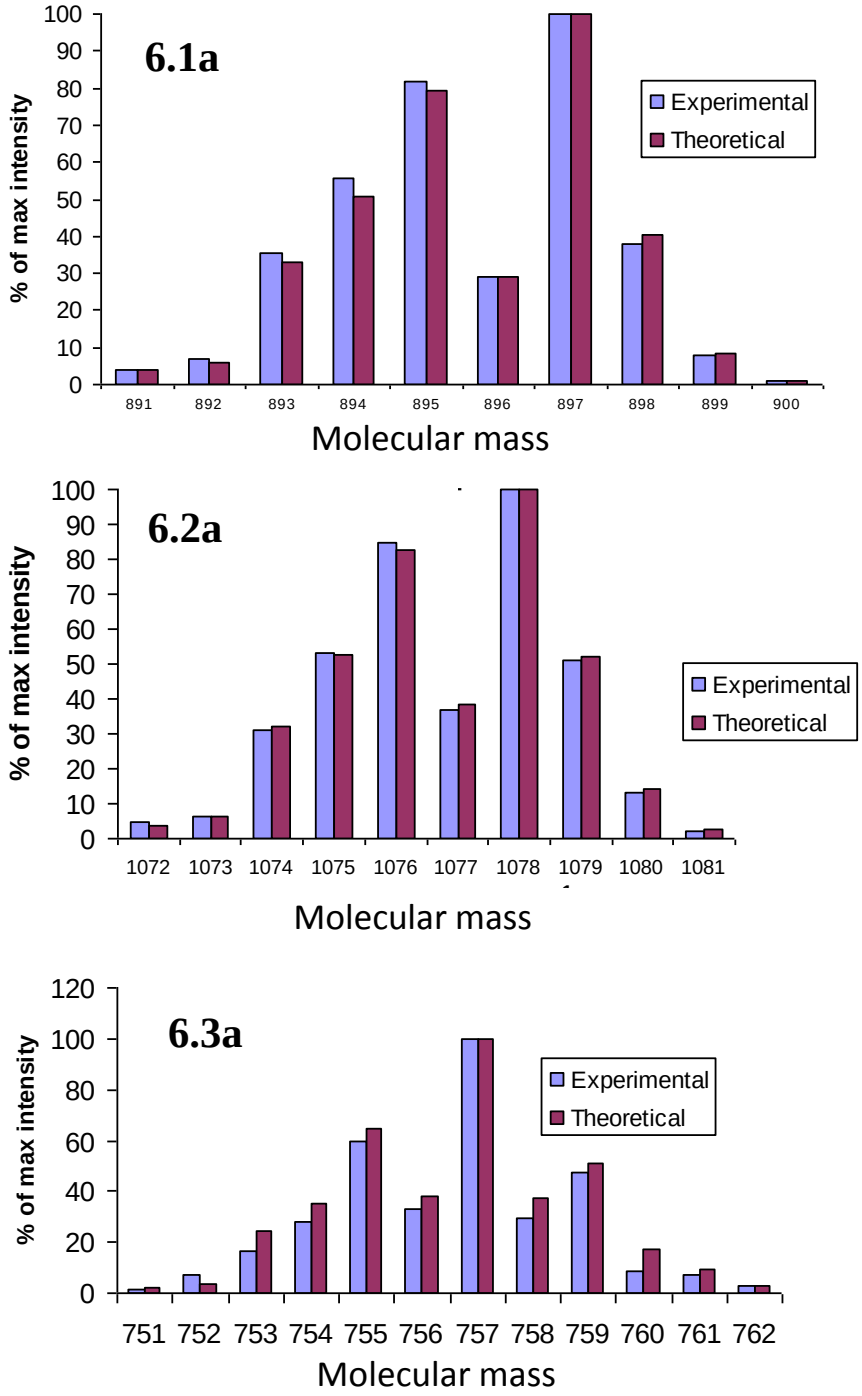

Figure 6.3. Observed isotopic distribution for the parent ion with the largest m/z value for complexes **6.1a**, **6.2a** and **6.3a** (blue). A computer generated model based on the known abundance of osmium, carbon, and chlorine isotopes is also presented for each complex (red).

6.3.1.2 Electrochemical characterization

The electrochemistry of complexes **6.1a**, **6.2a** and **6.3 a** was examined by CV and compared with electrochemistry of the corresponding osmium bipyridine complex (without amine substituted bipyridine ligands). The CVs of **6.1a** and $Os(bpy)_3.2PF_6$ in ACN / 0.1 M $TBABF_4$ are shown in Figure 6.4. Compound **6.1a** is less soluble in ACN than $Os(bpy)_3.2PF_6$ and likely less pure due to the difficulties encountered during chromatography. The result of this is a CV with less well defined peaks than those of $Os(bpy)_3.2PF_6$. There is a large oxidation wave present at 1 V for **6.1a** which is most likely due to oxidation of amines. This peak has been partially truncated to highlight the electrochemistry of the $Os^{2+/3+}$ couple. The $Os^{2+/3+}$ couple for $Os(bpy)_3.2PF_6$ (Figure 6.4, grey dashed line) is well defined with a $E_{1/2}$ of 527 mV *vs.* Ag/Ag^+. The $Os^{2+/3+}$ couple for **6.1a** (Figure 6.4, black line) has an $E_{1/2}$ of 508 mV

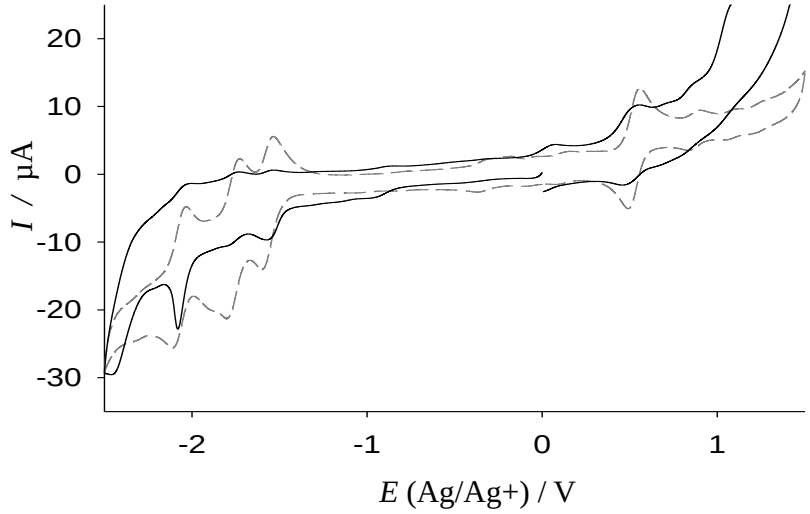

Figure 6.4. CV of a saturated solution of **6.1a** in ACN / 0.1 M $TBABF_4$ at 100 mV s^{-1} (black line) overlayed on a CV of 1 mM $Os(bpy)_3.2PF_6$ (grey dashed line) in the same electrolyte.

consistent with electron donation from aminophenyl bipyridine substitution. Electron donation contributes to a more electron rich metal center which is correspondingly easier to oxidize giving a less positive $E_{1/2}$ for the redox couple. The $E_{1/2}$ for the bipyridine redox couples of $Os(bpy)_3.2PF_6$ occur at -1.49, -1.69 and -2.00 V. The bipyridine signals

of **6.1a** are poorly defined and distorted but occur close to -1.6, -1.7 and -2.0 V, again shifted to more negative potentials than those of $Os(bpy)_3.2PF_6$.

CVs of saturated solutions of **6.2a** and **6.3a** are shown in Figure 6.5. Complex **6.2a** does not show a discernable $Os^{2+/3+}$ couple regardless of the initial direction of the potential scan, possibly due to poor solubility. The $Os^{2+/3+}$ couple for **6.3a** is poorly

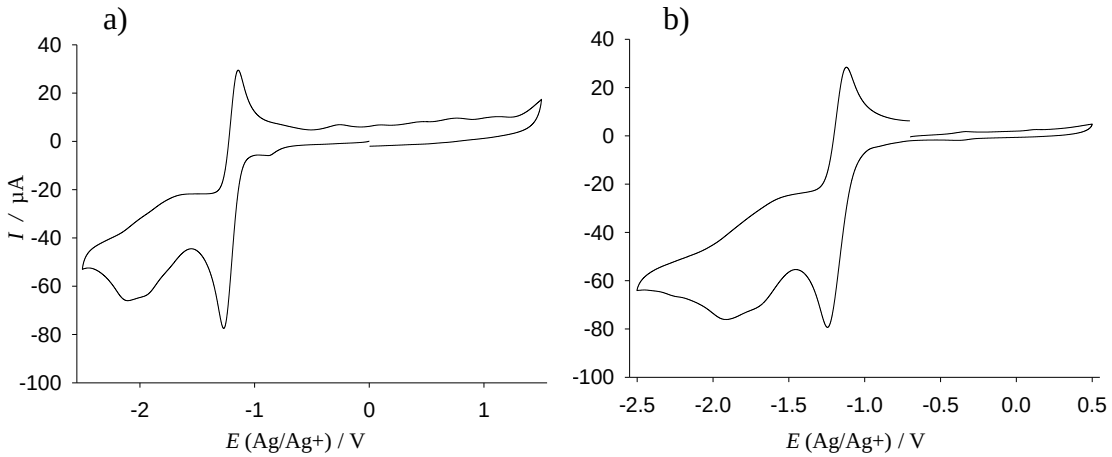

Figure 6.5. CVs of a) **6.2a** and b) **6.3a** in ACN / 0.1 M $TBABF_4$ at 100 mV s^{-1}. CV a) is commenced at 0 V and scanned to more negative potentials and b) is started at -0.5 and initially scanned in the positive direction.

resolved but discernable with an $E_{1/2}$ of -362 mV (Figure 6.6, black trace). This was compared to the CV of a sample of $Os(bpy)_2Cl_2$ (Figure 6.6, grey dashed trace) which has an $E_{1/2}$ of -343 mV. As with **6.1a** the $E_{1/2}$ is shifted to less positive values upon inclusion of an aryl amine functionality on the bipyridine ligands, consistent with a degree of electron donation making the metal centre more electron rich. The ΔE_p for **6.3a** is smaller than that of $Os(bpy)_2Cl_2$ suggesting that **6.3a** adsorbs to the electrode surface.

CVs of both **6.3a** and **6.2a** exhibit large unassigned redox couples at 1.18 and 1.21 V respectively (Figure 6.5). This couple persists with repeat scanning and is present regardless of which direction the CV is initiated in for either complex. The potential that this couple occurs at is inconsistent with osmium electrochemistry and therefore is most

likely associated with the ligands. Its origins have not been investigated further. For complexes **6.2a** and **6.3a** Figure 6.5 shows that there is also poorly defined redox activity between –1.7 and -2.1 V. By comparison with the CV of $Os(bpy)_3.2PF_6$ this is most reasonably assigned to reduction of the bpy-ph-NH_2 ligands.

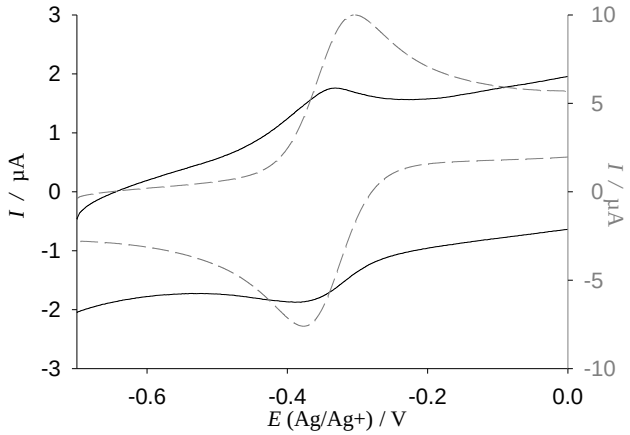

Figure 6.6. CV peaks associated with the $Os^{2+/3+}$ couples of **6.3a** (black line) and $Os(bpy)_2Cl_2$ (grey dashed line) in ACN / 0.1 M $TBABF_4$ at scan rate = 100 mV s^{-1}.

6.3.2 Grafting of osmium complex diazonium salts

6.3.2.1 Grafting of 6.1d and 6.2d

Isolation of diazonium cations as tetrafluoroborate salts is a common method of producing diazonium salts which are stable as dry solids. [15] This work utilizes the most common method of synthesis, i.e. diazotization in aqueous fluoroboric acid giving a precipitate of the diazonium tetrafluoroborate salt. After conversion of the two tris bipyridine substituted osmium complexes to their respective diazonium tetrafluoroborate salts (**6.1d** and **6.2d**), CVs were recorded in order to examine their grafting behavior at a glassy carbon disc electrode. Figure 6.7 shows every tenth CV of 80 repeat CVs from 0 to -1.1 V returning to +1.0 V, for **6.2d**. The CVs show a peak close to –1.0 V attributed to reduction of the diazonium functionality and a well defined $Os^{2+/3+}$ couple, the current of which increases with each repeat cycle. The surface concentrations of osmium complex

were calculated from the area under the oxidation peak, of the $Os^{2+/3+}$ couple, for every fifth cycle and are shown in Figure 6.8 a). Also shown are the ΔE_p and $E_{1/2}$ values for every fifth cycle (Figure 6.8 b)). Initially the rate of deposition was slow at 0.47×10^{-10} mol cm^{-2} per CV (Figure 6.8 a)) followed by an increase between scans 20 and 40 to 1.57×10^{-10} mol cm^{-2} per CV and then a decrease to a constant deposition rate of 0.96×10^{-10} mol cm^{-2} per CV over the final 30 - 40 grafting cycles. The first CV had a ΔE_p of 75 mV which is consistent with a species diffusing from solution (Figure 6.8 b) blue trace). With repeated cycling the ΔE_p rapidly decreased to a minimum of 26 mV after 18 cycles. This value is too small for a diffusing species indicating that the osmium complexes are

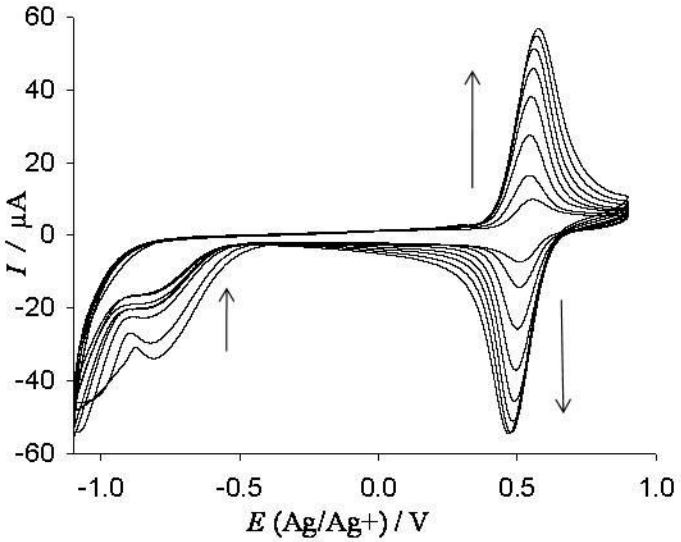

Figure 6.7. Repeat CVs obtained in a saturated solution of **6.2d** in ACN / 0.1 M $TBABF_4$ at scan rate = 100 mV s^{-1}. Depicted is every 10^{th} cycle of 80 showing increasing peak currents for the $Os^{2+/3+}$ couple.

surface bound. ΔE_p steadily increased to 118 mV after 80 cycles reflecting an increase in the resistance to charge transfer through the growing film. Figure 6.8 b) (pink trace) shows $E_{1/2}$ =540 mV for the first cycle. This value is more positive than that established for $Os(bpy)_3^{2+}$ ($E_{1/2}$ =527 mV), consistent with the electron withdrawing nature of the diazonium substituents on the ligands making the complex more difficult to oxidize. As the film formed, the $E_{1/2}$ decreased over 30 cycles to an average value of 523 ± 2 mV.

This is consistent with loss of the diazonium functionality and an osmium environment in the film similar to that in the $Os(bpy)_3^{2+}$ cation.

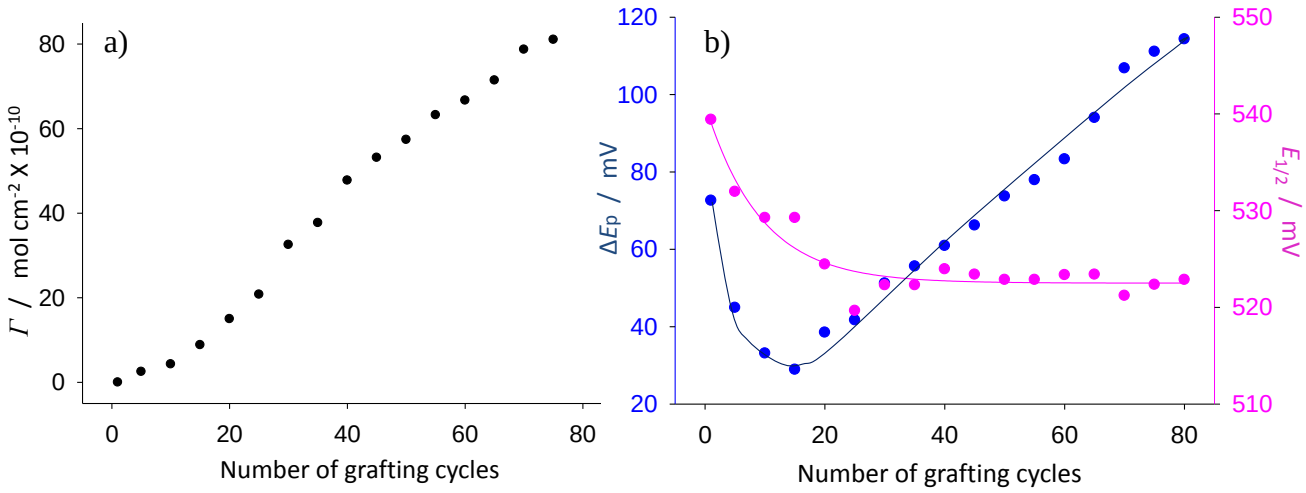

Figure 6.8. a) concentration of surface bound osmium complex *vs.* scan number for grafting from a saturated solution of **6.2d** in ACN / 0.1 M $TBABF_4$ at scan rate = 100 mV s^{-1}. b) ΔE_p (blue line) and $E_{1/2}$ (pink line) for the $Os^{2+/3+}$ couple *vs.* scan number.

CVs of **6.1d** were also consistent with grafting of osmium complexes. Figure 6.9 a) shows every fifth cycle of 50 scans commenced at 0 V and scanned in the negative direction to -0.8 V and back to 0.9 V in a saturated solution of **6.1d**. There is a clearly defined $Os^{2+/3+}$ couple with $E_{1/2} \approx 0.5$ V and peak currents that increased with each repeat cycle. The concentrations of osmium complex for each cycle in Figure 6.9 a) was calculated by integration of the $Os^{2+/3+}$ couple oxidation peak and are shown in Figure 6.10 a) i). For comparison, the first 20 cycles for grafting of **6.2d** are shown (Figure 6.10 a) ii)). Clearly the deposition rate of **6.1d** is significantly lower than that of **6.2d**. This difference is undoubtedly due, at least in part, to the lower solubility of **6.1d** than **6.2d** in ACN. The fact that **6.1d** has only one diazonium-substituted ligand compared to three for **6.2d** may also be a contributing factor.

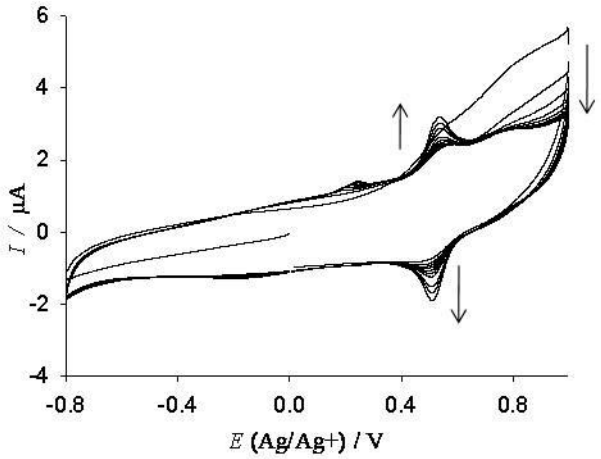

Figure 6.9. 50 repeat CVs obtained in a saturated solution of **6.1d** in ACN / 0.1 M $TBABF_4$ at scan rate = 100 mV s^{-1}.

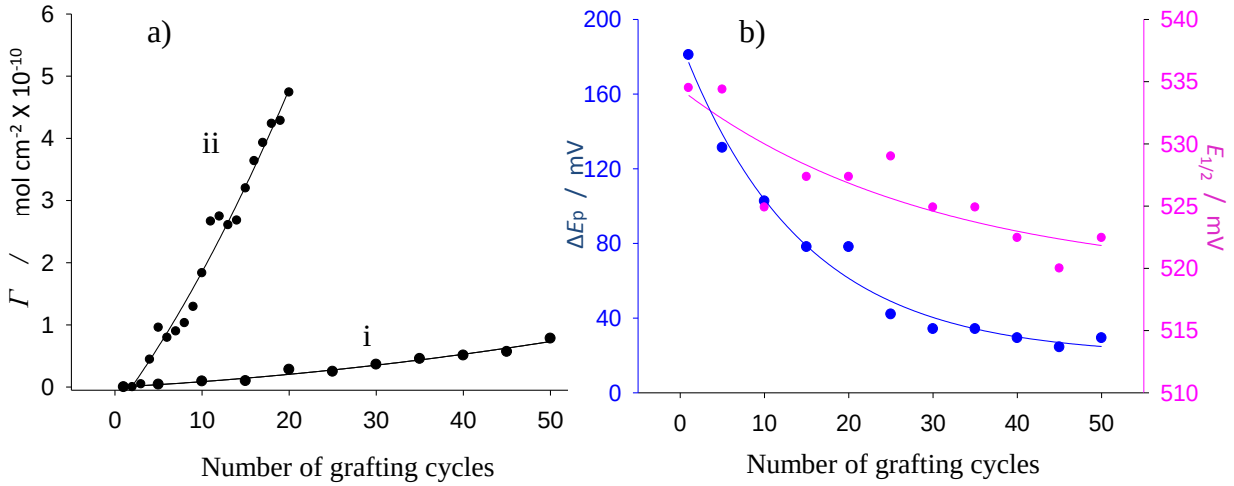

Figure 6.10. a) Concentration of surface bound osmium complex *vs.* grafting scan number in a saturated solution of **6.1d** (i) and **6.2d** (ii) both in ACN / 0.1 M $TBABF_4$ at scan rate = 100 mV s^{-1}.(b) ΔE_p (blue trace) and $E_{1/2}$ (pink trace) for the $Os^{2+/3+}$ couple *vs.* grafting scan number.

The ΔE_p and $E_{1/2}$ values for the $Os^{2+/3+}$ couple from each of the grafting cycles in Figure 6.9 a) are shown in Figure 6.10 b). The ΔE_p of the $Os^{2+/3+}$ couple in the first cycle was 170 mV indicating slow kinetics for this molecule diffusing from solution to a GC electrode. After 50 cycles the ΔE_p decreased to 38 mV showing that the osmium complex was surface bound. The low concentration of the surface bound osmium complex

concentrations for **6.1d** is the likely reason why there is no increase in ΔE_p with increasing scan number. The $E_{1/2}$ for the $Os^{2+/3+}$ couple in the first CV was 535 mV which is very close to that of **6.2d** (540 mV). The $E_{1/2}$ decreased over 50 cycles to 522 ± 3 mV. This value is the same as for the film derived from **6.2d** ($E_{1/2}$ = 523 ± 2) and is consistent with loss of the diazonium functionality and an osmium environment similar to that of $Os(bpy)_3^{2+}$. Because **6.1d** had lower solubility, was more difficult to synthesize, had slower grafting rates and generally showed similar electrochemical behavior to **6.2d**, it was not investigated further.

6.3.2.2 Effect of grafting potential on the grafting rate of 6.2d

A series of CVs were conducted using a saturated solution of **6.2d** to examine the effect of grafting potential on the osmium complex film deposition rate. CVs were commenced at 0 V and scanned first in the negative direction to a selected value and then back to 0.9 V to detect the development of the film. Twenty repeat CVs to lower potential limits of -0.6, -0.8, -1.0, -1.2, and -1.4 V were recorded and the surface bound concentration of osmium was calculated for each CV from the area under the $Os^{2+/3+}$ oxidation peak. The 20^{th} cycle for each set is shown in Figure 6.11 and the surface bound osmium complex concentrations *vs.* grafting number for each set are shown in Figure 6.12.

The set of CVs to a lower potential limit of -0.6 V (Figure 6.11 and Figure 6.12 black trace) shows no change in the Os^{2+3+} couple over the 20 cycles indicating that no grafting is occurring at this potential. The 20^{th} cycle had an $E_{1/2}$ of 541 mV consistent (by comparison with Figure 6.8 b) with the osmium diazonium complex in solution. The sets of CVs to lower potentials of -0.8 and -1.0 V (Figure 6.11 and Figure 6.12 pink and blue traces respectively) exhibited increased peak currents for the $Os^{2+/3+}$ couple and a decrease in both the $E_{1/2}$ and the ΔE_p of the $Os^{2+/3+}$ couple on reapeat scans consistent with loss of the diazonium functionality leading to surface bound complexes. The set of CVs with a lower potential limit of -1.2 V (Figure 6.11 and Figure 6.12 green trace) showed a

marked increase in the deposition rate and a final $E_{1/2}$ = 520 mV and ΔE_p = 52 mV in agreement with the previously described films. The sharp increase in the grafting rate of osmium complexes when the lower potential limit of the grafting CVs is below -1.0 V strongly supports the assignment of the peak between -1.0 and -1.2 V to reduction of the diazonium functionality.

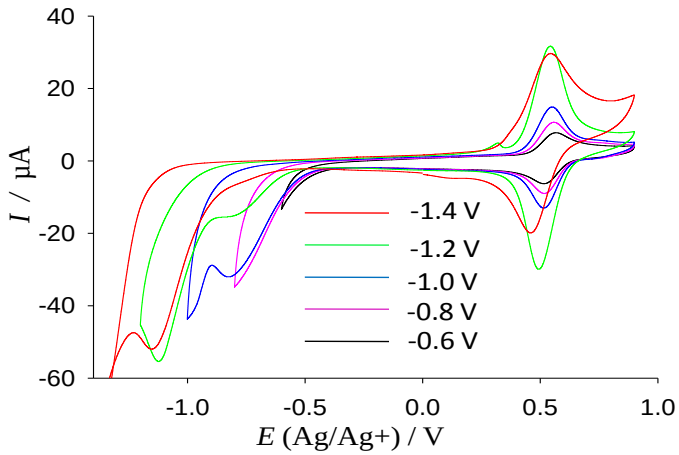

Figure 6.11. The 20th cycle of sets of CVs with the lower potential limits listed in the insert for a saturated solution of **6.2d** in ACN / 0.1 M $TBABF_4$, scan rate = 100 mV s^{-1}.

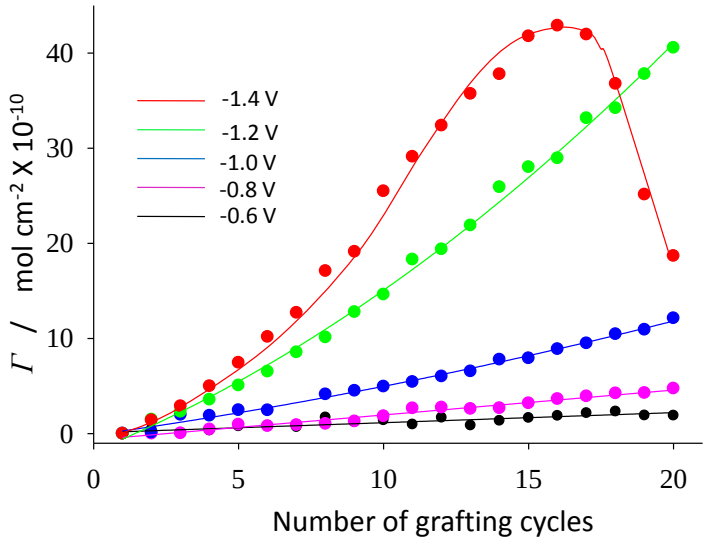

Figure 6.12. Surface concentration of osmium complex *vs.* number of grafting cycles to the lower potential limits listed in the insert for a saturated solution of **6.2d** in ACN / 0.1 M $TBABF_4$, scan rate = 100 mV s^{-1}.

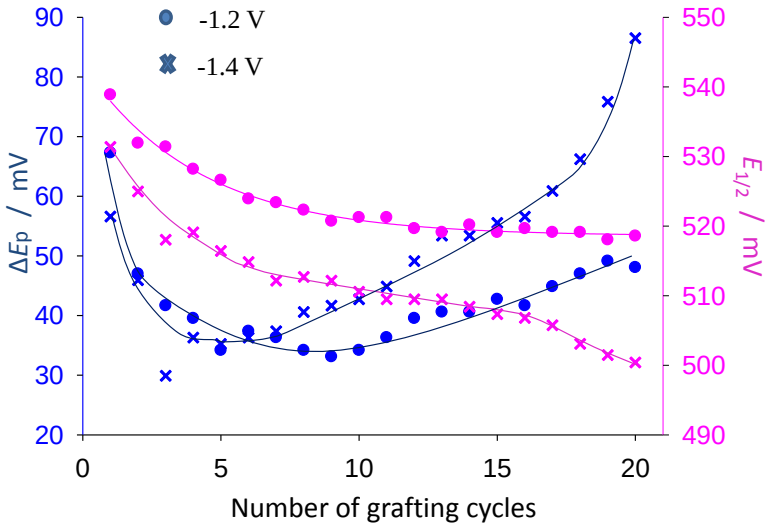

Figure 6.13. $E_{1/2}$ (pink) and ΔE_p (blue) values for the $Os^{2+/3+}$ couple *vs.* number of grafting cycles in a saturated solution of **6.2d** to the lower potential limits of -1.2 V (closed circles) and -1.4 V (crosses) in ACN / 0.1 M $TBABF_4$, scan rate = 100 mV s^{-1}.

The peak currents associated with the $Os^{2+/3+}$ couple of the grafting cycles with a lower potential limit of -1.4 V (Figure 6.11 and Figure 6.12 red trace) increased rapidly up to the 15th cycle but then decreased. The $E_{1/2}$ and ΔE_p values for the $Os^{2+/3+}$ couple for the same cycles also exhibited differences from those obtained with more positive lower potential limits. Figure 6.13 shows the $E_{1/2}$ (pink trace) and ΔE_p (blue trace) values for the films grafted with lower potential limits of -1.2 V (closed circles) and -1.4 V (crosses). The film grafted with a lower potential limit of -1.2 V showed the expected trends in $E_{1/2}$ and ΔE_p as discussed in the previous paragraph. The film grafted with a lower potential limit of -1.4 V behaved as expected for the first 15 cycles, but then showed rapid changes in the $E_{1/2}$ and ΔE_p over cycles 16 -20. The apparent decrease in surface concentration of osmium complex suggests that significant changes in the grafted film structure occur when grafting with a lower potential limit of -1.4 V. This phenomenon was reproducible and is discussed further in the film stability section (6.3.4).

6.3.2.3 Grafting of 6.3d

A series of similar experiments to those described for **6.2d** were conducted using **6.3d.** The surface concentration of osmium complex and the $Os^{2+/3+}$ couple $E_{1/2}$ and ΔE_p values are shown in Figure 6.14. As found for **6.2d** the rate of deposition of osmium complex was negligible when the lower potential limit was -0.6 V and was slow when the limit was -0.8 V (Figure 6.14 black and pink trace). The deposition rate increased significantly with a lower potential limit of -1.0 V (Figure 6.14 blue trace) and -1.2 V (Figure 6.14 green trace). This supports the assignment of the peak at -1.0 V to -1.2 V to reduction of the diazonium functionality. The CV for the sample with the lower potential limit of -1.4 V (Figure 6.14 red trace) shows the fastest rate of osmium complex

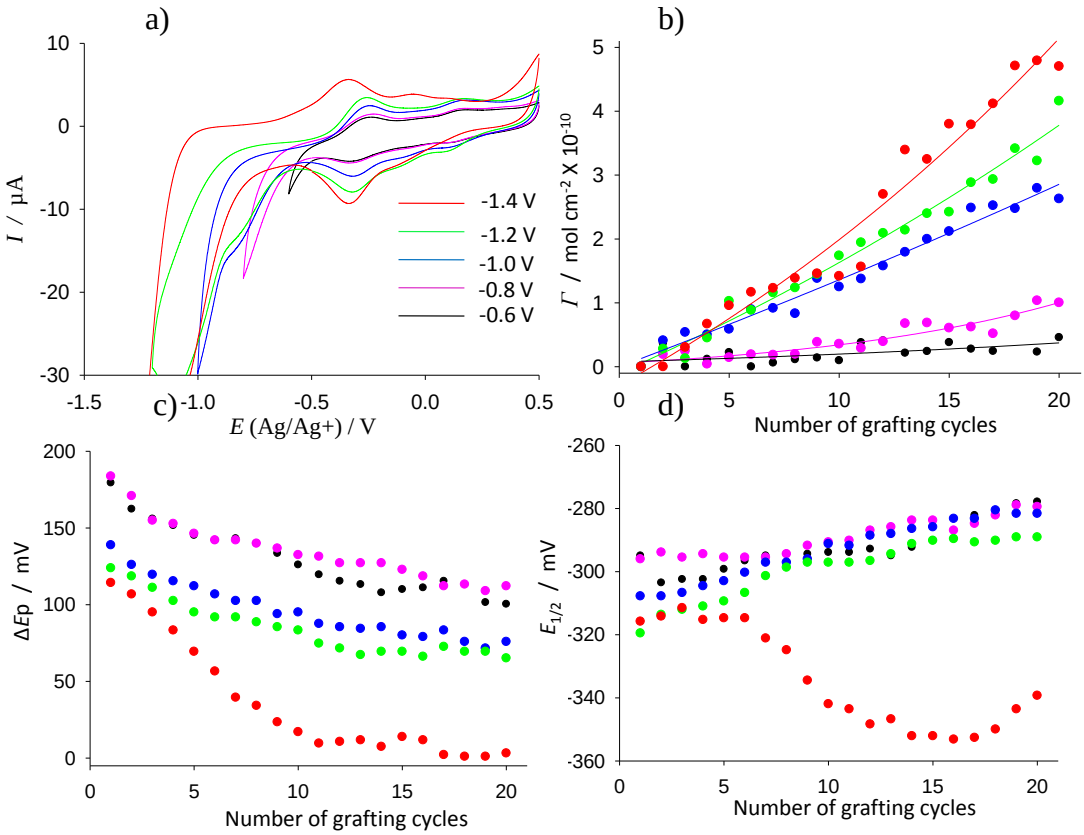

Figure 6.14. a) The final scan of 20 CVs to the lower potential limits listed in the insert. b) Surface bound osmium complex concentration *vs.* scan number of for each cycle. c) ΔE_p and d) $E_{1/2}$ values *vs.* scan number for the $Os^{2+/3+}$ couples for each cycle. The colour coding for the potential limits in plot a) apply to all four graphs and all CVs were obtained in a saturated solution of **6.3d** in ACN / 0.1 M $TBABF_4$, scan rate = 100 mV s^{-1}

deposition which, unlike the corresponding CV of **6.2d (**Figure 6.12**),** does not begin to decrease at high grafting cycle counts. There is however a significant increase in the background current of the CV indicating that changes in the film have occurred. For all grafting CVs the ΔE_p for the Os^{2+3+} couple decreased with repeated grafting cycles. As explained earlier, this is consistent with a contribution to the electrochemical response from surface confined osmium complexes. The decrease in ΔE_p for the Os^{2+3+} couple was greater for grafting using more negative potential limits consistent with formation of a thicker film and a greater proportion of redox activity arising from surface confined osmium complexes. Interestingly the ΔE_p of the film grafted at -1.4 V dropped to almost zero, substantially lower than the films formed at more positive lower potentials. The $E_{1/2}$ values for the Os^{2+3+} couples in initial scans were close to -310 mV. This value is more positive than that of $Os(bpy)_2Cl_2$ (-343 mV) consistent with the electron withdrawing diazonium functionality on the ligands in **6.3d**. With repeat cycling to all lower potential limits (except -1.4 V) the $E_{1/2}$ increased slightly. This is unexpected as loss of the electron withdrawing diazonium should result in a more electron rich metal center which should be correspondingly easier to oxidize. The $E_{1/2}$ values for the $Os^{2+/3+}$ couple for the CVs with a lower potential limit of -1.4 V decreased by 30 mV over 20 cycles. The differences in the trends in the $Os^{2+/3+}$ $E_{1/2}$ and ΔE_p values for the grafting CVs with a lower potential limit of -1.4 V compared with those with more positive limits indicates that changes in the film structure occur when grafting CVs are extended to – 1.4 V.

6.3.3 Electron transfer kinetics

6.3.3.1 Low scan rate CV behavior

The electron transfer kinetics of the $Os^{2+/3+}$ couple for films derived from **6.3d** and **6.2d** were examined by CV. In both cases the films were grafted using 20 repeat CVs with a lower potential limit of -1.2 V. The modified electrodes were removed from the grafting solution and cleaned by sonication in ethanol and Milli-Q water and CVs of the clean films were recorded in fresh ACN and PBS electrolyte solutions.

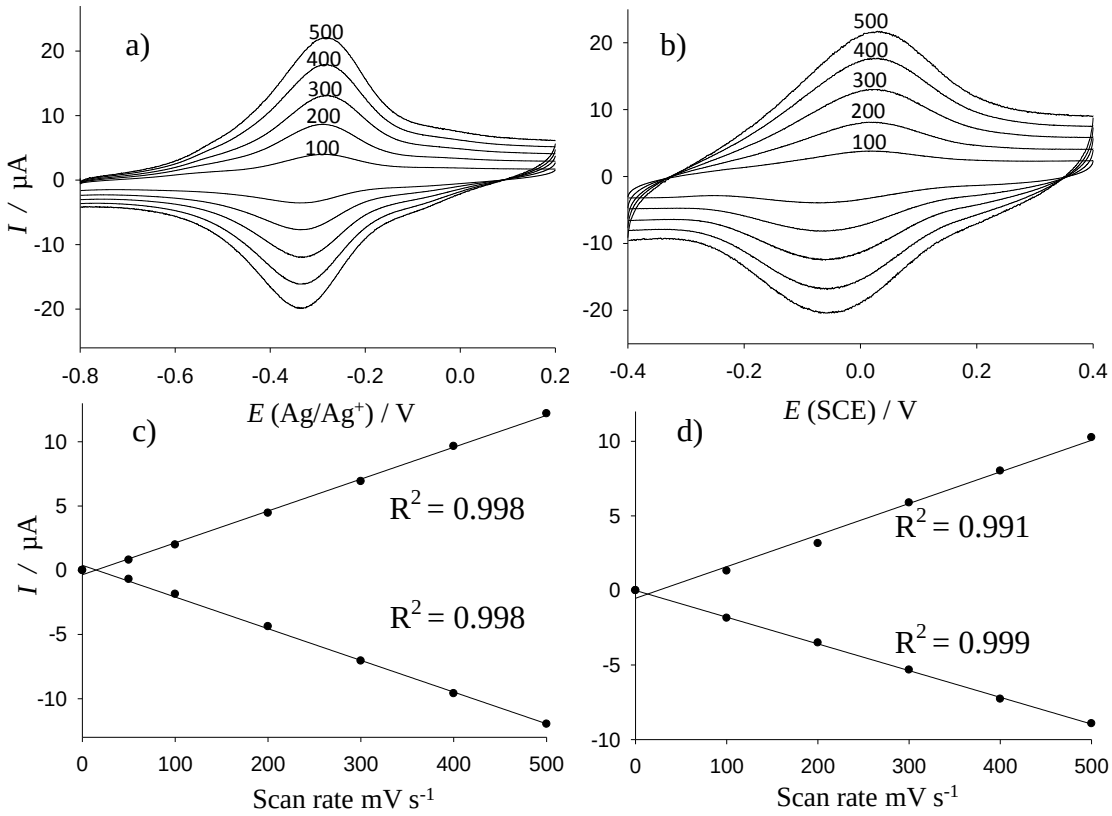

Figure 6.15. CVs of films derived from **6.3d** in a) ACN / 0.1 M $TBABF_4$ and b) 50 mM PBS / 0.1 M KCl. The scan rates are indicated on the CVs in mV s^{-1}. Also shown are plots of the background corrected oxidation and reduction peak currents for each CV obtained, c) in ACN and d) PBS.

The peak potentials for the CVs derived from **6.3d** are independent of scan rate below 500 mV s^{-1} in both ACN (Figure 6.15 a)) and PBS (Figure 6.15 b)). Figure 6.15 c)

and Figure 6.15 d) show plots of the oxidation and reduction peak currents *vs.* scan rate in ACN and PBS respectively. Both Figure 6.15 c) and Figure 6.15 d) show linear relationships for peak current *vs.* scan rate of the $Os^{2+/3+}$ redox process and *y* intercepts that are close to zero. This strongly indicates a surface confined species. The slope for the lines in Figure 6.15 c) are 0.025 ± 0.005 and -0.025 ± 0.005 (error estimate corresponds to the standard error of the slope, calculated during the linear regression) for the oxidation and reduction peak currents respectively. The corresponding slopes for Figure 6.15 d) are 0.023 ± .001 and -0.021 ± .001. In both cases the slopes are symmetrical around the *x* axis indicating that the oxidation and reduction processes for the $Os^{2+/3+}$ couple in ACN and PBS are chemically reversible. Figure 6.16 shows the same data for a film derived from **6.2d**. In ACN the CVs exhibit scan rate independent peak potentials and peak currents that depend linearly on scan rate (Figure 6.16 a) and c)). The slopes for the lines

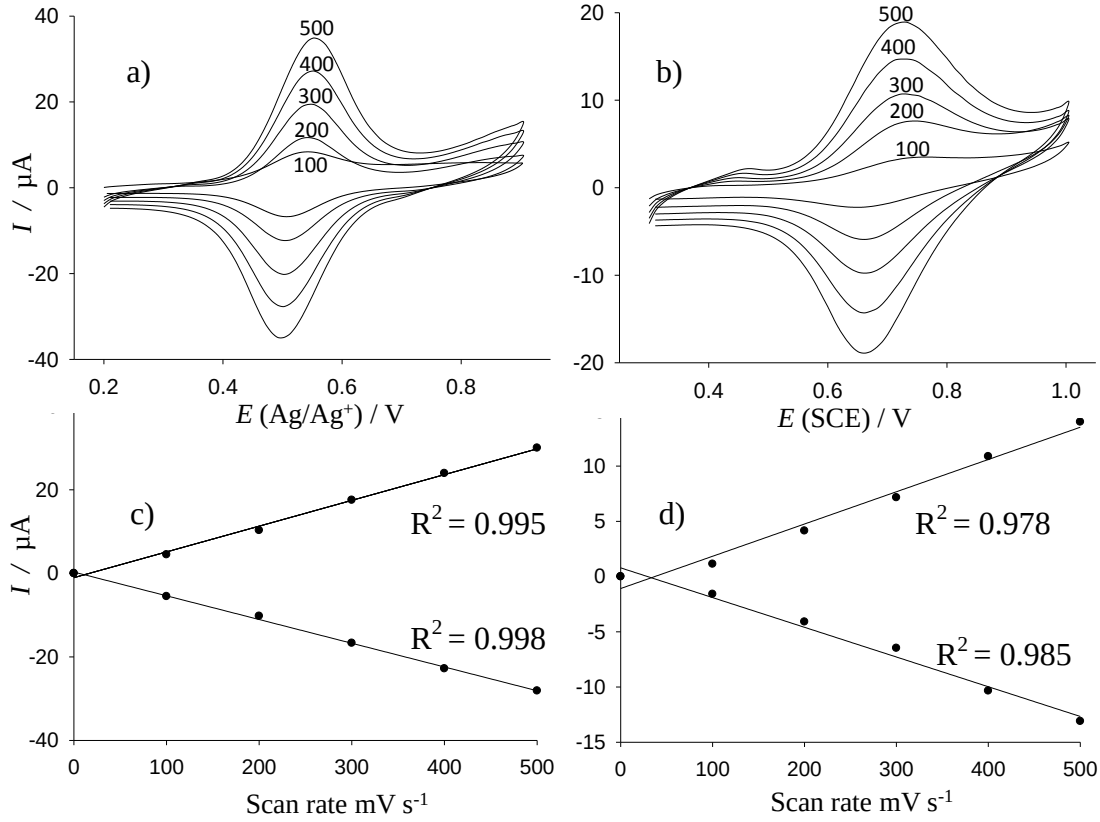

Figure 6.16. CVs of films derived from **6.2d** in a) ACN 0.1 / M $TBABF_4$ and b) 50 PBS / 0.1 M KCl. The scan rates for the CVs are indicated on the plots in mV s^{-1}. Also shown are plots of the background corrected oxidation and reduction peak heights for each CV c) in ACN and d) in PBS.

in Figure 6.16 c) are 0.062 ± 0.002 and -0.057 ± 0.0012. The small differences in the values of the slopes obtained may indicate that the film environment has an influence on the response. The CVs for the same film in PBS did not follow well-behaved surface confined redox behavior. Although the reduction peak potentials did not change for scan rates up to 500 mV s^{-1}, the potential of the oxidation peaks decreased as the scan rate increased (Figure 6.16 b)). This gave peak current against scan rate plots that showed poorer linearity than those obtained in ACN and best fit lines that did not pass through the origin (Figure 6.16 d). It appears that this film undergoes rearrangement during CV in PBS. The low scan rate CVs were conducted first, after obtaining CVs in ACN, and have been influenced by this process. Further evidence of this rearrangement was also seen in the plots discussed in the next section and in the film stability section (6.3.4)

6.3.3.2 Calculation of heterogeneous rate transfer coefficients

Heterogeneous rate transfer coefficients and transfer constants were calculated for grafted films derived from **6.2d** using the well known Laviron formalism. [16-18]**.** The film was grafted to the working electrode using 20 repeat CVs in a saturated solution of **6.2d** in ACN / 0.1 M $TBABF_4$, scan rate 100 mV s^{-1}, to a lower potential limit of -1.2 V. The Laviron formalism is based on equations 6.3.3.1 and 6.3.3.2 for CVs of a surface bound redox active film, where: E_{pc} and E_{pa} are the $Os^{2+/3+}$ couple cathodic and anodic peak potentials; $E^{0'}$ is the formal reduction potential of the complex (estimated as the average $E_{1/2}$ from all CVs); and α is the $Os^{2+/3+}$ couple transfer coefficient (0.5 is a kinetically symmetrical redox process); n is the number of electrons in the redox process; v is the potential scan rate of the CV; κ_c and κ_a are the $Os^{2+/3+}$ couple cathodic and anodic rate transfer coefficients and F,R and T take their usual meanings.

$$E_{pc} = E^{0'} - (2.3RT/\alpha nF)\log(\alpha nFv/RT\kappa_c) \qquad 6.3.3.1$$

$$E_{pa} = E^{0'} - (2.3RT/(1-\alpha)nF)\log((1-\alpha)nFv/RT\kappa_a) \qquad 6.3.3.2$$

.

CVs were recorded at scan rates from 0.05 V s^{-1} to 30 V s^{-1} for a film derived from **6.2d.** Plots of (E_{pc} - $E^{0'}$) and (E_{pc} - $E^{0'}$) against log(v) in ACN are shown in Figure 6.17 a) and PBS Figure 6.17 b). Figure 6.17 shows straight lines of best fit for the high scan rate data extrapolated to the x axis to give the critical scan rates v_c and v_a. The value of α can be calculated from the slopes of the lines allowing the rate transfer coefficients κ_c and κ_a to be calculated according to equations 6.3.3.3 and 6.3.3.4.

$$\kappa_c = \alpha n F v_c / RT \qquad 6.3.3.3$$

$$\kappa_a = (1-\alpha) n F v_a / RT \qquad 6.3.3.4$$

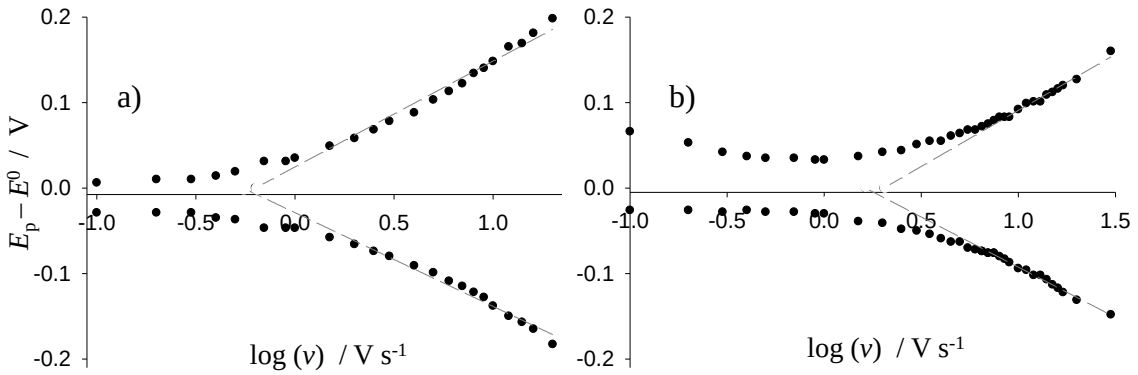

Figure 6.17. Plots of (E_{pc} - $E^{0'}$) and (E_{pc} - $E^{0'}$) against log(v) for a film derived from **6.2d** in a) ACN 0.1 M $TBABF_4$ and b) 50 mM PBS 0.1 M KCl.

The plots for the CVs obtained in ACN (Figure 6.17 a)) shows that ΔE_p increases significantly at scan rates greater than 1 V s^{-1} (zero on the log scale). A linear fit of these data points gives α = 0.483 (from the oxidation peaks) and (1- α) = 0.544 from the reduction peaks to give an average α = 0.47. Extrapolation of the high scan rate data to the x axis gives v_a = 0.630 and v_c = 0.549 V s^{-1} and rate coefficients κ_c = 11.3 s^{-1} and κ_a = 11.5 s^{-1} the average of which estimates the apparent heterogeneous rate transfer coefficient κ_{app} = 11.4 s^{-1}. The plots for the same surface in PBS (Figure 6.17 b)) show that the ΔE_p decreases as the scan rate increases. This is attributed to rearrangement of the

film during the initial CV cycles in PBS as discussed in section 6.3.3.1. The values obtained after extrapolation of the high scan rate data are $\alpha = 0.455$ and $(1 - \alpha) = 0.509$ to give and average α value of 0.47 in agreement with the value in ACN. The critical scan rate values were v_a = 2.028 and v_c = 1.630 V s^{-1} yielding respective transfer coefficients of $\kappa_a = 37.4\ s^{-1}$ and $\kappa_c = 33.5\ s^{-1}$ and $\kappa_{app} = 35.4\ s^{-1}$.

The heterogeneous rate transfer coefficients of the diazonium derived films are similar to values established for ferrocene methanol attached to carbon nanotubes films $\kappa_{app} = 15.6$ [19] and $\kappa_{app} = 21\ s^{-1}$ [20] but are low compared to a ferrocene monolayer directly attached to silicon which has been measured at $\kappa_{app} = 6.5 \times 10^4\ s^{-1}$.[21] The low κ_{app} for ferrocene on carbon nanotubes was attributed to barriers to electron tunneling through the nanotube assemblies.[20] The values established for the films discussed in this work are also low compared to those for monolayers of osmium complexes on platinum microelectrodes [22, 23] and lower than the value of 90 s^{-1} established by Boland *et al.* [24] for osmium complexes covalently coupled to a carboxyphenyl tether layer on GC. In the first study Forster and Faulkner determined heterogeneous rate coefficients for $Os(bpy)_2Cl_2$ phyisisorbed to platinum as $6.3 \times 10^4\ s^{-1}$ in H_2O / 0.1 M $NaClO_4$ and $1.8 \times 10^4\ s^{-1}$ in ACN / 0.1 M tetraethylammonium perchlorate. They explain the higher κ_{app} in water by application of the Frank-Condon principle as it applies to solvation which predicts a higher κ_{app} in water due to the short relaxation time of water compared to that of ACN. In this study and that of Boland *et al.* the osmium complexes are either directly adsorbed or very close to the electrode surface which may account for the faster transfer rates than those established for the very thick films formed in this work. If, as Schuhman *et al.* [7] propose, the conductivity of osmium complex polymer films is due to electron hopping between metal centers, then the conductivity of the film must be limited by the distance between the metal centers. The low κ_{app} for the diazonium derived film suggests that the metal centers are not tightly packed and significant barriers to tunneling between metal centers exist.

6.3.4 Film stability

Films derived from **6.3d** and **6.2d** were exposed to a range of conditions and potentials to establish their electrochemical stability. The films were electrografted using the same conditions as those described in sections 6.3.3.1 and 6.3.3.2. The films were subjected to continuous CV cycling using moderate potential limits, first in ACN and then in PBS. Separate films were exposed to extreme negative potentials to ascertain if film structure changes occur.

Figure 6.18 a) shows no change in the appearance of the $Os^{2+/3+}$ couple between the first (gray dash) and 100th cycle (black trace) for CVs obtained using potential limits of 0.2 and 1 V in ACN / 0.1 M $TBABF_4$ for the film derived from **6.2d**. The lack of change indicates that the film is stable under these conditions. The film derived from **6.3d** in ACN (Figure 6.18 c)) has several large irreversible oxidation peaks on the first scan (grey dash) which rapidly disappear with repeat cycling. There is also an unassigned redox couple ($E_{1/2}$ = 140 mV) which persists during the 100 cycles (Figure 6.18 c) black trace). The current due to the $Os^{2+/3+}$ couple of **6.3d** is unchanged after 100 cycles indicating high stability. Both films were transferred to PBS and subjected to a further 50 CVs. Figure 6.18 b) shows the first (gray dash), 10th (black trace) and 50th (red trace) scan for the film derived from **6.2d**. There is a large oxidation wave, which obscures the $Os^{2+/3+}$ couple, present on the first scan which becomes smaller with repeat cycling. After 50 cycles the $Os^{2+/3+}$ couple is evident ($E_{1/2} \approx 0.7$ V) and the CV ceases to change significantly. A further set of CVs in ACN Figure 6.18 a) (red trace, 10th cycle) shows a significant decrease in the $Os^{2+/3+}$ couple oxidation peak size and changes in the $E_{1/2}$, ΔE_p and symmetry of the CV. The response however is stable to repeat scanning. These results indicate that significant changes occur in the film when exposed to moderate potentials in PBS. Currently these changes are not understood and clearly require further investigation. It is worth noting that after cycling in ACN, then PBS, then again in ACN the altered film is extremely stable and withstood 30 min of ultrasonication in acetone with no observable changes. Figure 6.18 d), shows the first (black trace) and 50th (red trace) cycle for the film derived from **6.3d** in PBS. The first CV shows the expected $Os^{2+/3+}$ couple at $E_{1/2}$ = 15 mV and the unassigned second system at $E_{1/2}$ = 412 mV.

During 50 cycles the second couple decreases and the $Os^{2+/3+}$ couple $E_{1/2}$ shifts to -5 mV with reduced peak currents. When returned to the ACN electrolyte and exposed to a further 10 cycles Figure 6.18 c) (red trace) the unassigned second redox system remained absent and the $Os^{2+/3+}$ couple was similar in appearance to the first CV in ACN (Figure 6.18 c) (black trace)). Clearly the film derived from **6.3d** is stable in ACN with repeated cycling over moderate potentials. In PBS the film undergoes a short break-in process that removes some unidentified redox species but does not lead to significant changes in the $Os^{2+/3+}$ electrochemistry.

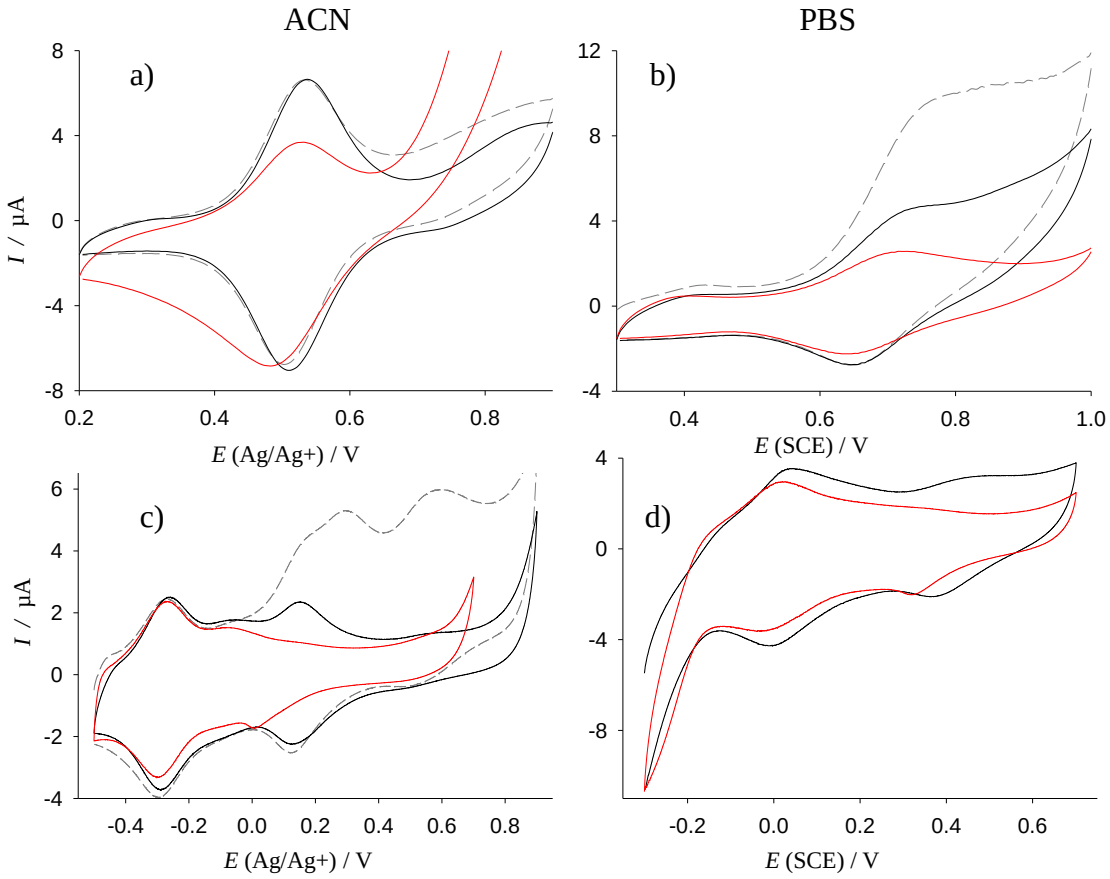

Figure 6.18. CVs of films derived from **6.2d** (a) and b)) and **6.3d** (c) and d)) in ACN and PBS as indicated. Plots a) and c) show scan 1 (grey dash) and scan 100 (black) in ACN and a CV after cycling in PBS (red). Plot b) shows scan 1 (grey dash), scan 10 (black) and scan 50 (red). Plot d) shows the 1st (black) and 50th (red) CV.

For both of the films discussed here exposure to potentials more negative than -1.4 V led to dramatic irreversible changes in the film electrochemistry including a complete loss of the $Os^{2+/3+}$ couple. CVs for the two derived films are shown in Figure 6.19. In each case CVs were commenced at a potential 500 mV below the $E_{1/2}$ for the $Os^{2+/3+}$ couple and scanned in the positive direction to 0.9 V before reversing to -2.5 V. The $Os^{2+/3+}$ redox couples for the two films appear on the first cycle at the expected potentials (Figure 6.19 (grey dashed traces)). On the reverse scan both CVs exhibit sharp, multi-electron, irreversible reduction peaks at $E_p \approx$ -1.5 V. The film derived from **6.3d**

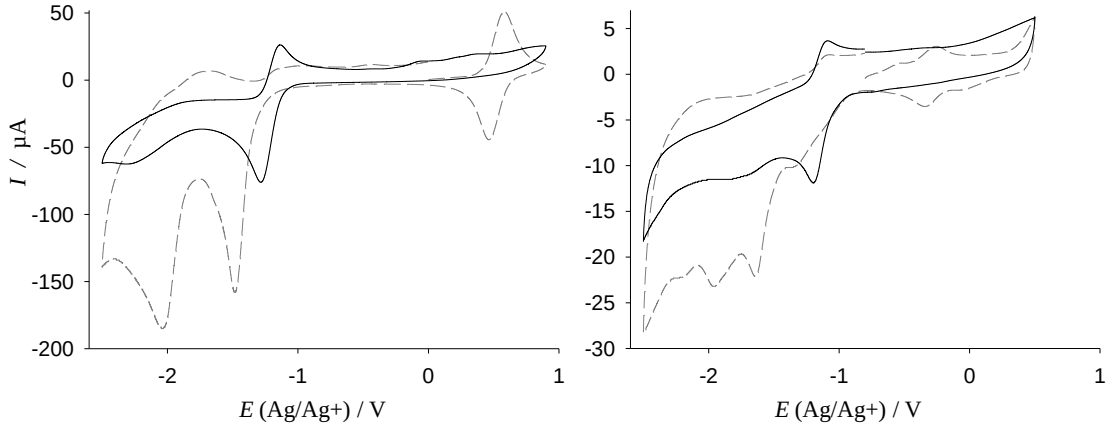

Figure 6.19. CVs of films derived from **6.2d** a) and **6.3d** b) in ACN / 0.1 M $TBABF_4$. Shown is the 1st (grey dash) and 5th (black) CV.

has reduction peaks at -1.64 and -1.97 V and the film derived from **6.2d** has peaks at -1.48 and -2.04 V. None of these peaks were observed in the CVs of the aminophenyl derivatives of these complexes (Figure 6.5) but the potentials are in the region of the bipyridine reductions for $Os(bpy)_3^{2+}$ (Figure 6.4 a) grey dash). Osmium has no known electrochemistry within the potential range of -1.5 to -2 V *vs.* Ag/Ag^+, therefore the observed peaks are most reasonably assigned to reduction of the ligands. On subsequent CVs the ligand reduction peaks and the $Os^{2+/3+}$ couple for both films are replaced by a single reversible couple at -1.21 V for the film derived from **6.2d** and -1.14 V for **6.3d.** These large reversible signals are also present in the CVs of the corresponding aminophenyl derivatives (Figure 6.5) with $E_{1/2}$ values of -1.21 V for **6.2a** and -1.18 V for **6.3a** hence it appears that 6.2a and 6.3a may adsorb to the surface and form film**s** and form redox active films when exposed to extreme negative potentials. The structure of

these films and the mechanism of the loss of the $Os^{2+/3+}$ redox chemistry in the diazonium osmium complex derived films has not been investigated further.

6.3.5 SEM and AFM analysis

Films derived from **6.3d** and **6.2d** were grafted onto PPF electrodes. Films were grafted by 20 repeat CVs to lower potential limits of -0.8 or -1.2 V using the same conditions as those previously described. The films were visualized by SEM and the thickness of the films established by the AFM scratching method described in the experimental section. SEM images for the films are shown in Figure 6.20. The images show that the films are uneven and globular in appearance. The films derived from **6.2d** are lumpy with protruding outgrowths (Figure 6.20 a) and b)). These outgrowths are of the order of 100 nm in diameter. When a lower grafting potential limit of -0.8 V was used the outgrowths are smaller and less frequent (Figure 6.20 b)). SEM images of films derived from **6.3d** were more homogeneous but notably rougher then those of **6.2d** (Figure 6.20 c) and d)). Again the roughness and outgrowth size increased with more negative grafting potential limits. It has been previously observed with grafting of diazonium films that more negative lower potential limits form higher roughness films. [25]

The films grafted at -1.2 V shown above in Figure 6.20 were depth profiled by AFM. One AFM cantilever was used to remove a section of the film and a second to image the depth of the resulting trench. Figure 6.21 shows AFM images and trench profiles for films derived from a) **6.2d** and b) **6.3d**. The thicknesses for the two films were measured as 42 ± 2 and 28 ± 2 nm respectively. The roughness at base of the trenches was between 1 and 0.55 nm which is consistent with bare PPF confirming that the film had been completely removed. In both cases the films are exceptionally thick for diazonium salt derived films. [26, 27] Typically films derived from aryl diazonium salts terminate at thicknesses below 10 nm. This once again confirms the conducting nature of the films and their ability to continue to reduce diazonium cations in solution even when the film has become very thick. The concentration of electrochemically active osmium complex for each film that was profiled was calculated from the area under the oxidation peak from their respective CVs and compared to a theoretical densely packed film. The

concentration of the film derived from **6.2d** was 19 x 10^{-10} mol cm^{-2} and 4.4 x 10^{-10} mol cm^{-2} for **6.3d**. A close packed monolayer of complexes with the general formula $M(bpy)_3^{n+}$ (where M is any metal) is generally estimated as 1 x 10^{-10} mol cm^{-2}. [10, 28] This equates to a molecular radius of 0.7 nm assuming that the complexes are spherical and packed hexagonally. This gives a film density value of 55 % for **6.2d** and 18.3 % for **6.3d**. The density of nitrophenyl films derived electrochemical reduction of diazonium salts has been determined previously as 21 ± 3% of the theoretical maximum using the same AFM scratching method. [26] Considering that the molecules in question here are larger than the $M(bpy)_3^{3+}$ model used to calculate the theoretical densely packed film means that the calculated density values are likely to be under estimations. Regardless of this it is clear that both of the films are loosely packed multilayered films and films derived from **6.2d** have a higher packing density than **6.3d**.

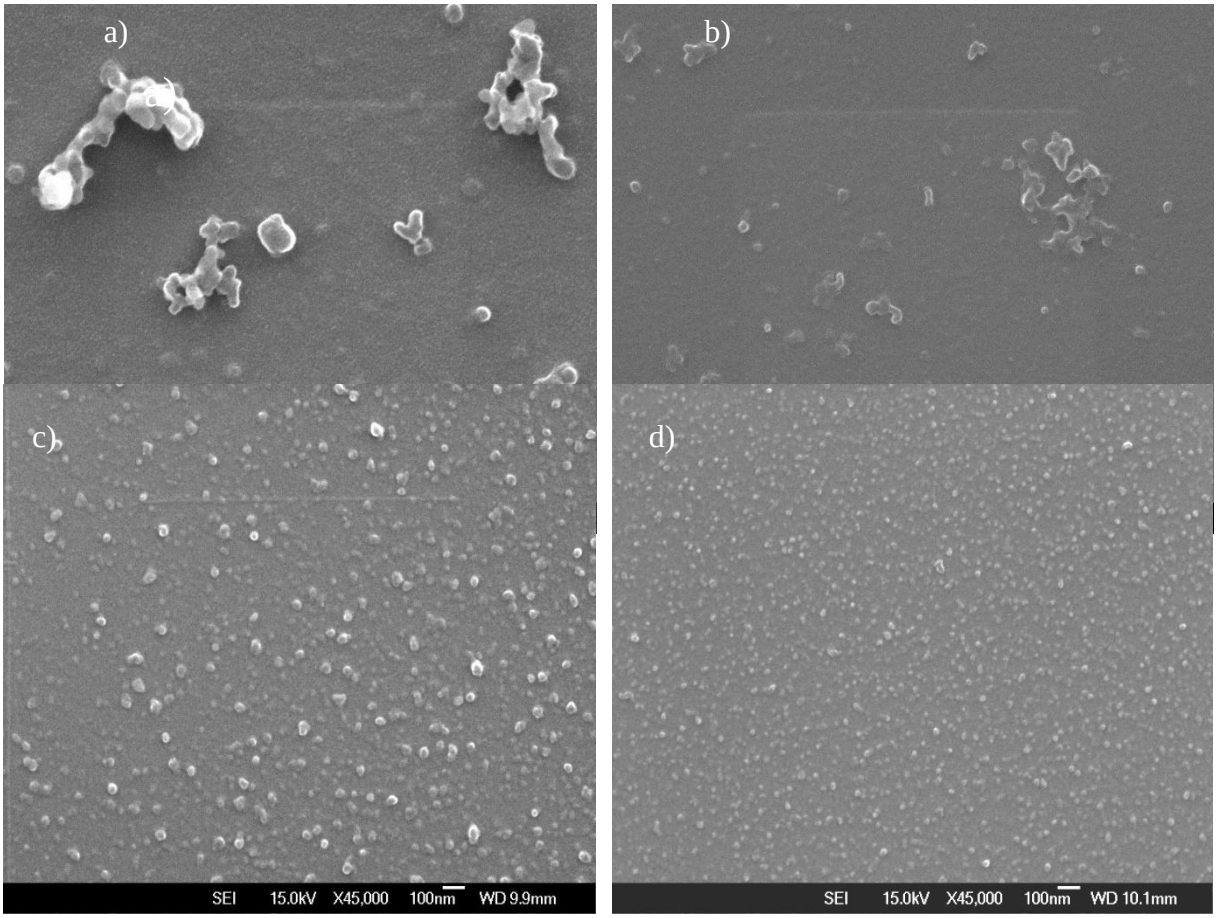

Figure 6.20. Magnified view of films derived from **6.2d** grafted by 20 CVs down to a) -1.2 and b) -0.8 V in ACN 0.1 M $TBABF_4$ at 100 mV s^{-1} and **6.3d** to c) -1.2 and d) -0.8 V

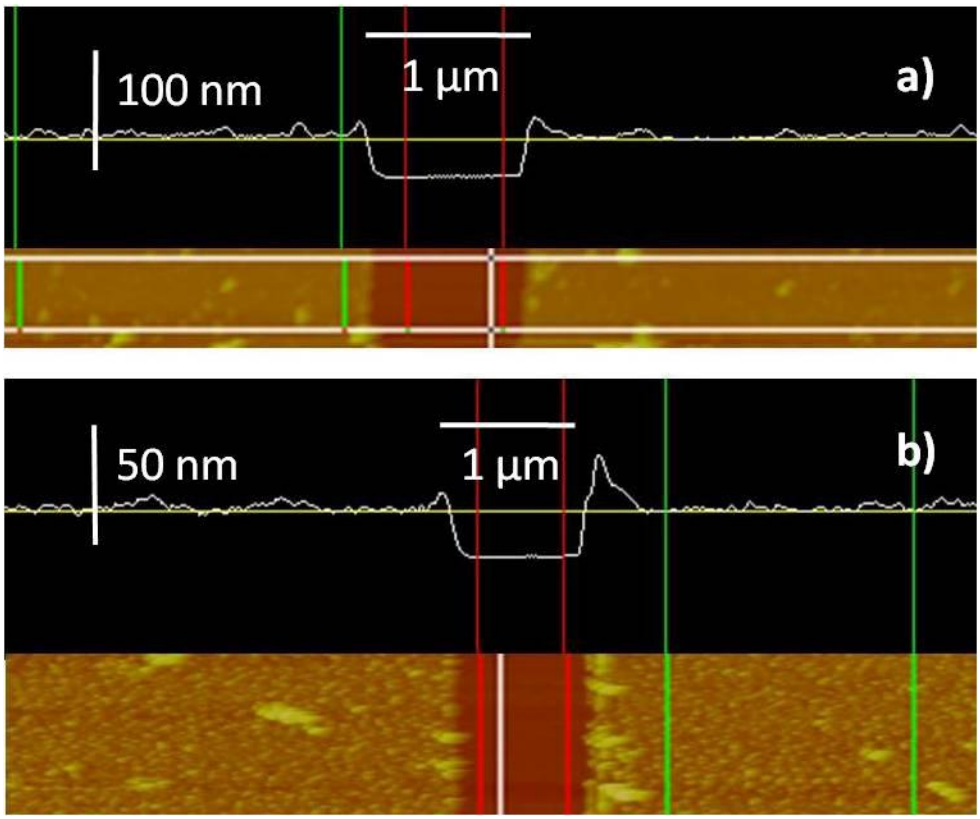

Figure 6.21. AFM images and thickness profiles for films derived from a) **6.2d** and b) **6.3d** grafted to -1.2 V in ACN / 0.1 M $TBABF_4$.

6.3.6 Further discussion

The films derived from **6.2d**, and **6.3d** have the highest electrochemically active osmium concentrations recorded for a film on a flat substrate. The highest $Os^{2+/3+}$ concentration for a film derived from **6.2d** was 70 x 10^{-10} mol cm^{-2} and 5 x 10^{-10} mol cm^{-2} for films derived from **6.3d**. The highest concentrations recorded for osmium complexes covalently attached to tether layers are below 3 x 10^{-10} mol cm^{-2}. [24] The films are also rough which increases the surface area presented to the electrolyte solution. The high concentration of redox mediator and high surface area are likely to increase the ability of the films to act as effective mediators for adsorbed analytes.

In the recent work of Agnes *et al.* [11] an XPS analysis of a film derived electrochemically from $[Ru(bpy)_2(bpy\text{-}ph\text{-}N_2^+)]^{3+}$ was undertaken. In discussing that work they note that there appears to be a significant contribution from azo bonds in the film as well as a contribution from free ligands. The structure of the film they propose is depicted in Figure 6.22. The low packing densities established by AFM and the slow electron transfer that the films exhibit are strong evidence that films derived from osmium diazonium complexes adopt a similar structure.

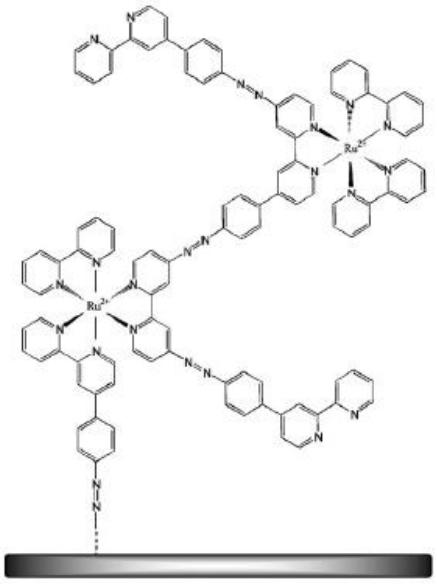

Figure 6.22. The structure of a film derived from $[Ru(bpy)_2(bpy\text{-}ph\text{-}N_2^+)]^{3+}$ proposed by Agnes *et al.* (Figure taken from reference 11)

The lower density of films derived from **6.3d** than **6.2d** may indicate that **6.3d** retains a higher proportion of ligand fragments and azo bonds. Unlike the film derived from **6.2d,** the $E_{1/2}$ for the film derived from **6.3d** remained the same as the parent complex (unless the lower grafting potential limit was -1.4 V). This implies that the osmium environment in the film is similar to the parent complex. This could also be explained by a high proportion of the diazonium functionalities remaining in the film as azo bonds. Doppelt and Pinson *et al.* have analyzed the azo component of films derived

from benzenediazonium salts on Cu by TOF-SIMS. [29] They found no relationship between grating potential limit and azo bond concentration but note that the azo bond concentration is highest at the surface of the film and consequently in films that are thin or very rough. The films derived from **6.3d** are thinner and rougher than those of **6.2d** so it is possible that a higher proportion of azo bonds is retained. Once again a surface structure analysis technique such as TOF-SIMS could benefit this work.

6.4 Conclusion

Diazonium salts of three osmium complexes were synthesized and electrochemically grafted to glassy carbon electrodes. The resultant films were found to be conducting which led to continuous grafting of osmium diazonium complexes with repeat CV scanning. When grafted at potentials between -0.8 and -1.4 V in ACN the derived films retained the $Os^{2+/3+}$ electrochemistry with $E_{1/2}$ values concordant with the parent complex. As with other diazonium salt derived films more negative grafting potentials resulted in faster film growth. The films were electrochemically stable in ACN but underwent some irreversible changes in PBS with repeated cycling. A film derived from **6.2d** exhibited relatively slow electron transfer kinetics for a surface bound redox species most likely due to a loosely packed structure inhibiting electron hopping between metal centers. The apparent heterogeneous electron transfer coefficients for that film were 11.4 s^{-1} in ACN and 35.4 s^{-1} in PBS. SEM investigation revealed highly irregular films that increased in roughness with more negative lower grafting potential limits. AFM depth profiling of the films gave thicknesses of 40 nm for **6.2d** after 20 CVs to a lower potential limit of -1.2 V. The packing density of that film was estimated to be 55 %. The equivalent film derived from **6.3d** resulted in a 28 nm thick film with a packing density of 18 %. This confirms that the films are loosely packed multilayered films in agreement with the findings of others.

This chapter describes a new method for producing electroactive, conducting films at with a range of $Os^{2+/3+}$ redox potentials the surface concentrations of which can be varied over a wide range. The method could have far reaching implications in the areas of

electrochemical sensing, dye sensitized solar cells and bio-electrochemical charge transport mediation. Further work is required to fully understand the film structure and the structure of the altered films formed when exposed to extreme negative potentials. Films grafted onto transparent electrodes such as indium tin oxide (ITO) may be amenable to UV-Vis and IR spectroscopy, XPS and TOF-SIMS analysis could provide further insight into film structure. More synthesis should yield a library of complexes with a wide range of redox potentials.

6.5 References

1. Zakeeruddin, S. M.; Fraser, D. M.; Nazeeruddin, M. K.; Gratzel, M., Towards Mediator Design - Characterization of Tris-(4,4'-Substituted-2,2'-Bipyridine) Complexes of Iron(Ii), Ruthenium(Ii) and Osmium(Ii) as Mediators for Glucose-Oxidase of Aspergillus-Niger and Other Redox Proteins. *J. Electroanal. Chem.* **1992,** 337, (1-2), 253-283.
2. Kober, E. M.; Caspar, J. V.; Sullivan, B. P.; Meyer, T. J., Synthetic Routes to New Polypyridyl Complexes of Osmium(Ii). *Inorg. Chem.* **1988,** 27, (25), 4587-4598.
3. Vostiar, I.; Ferapontova, E. E.; Gorton, L., Electrical "wiring" of viable Gluconobacter oxydans cells with a flexible osmium-redox polyelectrolyte. *Electrochem. Commun.* **2004,** 6, (7), 621-626.
4. Timur, S.; Anik, U.; Odaci, D.; Lo Gorton, L., Development of a microbial biosensor based on carbon nanotube (CNT) modified electrodes. *Electrochem. Commun.* **2007,** 9, (7), 1810-1815.
5. Jenkins, P. A.; Boland, S.; Kavanagh, P.; Leech, D., Evaluation of performance and stability of biocatalytic redox films constructed with different copper oxygenases and osmium-based redox polymers. *Bioelectrochem.* **2009,** 76, (1-2), 162-168.
6. Hudak, N. S.; Gallaway, J. W.; Barton, S. C., Formation of mediated biocatalytic cathodes by electrodeposition of a redox polymer and laccase. *J. Electroanal. Chem.* **2009,** 629, (1-2), 57-62.
7. Habermuller, K.; Ramanavicius, A.; Laurinavicius, V.; Schuhmann, W., An oxygen-insensitive reagentless glucose biosensor based on osmium-complex modified polypyrrole. *Electroanalysis* **2000,** 12, (17), 1383-1389.
8. Kavanagh, P.; Boland, S.; Jenkins, P.; Leech, D., Performance of a Glucose/O-2 Enzymatic Biofuel Cell Containing a Mediated Melanocarpus albomyces Laccase Cathode in a Physiological Buffer. *Fuel Cells* **2009,** 9, (1), 79-84.
9. Boland, S.; Foster, K.; Leech, D., A stability comparison of redox-active layers produced by chemical coupling of an osmium redox complex to pre-functionalized gold and carbon electrodes. *Electrochim. Acta* **2009,** 54, (7), 1986-1991.
10. Jousselme, B.; Bidan, G.; Billon, M.; Goyer, C.; Kervella, Y.; Guillerez, S.; Abou Hamad, E.; Goze-Bac, C.; Mevellec, J. Y.; Lefrant, S., One-step electrochemical

modification of carbon nanotubes by ruthenium complexes via new diazonium salts. *J. Electroanal. Chem.* **2008,** 621, (2), 277-285.
11. Agnes, C.; Arnault, J. C.; Omnes, F.; Jousselme, B.; Billon, M.; Bidan, G.; Mailley, P., XPS study of ruthenium tris-bipyridine electrografted from diazonium salt derivative on microcrystalline boron doped diamond. *Phys. Chem. Chem. Phys.* **2009,** 11, (48), 11647-11654.
12. Bidan, G.; Jousselme, B.; De Bettignies, R. Polymerizable diazonium salts, process for the preparation thereof and uses thereof. 2008. United States Patent 7812139
13. Johansson, O.; Borgstrom, M.; Lomoth, R.; Palmblad, M.; Bergquist, J.; Hammarstrom, L.; Sun, L. C.; Akermark, B., Electron donor-acceptor dyads based on ruthenium(II) bipyridine and terpyridine complexes bound to naphthalenediimide. *Inorg. Chem.* **2003,** 42, (9), 2908-2918.
14. Priimov, G. U.; Moore, P.; Maritim, P. K.; Butalanyi, P. K.; Alcock, N. W., Synthesis of two covalently linked bis(2,2 ': 6 ',2 "-terpyridine) (terpy) chelating ligands with different length spacers, comparison of the crystal structures of their mononuclear nickel(II) complexes, and kinetic and mechanistic studies of the reaction of one ligand with [Fe(terpy)(2)](2+). *J. Chem. Soc., Dalton Trans.* **2000**, (4), 445-449.
15. Delamar, M.; Hitmi, R.; Pinson, J.; Saveant, J. M., Covalent Modification of Carbon Surfaces by Grafting of Functionalized Aryl Radicals Produced from Electrochemical Reduction of Diazonium Salts. *J. Am. Chem. Soc.* **1992,** 114, (14), 5883-5884.
16. March, G.; Reisberg, S.; Piro, B.; Pham, M. C.; Delamar, M.; Noel, V.; Odenthal, K.; Hibbert, D. B.; Gooding, J. J., Electrochemical kinetic analysis of a 1,4-hydroxynaphthoquinone self-assembled monolayer. *J. Electroanal. Chem.* **2008,** 622, (1), 37-43.
17. Laviron, E., General Expression of the Linear Potential Sweep Voltammogram in the Case of Diffusionless Electrochemical Systems. *J. Electroanal. Chem.* **1979,** 101, (1), 19-28.
18. Bard, A. J.; Faulkner, L. R., *Electrochemical Methods Fundamentals and Applications 2nd Ed.* . John Wiley & Sons, Inc.: 2001.
19. Flavel, B. S.; Yu, J. X.; Shapter, J. G.; Quinton, J. S., Electrochemical characterisation of patterned carbon nanotube electrodes on silane modified silicon. *Electrochim. Acta* **2008,** 53, (18), 5653-5659.
20. Yu, J. X.; Shapter, J. G.; Johnston, M. R.; Quinton, J. S.; Gooding, J. J., Electron-transfer characteristics of ferrocene attached to single-walled carbon nanotubes (SWCNT) arrays directly anchored to silicon(100). *Electrochim. Acta* **2007,** 52, (21), 6206-6211.
21. Roth, K. M.; Yasseri, A. A.; Liu, Z. M.; Dabke, R. B.; Malinovskii, V.; Schweikart, K. H.; Yu, L. H.; Tiznado, H.; Zaera, F.; Lindsey, J. S.; Kuhr, W. G.; Bocian, D. F., Measurements of electron-transfer rates of charge-storage molecular monolayers on Si(100). Toward hybrid molecular/semiconductor information storage devices. *J. Am. Chem. Soc.* **2003,** 125, (2), 505-517.
22. Forster, R. J.; Faulkner, L. R., Electrochemistry of Spontaneously Adsorbed Monolayers - Effects of Solvent, Potential, and Temperature on Electron-Transfer Dynamics. *J. Am. Chem. Soc.* **1994,** 116, (12), 5453-5461.

23. Forster, R. J.; Faulkner, L. R., Electrochemistry of Spontaneously Adsorbed Monolayers - Equilibrium Properties and Fundamental Electron-Transfer Characteristics. *J. Am. Chem. Soc.* **1994,** 116, (12), 5444-5452.
24. Boland, S.; Barriere, F.; Leech, D., Designing stable redox-active surfaces: Chemical attachment of an osmium complex to glassy carbon electrodes prefunctionalized by electrochemical reduction of an in situ-generated aryldiazonium cation. *Langmuir* **2008,** 24, (12), 6351-6358.
25. Adenier, A.; Cabet-Deliry, E.; Chausse, A.; Griveau, S.; Mercier, F.; Pinson, J.; Vautrin-Ul, C., Grafting of nitrophenyl groups on carbon and metallic surfaces without electrochemical induction. *Chem. Mater.* **2005,** 17, (3), 491-501.
26. Brooksby, P. A.; Downard, A. J., Electrochemical and atomic force microscopy study of carbon surface modification via diazonium reduction in aqueous and acetonitrile solutions. *Langmuir* **2004,** 20, (12), 5038-5045.
27. Ceccato, M.; Nielsen, L. T.; Iruthayaraj, J.; Hinge, M.; Pedersen, S. U.; Daasbjerg, K., Nitrophenyl Groups in Diazonium-Generated Multilayered Films: Which are Electrochemically Responsive? *Langmuir* **2010,** 26, (13), 10812–10821.
28. Abruna, H. D.; Meyer, T. J.; Murray, R. W., Chemical and Electrochemical Properties of 2,2'-Bipyridyl Complexes of Ruthenium Covalently Bound to Platinum Oxide Electrodes. *Inorg. Chem.* **1979,** 18, (11), 3233-3240.
29. Doppelt, P.; Hallais, G.; Pinson, J.; Podvorica, F.; Verneyre, S., Surface modification of conducting substrates. Existence of azo bonds in the structure of organic layers obtained from diazonium salts. *Chem. Mater.* **2007,** 19, (18), 4570-4575.

Chapter 7. Measuring electrical current from non-electrogenic bacteria

7.1 Introduction

The aim of this thesis research is to fabricate electrodes that can interact directly with the charge transport proteins and molecules operating in the cytoplasmic membranes of bacterial cells (see section 1.1.2 for an introduction to bacterial respiration). For the purpose of this thesis direct electron transfer (wiring) is defined as electron transfer that occurs between the bacteria and an electrode without mediation by a diffusing redox species. The surface immobilized mediator molecules used in this work are considered to be part of the electrode and therefore electron transfer through surface confined mediators is regarded as direct electron transfer under this definition.

The basic structure of a bacterium is shown in Figure 7.1. The role and chemical composition of the capsule varies greatly between bacterial species. It is typically comprised of polysaccharides or polyamides and performs functions such as chemical and biological defense, adhesion and biofilm formation. The cell wall is comprised of fibrous peptidoglycan and functions as structural support for the cell. Its porous structure allows diffusion of nutrients to the plasma membrane. The plasma membrane is a lipid bilayer that contains the protein elements necessary for cellular respiration and transport of molecules and ions between the cell exterior and the cytoplasm. Gram-positive *Bacillus subtilis (B. subtilis.)* and Gram-negative *Proteus vulgaris (P. vulgaris)* were used in the work described in this chapter.

B. subtilis is a rod shaped bacterium commonly found in soil (Figure 7.2 (A)). It has typical length of 1 - 2 µm and a diameter of 0.3 – 0.5 µm (Figure 7.2). The combined capsule and cell wall of *B. subtilis* is loose, fibrous, approximately 30 – 40 nm thick[1] and relatively rigid. Gram-positive bacteria have a cytoplasmic membrane directly inside the cell wall where the electron transport processes involved in respiration occur.

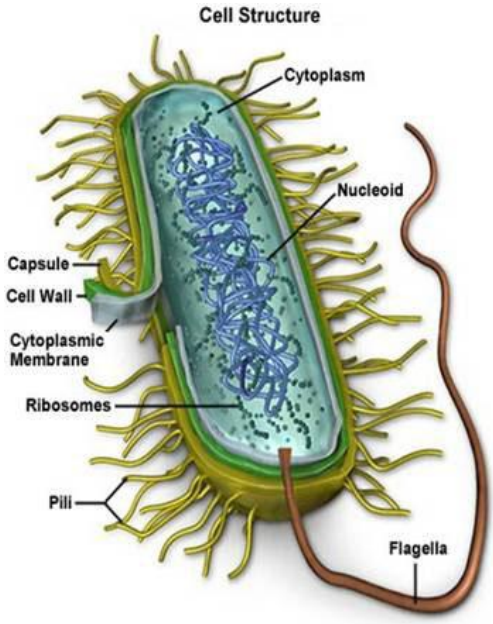

Figure 7.1. Cartoon depiction of the structure of a Gram-positive bacterium.http://ict-science-to-society.org/Pathogenomics/bacteria.htm

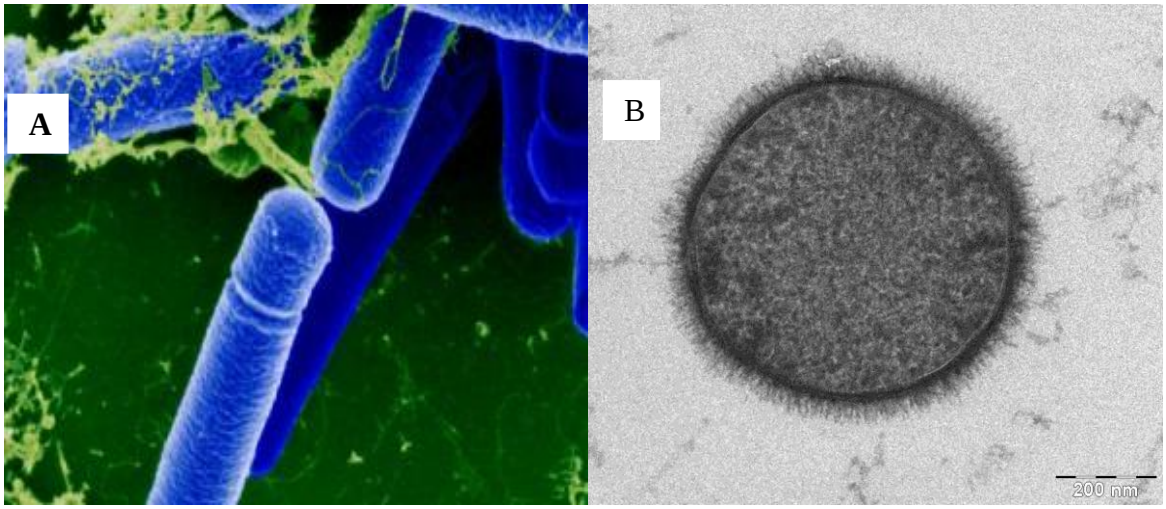

Figure 7.2. Artificially Colored SEM ((A), (www.waterscan.rs/ images/virusi-bakterije//Bacillus) and cross-sectional TEM ((B), Allon Weiner, The Weizmann Institute of Science, Rehovot, Israel. 2006, http://en.wikipedia.org/wiki/ File:Bacillus_subtilis.jpg**)** images of *B. subtilis.* Scale bar = 200 nm.

The cytoplasmic membrane is 10 -15 nm thick and is visible in Figure 7.2 (B) appearing as a faint white line at the edge of the cytoplasm. Several studies have suggested that mediator molecules need not necessarily be in direct contact with the cytoplasmic membrane in order to facilitate charge transfer from Gram – positive bacteria. Recently Coman*et al.* demonstrated that *B. subtilis* is capable of passing electrons directly to a flexible osmium redox polymer.[2] The authors employ electrodes modified with polyvinylimidazole functionalized with osmium complexes on long flexible tethers. They make the point that it is unlikely that the pendant osmium complexes are able to penetrate through the relatively thick capsule and cell wall and into the cytoplasmic membrane but observe efficient electron transfer from the bacteria despite this. The chemical composition of the cell wall of *B. subtilis* is predominantly teichoic acids and peptidoglycan which generate an anionic environment within the cell wall.[3] Ehrlich suggests that the anionic cell wall could act as a conducting pathway for electron transfer between the cytoplasmic membrane and the exterior of the cell.[4] The strain of *B. subtilis* used by Coman*et al.* is one that overproduces succinate quinone oxidoreductase (SQR). SQR is often referred to as complex II in the respiratory chain in bacteria (see Figure 1.5, section 1.1.2). The authors show that successive addition of succinate to *B. subtilis* immobilized on an electrode modified with an osmium redox polymer electrode leads to measurable increases in the current produced by the bacteria. This indicates that the observed current is produced by bacterial respiration and that electrical wiring to SQR is likely. In another example Marshal *et al.* recently demonstrated that the thermophilic Gram-positive bacterium *Thermincola ferriacetica* is capable of passing electrons to mediatorless solid electrodes.[5] There most compelling evidence for direct electron transfer is the appearance of a reversible redox system at -0.28 V in the CV of a biofilm of *Thermincola ferriacetica* which the authors assign to membrane bound cytochromes.

P. vulgaris is a rod like bacterium commonly found in the intestinal tracts of mammals. It can cause wound and urinary tract infections but otherwise is not pathogenic. *P. vulgaris* cells are 4 – 6 μm in length and 0.5 – 1 μm in diameter, and highly motile due a high number of long flagella (Figure 7.3). *P. vulgaris* has a typical Gram-negative bacterial cytoskeleton with a thin peptidoglycan cell wall (thickness ≈ 10 nm) positioned

between an inner (cytoplasmic) and outer bilayer membrane. It also has a thin capsule constructed from polysaccharides surrounding the cell wall/cell membrane complex.

Figure 7.3. SEM image of *P. vulgaris* showing numerous flagella. Image courtesy of Garth Hogan, American Society for Microbiology, http://www.microbeworld.org/index.php?option=com_jlibrary&view=article&id=1227.

membrane. Currently there are no reports of direct electron transfer from *P. vulgaris* to solid electrodes, however most of the bacteria that are capable of direct transfer are Gram-negative (see section 1.1.1 and 1.1.2).[6-9] Electrogenic bacteria are known to possess higher numbers of electron transfer cytochromes in their outer membranes than non-electrogenic bacteria. The outer membrane of Gram-negative bacteria is physically more accessible than the cyctoplasmic membranes of Gram-positive bacteria due its location outside the cell wall.

This chapter describes preliminary experiments investigating direct electron transfer from *B. subtilis* and *P. vulgaris* using the electrodes described in Chapters 3 and 4 covalently modified with compound **5.1** as described in Chapter 5. Compound **5.2** was not investigated because of limited availability and **5.3** was not investigated because of the instability of the ferrocinium ion. Due to time constraints the DDMB modified electrodes (described in section 5.3.2) were not used in conjunction with bacterial cells but will be investigated by other workers in further studies. Finally an electrode modified

with an electrochemically grafted film of **6.2d** (see Chapter 6) was shown to be capable of direct electron transfer interactions with *B. subtilis.*

7.2 Experimental

7.2.1 Bacterial culture storage and growth conditions.

Stock cultures of wild type *P. vulgaris* and *B. Subtilis* were stored on triptych soy agar (TSA) plates at 4 ^{o}C. New stock plates were prepared periodically such that the stock culture in use was less than 2 weeks old. Cell cultures for electrochemical experiments were prepared by inoculation of a liquid media broth. The broth was Organic Media #79[10] which contains 10 g of D-glucose (BDH), 10 g of peptone (MERCK), 6 g of NaCl, 2 g of pancreatic digest of casein (Life Technologies) and 2 g of yeast extract (OXOID Ltd) per 1 L of water. The broth was divided into 100 mL aliquots in culture flasks which were autoclaved at 121^{o}C for 15 min. Sterile media was inoculated with bacteria and placed in a shaker incubator (Infors) at 37^{o}C at a stir rate of 180 rpm for 16 h. The cells were harvested by centrifugation at 4500 rpm for 8 min at 4 ^{o}C (HaraeusMultifuge 1 S-R) and transferred to sterile PBS. This process was repeated a further two times, each time resuspending the bacteria in fresh PBS to remove all of the growth medium. During the final cycle of centrifugation and PBS replacement the cell suspension was concentrated to an optical density (OD, absorption at λ = 660 nm) of 10 (Bio RadSmartSpec Spectrophotometer). The concentrated cell suspensions were stored at 4 ^{o}C and were used for electrochemical experiments within 5 h of harvesting.

7.2.2 Electrochemical equipment and experimental

All electrochemical experiments were conducted in an incubator set to 37^{o}C unless otherwise stated. Cell suspensions were prepared by mixing PBS, 0.1 M glucose in PBS and the bacterial cells at an OD of 10 bacterial cells to achieve the desired concentration of each component. Where stated the standard conditions were: 10 mM glucose, OD 1 bacterial cells in PBS. Before electrochemical experiments, the bacterial suspensions were introduced to the electrochemical cells and allowed to warm to 37^{o}C. The electrochemical cells were left for a minimum of 30 min to allow the bacteria to settle

onto the electrode surface. An EG & G PAR 362 or an EG & G PAR 173 potentiostat controlled and monitored by a PowerLab/4sp (ADI instruments) analogue to digital converter were used for all experiments. All CV and linear sweep voltammogram (LSV) studies were recorded using EChem v.1.5.2 (ADI instruments) software and all chronoamperometric (CA) experiments were recorded using Chart v.4.2.2 (ADI Instruments) software.

*7.2.3 Bacteria on PPF and PPF / SWCNT electrodes and films derived from **6.2d***

PPF (see section 2.3.1) and PPF / SWCNT working electrodes (see Chapter 3) were prepared and the osmium complex **5.1**(see figure 5.4) was coupled to the electrodes by the method described in section 5.2.3. LSVs were recorded in PBS or standard bacterial cell suspensions of *B. subtilis* and *P. vulgaris* The LSVs were initiated at 0 V and swept to 500 mV *vs.* Ag/ AgCl (to detect the oxidation peak of coupled **5.1,** $E_{pa} \approx 0.3$ V *vs.* Ag/ AgCl) at either 100 mVs^{-1} or 2 mV s^{-1}. LSVs recorded using a scan rate of 100 mVs^{-1} were recorded in PBS only and were used to determine the concentration of **5.1** coupled to the electrode as described in section 2.2.3. LSVs recorded at 2 mVs^{-1} were recorded before and after the addition of bacterial cells.

CA studies were undertaken using the same electrodes as described in the previous paragraph using the Teflon electrochemical cell block depicted in section 2.2.1. The Teflon block incorporated three independent electrochemical cells. The potential of each working electrode was set at 0.3 V *vs.* Ag/AgCl using the manual controls on the potentiostats. The electrical current produced by each cell was measured by connecting each potentiostat to one of the monitoring channels on the PowerLab. By this method up to three CA experiments could be monitored simultaneously.

7.2.4 Preparation of films derived from 6.2d

A film was electrografted to PPF from a saturated solution of **6.2d** in ACN with 0.1 M $TBABF_4$ by 4 CVs from 0 to –1.2 V *vs.* Ag/Ag+(0.01 M $AgNO_3$) using the PPF plate electrochemical cell fitted with a 5 mm o-ring. The stated concentration of osmium complexes in the film was established by integration of the oxidation peak obtained from a CV of the film in PBS recorded at scan rate = 100 mV s^{-1}.

7.2.5 SEM imaging

After use for electrochemical measurements electrodes were prepared for SEM investigation by gently washing the electrode surface with water and methanol and drying with N_2. SEM images were recorded using a JEOL 7000 HRSEM. Some samples were coated with gold using a sputter coater. Uncoated samples required low accelerating voltages (2 – 4 KV) so that the thin bacterial cell membranes did not appear translucent.

7.3 Results and discussion

Figure 7.4 shows the electrochemical set up for the experiments described in this chapter. The PPF,

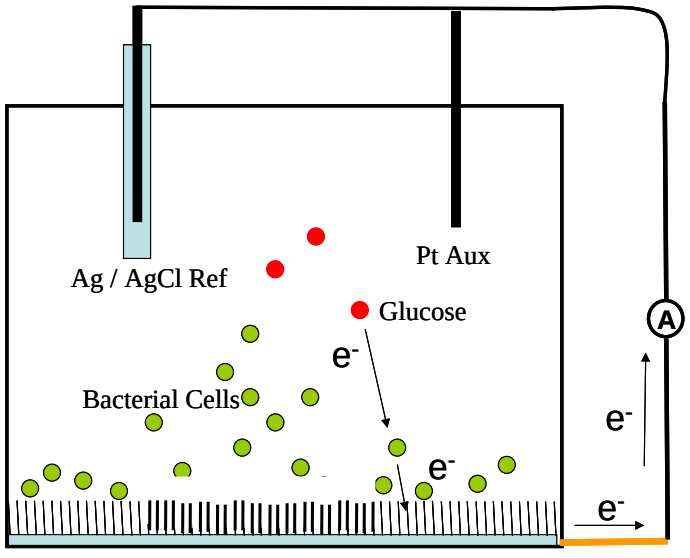

Figure 7.4. Electrochemical cell design for measuring electron transfer from bacteria.

chemically assembled SWCNT or MWCNT / epoxy electrodes are positioned at the bottom the electrochemical cell so that bacteria can settle onto the electrode surface under gravity. The potential of the working electrode is controlled by a potentiostat which also measures any electrical current arising from the activity of the bacteria. The various electrode designs described in this thesis thus far feature nanosize structures that may reach into the outer layers of bacterial cytoskeletons and access the proteins operating in their cytoplasmic membranes.

7.3.1 Amide linked complexes on SWCNT electrodes

A series of LSVs recorded in the standard bacterial suspension of *B. subtilis* on a SWCNT / PPF electrode modified with osmium complex **5.1** (Γ = 1.7 × 10^{-10} mol cm^{-2}) and PPF modified with **5.1** (Γ = 1.9 × 10^{-10} mol cm^{-2}) is shown in Figure 7.5(a) and (b) respectively. LSVs recorded on SWCNT / PPF and PPF electrodes with no attached complex are shown in Figure 7.5 (c) and (d) respectively. In each of the plots the solid black line corresponds to an LSV recorded before the introduction of bacteria. The peaks obtained in the absence of bacteria at $E_{pa} \approx 0.3$ V in (a) and (b) are assigned to oxidation of **5.1** coupled to the electrode surface**.** The LSV obtained in the absence of bacteria at an electrode incorporating SWNCTs but with no attached complex (solid line, plot (c)), also has a broad peak with $E_{pa} \approx 0.3$ V. This was often observed on SWCNT modified surfaces and is tentatively assigned to quinonoid functionalities on the SWCNTs as discussed in section 4.3.1.3. The LSV recorded in the absence of bacteria on PPF, (d) is featureless. The LSVs recorded after addition of a standard *B. subtilis* suspension, heating to 37^{o}C and allowing to stand for 1 h (dashed lines) all show an increase in recorded current at and above $E \approx 0.3$ V. The largest current increases were observed in the two samples modified with **5.1** indicating that surface confined **5.1** is capable of mediating electron transfer from *B. subtilis.* The coincidence of the E_{pa} of **5.1** with the potential at which additional current is observed upon addition of bacteria is further evidence that **5.1** is acting as a mediator. The increase in recorded current after addition of *B. subtilis* to the

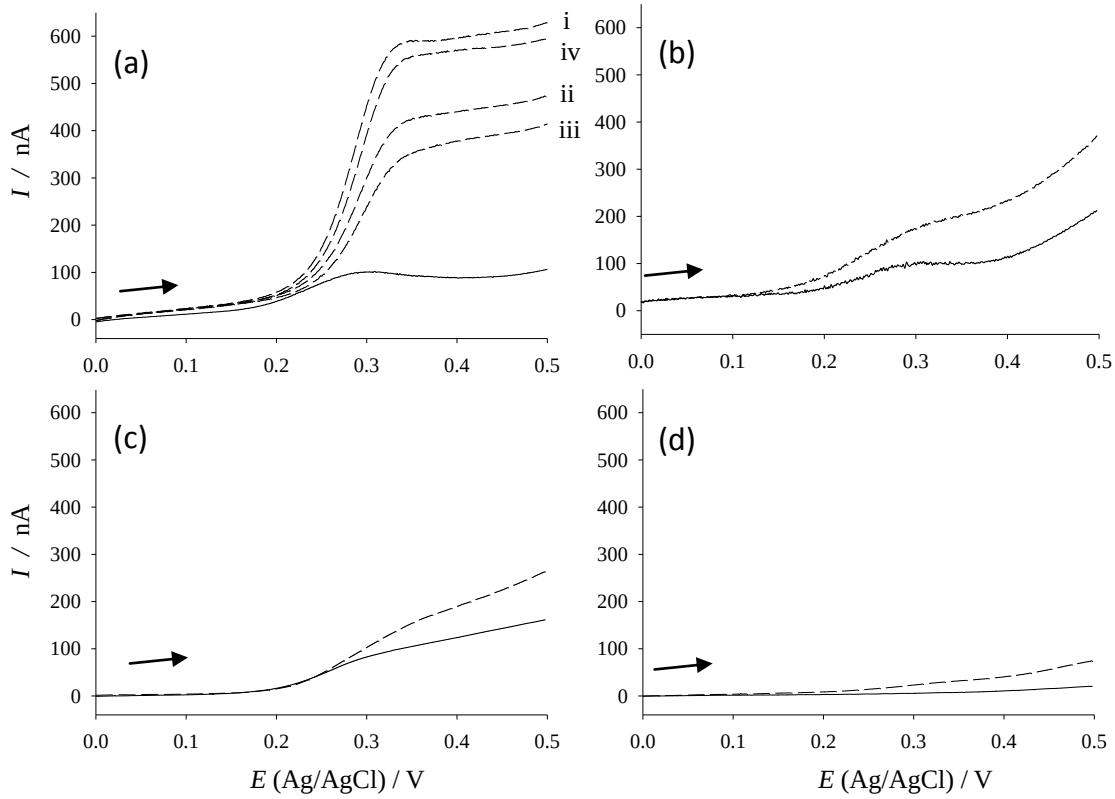

Figure 7.5. LSVs recorded at 2 mV s^{-1} in pH 7 PBS and 10 mM glucose, with (dash lines) and without (solid line) *B. subtilis* at OD 1. The electrodes used were (a) SWCNTs / PPF**,** Γ = 1.71 × 10^{-10} mol cm^{-2} **5.1**, (b) PPF / Γ = 1.86 × 10^{-10} mol cm^{-2} **5.1**, (c) SWCNTs / PPF and (d) PPF. The four LSVs recorded in the presence of *B. subtilis* in plot (a) are: (i) immediately after removal from a 37 ^{o}C incubator, (ii) after 6 min at room temperature, (iii) after 12 min at room termperature and (iv) after reheating to 37 ^{o}C.

SWCNT / PPF / **5.1** electrode was approximately 500 nA (Figure 7.5 (a) i), five times that recorded at the PPF / **5.1** electrode (Figure 7.5 (b) dashed) indicating that inclusion of SWCNTs may help to facilitate electron transfer from *B. subtilis* Figure 7.5 (a) shows three sequential LSVs that were recorded in the presence of *B. subtilis*, outside of the incubator (i, ii, and iii). A fourth LSV (iv) was recorded after returning the cell to the incubator for 15 min. The currents of the LSVs decreased in the order i) > ii) > iii) which is most reasonably attributed to the slowing of the bacterial metabolism due to cooling. The increase in the current of LSV (iv), which was recorded after reheating of the cell

solution, is strong evidence that the observed current is linked to the metabolic rate of the bacteria.

Figure 7.6 shows plots for the equivalent experiment to that described in the preceding paragraph but recorded with the Gram negative bacterium *P. vulgaris.* There is a significant increase in current associated with the oxidation of **5.1** after a 1 h incubation in a standard *P. vulgaris* solution (dashed trace). Figure 7.6 (a) shows a 400 nA increase in recorded current at a SWCNT / PPF/ **5.1** ($\Gamma = 0.7 \times 10^{-10}$ mol cm^{-2}) electrode over the LSV recorded without *P. vulgaris* (solid line). The same experiment recorded at a PPF / **5.1** ($\Gamma = 0.9 \times 10^{-10}$ mol cm^{-2}) electrode (Figure 7.6 (b)) gave currents of approximately 100 nA in the presence of bacteria. Again this indicates that SWCNT may facilitate direct electron transfer from *P. vulgaris.* Only very small enhancements in current were observed upon addition of *P. vulgaris* to electrodes with no **5.1** attached (not shown).

The LSV shown here were chosen because of the closely matched concentrations of **5.1** on the various electrodes used. Hence for electrodes modified with the same amount of **5.1** there appears to be a significant advantage in terms of the current generated in using vertically aligned SWCNTs. However, it is important to point out that the data sets recorded using SWCNT / PPF / **5.1** electrodes and the PPF / **5.1** electrodes for both bacteria were recorded on different days and with different batches of bacterial cells. Thus variation in the metabolic activity and / or variation in the ratio of viable to non-viable cells of the bacteria between batches could also contribute to the observed trends in recorded currents. Experiments using different electrodes but with the same surface concentration of osmium complex and the same batch of cells could not be performed because of the difficulty of obtaining electrode surfaces with a selected concentration of complex.

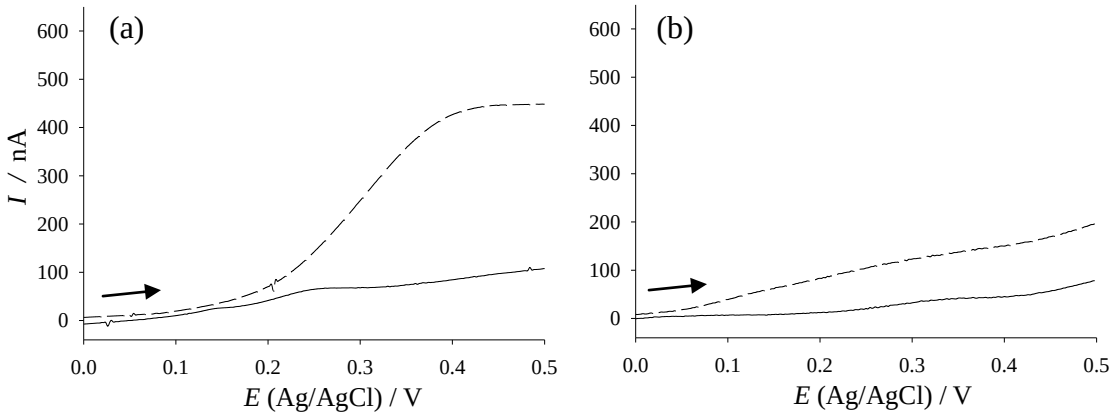

Figure 7.6. LSVs recorded at 2 mV s^{-1}in pH 7 PBS and 10 mM glucose, with (dash lines) and without (solid line) OD 1 *P. vulgaris* The electrodes used were (a) SWCNTs / PPF/ **5.1,** Γ = 0.69 × 10^{-10} mol cm^{-2}**5.1**, (b) PPF / **5.1,** Γ = 0.9 × 10^{-10} mol cm^{-2}**.**

7.3.2 Chronoamperometry

Figure 7.7 shows typical chronoamperograms (CAs) recorded using the Teflon bodied electrochemical cell block shown in Figure 2.3. This electrochemical cell design allows for up to three experiments to be conducted concurrently using the same bacterial cells. A SWCNT / PPF / **5.1** (Γ = 0.6 × 10^{-10} mol cm^{-2}) and a PPF / **5.1** (Γ = 1.4 × 10^{-10} mol cm^{-2}) electrode were positioned in the electrochemical cell block and PBS was added to each cell and a potential of 0.3 V *vs.* Ag/AgCl was applied to the working electrodes. The cell block was heated to 37 ^{o}C over 30 min then *P. vulgaris* in PBS was added to both electrochemical cells to make a solution with OD 1 (Figure 7.7 first vertical dashed line). Over the following hour the temperature was maintained at 37 ^{o}C and no additional current was observed indicating that the bacteria remain dormant in the absence of a food source. Upon the addition of glucose (final concentration 10 mM), firstly to the PPF / **5.1** electrode (second vertical dashed lined and dashed trace) and secondly to the SWCNT / PPF / **5.1** electrode (third vertical dashed line and solid trace) an increase in current was observed at both electrodes. Again this is strong evidence that the measured current is linked to the metabolic activity of the bacteria. The measured current for both electrodes

increased to a maximum over two to three hours. The SWCNT / PPF / **5.1** electrode produced 400 nA at its maximum**,** four times that of the PPF / **5.1** electrode despite the PPF / **5.1** electrode having three times the concentration of mediator at the surface. As the bacteria used in this experiment are from the same batch and are of the same age and the experiments are conducted concurrently variation in the relative metabolic activity between the two experiments is unlikely. Therefore it is clear that the inclusion of SWCNTs on the electrode appears to facilitate electron transfer from *P. vulgaris.*

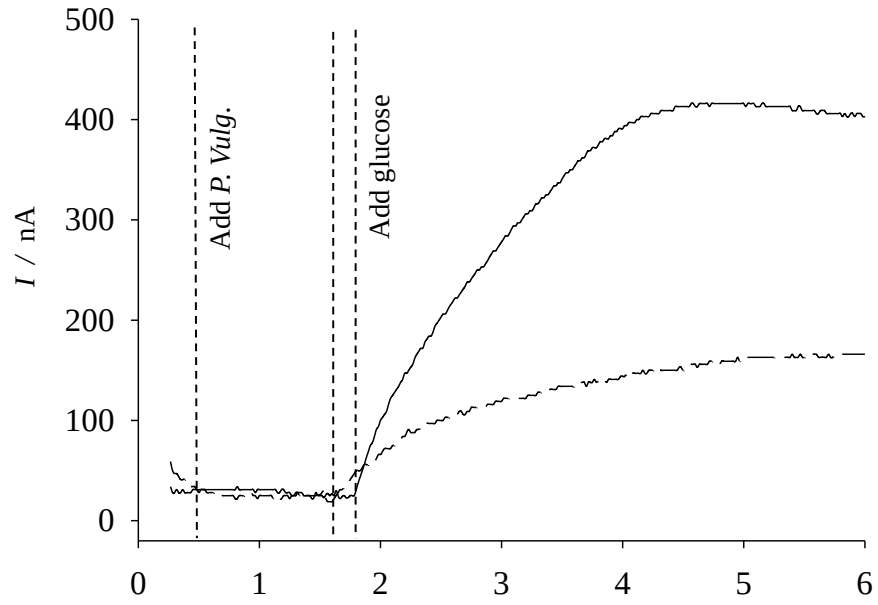

Figure 7.7. CA at a PPF / **5.1** (Γ = 1.4 × 10^{-10} mol cm^{-2}, dashed line) and SWCNT / PPF (Γ = 0.6 × 10^{-10} mol cm^{-2}, solid line) electrode in PBS. The vertical dashed lines indicate the addition of *P. vulgaris* to an OD of 1 and the addition of glucose to a concentration of 10 mM as indicated on the plot. The CAs were recorded concurrently and both electrodes were held at E = 0.3 V *vs.* Ag/AgCl during the measurement.

7.3.3 Amide linked complexes on MWCNT electrodes

A selection of vertically aligned MWCNT / epoxy (see section 4.3.1.2) electrodes were modified with **5.1** and similar experiments to those described in sections 7.3.1 and 7.3.2 were conducted. LSVs for the modified electrodes were conducted in PBS to

establish a base line and the surface concentration of **5.1** for each electrode. Figure 7.8 (a) shows a CA recorded using electrode 1 at E = 0.3 V *vs.* Ag/AgCl initially in PBS with 10 mM glucose, preheated to 37 ^{o}C.

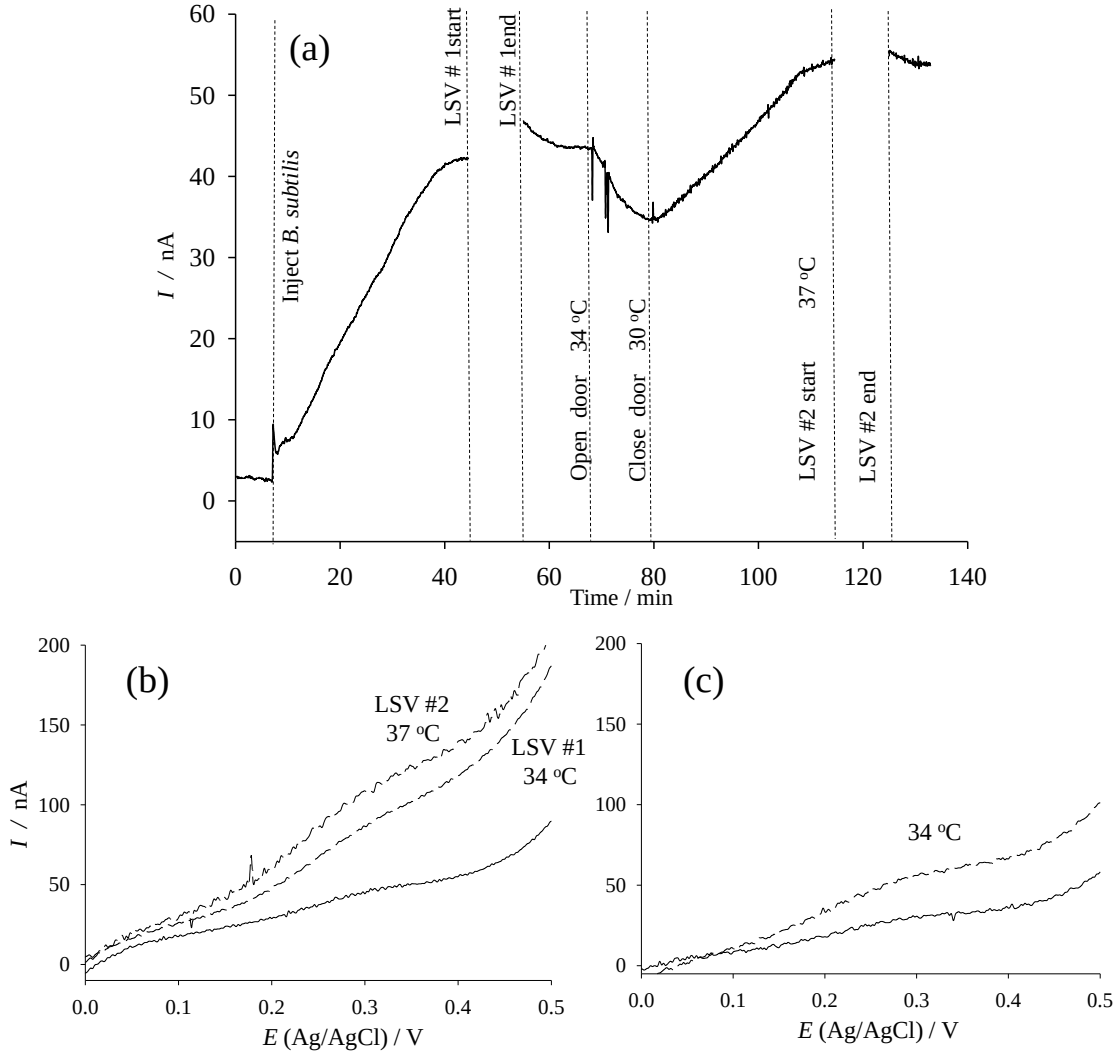

Figure 7.8. (a) CA showing the anodic current recorded at a MWCNT / epoxy / **5.1** (Γ = 1.5 × 10^{-10} mol cm^{-2}) electrode poised at 0.3 V *vs.* Ag/AgCl after the addition of OD 1 *B. subtilis* in pH 7 PBS and 10 mM glucose. (b) LSVs recorded with the same electrode as that used in (a) in pH 7 PBS and 10 mM glucose (black line) and during the breaks indicated in (a) after addition of *B. subtilis* (c) LSVs recorded using a MWCNT / epoxy / **5.1** (Γ = 0.8× 10^{-10} mol cm^{-2} electrode and the same conditions as (b) before (black line) and after (dashed line) addition of *B. subtilis*

After 5 min *B. subtilis* was introduced resulting in a rapid increase in current. The current increased to a maximum of 42 nA after 45 min which is a significantly faster increase than the equivalent CA recorded at PPF or SWCNT / PPF (Figure 7.7). Figure 7.8 (b) and (c) (black trace) shows the LSVs at scan rate = 2 mV s^{-1} for electrode 1 (Γ = 1.5 × 10^{-10} mol cm^{-2} **5.1**) and electrode 2 (Γ = 0.8 × 10^{-10} mol cm^{-2} **5.1**). An LSV recorded after 45 min (Figure 7.8 (b) dashed line, LSV #1) is similar in appearance to those recorded at PPF and SWCNT / PPF but with lower currents. Again the steepest rise in the current plots is coincident with the oxidation peak of **5.1** indicating that the complex is mediating the electron transfer. Figure 7.8(c) shows the CA results for the same experiment recorded at a MWCNT / epoxy electrode with half the concentration of **5.1** as the electrode used to record the LSV shown in Figure 7.8 (b).Clearly the current increase upon addition of bacteria is smaller at the electrode with the lower concentration of **5.1** suggesting that the current enhancement increases with the surface concentration of the mediator.

As a demonstration of how the system described here might be used as an environmental monitor the door of the incubator was opened to allow the electrochemical cell assembly to cool (as indicated on Figure 7.8 (a)). A mercury thermometer was inserted and the temperature and current from the bacteria were monitored simultaneously. The current produced by the bacteria begins to decrease within a minute of the door opening and closely follows the rate of cooling. At 30 ^{o}C the door of the incubator was closed and the temperature ramped to 37 ^{o}C over 30 - 40 min resulting in a corresponding linear increase in current to a maximum of 54 nA. An LSV recorded at 37 ^{o}C (Figure 7.8 (b) LSV #2) exhibits approximately a 10 nA increase in current over LSV #1 (34 ^{o}C) which is approximately the same current increase between the CA current plateau at 34 ^{o}C and that at 37 ^{o}C. This experiment demonstrates that bacterial interactions with any environmental stimulus that can induce a change in the metabolic rate of a bacterium can be detected in real time. Furthermore the method could be applied to detect chemical analytes (for example, toxic compounds) provided the analyte in question is not electrochemically active over the potential range used to monitor bacterial metabolism.

7.3.4 Direct electron transfer to films derived from electrochemical reduction of osmium diazonium salt complexes

A thin film derived from **6.2d** (Γ = 0.3 × 10^{-10} mol cm^{-2}) was prepared on a PPF plate electrode. Figure 7.9 (i) shows an LSV recorded using this electrode in PBS, 10 mM glucose at 37 ^{o}C. The concentration of osmium on this electrode is too low for the oxidation peak at ≈ 0.75 V to appear at a scan rate of 2 mV s^{-1} in particular against the steeply rising background current. Figure 7.9 (ii) shows an LSV recorded immediately after addition of *B. subtilis.* Some addition current is evident in this LSV and the oxidation peak due to the $Os^{2+/3+}$ couple appears at ≈ 0.8 V. After 30 min (Figure 7.9 (iii)) a current increase of 600 nA is observed at 0.75 V over that recorded at the electrode in the absence of bacteria. The coincidence of the current increase potential and the E_{pa} established (0.75 V) for this film shows that the film is mediating electron transfer from *B. subtilis.* The lack of any additional current at 0.3 V is further evidence that mediation by osmium complex **5.1** was responsible for the current increase in the preceding experiments. The 30 min time delay before the maximum current increase is observed is evidence that the bacteria need to settle and be in contact with the electrode in order to efficiently transfer electrons.

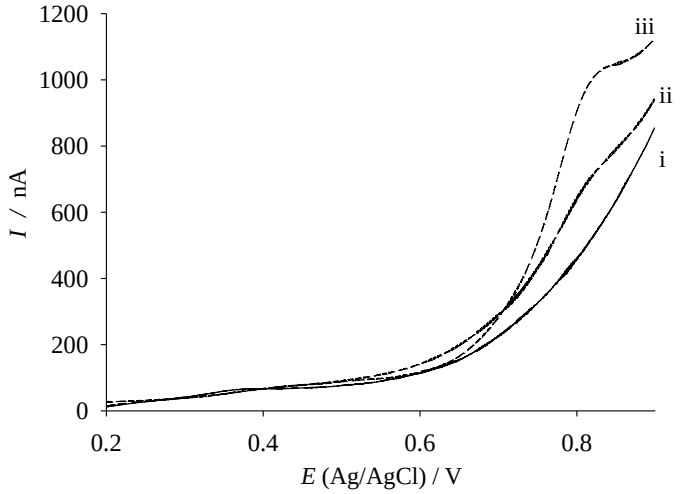

Figure 7.9. LSVs recorded at a PPF electrode modified with a film formed by electrochemical reduction of **6.2d.** (i) in PBS, 10 mM glucose at 37 ^{o}C, (ii) immediately following addition of *B. subtilis*, and (iii) after 30 min incubation at 37 ^{o}C with *B. subtilis*, Scan rate = 2 mV s^{-1}.

7.3.5 SEM investigation

SEM images of *P. vulgaris* and *B. subtilis* on PPF and SWCNT / PPF electrodes are shown in Figure 7.10. The appearance of both bacteria was consistent with typical examples of their species and there was no evidence of contaminant bacteria. *P. vulgaris* remained on the electrodes in greater numbers after gentle washing than *B. subtilis.* The tendency of *Proteus* bacteria to swarm and the entanglement of their long flagella are likely to account for this. On PPF (Figure 7.10 (a)) *P. vulgaris* appears intact but has shrunk during fixing in methanol and in the high vacuum conditions of the SEM chamber. Interestingly the *P. vulgaris* on the SWCNT / PPF electrode appear to have flattened onto the surface perhaps indicating better adhesion of the bacterium to this surface.

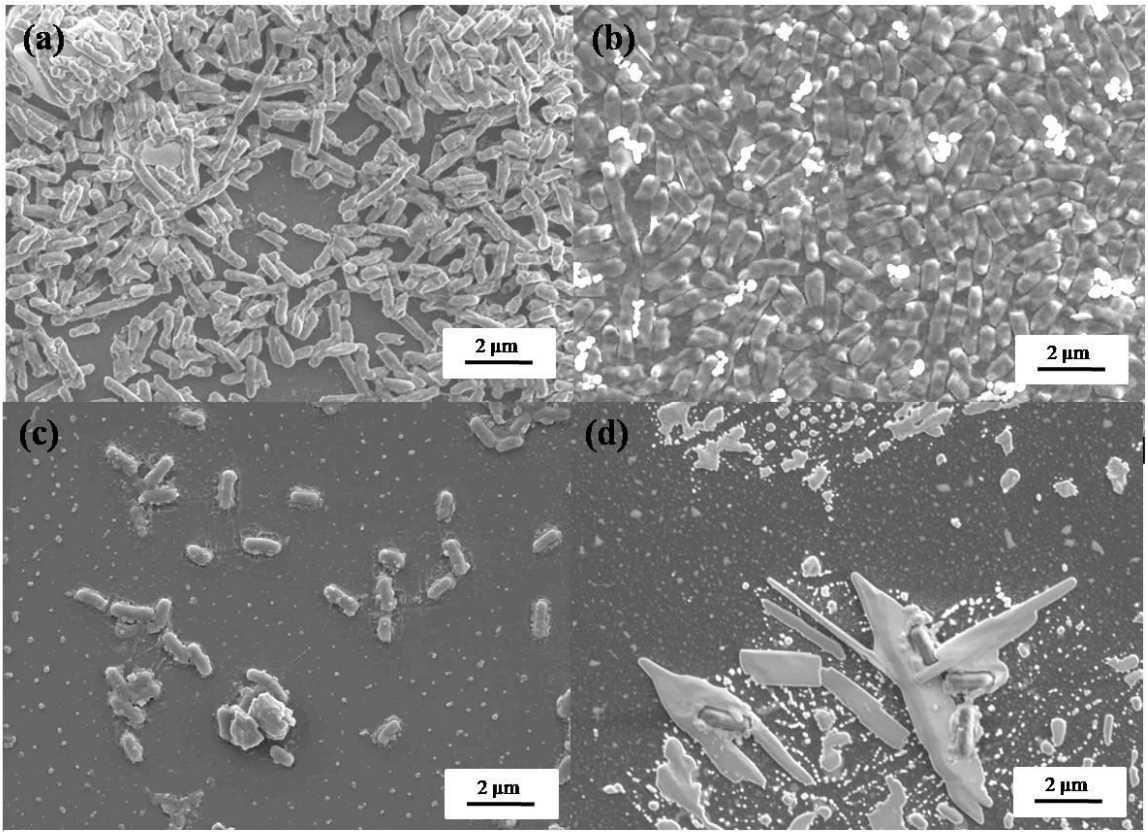

Figure 7.10.SEM images of *P. vulgaris* on PPF (a) and SWCNTs / PPF (b) and *B. subtilis* n PPF (c) (gold coated) and SWCNTs / PPF (d).

After gentle rinsing only small amounts of *B. subtilis* were observed on both the PPF (Figure 7.10 (c)) and SWCNT (Figure 7.10 (d)) surface indicating that adhesion of

this bacterium is poor. The bacteria appear to be less collapsed than the *P. vulgaris* sample which is consistent with the thicker and more rigid cell wall of *B. subtilis* which reinforces the bacterial cytoskeleton. The crystalline structures in Figure 7.10 (d) are most likely buffer salts, which were not fully removed during washing.

7.3.6 Is wiring occurring?

Electron transfer to electrodes from the bacteria discussed in this chapter is most likely to occur by one of two methods. The first possible method is through 'wiring'. For the purposes of this thesis 'wiring' implies that electrode-bound mediator molecules are positioned at the bacterium exterior such that they can be reduced either directly by electron transfer proteins or via a conducting pathway acting within the bacterial cytoskeleton. The most likely alternative scenario is that the bacteria are producing and electroactive molecule in solution (an endogenous mediator) which can diffuse to the electrode surface and be catalytically oxidized by the electrode-bound mediator.

Figure 7.8 (a) shows the responses of *B. subtilis* on a MWCNT / epoxy electrode as the temperature is altered. If *B. subtilis* was producing an endogenous mediator into the solution then a change in metabolic rate of the bacteria would not be detected at the electrode until the concentration of the endogenous mediator changed significantly. Considering that the solution volume used was 10 mL and the electrode geometric area was 0.12 cm^2 there would likely be a considerable delay before the concentration of a mediator in solution resulted in a significant change in measured current. Concurrently however temperature also affects rates of diffusion significantly so the possibility of exogenous mediators can not be discounted using this experiment. If, however endogenous mediators are being produced then the current detected by the electrodes will be under diffusion control. It was established in Chapter 4, section 4.3.1.3 that the MWCNT /epoxy electrodes behave like macro electrodes under diffusion control due to close spacing of the tips of nanotube bundles. Therefore the MWCNT / epoxy electrodes should produce the same current as PPF or SWCNT / PPF electrodes for the same

concentration of redox molecule. The CA and LSVs recorded at the MWCNT / epoxy electrodes produce significantly less current than the SWCNT / PPF or PPF electrodes and therefore the current is not likely to come from a diffusion limited process. Therefore it is more likely that electron transfer is occurring via 'wiring' than exogenous mediators.

7.4 Conclusion

CA and LSV experiments were conducted to determine if the various electrodes developed in Chapters 3 and 4, both unmodified and modified with osmium complex **5.1** were capable of direct electron transfer interactions with the common bacteria *P. vulgaris* and *B. subtilis* All the electrodes tested yielded measurable increased currents after the addition of bacteria to the electrolyte solutions. he highest currents were measured with electrodes modified with mediator complex **5.1** indicating that the osmium complex is an efficient mediator for bacterial electron transfer. Of the electrodes modified with **5.1** the largest currents were recorded using electrodes also modified with SWCNTs indicating that electrodes nanostructured with CNTs may facilitate electron transfer from bacteria. Current was only produced by the bacteria after glucose was introduced to the bacteria solution showing that the measured current is linked to cell metabolism. Considering that the concentration of **5.1** on all of the electrodes was hard to control and that data sets from different days were compared to accommodate for this, more experiments need to be conducted before the advantage of SWCNTs can be confirmed.

Using MWCNT / epoxy electrodes modified with **5.1**, current produced by *B. subtilis* was measured. The electrodes produced lower currents than PPF or SWCNT / PPF electrodes under the same conditions but also exhibited very low background currents and hence had high signal to noise ratios. The currents recorded at the electrodes were shown to be linked to the metabolic rate of the bacteria by lowering and raising the temperature of the electrochemical cell assembly.

7.5 References

1. Graham, L. L.; Beveridge, T. J., Structural Differentiation of the Bacillus-Subtilis-168 Cell-Wall. *J. Bacteriol.* **1994,** 176, (5), 1413-1421.
2. Coman, V.; Gustavsson, T.; Finkelsteinas, A.; von Wachenfeldt, C.; Hagerhall, C.; Gorton, L., Electrical Wiring of Live, Metabolically Enhanced Bacillus subtilis Cells with Flexible Osmium-Redox Polymers. *J. Am. Chem. Soc.* **2009,** 131, (44), 16171-16176.
3. Neuhaus, F. C.; Baddiley, J., A continuum of anionic charge: Structures and functions of D-Alanyl-Teichoic acids in gram-positive bacteria. *Microbiol. Mol. Bio. Rev.* **2003,** 67, (4), 686-+.
4. Ehrlich, H. L., Are gram-positive bacteria capable of electron transfer across their cell wall without an externally available electron shuttle? *Geobiology* **2008,** 6, (3), 220-224.
5. Marshall, C. W.; May, H. D., Electrochemical evidence of direct electrode reduction by a thermophilic Gram-positive bacterium, Thermincola ferriacetica. *Energ. Environ. Sci.* **2009,** 2, (6), 699-705.
6. Reimers, C. E.; Tender, L. M.; Fertig, S.; Wang, W., Harvesting energy from the marine sediment-water interface. *Environ. Sci. Technol.* **2001,** 35, (1), 192-195.
7. Bond, D. R.; Holmes, D. E.; Tender, L. M.; Lovley, D. R., Electrode-reducing microorganisms that harvest energy from marine sediments. *Science* **2002,** 295, (5554), 483-485.
8. Bond, D. R.; Lovley, D. R., Electricity production by Geobacter sulfurreducens attached to electrodes. *Appl. Environ. Microbiol.* **2003,** 69, (3), 1548-1555.
9. Alferov, S.; Coman, V.; Gustavsson, T.; Reshetilov, A.; von Wachenfeldt, C.; Hagerhall, C.; Gorton, L., Electrical communication of cytochrome enriched Escherichia coli JM109 cells with graphite electrodes. *Electrochim. Acta* **2009,** 54, (22), 4979-4984.
10. Atlas, R. M.; Parks, L. C., *Handbook of Microbiological Media 2nd Edition*. CRC Press: London, 1997.

Chapter 8. Conclusion

Real time direct detection of electrical current produced by living cells is currently limited to a few species of electrogenic bacteria that are capable of electron transfer to solid electrodes. An ability to "wire" into terminal electron transfer processes and measure the production of current in real time for a wide range of cell types will be an enabling technology in the fundamental study of living cells, drug discovery, and microbial fuel cell research. The ability of cells to electronically interact with surfaces is well known to depend on the morphology and chemistry at the cell / surface interface. The aim of this thesis work was to fabricate and assess electrode assemblies with the ability to interact directly with charge transfer processes from "non" electrogenic bacteria. The electrodes were constructed from graphitic carbon allotropes (including carbon nanotubes) because of the ability of graphite to conduct electricity and its low cytotoxicity. The carbon nanotubes were vertically aligned to expose predominantly electroactive open tube ends at the electrode surface. To further enhance electron transfer from living cells a range of redox mediator molecules were covalently attached to the graphitic assemblies. Finally non electrogenic cells were allowed to settle on the electrodes and real time measurements of the electrical current produced by the cells were made.

A method was developed for vertical alignment of SWCNTs from solution onto PPF electrodes using a tether layer derived from electrochemical reduction of aryl diazonium salts. The method represents the first use of electrochemical reduction of aryl diazonium salts to form tether layers for SWCNTs and is one of only a few methods described for the assembly of SWCNTs on a carbon surface.[1] The assemblies proved to be highly stable over a wide potential window and in a range of solvents. Although the physical and electrochemical properties of the SWCNTs are appealing the electrodes are complicated and time consuming to fabricate. Hence they are likely to be useful primarily as a research tool. It was found during development of the electrodes that attachment of SWCNTs lowered the electrical resistance of the tether layers used for the attachment. Further work is required to better understand this phenomenon.

Methods were developed for the growth of MWCNTs by CVD using e-beam evaporated metal catalyst films and aqueous metal salt catalyst films directly on PPF electrodes. Photolithography was employed to demonstrate how the MWCNTs could be patterned for future development into electrode arrays. A simple method was developed for encapsulation of MWCNT electrodes in epoxy resin producing electrodes that could be regenerated many times by mechanical polishing. SEM analysis revealed that bundles of MWCNTs protrude from the epoxy making a random array of closely spaced nano-electrodes. When used with redox molecules in solution the electrodes exhibited behavior similar to flat macro-electrodes indicating that the protruding MWCNT bundles are closely spaced and the diffusion zones between them are overlapping. When activated by O_2 plasma etching, the electrodes exhibited fast kinetics for the common redox probe $Fe(CN)_6^{3-/4-}$ and a low overpotential for oxidation of NADH. Due to their predictable behavior, reusability and physical robustness the electrodes are a highly efficient tool for investigating electrochemical processes at MWCNTs. As a result of this they are highly likely to be used in a number of ongoing projects related to the work described in this thesis. The relative simplicity of the fabrication process and the ease with which the MWCNTs can be patterned make the system highly suitable for device applications.

Several osmium bpy complexes with AP groups appending their bpy ligands were synthesized and diazotized and isolated as tetrafluoroborate salts. By methods similar to reduction of other aryl diazonium salts the complexes could be electrochemically grafted to conducting substrates by reduction of the diazonium moiety. Unlike most diazonium salts the films were not self limiting but continued to grow with repeated CV cycling through the diazonium reduction potential ($E_{pc} \approx$ -1.2 V). The formed films were thicker than is typical for films derived from diazonium salts and retained high concentrations of electro-active osmium centers with the films. By varying the ligand shell of the diazonium salt parent complex a film with an $E_{1/2} \approx 0$ V and $E_{1/2} \approx 0.7$ V in PBS *vs.* Ag/AgCl were demonstrated. This illustrates how the reduction potential of films produced by this method could be tailored to suit specific applications. Molecules that may provide electro-active films with different potentials to those described in this thesis

could be synthesized in further work. The non-limiting growth of films derived from osmium complex diazonium salts provides control over the concentration of osmium centers in the growing films. As osmium complexes have been shown in this thesis and by others to be good mediators of electrons transferred from biological processes these films may offer an advantage in terms of controlling mediator concentration as an experimental variable for transfer of electrons from live bacteria. This was not investigated as part of this thesis work but may be developed further in future work.

A new redox mediator molecule closely related to coenzyme Q10 was successfully coupled to AP films on PPF by reductive amination. These films exhibited high stability and easily detectable redox chemistry associated with the quinone / quinol head group of the molecule. Due to time constraints, these films were not tested for their ability to mediate electron transfer from bacteria but should be investigated in further work.

Traditional methods were used to couple mediator molecules to the various electrodes via amide bond formation between carboxylic acid groups on the electrode surfaces and primary amines on the mediator molecules. Osmium bpy complexes coupled to the electrodes were readily electrochemically detectable and were stable to extended CV cycling. Concentrations of the mediators on the surface were difficult to control but were between 0.5 and 3×10^{-10} mol cm^{-2}. One mediator was tested for its ability to mediate charge transfer on a selection of the electrode types developed in this thesis. Electrodes modified with the mediator all demonstrated the ability to successfully mediate charge transfer from the common wild type bacteria *Proteus. vulgaris* and *Bacillus. subtilus.* This is the first example of direct measuring of electron transfer from surface confined wild type cultures of either species. The source of the measured electrical current was shown to be linked to the metabolic rate of the bacteria by a lack of any measured current before the introduction of a glucose food source and by the measured current closely following changes in temperature. The rapid response of the current to temperature change and the scaling of the current magnitude with active

electrode surface area indicates that the majority of charge transfer is via ‘wiring’ and not production of exogenous mediators.

The discovery of electrode types that can directly measure respiration rate changes in aerobic non-electrogenic bacteria could potentially find utility in a number of areas. Recent work using the electrodes developed in this thesis has demonstrated the use of an osmium complex modified PPF / SWCNT combined with *Proteus vulgaris.* as a toxicity sensor for a range of known toxins. The electrical response of the electrode was found to correspond well with plate viability experiments (a commonly used method of assessing toxicity). The rapid response of the MWCNT *Bacillus subtilu.* electrode to temperature change illustrates the potential of this system to be integrated into environmental monitoring applications. Monitoring of water quality by direct detection of electrical current produced by photosynthesizing prokaryotes could be one area of investigation. Finally extension of direct electrical detection to respiration of eukaryotic cells could enable fast screening of drug candidates for a variety of conditions including cancers. Early results using some of the electrodes developed in this thesis to directly detect current from eukaryotic yeast cells have been promising.

For both of the bacteria tested SWCNT modified electrodes recorded higher currents than unmodified electrodes. The highest currents were recorded on electrodes further modified with mediator molecules. This result suggests that the addition of SWCNTs to the electrodes may help to position the mediator molecules within the exterior of the bacterial cell facilitating transfer from membrane bound proteins. The tallest aggregates of SWCNTs measured were approximately 60 -70 nm tall which is long enough to penetrate into the exterior of both of the bacteria tested. The MWCNT epoxy electrodes recorded lower currents than the SWCNT modified electrodes for the same geometric area. The MWCNT electrodes are random arrays of nano scale CNT electrodes and therefore have significantly less electroactive area than the SWCNT modified electrodes. The MWCNT electrodes were shown to behave like macroelectrodes with redox molecules in solution. The fact that the currents recorded from bacteria on the MWCNT electrodes was significantly lower than those recorded at the macro electrodes

suggests that charge transfer is occurring through wiring of the bacteria and not by the bacteria producing electroactive species which diffuse to the electrode.

As more is discovered about the structure and function of transmembrane charge transfer proteins, electrodes that can interact specifically with a single family of proteins could be developed using protocols similar to those developed in this thesis work. The chemistry and surface modification methods used are highly applicable to a range of biologically important molecules which could include substrate mimics for membrane bound charge transfer proteins. By this method the response of a single respiratory pathway to external stimuli could be tracked in real time. This could have significant implications for the development of drugs and antibiotics and fundamental understanding of cellular respiratory processes.